Discrete Supramolecular Architectures of Bay-linked Perylene Bisimide Dimers by Self-Assembly and Folding

Dissertation zur Erlangung des
Naturwissenschaftlichen Doktorgrades
der Julius-Maximilians-Universität Würzburg

vorgelegt von
Christina Kaufmann
aus Nördlingen

Würzburg 2018

Eingereicht bei der Fakultät für Chemie und Pharmazie am:

20.09.2018

Gutachter der schriftlichen Arbeit:
1. Gutachter: Prof. Dr. Frank Würthner
2. Gutachter: Prof. Dr. Christoph Lambert

Prüfer des öffentlichen Promotionskolloquiums:
1. Prüfer: Prof. Dr. Frank Würthner
2. Prüfer: Prof. Dr. Christoph Lambert
3. Prüfer: Prof. Dr. Ingo Fischer

Datum des öffentlichen Promotionskolloquiums:

22.11.2018

Doktorurkunde ausgehändigt am:

_____

für meine Familie

Abbreviations

α_{agg}	degree of aggregation
AcOH	acetic acid
AFM	atomic force microscopy
B3LYP	Becke-3-parameter-Lee-Yang-Parr (an exchange-correlation functional)
Br	bromine
resp.	respectively
CCl_4	tetrachloromethane
$CHCl_3$	chloroform
COSY	homonuclear correlation spectroscopy
CT	charge transfer
DCM	dichloromethane
DFT	density functional theory
DMF	dimethylformamide
DOSY	diffusion order spectroscopy
eq.	equivalents
ESI	electrospray ionization
fs	femtosecond
FLUPS	femtosecond broadband fluorescence upconversion spectroscopy
GPC	gel permeation chromatography
h	hour(s)
HMBC	heteronuclear multiple bond coherence
HOMO	highest occupied molecular orbital
HOPG	highly-ordered pyrolytic graphite
HPLC	high performance liquid chromatography
HRMS	high resolution mass spectrometry
HSQC	heteronuclear single quantum coherence
J_{Coul}	long-range Coulomb coupling
J_{CT}	charge-transfer-mediated short-range coupling
K	binding constant
K_D	dimerization constant
LUMO	lowest unoccupied molecular orbital
m	multiplet

min	minute(s)
MALDI	matrix assisted laser desorption/ionization
MCH	methylcyclohexane
mp.	melting point
MS	mass spectrometry
NMR	nuclear magnetic resonance
ns	nanosecond(s)
OLED	organic light emitting diode
PBI	perylene bisimide
ppm	parts per million
ps	picosecond
ROESY	rotating-frame nuclear overhauser enhancement spectroscopy
rpm	revolutions per minute
rt	room temperature
s	second(s)
T	temperature
TCE	1,1,2,2-tetrachloroethane
THF	tetrahydrofuran
UV	ultraviolet
Vis	visible
wt.	weight

Table of Contents

Chapter 1

–

Introduction and Aim of the Thesis

In recent decades, much efforts have been made for the investigation of supramolecular self-assembly processes of dye molecules *via* non-covalent forces.[1] In the 1930s the scientists Scheibe[2-3] and Jelley[4] studied the formation of dye aggregates in solution, by investigating pseudoisocyanine chloride in solvents of different polarity where they observed unexpected spectral changes upon aggregation.[2-3] About 30 years later, Davydov[5] and Kasha[6-8] found a way to explain these spectral changes by developing the molecular exciton theory. Based on this theory, it is known that spectral changes upon aggregation are caused by an electronic coupling between the constituent chromophores. Depending on their arrangement a classification into H- and J-aggregates can be made, where different optical signatures can be observed. For H-aggregates a hypsochromically shifted absorption band arises compared to the respective monomer band, whereas for J-aggregates one can find a bathochromically shifted absorption band.[9] Because of this spectral differentiation important structural information for the respective dye assemblies can be gained. Although, the spectral features of many dye ensembles can be rationalized by assuming conventional long-range Coulomb coupling between the chromophores several examples are known where this picture fails.[10-12] In a recent work, Spano *et al.* could demonstrate that also charge-transfer mediated exciton coupling is needed to be included for calculating the overall exciton coupling of dye aggregates.[13-16] Notably, the interference between both couplings may lead to unexpected optical properties that can be beneficial for applications, which motivates for further investigation, as not only optical properties of dye aggregates are affected by the so-called ‘exciton coupling’. Also functional properties of organic semiconductors are highly influenced where changes of the absorption and emission properties can be correlated to the structural arrangements of the respective dyes giving insights into exciton and charge carrier properties, which are relevant for (opto-) electronic[17] and photovoltaic[18-20] applications. Thus, the investigation of exciton coupling

became a central point of current research in order to gain insights into functional properties and structural information of dye aggregates.[21-24]

Due to their ideal properties perylene bisimide (PBI) dyes evolved as one of the most utilized chromophores for such kind of studies.[25] Excellent photostability[26] and easily tuneable absorption and fluorescence properties[27-28] in combination with high fluorescence quantum yields make them attractive, especially for applications in the field of organic electronics[29-30] and photovoltaics.[20, 31-32] Moreover, PBI dyes have a strong tendency to self-assemble into extended aggregate structures due to strong π-π-interactions between their chromophores,[25] which can be vividly observed by spectral changes caused by their altered photophysical properties upon aggregation.[33] As it is very difficult to investigate the structure-property relationships of such extended dye stacks with an undefined number of interacting chromophores, well defined model systems are needed for this kind of studies where the exact size and structure of the assemblies are well characterized. Therefore, the aim of this thesis is to limit the growth of PBI dyes to discrete, finite-sized supramolecular architectures in solution, which are perfectly suited for investigating fundamental questions like exciton coupling or exciton delocalization. Hereby a carefully considered design of the respective PBI dyes is necessary. Thus, bay-linked PBI dyes were selected and synthesized based on molecular modelling studies that are covalently linked by spacer units of different length and sterically demand. Following this approach discrete PBI π-stacks can be generated by *intra*molecular folding (Figure 1a) or *inter*molecular self-assembly (Figure 1b) to form well-defined double or quadruple PBI π-stacks, respectively. If the used linker unit reaches a certain length, also the formation of larger oligomeric PBI π-stacks (Figure 1c) becomes possible.

The synthetic part of this work was inspired by the former work of the Würthner group[34-36] where covalently linked PBI dyes were already investigated concerning their aggregation behaviour. But, different from previously reported examples of tethered Bis-PBI dyes[36-38] the imide positions should be utilized to introduce long, branched solubilizing alkyl chains to ensure adequate solubility in nonpolar solvents. This enables spectroscopic studies also in a wide concentration range and accordingly, here for the first time an ether functionality in bay area was used to anchor the tether. By using conventional spectroscopic methods like UV/Vis, fluorescence and NMR measurements an in-depth comparison of the molecular and optical properties of the respective PBI dyes can be elucidated in solution both, in their non-stacked and aggregated state to reveal structure-property relationships. Moreover, the spectroscopic findings could be further substantiated by quantum chemical calculations.

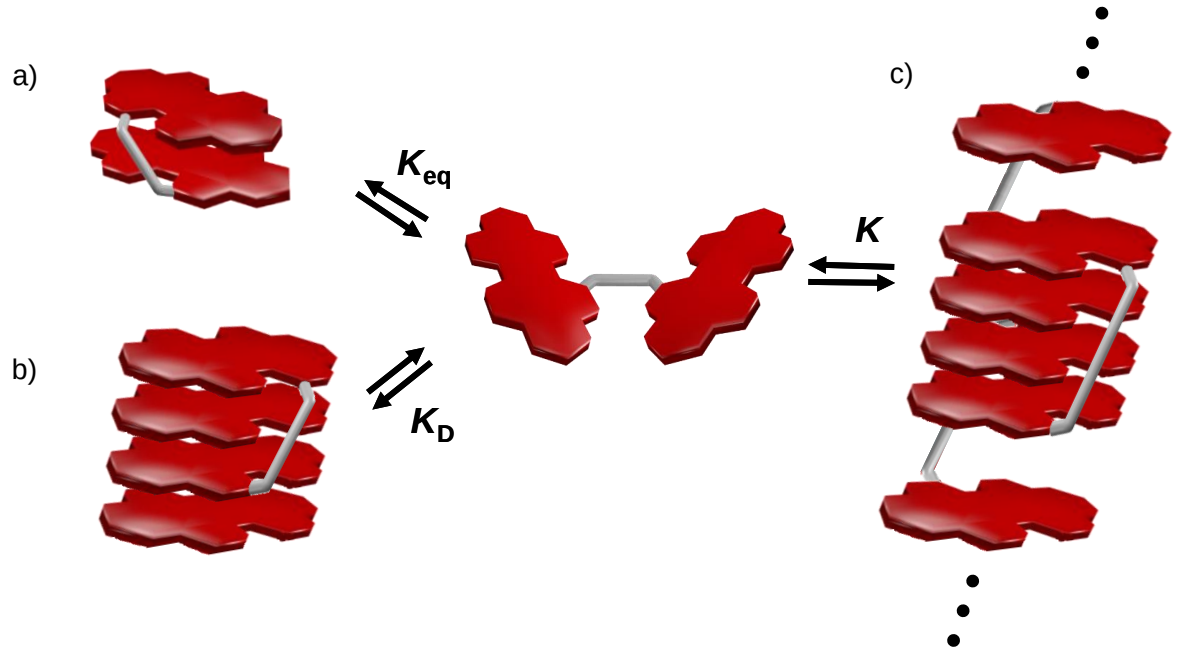

Figure 1. Schematic illustration of the self-assembly pathways of bay tethered perylene bisimide dyes into a) folda-dimers, b) bimolecular stacks of four PBI units and c) supramolecular PBI polymers in solution by using linker units of different length and sterically demand.

Chapter 2 gives an overview on planar, untwisted PBI dyes found in recent literature with focus on the investigation of their self-assembly behaviour by different analytical techniques for structural characterization, also with regard to the related theoretical background concerning Kasha's exciton theory, the exciton-vibrational coupling of PBI dyes and the influence of the short-range exciton coupling in closely π-stacked PBI aggregates. Moreover, the survey covers the introduction of finite-sized Bis-PBI dyes that are covalently linked either in the imide or bay position in order to gain discrete π-stacks with a well-defined number of interacting PBI chromophores.

Synthesis details for all Bis-PBI dyes, related reference compounds and intermediates are given in *Chapter 3*. All target compounds were fully characterized by ^{1}H and ^{13}C NMR spectroscopy in combination with high resolution ESI mass spectrometry.

PBI dimer aggregates are one of the most suited model systems for theoretical investigations to understand fundamental dye-dye interactions. Thus, by using one highly defined PBI quadruple π-stack in-depth investigations of exciton delocalization, localization and excimer formation dynamics could be performed by UV/Vis studies and broadband fluorescence upconversion spectroscopy which will be discussed in *Chapter 4*.

Chapter 5 is focused on the stacking of four bay-linked Bis-PBI dyes following the foldamer approach, which could be elucidated based on in-depth UV/Vis, CD, fluorescence and 1D and 2D NMR studies. Despite only slightly different arrangements of the π-stacked PBI chromophores, very distinct optical properties could be revealed for the respective PBI π-stacks providing fundamental insights into the interplay of long- (J_{Coul}) and short-range (J_{CT}) exciton coupling of π-stacked PBI assemblies.

Chapter 6 introduces a series of Bis-PBI dyes that show backbone-driven self-assembly into different supramolecular architectures depending on the nature of the used linker moieties. Thus, π-stacks of four PBI chromophores as well as even larger oligomeric systems could be generated by systematically extending the backbone length from 7 to 15 Å. This could be investigated by in-depth UV/Vis and fluorescence spectroscopy in combination with 2D-DOSY-NMR spectroscopy, ESI mass spectrometry and AFM measurements.

A summary of this thesis is given in *Chapter 7* and *Chapter 8* both in English and German.

In *Chapter 9*, the experimental part of this work is presented including synthetic procedures and characterization details. Furthermore, used materials and methods are described as well.

Chapter 2

–

Literature Survey

Perylene bisimide (PBI) dyes in particular, like many other π-conjugated aromatic systems, have a strong tendency to form extended aggregated structures, where spectral changes can be observed due to their altered optical properties upon aggregation.[33] However, to identify structure-property-relationships of self-assembled systems, discrete architectures are needed without any structural inhomogeneities or size-variations. One possible approach to create well-defined, small PBI architectures, is to covalently link two PBI chromophores, most conveniently either in the imide- or bay-position. This ensures a discrete interplanar distance between the two chromophores, where either an *intra*molecular folding or an *inter*molecular self-assembly of the respective Bis-PBI dyes becomes more likely than the formation of extended PBI aggregates, which facilitates the in-depth investigation of the discrete dye assemblies concerning their structural and optical properties.

In this chapter some theoretical background concerning the exciton coupling in PBI aggregates will be explained and discussed based on different examples of PBI assemblies found in recent literature. For this purpose, Kasha's exciton theory, the exciton-vibrational coupling of PBI dyes and the influence of the short-range exciton coupling in closely π-stacked PBI aggregates is introduced in the first part of this chapter (2.1). In relation to this introductory part, examples of simple, flat, non-core-twisted PBI-systems will be summarized with focus on their individual aggregation behaviour in solution (2.2). Furthermore, examples of covalently linked PBI dyes will be presented with regard to their backbone-driven self-assembly into defined molecular architectures (2.3).

2.1 Exciton Coupling in PBI Aggregates

Due to their unique spectral properties (absorption in the visible range and high fluorescence quantum yields) PBI dyes have attracted great attention during the past decade.[25, 27-28, 39] Upon self-assembly, PBI dyes reveal different spectral features depending on the molecular arrangement of the PBI units in the aggregated state (Figure 2).[25, 40-42] Consequently, the absorption maxima of PBI aggregates can either be shifted to shorter wavelengths (hypso-chromically) or to longer wavelengths (bathochromically), as shown for the PBI dyes **1**[40] (Figure 2a) and **2**[42] (Figure 2b).

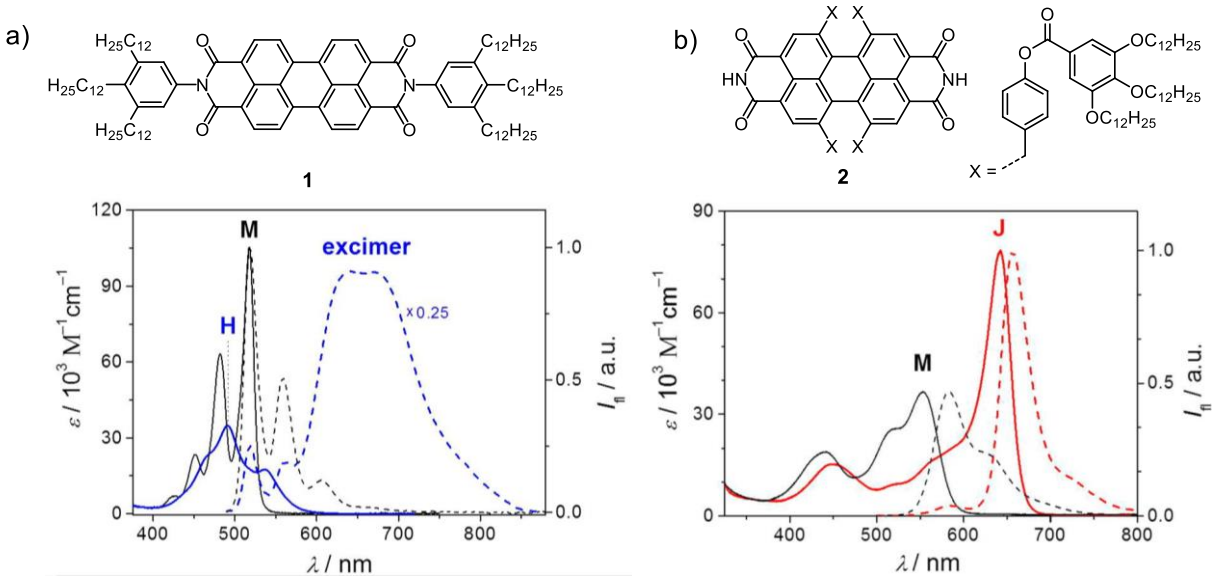

Figure 2. a) Chemical structure of PBI **1** and UV/Vis absorption (black, solid line) and emission spectra (black, dashed line) of PBI **1** at low concentration in methylcyclohexane (c_0 = 2 × 10^{-7} M, 25 °C). Also shown are the hypsochromically shifted H-aggregate absorption (blue, solid line) and bathochromically shifted broad excimer emission spectra (blue, dashed line) of PBI **1** upon aggregation at higher concentration in methylcyclohexane (c_0 = 1 × 10^{-3} M, 25 °C). b) Chemical structure of PBI **2** and UV/Vis absorption (black, solid line; c_0 = 6 × 10^{-7} M, 90 °C) and emission spectra (black, dashed line; c_0 = 2 × 10^{-7} M, 50 °C) of PBI **2** in methylcyclohexane. Also shown are the bathochromically shifted J-aggregate absorption (red, solid line; denoted as J) and emission spectra (red, dashed line) of PBI **2** in methylcyclohexane at 15 °C. Adapted with permissions from refs[40] and [42]. Copyright 2007 Wiley-VCH Verlag GmbH.

In both cases not only pronounced spectral shifts of the respective absorption maxima can be detected upon self-assembly. For both systems also altered spectral signatures of the respective absorption bands can be observed compared to the monomer absorption bands with a spectral

band broadening and a loss of intensity in the case of PBI **1** (Figure 2a) and a significant band sharpening and an increase in intensity for PBI **2** (Figure 2b).

Davydov[5] and Kasha[6-8] found a way to explain these spectral shifts to longer or shorter wavelength upon aggregation by developing the molecular exciton theory. The theory was introduced by Davydov in the 1960s, where he could describe for the first time the optical properties of organic crystals also with regard to the characteristic Davydov splitting, which can be observed in the absorption spectra of molecular crystals.[5]

In this model the excited molecule is considered as a Frenkel exciton, which means it is regarded as a strongly Coulomb bound electron hole pair.[43] After excitation the electron will be located in the lowest unoccupied molecular orbital (LUMO) whereas the corresponding hole will be located in the highest occupied molecular orbital (HOMO). If the distance between two molecules is close enough the excitation is delocalized *via* intermolecular interactions. This results in drastic changes of the absorption and emission properties of the aggregates compared to the monomeric species. Kasha extended this theory with regard to aggregation processes in solution. Thus, he could show that the Coulombic coupling (J_{Coul}) between the transition dipole moments of two dye molecules, strongly influences the optical properties of the corresponding dye assemblies.[6, 8] With that, the exciton coupling energy can be calculated using the so-called point-dipole approximation. For two parallel aligned chromophores, the exciton coupling energy can be calculated as:

$$J = \frac{\mu_{eg}^2}{4\pi\varepsilon_0 r^3} \left(\cos\alpha - 3\cos\Theta_1 \cdot \cos\Theta_2\right) \qquad (1)$$

where r is the centre-to-centre distance, α represents the rotational angle, and Θ_1 and Θ_2 are the angles between the two transition dipole moments as shown in Figure 3. ε_0 represents the vacuum permittivity.

The exciton state diagram for co-planar transition dipole moments is illustrated in Figure 3, where the transition dipole moments are tilted towards their interconnecting axis by the slip angle Θ. Based on Kasha's exciton coupling theory, it is possible to differentiate between two aggregated systems: H- and J-aggregates.[8] According to equation 1 the overall exciton coupling energy J is positive for chromophores that are aligned in a "side-by-side" arrangement. Here the transition dipole moments are arranged parallel to each other ($\Theta = 90°$) which results in two exciton states. The lower exciton state is forbidden, because here the transition dipole moments are coupled in an out-of-phase fashion, whereas an in-phase coupling results in a higher exciton state, which is allowed. This causes a hypsochromic shift of the absorption

maximum compared to the optical signatures of the monomeric chromophore. These dye assemblies are called H-aggregates (H for hypsochromic). Because of the forbidden lower exciton state these aggregates usually show prominent fluorescence quenching and large Stokes shifts.[44-45] A decrease of the slip angle Θ results in a reduced energy difference $2J$ between the two exciton states until the magic angle is reached at $\Theta = 54.7°$, where the exciton coupling energy J has a value of zero. This special case corresponds to the crossing point in Figure 3 where two degenerated exciton states are formed.

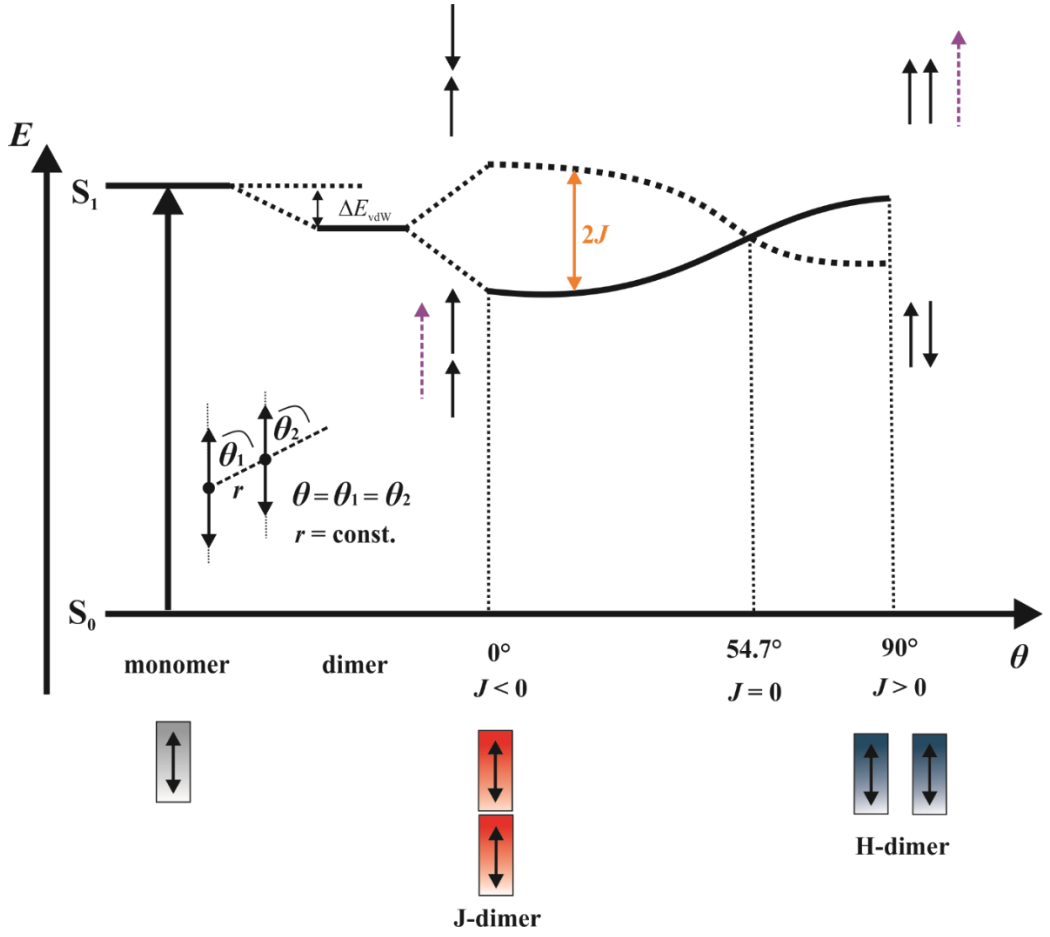

Figure 3. Exciton state diagram of two chromophores with parallel alignment of their coupled transition dipole moments ($\Theta = \Theta_1 = \Theta_2$) regarding the influence of the slip angle Θ between two co-planar transition dipole moments at a constant distance r.

By further decreasing the slip angle Θ ending up in a "head-to-tail" arrangement of the chromophores ($\Theta = 0°$), the sign of the exciton coupling energy J becomes negative. In this case, the higher exciton state is forbidden, because of an out-of-phase coupling of the transition dipole moments resulting in a repulsive Coulomb interaction, whereas an in-phase coupling results in a lower exciton state, which is allowed. This causes a bathochromic shift of the

absorption maximum compared to the absorption band of the monomeric chromophore.[9] These dye assemblies are called J-aggregates (J for Jelley[4, 46] or Scheibe-aggregates[2-3]). In contrast to H-aggregates, now the lowest exciton state is strongly allowed which commonly results in high fluorescence quantum yields and small Stokes shifts.[9]

For PBI dyes, which can form both H- and J-type aggregates,[47-49] it is not possible to fully elucidate their altered optical properties upon aggregation by only using Kasha's exciton theory. This can be nicely seen from Figure 2, where additionally changes of the spectral signatures for PBI **1** and **2** can be detected in the aggregated state, like a spectral band broadening / sharpening or drastically decreased / increased absorption band intensities, as it can be observed for several other PBI dyes.[25, 50-51]

This can be explained due to the aromatic carbon-carbon stretching vibrations in PBI chromophores where vibronic progression of the spectral signatures results in an exciton-vibrational coupling between the chromophores.[52-54] Thus, to adequately describe the absorption spectra of respective PBI dye assemblies vibrational contributions have also to be taken into account.[55-56] This phenomenon was investigated by Würthner and Engel *et al.* for PBI dye assemblies *via* quantum dynamic calculations (Figure 4).[52-53, 57]

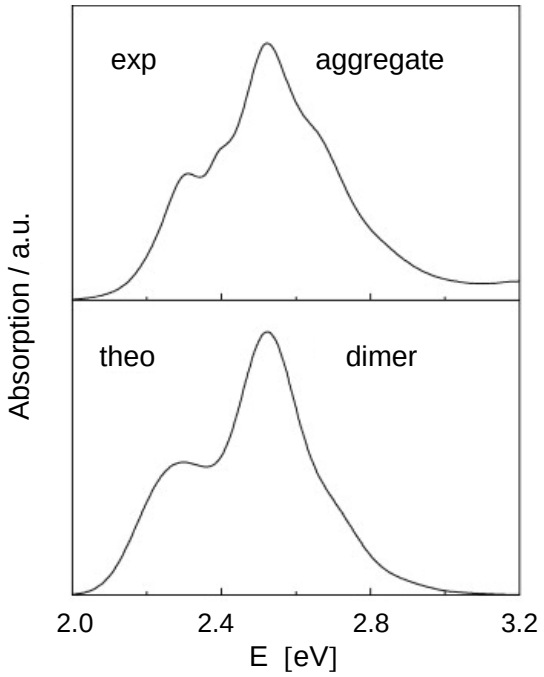

Figure 4. Comparison of the measured UV/Vis absorption spectrum of PBI **1** (Figure 2a) H-aggregates at a concentration of c = 2.2 x 10^{-4} M in methylcyclohexane and the calculated UV/Vis absorption spectrum of a PBI **1** H-dimer with a resolution of 196 meV. Adapted with permissions from ref. [52] Copyright 2006 Elsevier.

For PBI **1** H-dimers (Figure 2a) a reversal of the 0–0 and 0–1 absorption band intensities can be observed both experimentally and theoretically (Figure 4) in addition to a hypsochromically shifted absorption maximum compared to the respective monochromophoric reference dye.[52] These drastic changes of the oscillator strengths are based on a vibrational broadening of the electronic transitions, typically observed in the so called intermediate coupling regime, where the vibrational frequency ω ($\approx$ 1400 cm^{-1}) is comparable to the exciton coupling energy J.[53] Also for PBI **2** J-dimers (Figure 2b) similar observations can be made with a drastically increase of the ratio of the 0–0 and 0–1 absorption bands in addition to a prominent bathochromic shift of the absorption maximum compared to the monomeric species.

According to Spano *et al.*[56] the excitation in an aggregated system can be described by Frenkel excitons or so-called excitonic polarons, consisting of a vibronically excited central molecule surrounded by vibrationally excited molecules. This can be illustrated by a ball on a mattress, where the ball and the spring directly underneath correspond to the vibronically excited molecule, while all other neighbouring springs correspond to the surrounding vibrationally excited molecules. With this model the exciton coupling and its influence on the optical properties of aggregated systems can be investigated with regard to exciton-vibrational couplings, as it is demonstrated in Figure 5.[56] Here, the calculated absorption (blue lines) and emission spectra (red lines) of an linear H- and J-aggregate is shown containing 20 molecules with nearest-neighbour-only coupling in dependence on the exciton coupling strength.[56] For a weak and intermediate coupling between the interacting chromophores only a small blue (red) shift of the absorption maxima with a change of the 0–0 and 0–1 absorption band intensities can be observed for H- (J-) aggregates compared to the monomer spectrum (grey line). This is in very good agreement with the observations for PBI **1** H-dimers,[52] which also reveal an intermediate coupling between their chromophores.

By further increasing the exciton coupling strength (strong coupling regime) the absorption band of H- (J-) aggregates is shifted more drastically to shorter (longer) wavelengths. Usually, perfectly aligned H-aggregates do not show pronounced emission properties because of the forbidden lowest exciton state, but due to additional vibrational couplings, sideband emission becomes allowed (Figure 5, left, red lines), which explains why for H-aggregates with vibronic contribution considerably high fluorescence quantum yields can be measured.

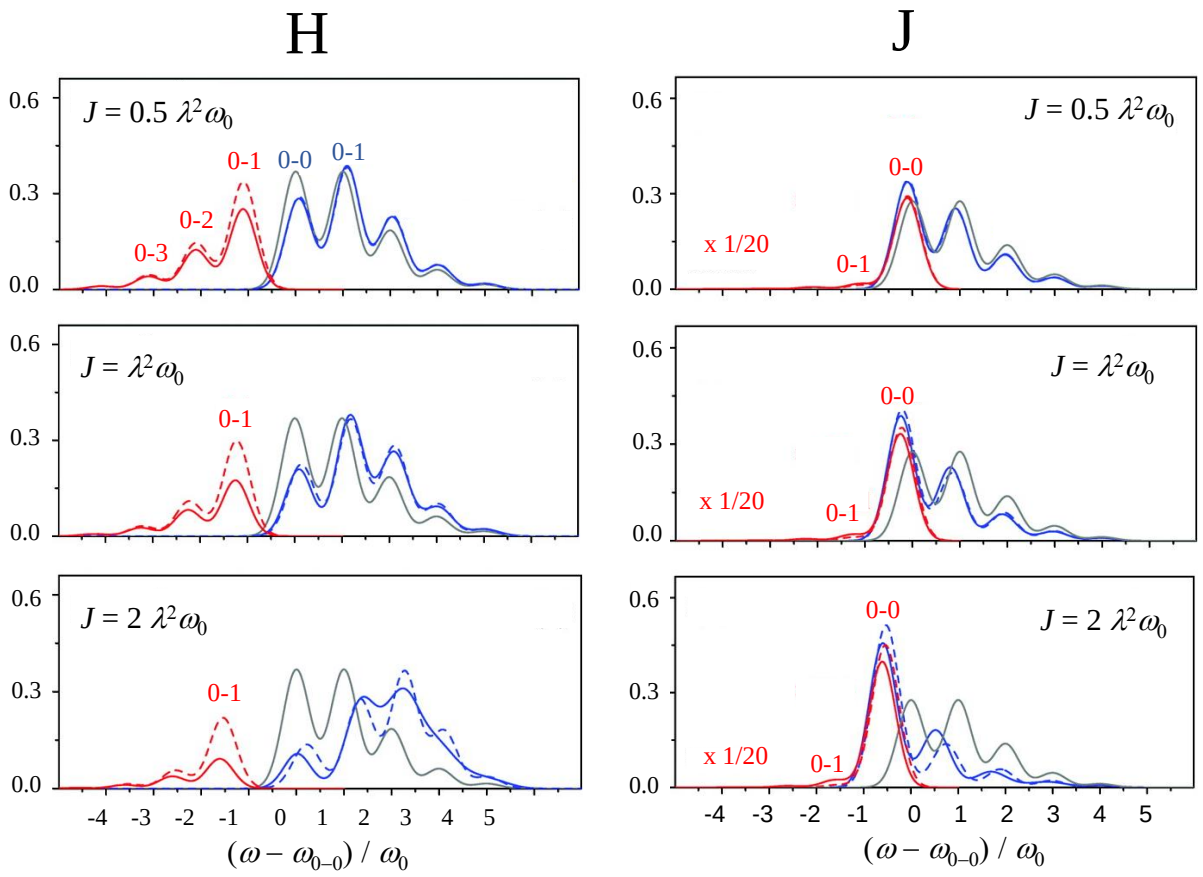

Figure 5. Calculated absorption (blue) and fluorescence (red) spectra for ideal H-aggregates (left) and ideal J-aggregates (right) containing 20 molecules with nearest-neighbour-only coupling for different exciton coupling energies. In all spectra the vibrational frequency ω_0 is taken to be 1400 cm^{-1} and J and λ^2 represent the exciton coupling energy and the Huang-Rhys factor, respectively. Solid spectra are evaluated using one- and two-particle states, while dashed spectra use only one-particle states. The grey solid lines represent the monomeric absorption spectra. Adapted with permissions from ref.[56] Copyright 2010 American Chemical Society.

Although the spectral features of many PBI dye aggregates can be rationalized by assuming conventional Coulomb coupling between the chromophores along with vibrational contributions,[40, 58-60] several examples are known where this picture fails.[10-12]

For short interchromophoric distances as present in PBI π-stacks, the wave function overlap of two interacting chromophores also allows charge transfer processes. Due to these additional interactions it is needed to include charge-transfer-mediated excited states for calculating the overall exciton coupling which can be significant and thus, highly influence the absorption properties of the corresponding aggregates.[14, 16, 54, 61] These charge transfer (CT) states are created when an electron in the LUMO of the excited molecule is transferred to the LUMO of a neighbouring molecule in the ground state. Same holds true for the corresponding hole

transfer of an electron in the HOMO of an unexcited neighbouring molecule to the HOMO of the excited molecule.[14, 62] The importance of charge-transfer-mediated excited states and its influence on the optical properties of aggregates was first investigated by Scholes *et al.*[13, 63] Spano extended this theory including exciton-vibrational coupling shown by π-conjugated systems.[54, 64]

Under the assumption that the charge-transfer state and the local Frenkel exciton state are well separated (perturbative limit), the exciton coupling energy for the short-range coupling can be calculated by: [14, 54]

$$J_{CT} = -2\frac{t_e t_h}{E_{CT} - E_{S_1}}\ ,\ \left|E_{CT} - E_{S_1}\right| \gg |J_{Coul}|, |t_e|, |t_h| \qquad (2)$$

where $E_{CT} - E_{S_1}$ is the energy difference between the charge transfer and the local Frenkel exciton state and t_e and t_h are the electron and hole transfer integrals, respectively.

As t_h and t_e derive from the overlap between neighbouring HOMOs and LUMOs, respectively, they are highly sensitive to small transvers displacements of the interacting chromophores, as shown by Kazmeier and Hoffman.[65] As it can be seen from equation 2, J_{CT} can be either positive or negative depending on the respective signs of the charge transfer integrals and the energy difference $E_{CT} - E_{S_1}$. If the latter bears a positive sign, which is normally the case for PBI dyes,[66] this results in a J-like short-range coupling for $t_e t_h > 0$ and in a H-like short-range coupling for $t_e t_h < 0$. Due to the high sensitivity of the charge transfer integrals to small transverse displacements, J_{CT} is highly influenced by a changed packing arrangement of the respective interacting chromophores, as it can be seen from Figure 6.[54] For J_{Coul} a longitudinal slip of > 6 Å along the long-axis of the perylene core is needed to induce only one change from positive to negative sign, corresponding to the transformation from a H- to a J-aggregate. In contrast, for J_{CT} the sign changes almost three times over the same distance. Thus, only a longitudinal slip of approximately 1.6 Å is needed for the first H- to a J-aggregate transformation in the case of J_{CT}, giving rise to a whole variety of different geometries ending up in either constructive or destructive interferences between J_{Coul} and J_{CT}.[54]

This enables a new classification of aggregates with unexpected optical properties, for which a new nomenclature (HH, HJ, JH or JJ) was introduced by Spano,[54] where the first / second letter represents the long-range Coulomb coupling J_{Coul} / short-range charge-transfer mediated coupling J_{CT} and small / capital letter describe weak / strong coupling. Regarding to electronic devices this becomes very important for developing promising organic materials. For solar cell applications materials with strong exciton coupling (H-type aggregates) between their

chromophores would be highly suitable as a rapid energy transport would be ensured. On the opposite, J-type aggregates would be promising candidates in the field of organic light emitting diodes (OLED) due to their strong emission properties.[54]

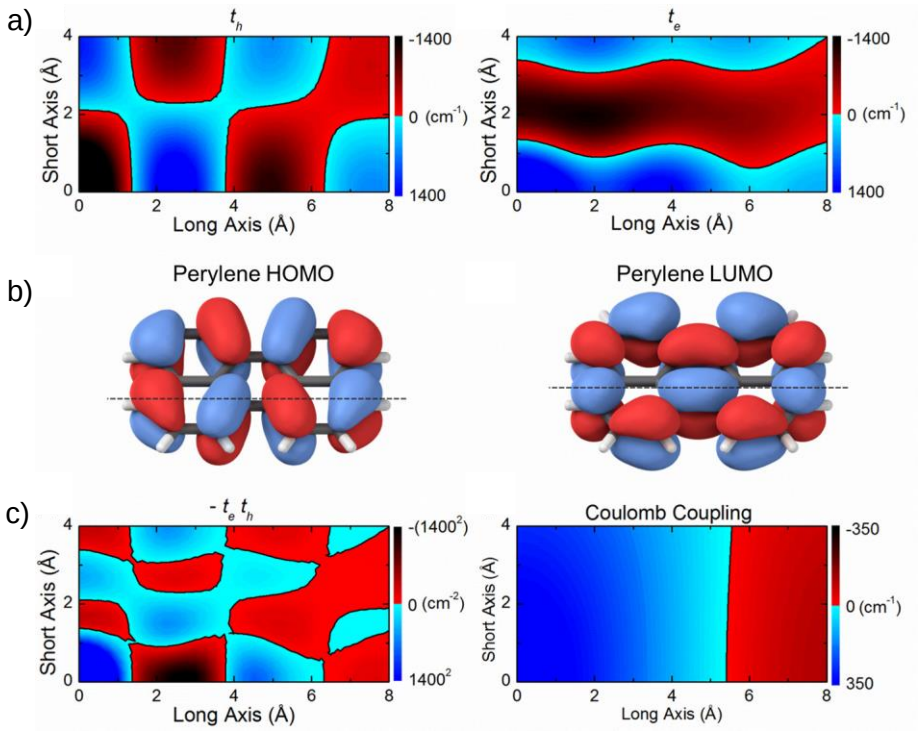

Figure 6. a) Plots of the hole transfer integral t_h (left) and electron transfer integral t_e (right) of a perylene dimer with a stacking distance of 3.5 Å between the chromophores against the transverse displacement evaluated from DFT calculations (B3LYP, cc-pVDZ). b) Calculated HOMO (left) and LUMO (right) of a PBI unit (DFT (B3LYP, cc-pVDZ). c) Plots of the product of the charge transfer integrals $-t_e t_h$ (left) and the Coulomb coupling J_{Coul} (right) against the transverse displacement evaluated from TDDFT (B3LYP, cc-pVDZ). In all panels the red (blue) regions correspond to a J- (H-) type coupling. Adapted with permissions from ref.[54] Copyright 2017 American Chemical Society.

2.2 Self-Assembly of Core-Unsubstituted PBI Dyes into Extended π-Stacks

In general, the aggregation behaviour of PBI dyes is highly influenced by the variety of substituents, that can be introduced to the perylene core or in the imide positions. Unsubstituted, planar PBI chromophores exhibit a much stronger tendency to form extended aggregate structures compared to their substituted analogues. During the past decade a large number of

core-unsubstituted PBI dyes have been investigated concerning their aggregation behaviour both in solution and the solid state.[25, 67-72]

Hereafter, however, only some specific examples will be discussed in more detail in order to highlight their special optical properties, as for example PBI **3**, which was recently reported by Würthner and co-workers concerning its self-assembly behaviour in solution.[73] The concentration-dependent UV/Vis absorption spectra of core un-substituted PBI **3** in methyl-cyclohexane are depicted in Figure 7, where significant spectral changes can be observed by increasing concentration, with a hypsochromic shift of the absorption maximum and an almost complete vanishing of the optical fine structure (spectral line broadening) due to strong π–π–interactions between the planar PBI chromophores.[73]

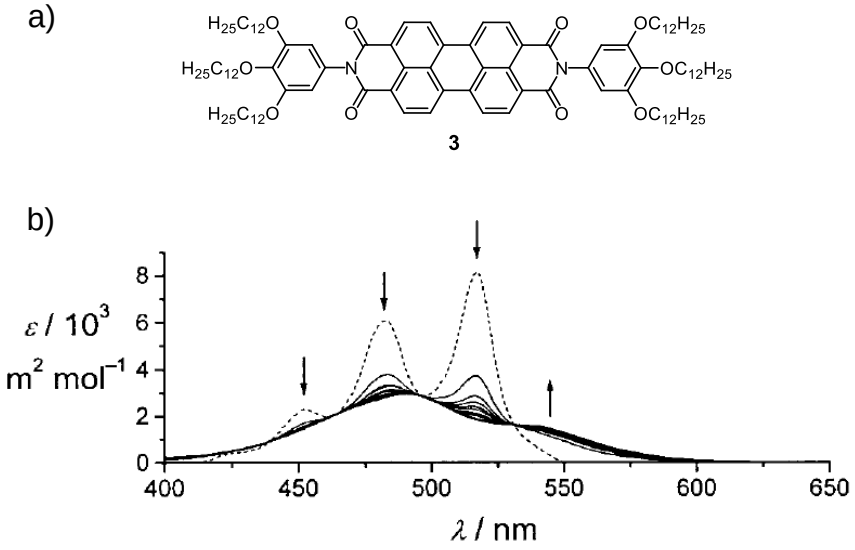

Figure 7. a) Chemical structure of PBI **3**. b) Concentration-dependent UV/Vis absorption spectra of PBI **3** (c_0 = 10^{-7} – 10^{-5} M) in methylcyclohexane. Arrows indicate changes in intensity upon increasing concentration. Also shown are the spectra of the monomeric and aggregated species (dotted lines) calculated from the respective data set. Adapted with permissions from ref.[73] Copyright 2001 WILEY-VCH Verlag GmbH.

The corresponding aggregation mechanism for supramolecular self-assembly processes can be clarified by fitting the experimental data with different mathematical models, as the monomer-dimer or the isodesmic model.[33, 74] For the monomer-dimer model an equilibrium between two species, *i.e.* monomer and dimer with differing absorption spectra, is considered. Thus, only one of the two π-surfaces is involved in the aggregation process. In contrast, the isodesmic model assumes the involvement of both π-surfaces with equal binding constants for all binding events, leading to one-dimensional architectures independent of the final size of the aggregate.

Additionally, the isodesmic model can be further modified by assuming different binding constants for both, the formation of the initial binding event (nucleus step) and the elongation process. If the nucleus formation is less favoured than the elongation, the aggregation process is called cooperative. If the elongation is less favoured latter than the formation of the nucleus, the aggregation process is called anti-cooperative. This case appears to be very likely if dimerization is favoured for electronic or steric reasons.

Indeed, for PBI **3** the concentration-dependent data could be properly fitted with the isodesmic model ending up with a high binding constant $K \approx 10^7$ L mol^{-1} in methylcyclohexane. The altered optical properties of PBI **3** upon aggregation can be explained by exciton theory, where close π–π–distances between PBI chromophores result in a strong exciton coupling of their transition dipole moments leading to completely different spectral features of the resulting dye assemblies. Consequently, small distances between the PBI chromophores lead to dramatic changes of the optical properties.[73] By performing fluorescence studies of PBI **3** a drastically decreased fluorescence quantum yield could be found, which can be attributed to a photo-induced electron transfer from the electron-rich trialkyloxyphenyl groups to the electron-poor PBI unit.[73]

Similar results were obtained for PBI **1** (*vide supra*) containing trialkylphenyl groups, instead of trialkoxyphenyl groups in the imide positions (Figure 2a).[40, 75] Also in this case a hypsochromic shift of the absorption maximum with a reversal of the 0–0 and 0–1 absorption band intensities could be observed with a significant band broadening by performing concentration- and temperature-dependent UV/Vis studies in methylcyclohexane (Figure 8a and b) revealing a H-type exciton coupling between the interacting chromophores.[40] Fitting analysis of the concentration-dependent data suggests an isodesmic growth for PBI **1** into extended π–stacks upon aggregation with a binding constant of $K = 9.7 \times 10^4$ L mol^{-1} in methylcyclohexane. This binding constant is much smaller than the one observed for structurally related PBI **3**[73] demonstrating the high influence of the individual imide-substituents on the aggregation strength, as it can be observed for many other PBI dyes.[67-72]

Interestingly, in contrast to PBI **3**, PBI **1** exhibits strong fluorescence properties with a high fluorescence quantum yield of 65% in methylcyclohexane.[40] By performing concentration- und temperature-dependent fluorescence measurements (Figure 8c and d), a new, very broad emission band with a drastic bathochromic shift could be observed at higher concentrations and lower temperatures. These spectral features could be explained by in-depth theoretical studies, where a rotational displacement (~ 30°) of the π-stacked PBI **1** chromophores is preferred in

the ground state, whereas in the excited state the energy minimum was found for an almost perfect "side-by-side" arrangement (~ 0°) of the PBI units.[40]

Thus, according to Figure 3, the UV/Vis and fluorescence spectra of PBI **1** can be rationalized by the rotational displacement of the π-stacked PBI chromophores, which partially allows the forbidden optical transition for H-aggregates, resulting in a considerably high fluorescence quantum yield for PBI **1** in methylcyclohexane.

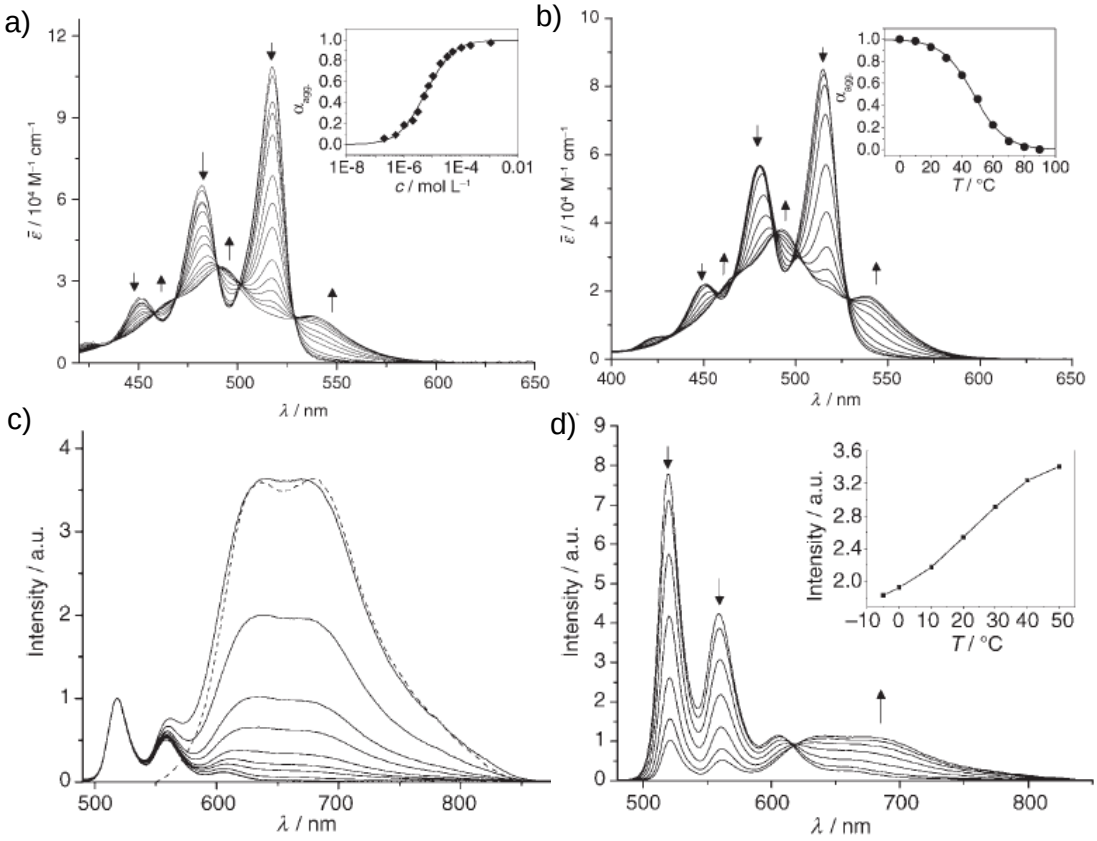

Figure 8. a) Concentration-dependent UV/Vis absorption spectra of PBI **1** (c_0 = 2 x 10^{-7} - 1 x 10^{-3} M) in methylcyclohexane at room temperature. Arrows indicate the changes upon increasing concentration. Inset: Plot of α_{agg} against the concentration c at λ = 517 nm fitted by the isodesmic model. b) Temperature-dependent UV/Vis absorption spectra of PBI **1** from 0 to 90 °C (c_0 =5.0 x 10^{-4} M). Arrows indicate the changes upon decreasing temperature. Inset: Plot of α_{agg} against the temperature T. c) Concentration-dependent fluorescence spectra of PBI **1** (λ_{ex} = 469 nm, c_0 = 2 x 10^{-7} - 2 x 10^{-4} M) in methylcyclohexane (solid lines) and as thin film (dashed line) at room temperature. d) Temperature-dependent fluorescence spectra of PBI **1** from –5 to 50°C (λ_{ex} = 469 nm, c_0 =1 x 10^{-6} M) in *n*-hexane. The arrows indicate the changes upon increasing concentration and decreasing temperature, respectively. Inset: Plot of the fluorescence intensity against the temperature T. Adapted with permissions from ref.[40] Copyright 2007 Wiley-VCH Verlag GmbH.

However, in-depth studies of the exact structure of supramolecular dye stacks in solution require well-defined orientations of the chromophores as given in the crystalline state. Otherwise revealing the structure-properties-relationships of the assembled systems remains very difficult, as it was the case for PBI **1**. Here it was not possible to investigate the structure-property-relationships of the corresponding aggregates *via* temperature-dependent NMR studies due to highly complex ^{1}H NMR spectra of PBI **1** in [(D_{14})MCH)], where drastic changes could be observed upon aggregation. Therefore, the individual proton signals could not be clearly assigned to the corresponding perylene protons. In striking contrast, simple pattern of sharp ^{1}H NMR signals could be found for PBI **1** in $CDCl_3$, where only monomeric species are present.

Nevertheless, based on UV/Vis studies and quantum chemical calculations self-assembly of PBI **1**[40, 75] and PBI **3**[73] into helical columnar π-stacks seemed to be mostly likely. But, as no chiral information is given for PBI **1** or **3**, the resulting helical assemblies are expected to form a racemic mixture of either *M* or *P* conformers, with equal intermolecular interaction energies. By introducing chiral side chains to the PBI chromophores, a preferred helicity can be gained where non-racemic helical supramolecular architectures can be built. Indeed, PBI **4** (Figure 9a) with six appended chiral side chains affords helical superstructures upon self-assembly, that were studied by concentration-dependent UV/Vis and CD spectroscopy in methylcyclohexane. Again, sharp and well-resolved absorption bands could be observed for PBI **4** at low concentrations (Figure 9b) in methylcyclohexane at room temperature.[41] By increasing concentration, a hypsochromic shift of the absorption maximum from 517 nm to 491 nm was induced, accompanied by a dramatic decrease of the extinction coefficient from approximately ε_{max} = 95000 $M^{-1}\,cm^{-1}$ to 33000 $M^{-1}\,cm^{-1}$. Moreover, a second absorption band could be observed at longer wavelength (535 nm) with decreased band intensity. These spectral changes can be attributed to a strong exciton coupling between the closely π–π–stacked chromophores of PBI **4**. Interestingly, whereas three well-defined isosbestic points (469, 502 and 529 nm) could be observed during the concentration-dependent UV/Vis measurements (Figure 9b), no isodichroic points could be detected by performing concentration- and temperature-dependent CD studies (Figure 9c). Thus, it was proposed that at low concentrations and high temperatures the formation of PBI **4** *M*-dimers is preferred, which then further grow into extended right-handed π-stacks with *P*-configuration at higher concentrations and low temperatures (Figure 9d).[41, 52]

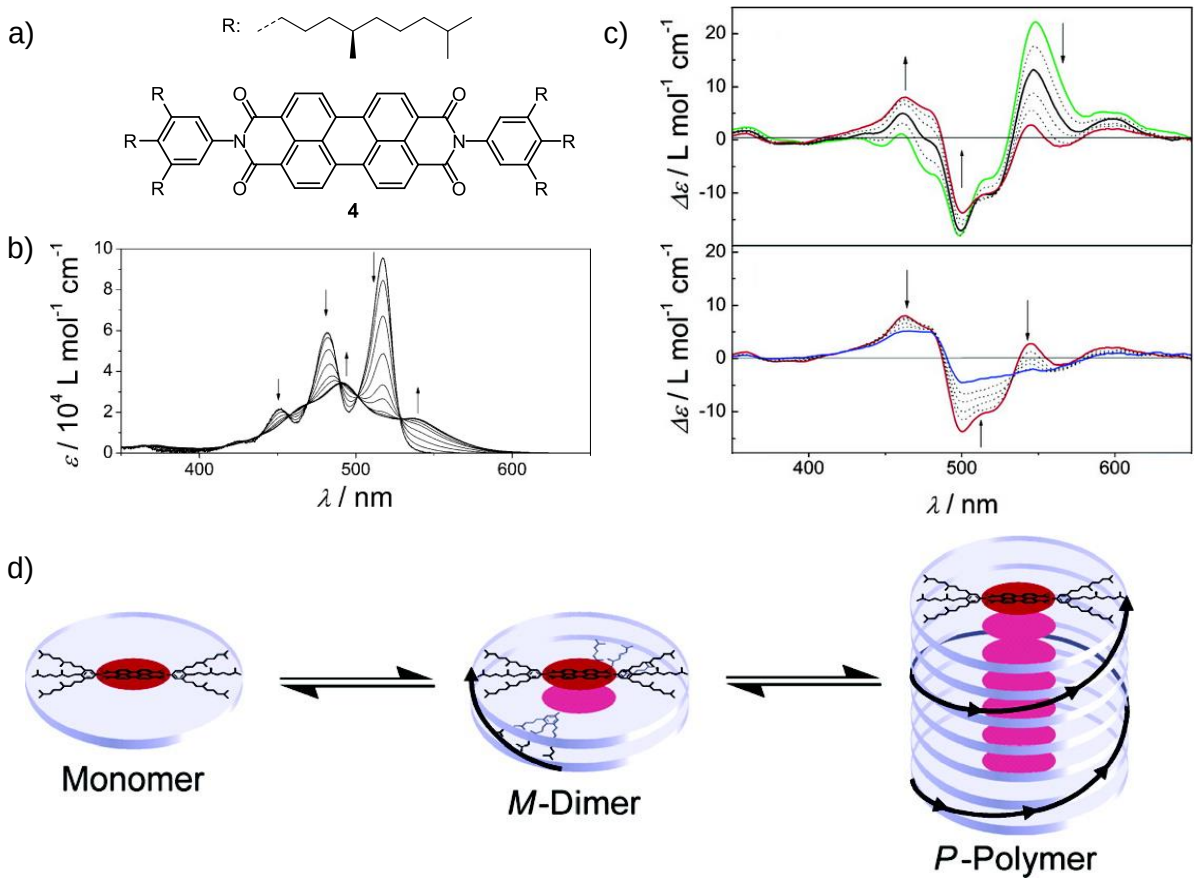

Figure 9. a) Chemical structure of PBI **4**. b) Concentration-dependent UV/Vis absorption spectra of PBI **4** (c_0 = 10^{-6}–10^{-3} M) in methylcyclohexane at room temperature. Arrows indicate the changes upon increasing concentration. c) Temperature-dependent CD spectra of PBI **4** (2 x 10^{-3} M) in methylcyclohexane from –10 °C (green line) to 40°C (red line) and from 40° to 90°C (blue line) in intervals of 10°C. Arrows indicate changes upon increasing temperature. d) Proposed equilibrium between monomer and aggregates of PBI **4** in solution, where *M*-dimers are formed at low concentrations or high temperatures which then further grow into extended right-handed π-stacks with *P*-configuration. Adapted with permissions from ref.[41] Copyright 2007 American Chemical Society.

2.3 Backbone-Directed Self-Assembly of Covalently Linked Bis-PBI Dyes

Different from simple PBI dyes which reveal an isodesmic aggregation growth into extended aggregate structures, covalently linked Bis-PBI dyes are well suited to form small, finite-sized architectures for investigating structure-property relationships.[25]

For such studies highly defined spacer moieties with regard to size and geometry are needed to ensure a distinct distance between the two π-scaffolds for studying the through space coupling of the corresponding chromophores. To generate covalently linked PBI dyes, two PBI units can be either linked in the imide or bay position.

2.3.1 Imide-linked Bis-PBI Dyes

20 years ago, one of the first examples of covalently linked PBI dyes that were linked in the imide position by just a rigid single bond was investigated by Langhals and Jona[76] (PBI **5**, Chart 1). Due to its linear arrangement, PBI **5** shows characteristic J-type coupling properties in chloroform with a bathochromically shifted absorption maximum (535 nm), a significantly sharpened absorption band with an increased extinction coefficient (ε_{max} = 241800 M^{-1} cm^{-1})[76] and an increased ratio A_{0-0}/A_{0-1} of the 0–0 and 0–1 absorption band intensities compared to a related reference compound bearing only one PBI unit (ε_{max} = 85700 M^{-1} cm^{-1}).[77] This can be attributed to the exciton-vibrational coupling between the interacting chromophores of PBI **5** as discussed in *Chapter 2.1*.

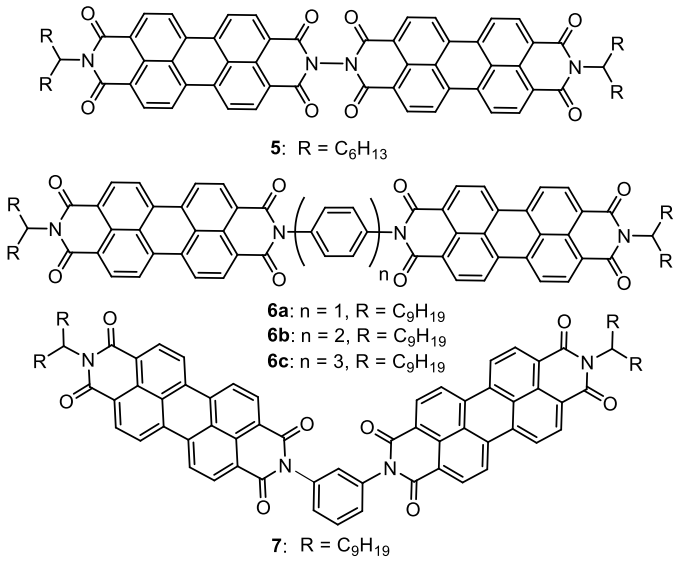

Chart 1. Imide-linked PBI dyes **5**-**7**.

By connecting two PBI chromophores with rigid π-conjugated *para*-(poly)-phenylene bridges, longer distances between the interacting π-scaffolds can be achieved (**6a**–**c**, Chart 1) which was investigated by Adams *et al*.[78] By performing transient fluorescence and femtosecond transient absorption spectroscopy they could show that the size of the bridging unit, the molecular arrangement of the chromophores and the polarity of the solvent, play an important role for the respective electron transfer in these dimers.[78]

Covalently linked Bis-PBI dyes can also be generated by utilizing non-linear spacer units, like in the case of PBI **7**[79] (Chart 1), where a *meta*-phenylene linker unit was used to connect two PBI chromophores in the imide position. Compared to its linear analogous PBI **6a**, PBI **7** displays a slightly larger bathochromic shift of the absorption maximum[79] which was

attributed to the shorter distance between the PBI π-scaffolds. This corroborates the delicate influence of the distinct molecular arrangement of the interacting chromophores on the optical properties.

By using rigid backbones of discrete length and steric demand it is further possible to pre-organize the constituent chromophores to their π-π-interactions. This could be nicely demonstrated for chiral PBI **8a**[80] and PBI **8b**[81] (Chart 2) that were investigated by Langhals *et al*., where the respective biphenylene (**8a**) and binaphthylene (**8b**) bridges cause an almost perpendicular arrangement (86 °) of the chromophores with fixed geometry because of the rigidity of the spacer units that do not allow any rotation around the linker axis.

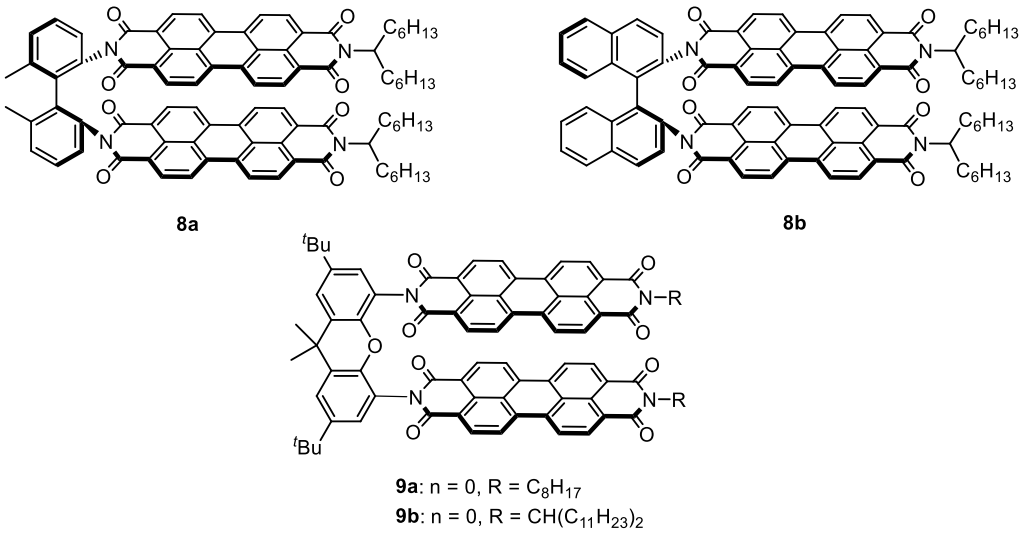

Chart 2. Imide-linked PBI dyes **8a**,**b** and **9a**,**b**.

Quantum chemical calculations indicate two almost planar chromophores for PBI **8b** with a separation of about 3 Å and a partial overlap of the π-scaffolds.[59, 80-81] The decreased distances between the two PBI chromophores compared to the in-line arranged PBI dyes in Chart 1, causes drastic changes in the absorption spectra with a decreased 0–0 absorption band and an additional shoulder at lower wavelength, strongly indicating H-type exciton coupling between the π-scaffolds. Similar close distances between the two PBI units can be achieved by using xanthene derivatives as bridging units, as it was done by Wasielewski and co-workers.[37, 82] First, they investigated the influence of imide substituents on the optical signatures of the respective PBI dyes by using linear alkyl chains (**9a**, Chart 2) compared to branched alkyl chains (**9b**, Chart 2). For both dyes H-type exciton coupling and broad excimer emission bands could be observed, where PBI **9a** exhibits a more decreased ratio of the 0–0 and 0–1 absorption

bands A_{0-0}/A_{0-1} = 0.69 and a significant lower fluorescence quantum yield of Φ_{Fl} = 2% compared to PBI **9b** (A_{0-0}/A_{0-1} = 0.91, Φ_{Fl} = 19%).[37] This substantiates a more pronounced H-type coupling for PBI **9a** bearing linear and with that less sterically demanding alkyl chains in the imide positions. Furthermore, Wasielewski and co-workers gained deeper insight into the influence of the molecular arrangement on the photophysical properties of the respective PBI dyes by varying the size of the phenylene-bridge between one PBI chromophore and the backbone (**10a** and **b**, Figure 10).[82]

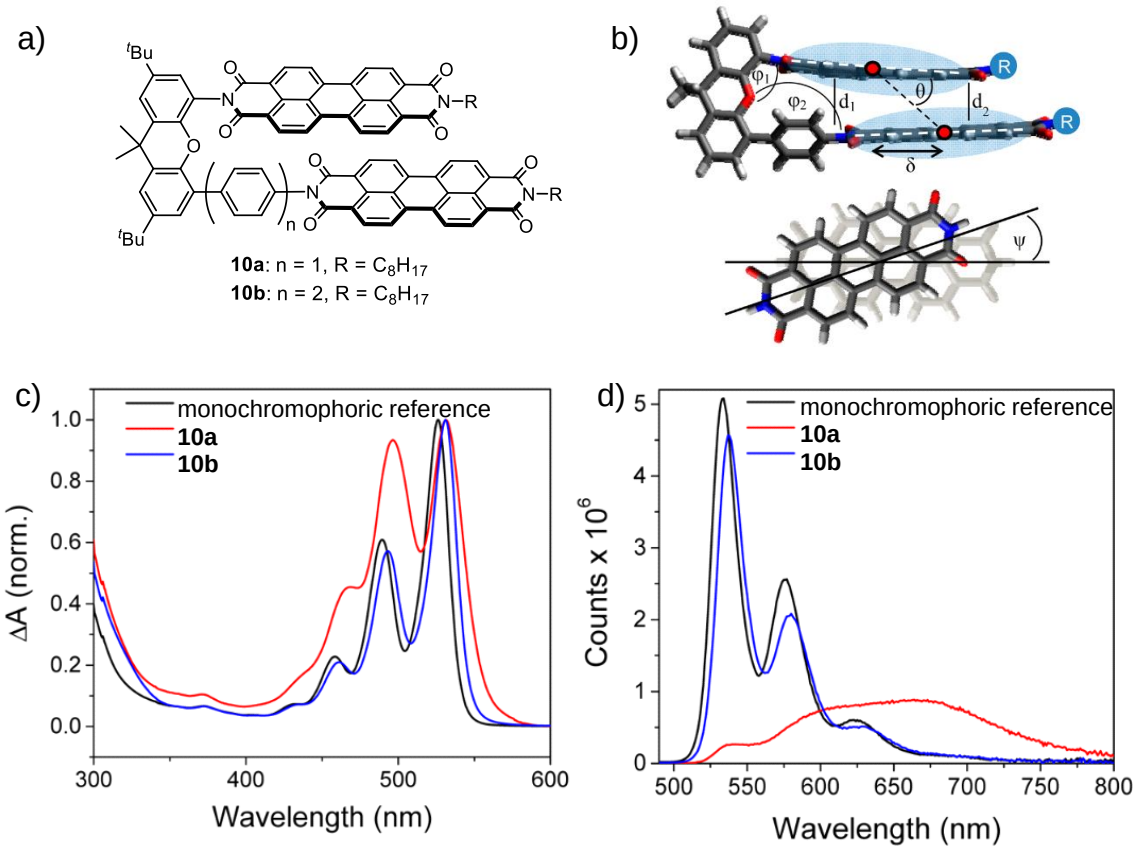

Figure 10. a) Chemical structures of PBIs **10a** and **b**. b) Schematic geometric structure of PBI **10a**. φ represents the dihedral angle between the PBI chromophores and the spacer unit. δ is the centre-to-centre distance between the PBI centres of mass (red dots), θ is the angle between the transition dipole moment, ψ is the rotational displacement angle and d_1, d_2 are the distances between the π stacked PBI units near the spacer and the terminal imide residues, respectively. c) UV/Vis absorption and d) fluorescence spectra of PBI **10a** (red), PBI **10b** (blue) and a monochromophoric reference compound (black) in toluene. Adapted with permissions from ref.[82] Copyright 2013 American Chemical Society.

This causes a longitudinal slip of the PBI chromophores (Figure 10b) which highly influences the energy splitting of the respective excitonic states (Figure 3). Hereby, the centre-to-centre distances δ (Figure 10b) between the two PBI chromophores could be increased from 3.5 Å

(**9a**) to 8 Å (**10b**). Thus, by performing UV/Vis absorption and fluorescence studies in toluene neither exciton coupling (Figure 10c) nor excimer emission (Figure 10d) could be observed for PBI **10b**, whereas PBI **10a** exhibits typical H-type exciton coupling with a drastically decreased ratio of the 0–0 and 0–1 absorption bands (Figure 10c) and a broad bathochromically shifted excimer emission band (Figure 10d). Therefore, other deactivation pathways except the formation of an excimer seem to be more favoured for PBI **10b**, like *e.g.* the formation of the triplet state, which can be reached either by conventional intersystem crossing (ISC) or singlet excitonic fission.[83] This demonstrates, that the evolution of an excimer becomes less important for larger distances and that the centre-to-centre distance drastically influences the photo-physical properties of PBI dyes.[82]

In contrast to the smaller linker units shown above, a more sterically demanding calix[4]arene spacer unit was used by Würthner and co-workers to generate discrete PBI-dimer π-stacks upon folding (PBI **11**, Figure 11).[84]

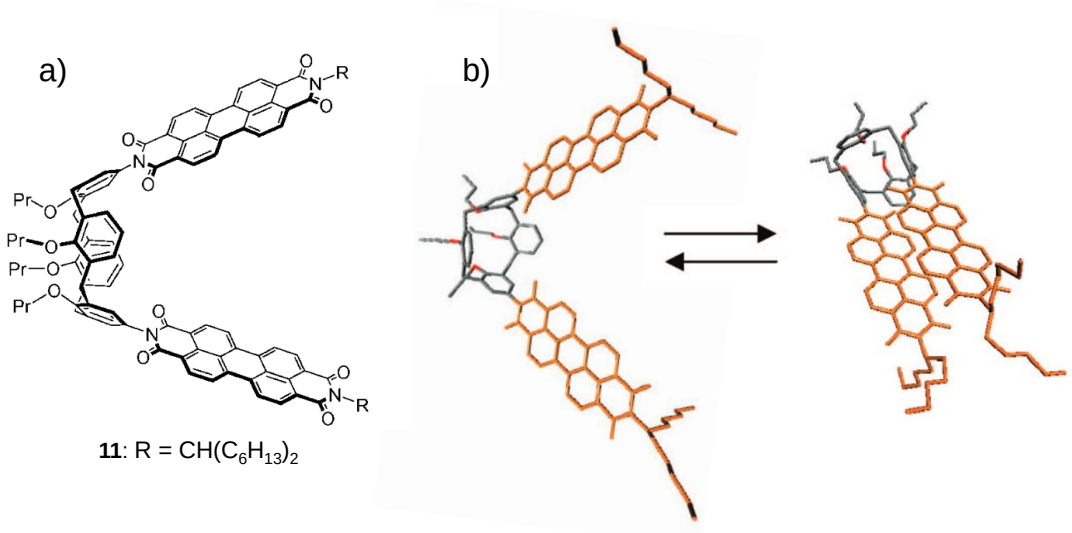

Figure 11. a) Chemical structure of PBI **11.** b) Schematic representation of the folding process of PBI **11**. Molecular structures were obtained from force field calculations (Amber 9, potential GAFF with AM1-BCC partial charges). Adapted with permissions from ref.[84] Copyright 2008 American Chemical Society.

Indeed, it could be shown that PBI **11** reveals characteristic absorption features of independent, monomer-like chromophores in polar solvents (*open* form), whereas in unpolar solvents the absorption bands indicate a π-stacked sandwich-type orientation (*folded* form). This nicely demonstrates that the folding and unfolding process or more generally the stacking and unstacking process of covalently linked PBI dyes, can be controlled by external conditions. The folding process of PBI **11** could be further investigated by ^{1}H NMR experiments, where the

relevant protons of the calix[4]arene unit undergo a drastically line broadening by changing the solvent from $CDCl_3$ to CCl_4, which indicates molecular motion on the NMR timescale. Thus, by using the foldamer approach a distinct π-stacked PBI system could be generated to study the optical properties of two π-stacked PBI chromophores in the excited state.

Another way to peruse the foldamer approach could be demonstrated by the phenylene ethynylene-tethered PBI **12** (Figure 12a).[36] Solvent-dependent UV/Vis studies of PBI **12** in $CHCl_3$/THF reveal two sharp absorption bands at 529 and 493 nm with extinction coefficients of 124000 and 96000 $M^{-1}cm^{-1}$ in pure $CHCl_3$ (Figure 12).

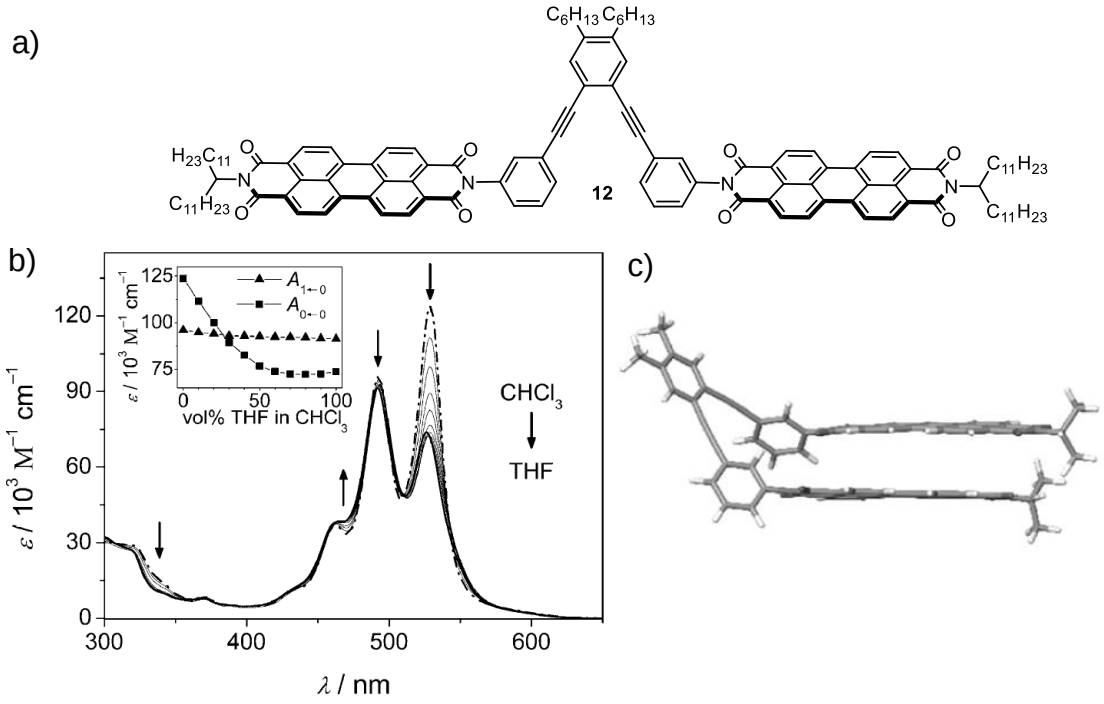

Figure 12. a) Chemical structure of PBI **12**. b) Solvent-dependent UV/Vis absorption spectra of PBI **12** (c_0 = 5 x 10^{-6} M) in $CHCl_3$/THF mixtures at room temperature from 100% $CHCl_3$ to 100% THF by increasing the THF content in steps of 10 vol%. Inset: Plot of the extinction coefficient against the THF content (0 to 100 vol%) in $CHCl_3$ at λ_{max} = 493 nm (A_{0-1}) and 529 nm (A_{0-0}). c) Geometry optimized structure (side view) of PBI **12** in the folded state obtained by force field optimization MM3. Adapted with permissions from ref.[36] Copyright 2015 WILEY-VCH Verlag GmbH.

Upon increasing the content of THF ending up in 100% pure THF, significant spectral changes can be observed with a reversal of the band intensities of the 0–0 and 0–1 absorption bands. Accordingly, the ratio of the absorption maxima A_{0-0}/A_{0-1} of PBI **12** was decreased from 1.29 in pure $CHCl_3$ to 0.80 in pure THF whereas the corresponding reference compound containing

only one PBI unit displays a A_{0-0}/A_{0-1} ratio of ≈ 1.65 in both solvents.[36] This clearly indicates the presence of co-facially π-stacked PBI chromophores in THF with pronounced H-type coupling, where the reversal of the band intensities arises from the interplay of exciton and vibrational coupling in the intermediate coupling regime, as discussed in *Chapter 2.1*.

By using a spacer unit of appropriate length, not only *intra*molecular folding, but also *inter*molecular aggregation of Bis-PBI dyes was observed. This could be shown by Würthner *et al*. for PBI **13** with a diacetylene-phenylene linker with a length of 6.9 Å (Figure 13a).[34] As this is exactly twice the π-π-distance, that is known to enable the intercalation of an additional chromophore,[85] precise control of self-assembly into quadruple π-stacks became possible (Figure 13b).

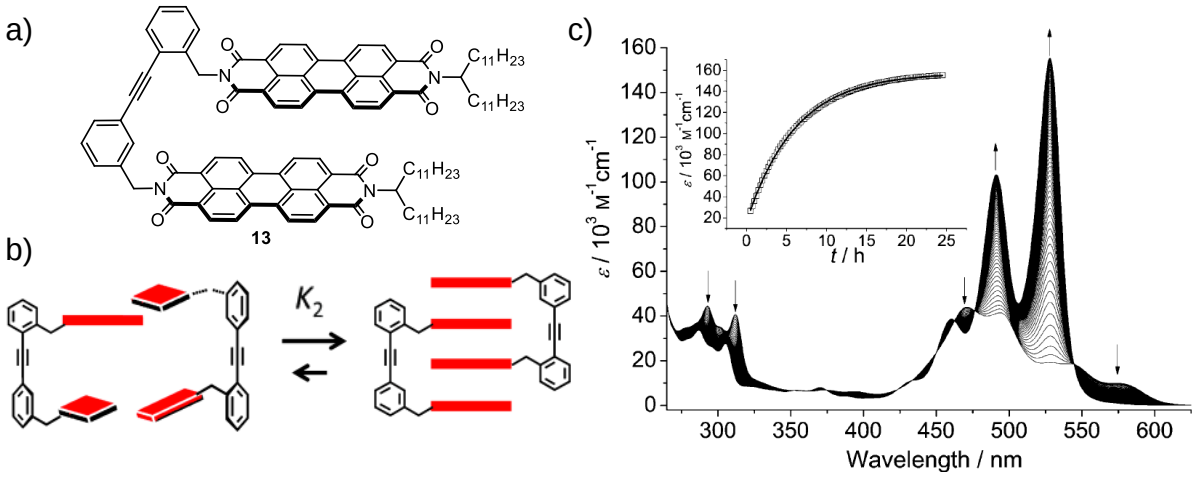

Figure 13. a) Chemical structure of PBI **13**. b) Schematic representation of the dimerization process of PBI **13**. c) Time-dependent UV/Vis absorption spectra of PBI **13** in chloroform monitoring the disassembly process from the dimeric into the monomeric species by diluting a highly concentrated stock solution ($c_0 = 10^{-2}$ M) to a final concentration of $c_0 = 10^{-5}$ M. Inset: Plot of the extinction coefficient against the time. Adapted with permissions from ref. [34] Copyright 2013 WILEY-VCH Verlag GmbH.

As a consequence, PBI **13** dimerizes into strongly bound quadruple PBI π-stacks with exceptional kinetic stability. This kinetic stability was investigated by time-dependent UV/Vis absorption studies where the disassembly process of PBI **13** dimers was monitored by diluting a highly concentrated stock solution of PBI **13** in chloroform (from $c_0 = 10^{-2}$ M to 10^{-5} M). Under these conditions the molecules have a strong thermodynamic driving force to be molecularly dissolved. At the beginning of the measurement where still the kinetic stable dimers are present, unique spectral signatures could be observed with four well-resolved absorption

bands at 470, 495, 550 and 580 nm. After 24 h, when the disassembly process was completed, an absorption spectrum with vibronic progression from 450 to 550 nm could be observed for PBI **13**, which is characteristic for PBI monomers. Moreover, well-defined isosbestic points (545, 477, 463, 450, 266 nm) confirm the equilibrium between two defined species, which can be attributed to the respective monomer and dimer.

Furthermore, Würthner *et al.*[35] could show an "arm-in-arm" aggregation into oligomeric PBI π-stacks (Figure 14) by extending the backbone-length between the two PBI chromophores from 6.9 Å (**13**) to 10.9 Å (**14**) using a diacetylene-phenylene spacer unit.

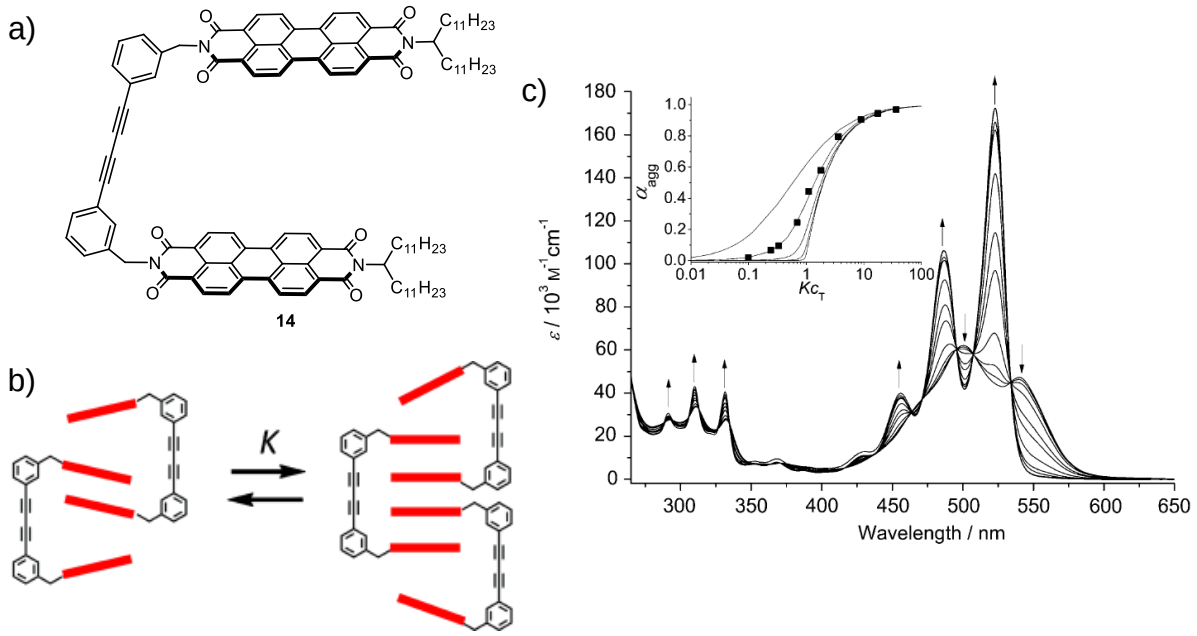

Figure 14. a) Chemical structure of PBI **14**. b) Schematic representation of the self-assembly process of PBI **14** into larger oligomers. c) Concentration-dependent absorption spectra of PBI **14** (c_0 = 5 x 10^{-7} - 2 x 10^{-4} M) in $CHCl_3$/MCH (*v*/*v*=3:7) at room temperature. Arrows indicate the spectral changes upon decreasing concentration. Inset: Plot of the degree of aggregation α_{agg} against the dimensionless concentration Kc_T using the cooperative model for several values of the cooperativity parameter σ = 1, 0.1, 0.01, 0.001, 0.0001, defined as K_2/K, where K_2 is the binding constant for the dimerization and K is the binding constant for the elongation process. Adapted with permissions from ref.[35] Copyright 2013 WILEY-VCH Verlag GmbH.

In striking contrast to PBI **13**, a more broadened absorption spectrum from 450 to 570 nm with λ_{max} = 500 nm could be observed for PBI **14** at high concentrations in a $CHCl_3$/MCH mixture (*v*/*v* = 3:7) where the corresponding concentration-dependent UV/Vis data could be properly

fitted with the isodesmic model. This clearly indicates the zipper-type aggregation[86] of PBI **14** into larger oligomers, whereas for PBI **13** kinetically stable dimers are formed.

Another nice example for an *inter*molecular aggregation process of an imide-linked PBI dye was recently reported by Chaudhuri *et al*. (Figure 15).[38] As the used *meta*-xylylene linker unit enables free rotation of the two PBI chromophores around the linker axis, PBI **15** can switch from a non-interacting *open* to an intermolecularly π-stacked *folded* form (Figure 15). After performing time-dependent UV/Vis absorption studies under kinetic control, the ratio of the 0–0 and 0–2 absorption bands A_{0-0}/A_{0-2} was plotted against the time revealing two distinct kinetic aggregation processes. First, the A_{0-0}/A_{0-2} ratio drastically decreases from 1.4 (*open* form) to 0.75 (*folded* state) within the first hours. Afterwards, a much slower decline of the A_{0-0}/A_{0-2} ratio could be observed until a value of 0.62 was reached. This two-state-behaviour as well as the absence of well-defined isosbestic points during the time-dependent absorption measurements implies the coexistence of multiple aggregated species, indicating a highly complex self-assembly process for PBI **15**.

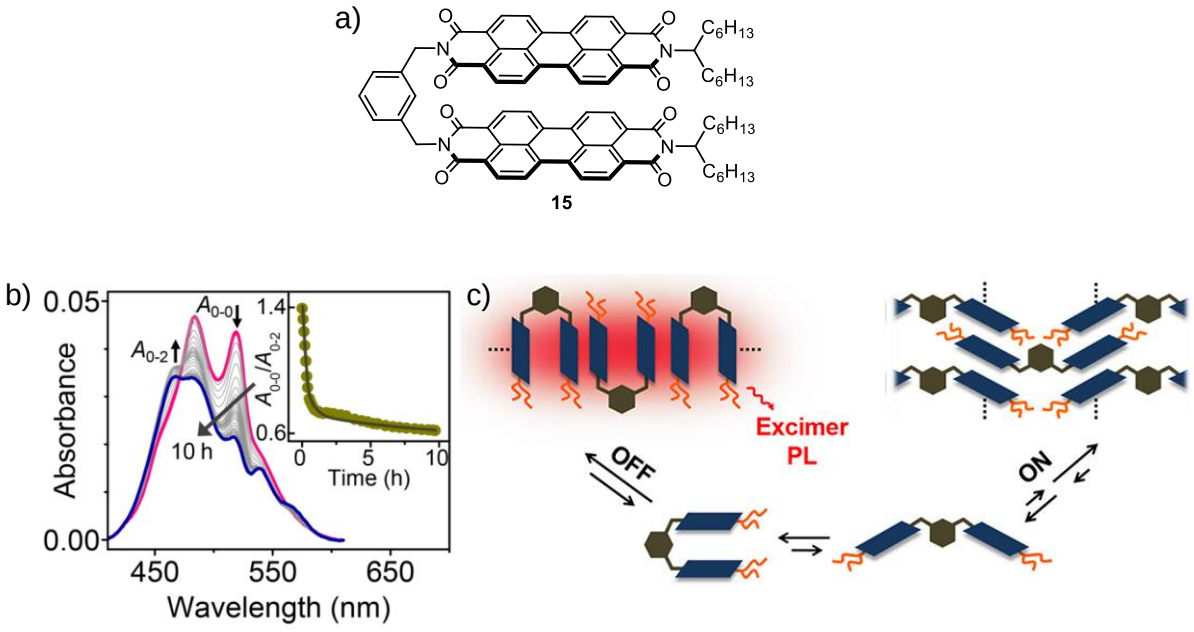

Figure 15. a) Chemical structure of PBI **15**. b) Time-dependent UV/Vis absorption spectra of PBI **15** in methylcyclohexane ($c_0 = 10^{-6}$ M) at room temperature. Inset: Plot of the A_{0-0}/A_{0-2} ratio against the time revealing two kinetic states of aggregation (before and after $t = 1$ h). c) Schematic representation of the folding process of PBI **15**. Also shown is the competition between the ON and OFF pathways visualized by tentative aggregate structures. Adapted with permissions from ref.[38] Copyright 2017 American Chemical Society.

Via various mechanistic studies Chaudhuri and co-workers could demonstrate, that there are two possible aggregation pathways. The OFF pathway aggregation, which is kinetically controlled, corresponds to an initial fast folding of PBI **15** followed by an isodesmic growth of the H-aggregates showing strong excimer emission properties. Some of these aggregates then reorganize into more stable, extended H-aggregate π-stacks following a cooperative ON pathway aggregation, with inhibited excimer formation (Figure 15).[38] This example nicely demonstrates that the individual aggregation behaviour of small covalently linked Bis-PBI dyes is highly influenced not only by the certain length of the used spacer unit but also by its flexibility or sterically hindrance regarding the free rotation of the PBI chromophores around the corresponding linker axis.

2.3.2 Bay-linked Bis-PBI Dyes

By tethering two PBI units in the bay position instead of the imide position, more conformational dynamics are present in the respective dyes, as it is shown for the diacetylene linked PBI dye **16**[87] (Figure 16). Due to its short *intra*molecular distance, PBI **16** reveals H-type exciton coupling with a drastically decreased ratio of the 0–0 and 0–1 absorption bands as well as a pronounced quenched fluorescence quantum yield compared to the corresponding monochromophoric reference compound.[87]

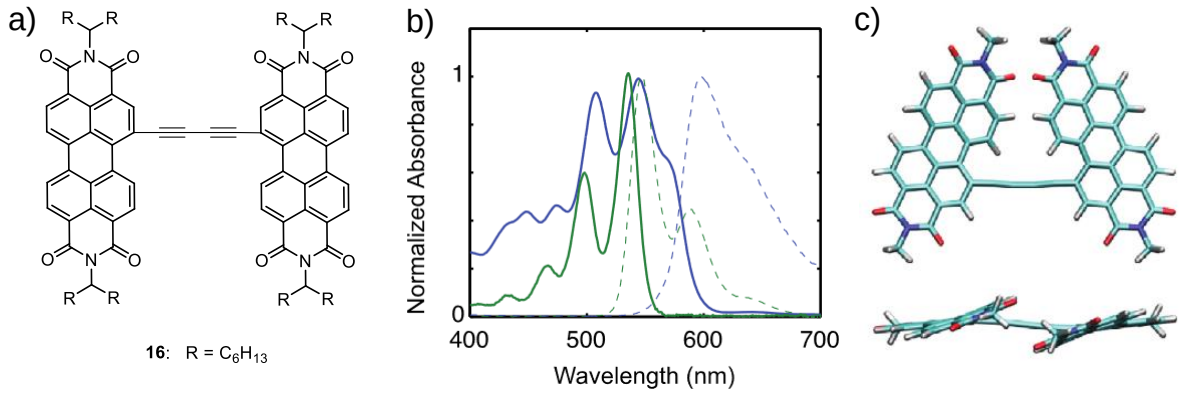

Figure 16. a) Chemical structure of PBI **16**. b) UV/Vis absorption (solid lines) and fluorescence spectra (dashed lines) of the monochromophoric reference compound (green) and PBI **16** (blue) in dichloromethane at room temperature. c) Geometry optimized structure of PBI **16** obtained by density functional theory (DFT).
Adapted with permissions from ref.[87] Copyright 2014 Elsevier.

Especially in the field of organic photovoltaics, a high number of bay-linked Bis-PBI dyes were reported in recent literature as they are promising candidates for non-fullerene acceptor materials in solar cells.[88-89] Hereafter, only some examples (PBI **17** and **18a**–**c**, Chart 3) will be presented, as *e.g.* PBI **17**[90] which shows a much broadened, blue-shifted absorption band with vibronic progression in the range of 400 to 600 nm compared to a related monomeric reference compound (absorption in *n*-heptane around 450 to 500 nm), indicating H-type exciton-coupling.[77]

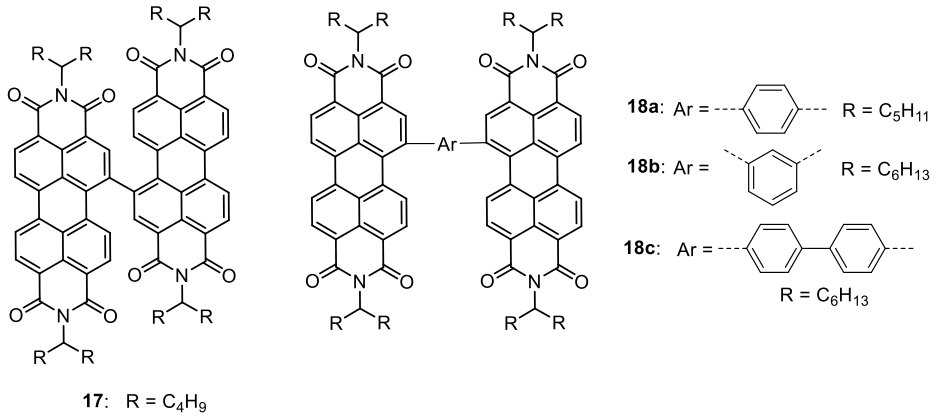

Chart 3. Bay-linked PBI dyes **17-18**.

Same observations could be made for the single *para*-phenylene-bridged PBI dye **18a**[91] and its analogue *meta*-phenylene bridged PBI **18b**.[92] As shown in Chart 3 also other (poly)-aromatic rings were used to construct covalently linked PBI dyes, as for example in the case of **18c**[93] also displaying less structured absorption bands with a blue-shifted absorption maximum at 534 nm compared to a reference compound bearing only one PBI unit (λ_{max} in *n*-heptane at 515 nm).[77]

As it could be shown, covalently linked Bis-PBI dyes can be synthesized by connecting two PBI chromophores either in the imide- or bay-position giving rise to different advantages and disadvantages. In comparison to Bis-PBI dyes that are linked in the imide-position, bay-linked Bis-PBI dyes show less structured absorption signatures due to the additional conformational dynamics that are present in the respective dyes. This makes it more difficult to examine their exact structure-property-relationship. On the other hand, up to four solubilizing groups can be introduced to the free imide positions of bay-linked Bis-PBI dyes. This highly improves the solubility of the respective dye assemblies which, on the other side, can facilitate their structural elucidation also in highly unpolar solvents or at high concentrations.

2.4 Conclusion

In this chapter, an overview on literature-known, core-unsubstituted PBI dyes was presented and their altered optical properties upon aggregation were explained using significant examples and theoretical information (*Chapter 2.1*).

As PBI dyes have a strong tendency to form extended aggregate structures, whose thermodynamic properties can be described by different mathematical models (*Chapter 2.2*), different strategies were presented in *Chapter 2.3* to achieve small finite-sized PBI architectures. As it could be demonstrated, covalently linked Bis-PBI dyes can be synthesized by connecting two PBI chromophores either in the imide- or bay-position. Depending on the nature of the used linker unit the corresponding self-assembly can then take place either *inter*- or *intra*molecularly, which could be illustrated by different examples.

As this literature survey reveals, planar, core-unsubstituted PBI dyes preferably self-assemble into extended, oligomeric π-stacks. Thus, a crucial issue of this thesis is to limit the growth of PBI dyes to well-defined, finite-sized supramolecular architectures for investigating fundamental questions like exciton coupling or exciton delocalization. As mostly UV/Vis and fluorescence experiments were used to provide insights into the structure-property-relationships of the investigated dye ensembles, also this work focuses on the optical properties of covalently linked PBI dye aggregates. Moreover, NMR-spectroscopy and quantum chemical calculations are included to rationalize the spectral features of the herein investigated dye assemblies.

Chapter 3

–

Synthesis

In this chapter, the synthesis of a variety of Bis-PBI dyes will be presented. For limiting the aggregate growth to defined aggregated structures, such as PBI folda-dimers or quadruple π-stacks, a careful design of the respective perylene bisimides dyes is necessary. Therefore, covalently linked Bis-PBI dyes were synthesized, which already show a preorganization towards small, defined aggregate structures by the virtue of their covalent binding. Thus, linker units are required which differ in both their length and flexibility, to separate the two PBI chromophores spatially. In previously reported examples of tethered Bis-PBI dyes,[34-38] the PBI subunits are connected in the imide positions of the respective PBI dyes. Hereby, the absence of bay substituents at the perylene core eliminates additional core twisting effects[94-95] which highly influences the aggregation behavior of the corresponding PBI dyes. However, despite long solubilizing alkyl chains in the remaining imide positions, these compounds suffered from significant solubility problems. In contrast, upon tethering two PBI chromophores in the bay position, up to four solubilizing groups can be introduced to the imide positions of the corresponding PBI units, which considerably increases the solubility and facilitates the investigation of the target compounds in nonpolar solvents also at high concentrations. Thus in this work, for the first time, an ether functionality was used in bay area to anchor the tether units.

The synthesis of the solubilizing imide residues and linker units will be described first, followed by the synthesis of the reference compounds and the bay-linked target compounds **Bis-PBIs 1-8**.

3.1 Synthesis of Solubilizing Imide Residue

The synthesis of 2-hexyldecylamine (**22**) was carried out according to literature known procedures[96] starting from 2-hexyldecanol (**19**) (Scheme 1). In the first step, bromination of 2-hexyldecanol (**19**) with elemental bromine in the presence of triphenylphosphine afforded compound **20** in a good yield of 76%. Subsequently, a Gabriel synthesis was carried out in which the alkyl halide **20** and the resulting phthalimide **21** could be converted almost quantitatively into desired amine **22** in the presence of hydrazine hydrate in methanol.

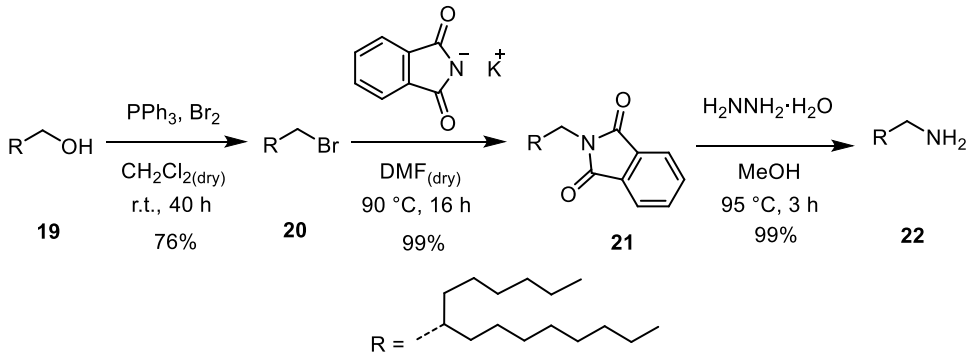

Scheme 1. Synthesis of the solubilizing amine **22**.

3.2 Synthesis of Linker Units

In this work, spacer units based on acetylene and polyphenylene units were used, with different lengths ranging between 3 - 15 Å. The *ortho*- and *meta*-linked polyphenyl linker building blocks were synthesized in a slightly modified two-step sequence according to Rathore *et al*.[97] The key step was realized by a Suzuki coupling reaction (Scheme 2). Starting from *ortho*- or *meta*-methoxyphenylboronic acid and the corresponding dihalogen compounds, the intermediates **23**-**26** could be obtained in the presence of tetrakis(triphenylphosphine)-palladium(0) and sodium carbonate under nitrogen atmosphere in good yields of up to 86%. In the second step, deprotection of the hydroxy-groups was achieved by cleavage of the methyl groups of **23**-**26** with borontribromid in dichloromethane at 0 °C affording the desired linker units **27**-**30** almost quantitatively.

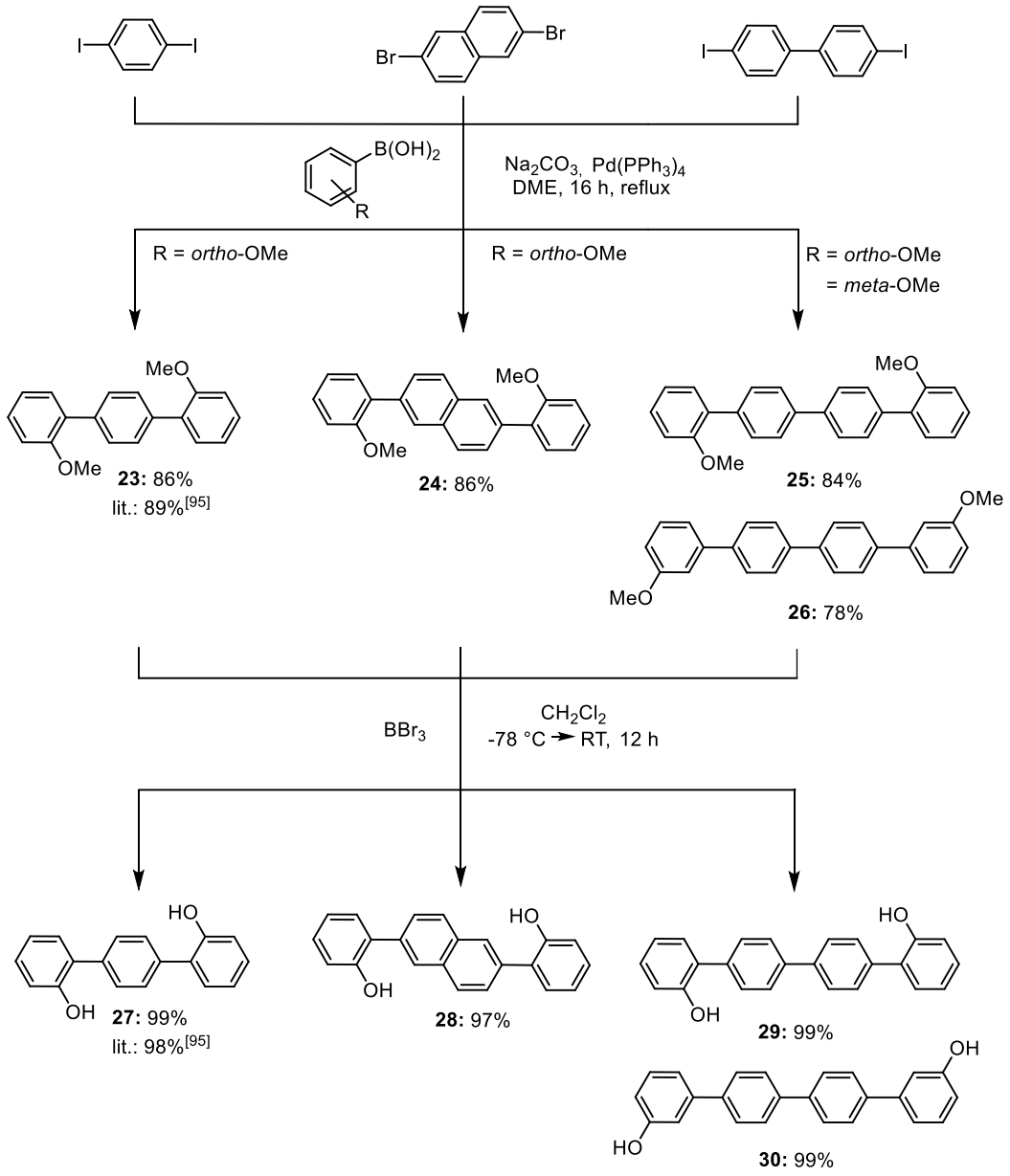

Scheme 2. Synthesis of *ortho*- and *meta*-linked polyphenyl linker units **27**-**30**.

3.3 Synthesis of Perylene Bisimide Dyes

3.3.1 Synthesis of Diacetylene-linked Bis-PBI 1 and Ref-PBI 1

The desired target compound **Bis-PBI 1** was synthesized according to the route outlined in Scheme 3. Condensation of 2-hexyldecylamine **22** with perylene bisanhydride (**31**) under well-established standard conditions[98] provided literature-known compound **32**.[71] Subsequent bromination[99] of **32** followed by nucleophilic aromatic substitution reaction[100] of the resulting mono-brominated precursor **33** with propargyl alcohol yielded desired reference compound

Ref-PBI 1 in very high yields of 92%. In the final step, Glaser coupling[101-102] reaction of **Ref-PBI 1** furnished desired **Bis-PBI 1** with an excellent yield of 94%.

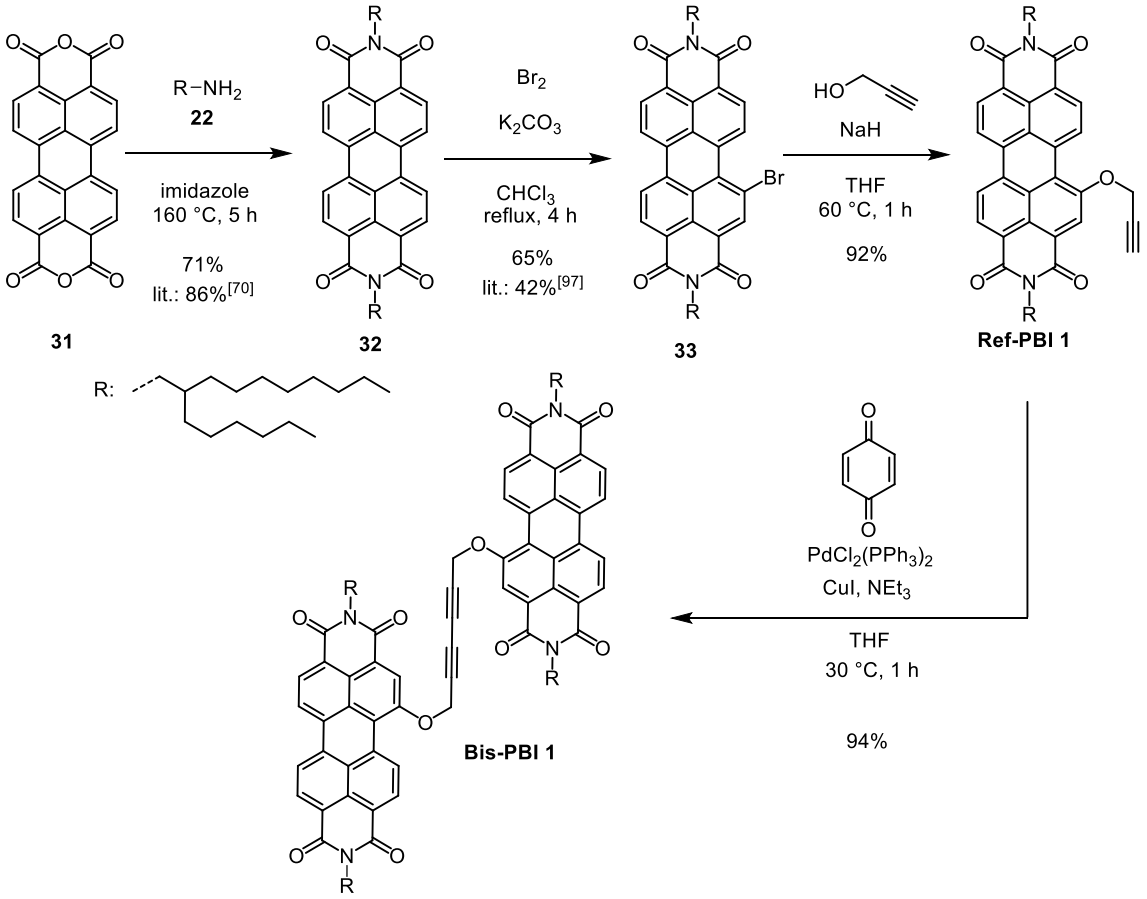

Scheme 3. Synthesis of reference compound **Ref-PBI 1** and diacetylene-linked **Bis-PBI 1**.

3.3.2 Synthesis of Phenyl-bridged Bis-PBIs 2-8 and Ref-PBI 2

For the series of polyphenylene-bridged Bis-PBI target compounds, first, linker units ranging between 3 - 6 Å were used, to especially allow *intra*molecular folding processes. The synthetic route for the corresponding polyphenylene-bridged **Bis-PBIs 2-4** is shown in Scheme 4. Nucleophilic aromatic substitution of mono-brominated pre-courser **33** with dihydroxy spacer unit **27** or commercially available *ortho*-biphenol (**34**) and (*S*)-, (*R*)- and (*S,R-rac*)-binaphthol (**35-37**) afforded **Bis-PBIs 2-4** in yields ranging between 20 – 30% by using a slightly modified literature known procedure.[100] The moderate yields of the desired Bis-PBI dyes can be assigned to incomplete conversion of the reaction, as always over 60% of the starting material **33** could be recovered. In contrast, further activation of the reaction by increasing base equivalents or varying reaction conditions like temperature or reaction time could not be

realized, as always a decomposition of the formed target compounds could be observed at higher temperatures or longer reaction times. Furthermore, purification of the target compounds turned out to be extremely cumbersome. First, conventional column chromatography was performed to separate the target compounds from impurities, followed by recycling GPC in order to finally isolate the pure Bis-PBI dyes.

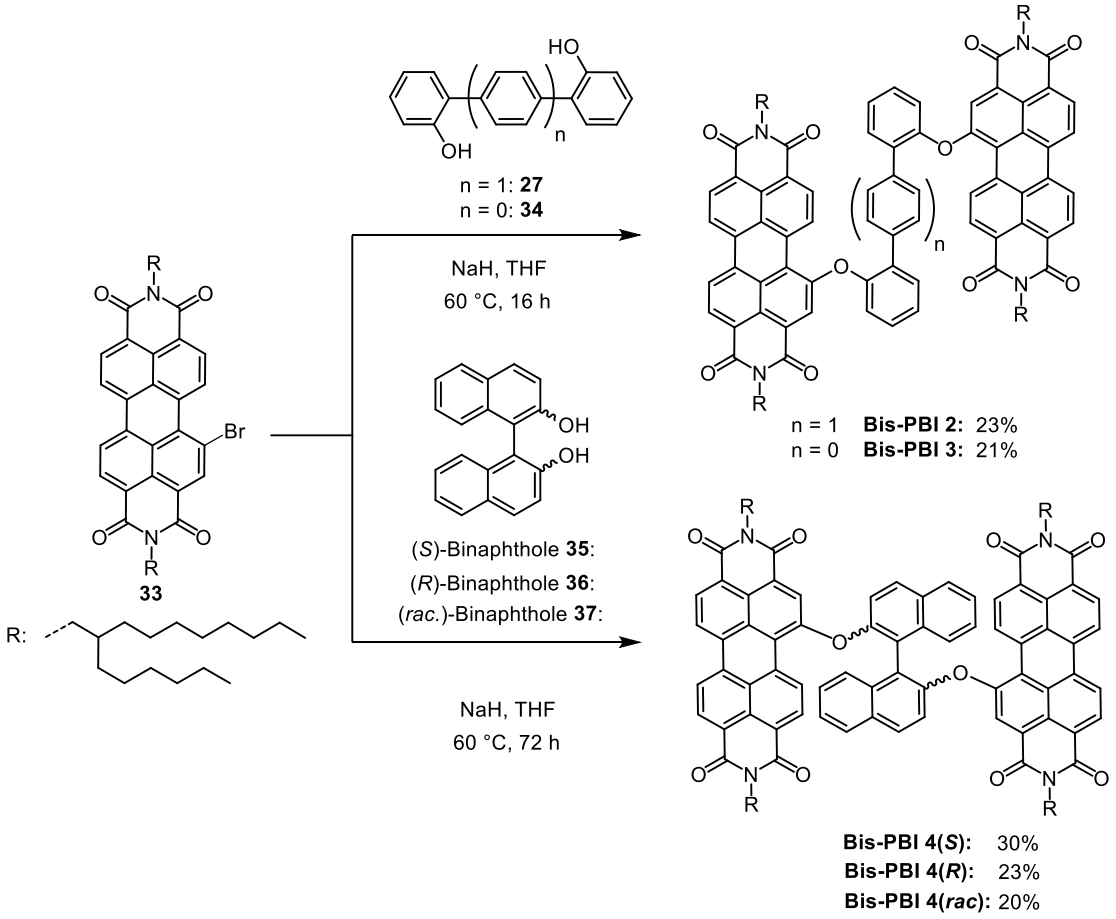

Scheme 4. Synthesis of **Bis-PBIs 2-4**.

In a similar manner structurally related reference compound **Ref-PBI 2** could be synthesized in a high yield of 97% (Scheme 5) by using mono-brominated pre-courser **33** and commercially available phenol (**38**).

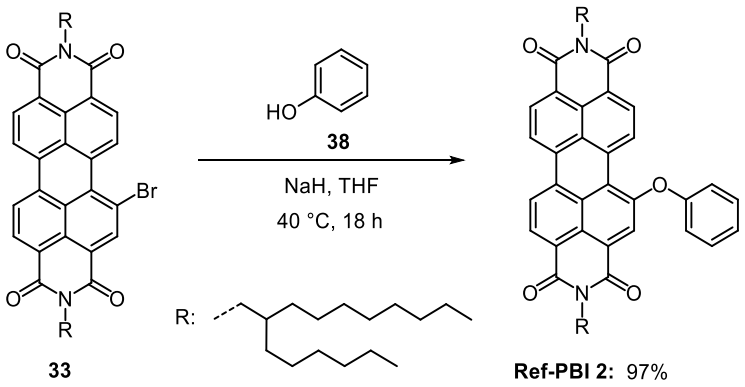

Scheme 5. Synthesis of monochromophoric reference compound **Ref-PBI 2**.

Consequently, for the series of longer (poly)phenylene-bridged target compounds **Bis-PBIs 5-8**, linker units with a length up to 15 Å were used, to especially allow *inter*molecular aggregation processes. The synthesis of **Bis-PBI 5** was realized, according to the previously described procedure (Scheme 6) using mono-brominated pre-courser **33** and commercially available 1,4-benzenedimethanol (**39**). Thus, **Bis-PBI 5** could be gained in a good yield of 60%.

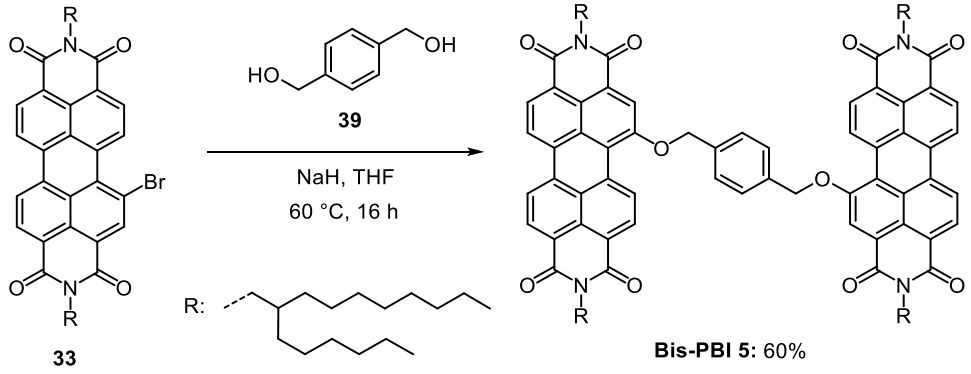

Scheme 6. Synthesis of **Bis-PBI 5**.

Finally, the synthesis of **Bis-PBIs 6-8** was performed in a similar manner *via* nucleophilic aromatic substitution reactions of mono-brominated pre-courser **33** and the respective dihydroxy spacer units **28-30** (Scheme 7).

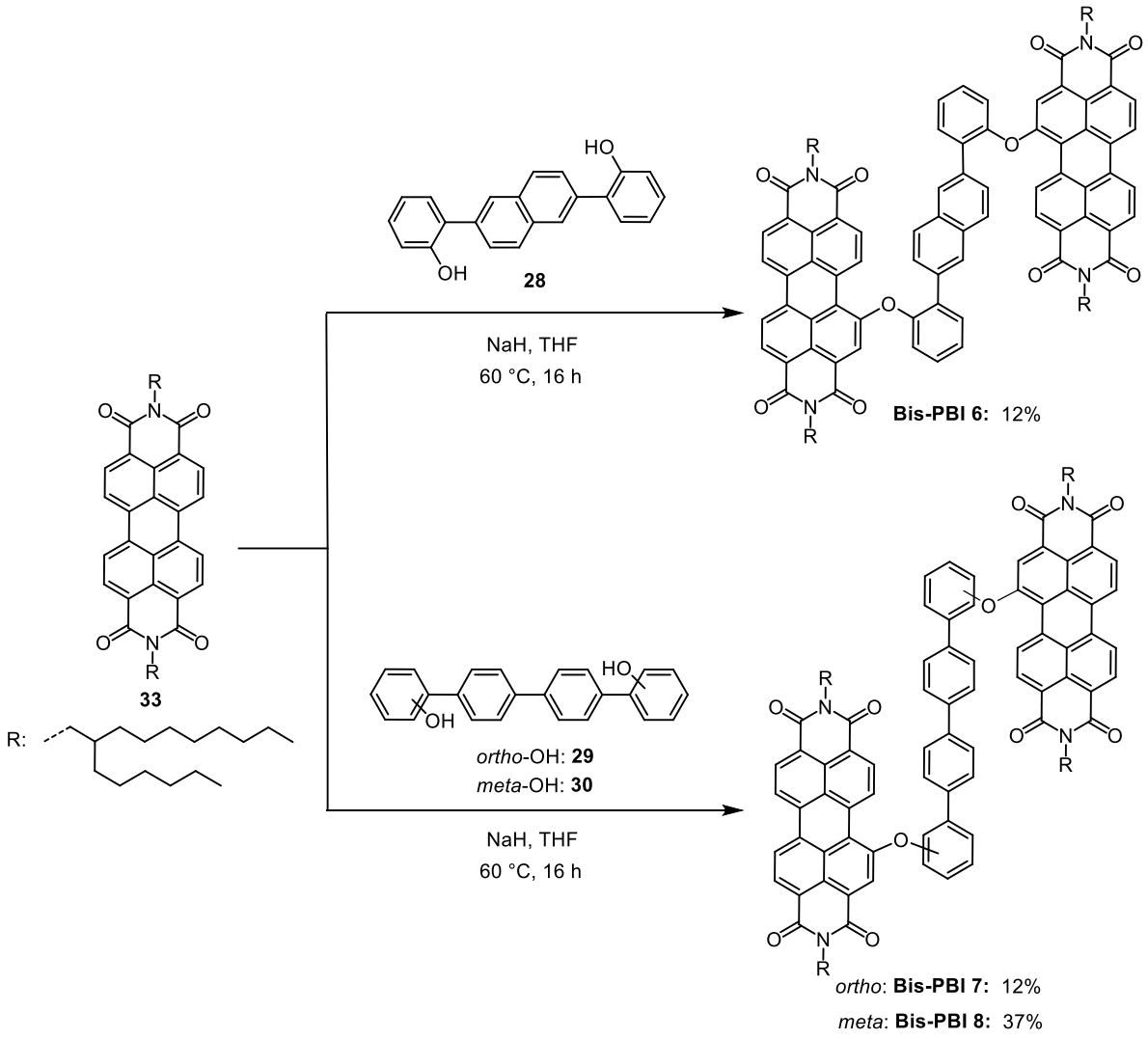

Scheme 7. Synthesis of **Bis-PBIs 6-8**.

Chapter 4

–

Ultrafast Exciton Delocalization, Localization and Excimer Formation Dynamics in a Highly Defined PBI Quadruple π-Stack[1]

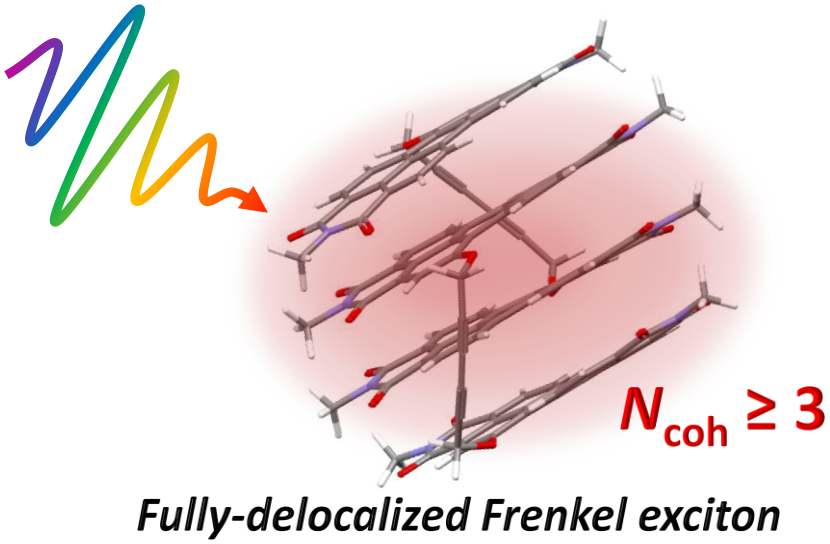

ABSTRACT: An adequately designed, bay-tethered perylene bisimide (PBI) dimer was synthesized which self-assembles exclusively and with high binding constants of up to 10^6 M^{-1}into a discrete π-stack of four chromophores. Steady state absorption and emission spectra show the signatures of H-type coupling among the dyes whilst broadband fluorescence upconversion spectroscopy (FLUPS) reveals an ultrafast dynamic in the optically excited state: A initially coherent Frenkel exciton state that is delocalized over the whole quadruple π-stack rapidly ($\tau \sim$ 200 fs) loses its coherence and relaxes into an excimer state.

[1] This chapter was accomplished in cooperation with the group of Dongho Kim from Yonsei University in Seoul and published in: Kaufmann C., Kim W., Nowak-Król A., Hong Y., Kim D., Würthner F., *J. Am. Chem. Soc.* **2018**, *140*, 4253–4258. Reproduced and adopted with permissions. Copyright 2018 American Chemical Society.
DFT calculations were performed by Dr. David Bialas (Würzburg). AFM measurements were performed by Dr. Vladimir Stepanenko (Würzburg). Femtosecond broadband fluorescence upconversion spectroscopy (FLUPS) and transient absorption and fluorescence spectroscopy were performed by W. Kim (Seoul).

4.1 Introduction

Fundamental questions of exciton coupling and delocalization or electronic coherences so far can only be studied for larger chromophore ensembles isolated from nature, *i.e.* light harvesting (LH) complexes,[103-104] rather undefined extended aggregates where size and exact packing are typically not well characterized[9] or small dimer aggregates.[105] For the latter, arranged as π-stacked H-coupled dimers, during the last years a lot of fundamental insights were gained that include the characterization of ultrafast relaxation of initial Frenkel exciton states into excimers,[106] symmetry breaking charge separation (SBCS),[107] or triplet state population either via SBCS or singlet fission.[83] Due to their ideal properties (strong π–π–stacking interactions, high fluorescence quantum yield, excellent photostability) perylene bisimide (PBI) dyes evolved as the most utilized chromophore for such studies.[25] Accordingly, to advance the understanding of excitons in molecular aggregates of highly defined size and geometry, stacks of four closely stacked dyes were envisioned which should become accessible in a zipper-type approach[108] by the self-assembly of properly designed covalent dimers (Figure 17).

Thus, the bay-tethered PBI dye **Bis-PBI 1** was designed by molecular modelling in which two PBI chromophores are covalently linked by a diacetylene spacer in the bay position and synthesized by Pd/Cu-catalyzed Glaser-type oxidative homocoupling (for synthetic details see *Chapter 3*) of the respective PBI building blocks (Figure 17).

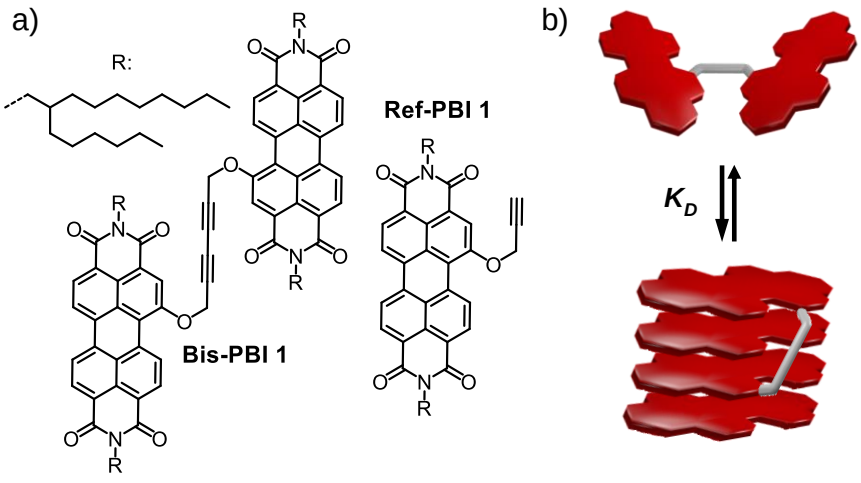

Figure 17. a) Chemical structure of **Bis-PBI 1** and **Ref-PBI 1** and b) schematic representation of the self-assembly of **Bis-PBI 1** into a quadruple PBI π-stack.

The spacer moiety ensures a distance of approximately 7 Å between the π-scaffolds. This is exactly twice the π–π-distance that is known to enable the intercalation of an additional chromophore,[85] which should allow the *inter*molecular aggregation of **Bis-PBI 1** into highly defined PBI quadruple π-stacks.

4.2 Results and Discussion

4.2.1 UV/Vis Spectroscopy

The self-assembly behavior of **Bis-PBI 1** was explored by concentration-dependent UV/Vis absorption studies in various solvents. To ascertain the suitable solvents or solvent combinations for these studies, first, steady state absorption spectra of **Bis-PBI 1** were measured in solvents of different polarity (Figure 18) as PBI dyes are known to show very distinct structure-property-relationships.

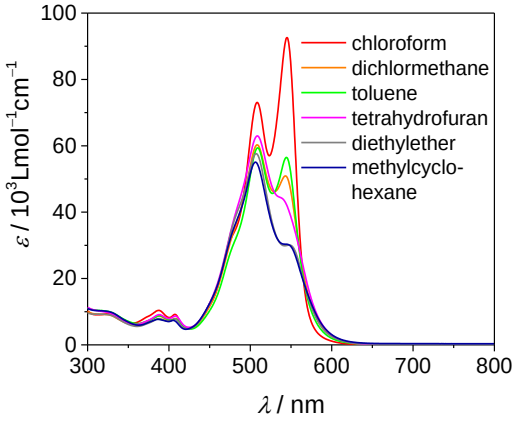

Figure 18. UV/Vis absorption spectra of **Bis-PBI 1** (c_0 = 2 x 10^{-5} M) in solvents of different polarity at 298 K.

After testing several conditions (Figure 19a-d), in toluene the transition from almost pure monomeric to almost fully aggregated species of **Bis-PBI 1** could be analyzed for the accessible concentration range of UV/Vis experiments. The corresponding spectra in toluene are shown in Figure 19e where significant spectral changes are induced by continuous concentration variations.

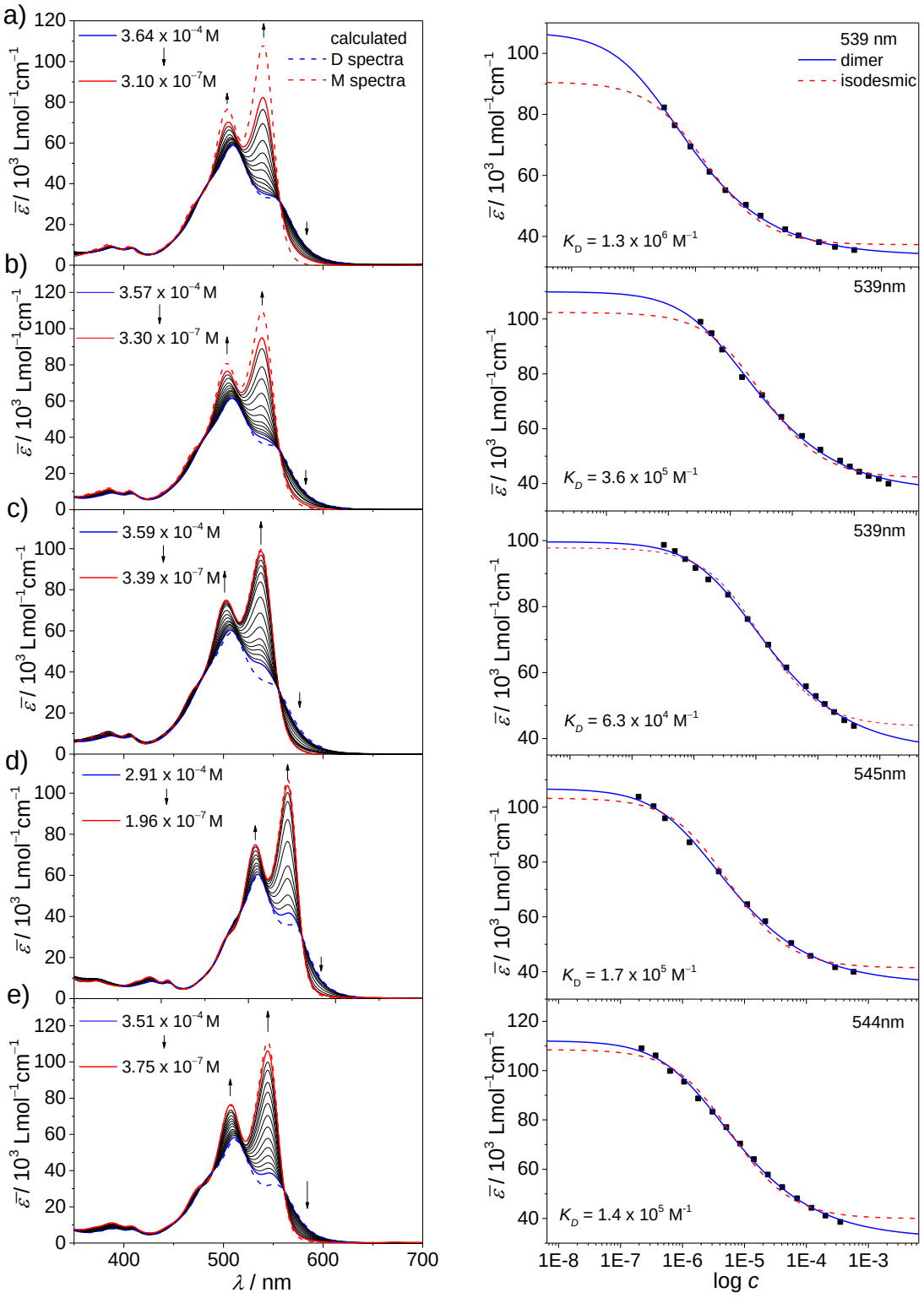

Figure 19. Concentration-dependent UV/Vis absorption spectra of **Bis-PBI 1** in a) THF at 298 K, b) THF at 313 K c) THF at 333 K, d) $CHCl_3$/THF 80:20 at 298 K and e) toluene at 298 K. Arrows indicate the changes in intensity of the 0–0 and the 0–1 band with decreasing concentration. Right: corresponding plot of the extinction coefficient (ε) at $\lambda_{max,M}$ as a function of the concentration. Fitting of the data with the dimerization model (blue solid line) fits properly, whereas the isodesmic model (red dashed line) fails.

At low concentrations (c_0 = 3.75 x 10^{-7} M), **Bis-PBI 1** displays a typical monomer absorption band for PBI chromophores with a maximum at 545 nm similar to the one of mono-chromophoric reference dye **Ref-PBI 1** (Figure 20).

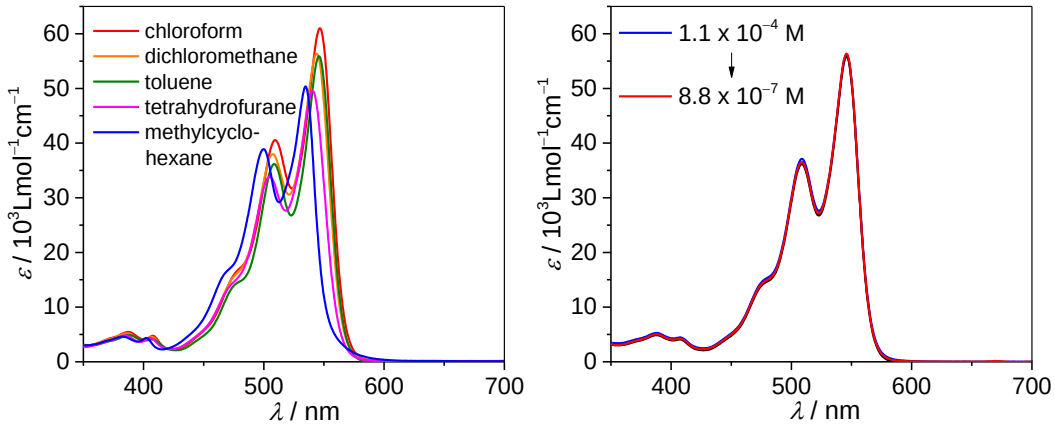

Figure 20. Left: UV/Vis absorption spectra of **Ref-PBI 1** ($c_0 \approx 2$ x 10^{-5} M) in solvents of different polarity at 298 K. Right: Concentration-dependent UV/Vis absorption spectra of **Ref-PBI 1** (c_0 = 1 x 10^{-4} – 9 x 10^{-7} M) in toluene at 298 K.

By increasing concentration a reversal of the intensities of the 0–0 and 0–1 absorption bands can be observed (Figure 19e) which is characteristic for a co-facial π-stacking of PBI dyes.[40-41] This arises from the interplay of exciton and vibrational couplings[52, 54] and can be taken as a clear indication for the formation of H-type aggregates. By performing concentration-dependent UV/Vis studies the aggregation mechanism for supramolecular self-assembly processes can be clarified by fitting the experimental data with different mathematical models[33, 74] as discussed in *Chapter 2.2*. Moreover, the spectral shift of the aggregate absorption band in comparison to the monomer absorption band can allow a classification to H- or J-type exciton coupling between the interacting PBI chromophores within Kasha's molecular exciton theory and its extended model by Spano.[8, 54]

Indeed, the data could be properly fitted by using the monomer-dimer model also in a global fit approach. In Figure 19e it is nicely shown that the global dimer fit, which is depicted as black dashed lines, is covering the complete spectra formed by the experimental data (colored lines),[33] providing a dimerization constant of K_D = 1.4 x 10^5 M^{-1} in pure toluene at 298 K. Also the observation of three well-defined isosbestic points at 561 nm, 489 nm and 477 nm, respectively, indicates the presence of a thermodynamic equilibrium between two species that can be clearly attributed to the respective monomers and dimers. Similar results were obtained

in THF with an even higher dimerization constant K_D = 1.3 x 10^6 M^{-1} (Figure 19a), whereas the concentration-dependent UV/Vis spectra of the monochromophoric reference compound **Ref-PBI 1** do not show any prominent changes upon dilution in the same concentration range (Figure 20b). All spectroscopic data are summarized in Table 1.

Table 1. UV/Vis spectroscopic data of **Bis-PBI 1** under various conditions.

	THF 298 K	THF 313 K	THF 333 K	$CHCl_3$/THF 80 : 20 298K	toluene, 298 K
monomer $\varepsilon_{max}/10^3 M^{-1}cm^{-1}$ (λ_{max}/nm)	83 (539)	96 (539)	100 (539)	104 (545)	107 (544)
dimer $\varepsilon_{max}/10^3 M^{-1}cm^{-1}$ (λ_{max}/nm)	60 (509)	61 (509)	60 (509)	60 (510)	59 (511)
K_D / M^{-1}	1.3 x 10^6	3.6 x 10^5	6.3 x 10^4	1.7 x 10^5	1.4 x 10^5

Furthermore, temperature-dependent UV/Vis absorption studies of **Bis-PBI 1** in toluene (Figure 21a) also revealed spectral changes from monomer to dimer species upon decreasing temperature. With increasing temperature, a reversal of the band intensities of the 0–0 and 0–1 absorption bands occurs, which confirms the observations of the concentration-dependent UV/Vis data. By performing concentration-dependent experiments at different temperatures in both pure toluene (Figure 21c) and THF (Table 1) it was also possible to calculate the thermodynamic parameters for **Bis-PBI 1** by a van't Hoff plot (Figure 21d) ending up with ΔH =– 48.13 kJmol^{-1}, ΔS = – 66.10 Jmol^{-1}K^{-1} and ΔG_{293K} = – 28.76 kJmol^{-1} in toluene.

From these studies conditions can be derived where > 95% of **Bis-PBI 1** are self-assembled in quadruple π-stacks. Thus, at 298 K (313 K) in THF concentrations c_0 > 1.5 x 10^{-3} M (6.0 x 10^{-3} M) and in toluene concentrations c_0 > 7.5 x 10^{-3} M (5.0 x 10^{-2} M) are needed.

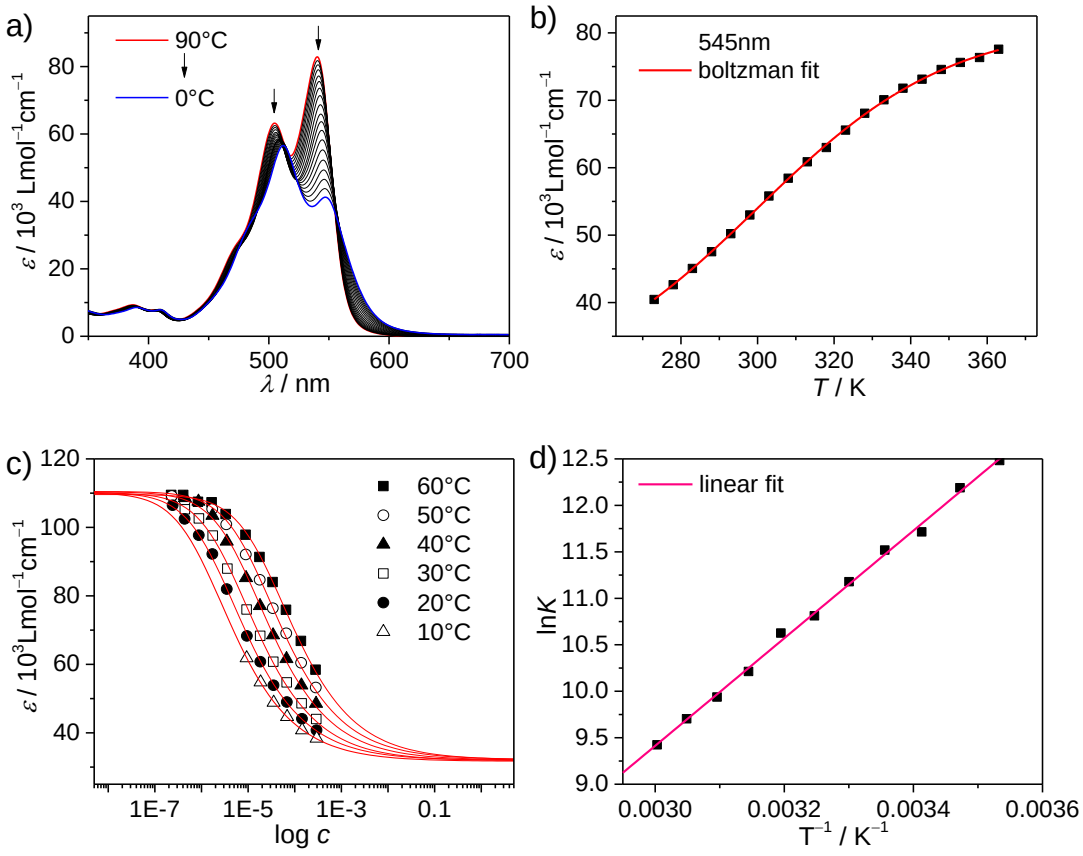

Figure 21. a) Density corrected temperature-dependent (90 → 0 °C) UV/Vis absorption spectra of **Bis-PBI 1** (c_0 = 2 x 10^{-5} M) in toluene. Arrows indicate changes in intensity of the 0–0 and the 0–1 band with decreasing temperature. b) Plot of the extinction coefficient ε against the temperature T at λ_{max} = 545 nm. c) Plot of the extinction coefficient ε against the concentration c from concentration-dependent UV/Vis absorption data of **Bis-PBI 1** (c_0 = 2.91×10^{-4} – 2.48×10^{-7} M) in toluene at different temperatures from 60 to 10°C. d) Calculation of the thermodynamic parameters of **Bis-PBI 1** from the van't Hoff plot.

4.2.2 Further Structural Investigations

To further confirm the presence of **Bis-PBI 1** dimer aggregates under the applied conditions two-dimensional diffusion ordered spectroscopy (DOSY) NMR studies (Figure 22a) were performed in toluene (c = 2 x 10^{-3} M, 313 K) providing a diffusion coefficient of D = 3.95 x 10^{-10} m^{2}s^{-1}. By solving the Stokes-Einstein equation a hydrodynamic radius of r = 12.1 Å can be calculated, which is in good agreement with the results gained from DFT calculations, taking into account that the long alkyl chains were not included in the calculations, where the geometry optimized structure of **Bis-PBI 1** dimers shows a perfect intermolecular distance of 3.2 – 3.3 Å for π-stacking between the PBI chromophores (Figure 22c).

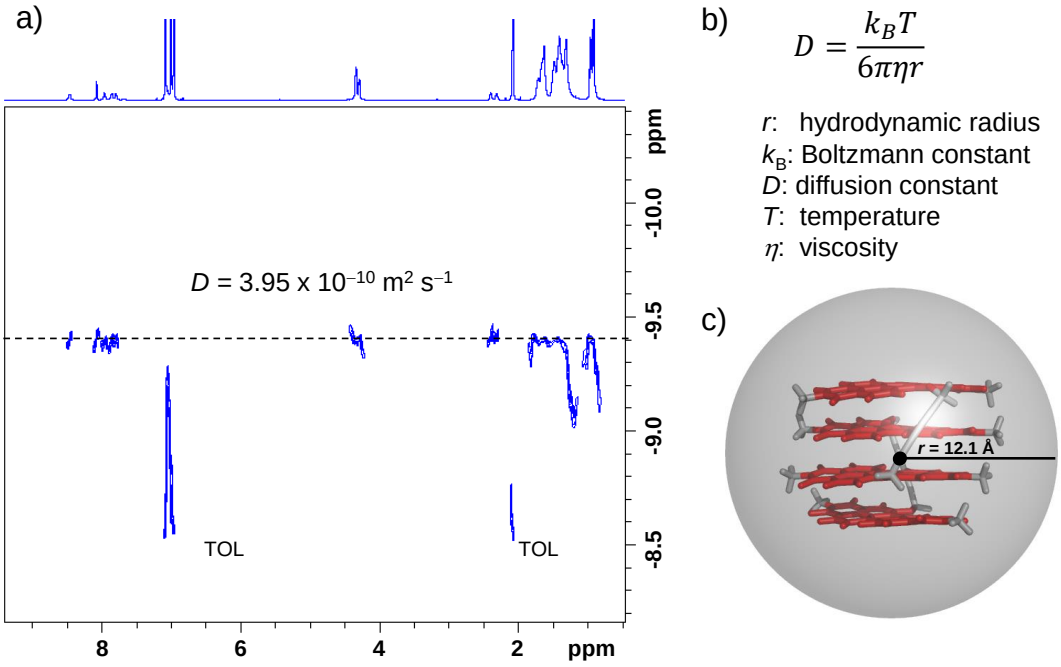

Figure 22. a) 2D plot of DOSY NMR (600 MHz, 313 K) spectrum of **Bis-PBI 1** in toluene-d_8 (c_0 = 2 x 10^{-3} M). b) Stokes-Einstein equation. c) Illustration of the energy minimized dimer structure of **Bis-PBI 1** obtained from DFT calculations (B97D3/def2-SVP) and hydrodynamic radius as received from the Stokes-Einstein equation.

Further evidence for the exclusive presence of discrete **Bis-PBI 1** dimers even at higher concentrations was obtained by ESI mass spectrometry (see the Appendix, Figure 26). Besides the singly charged monomer cation, also the singly charged dimer cation can be observed for **Bis-PBI 1** whereas no peaks at higher mass ratios could be detected which clearly confirms the absence of larger dye stacks under the applied conditions.

Moreover, atomic force microscopy (AFM) measurements (see the Appendix, Figure 27) were performed, where the sample was prepared by spin-coating a methylcyclohexane solution of **Bis-PBI 1** (c_0 = 2×10^{-5} M) onto highly oriented pyrolytic graphite (HOPG) with 4000 rpm. Hereby, spherical nanoparticles could be observed with a diameter varying from 4.4 ± 0.2 nm, while the height of the aggregates was measured to be 0.7 – 0.9 nm. This further confirms that no larger oligomeric π-stacks are present for **Bis-PBI 1** in the aggregated state.

4.2.3 Fluorescence Spectroscopy

With these structural features **Bis-PBI 1** dimers are ideally suited to unravel the electronic interactions among PBI chromophores in their quadruple H-aggregated state by fluorescence

spectroscopy (Figure 23). In chloroform at low concentrations ($c_0 = 10^{-7}$ M), where only monomeric species are present, the UV/Vis and fluorescence spectra of **Bis-PBI 1** (Figure 23b) show very characteristic well-resolved vibronic structures with mirror-image relationship, a small Stokes shift of 525 cm^{-1} and a high fluorescence quantum yield of about 76%, similar to monochromophoric **Ref-PBI 1** (Figure 23a).

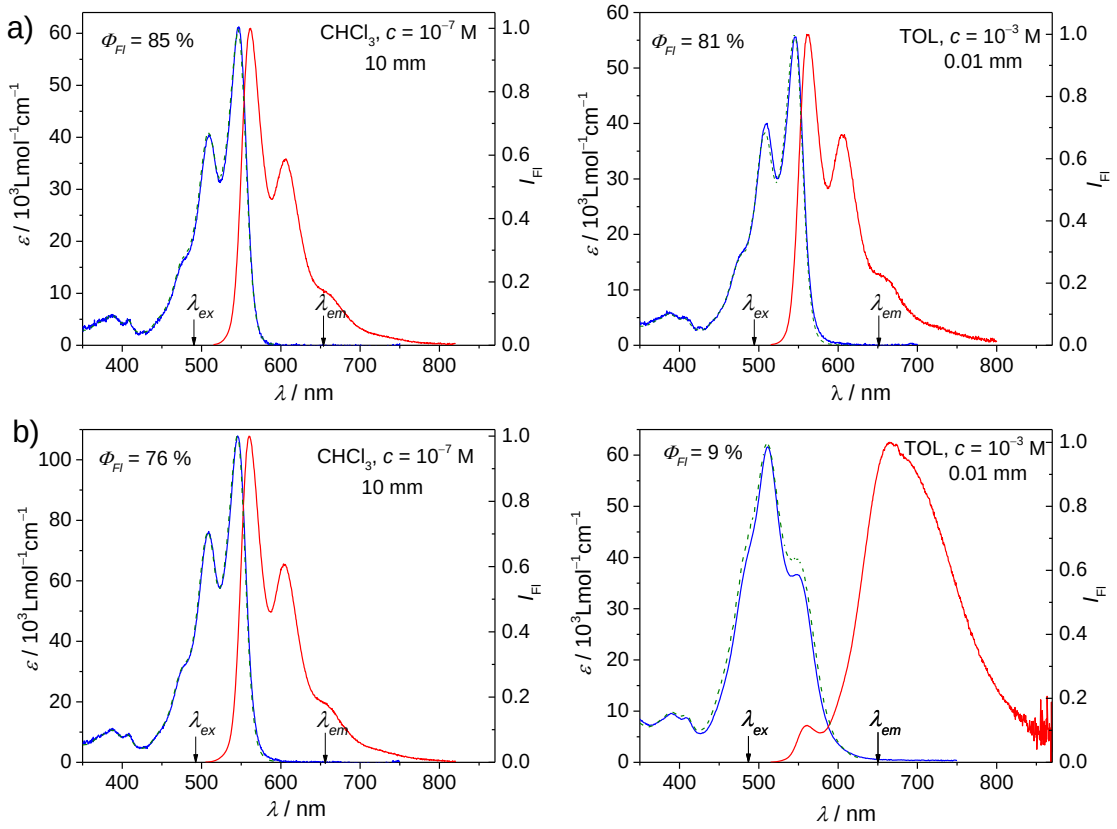

Figure 23. Steady state absorption (blue solid lines), fluorescence spectra (red solid lines) and excitation spectra (green dashed lines) of a) **Ref-PBI 1** and b) **Bis-PBI 1** in chloroform (left, $c_0 = 10^{-7}$ M) and in toluene (right, $c_0 = 10^{-3}$ M) at 298 K.

On the contrary, for **Bis-PBI 1** dimers at high concentrations ($c_0 = 10^{-3}$ M) in toluene, a prominent hypsochromic shift of the absorption maximum from 545 nm to 510 nm can be observed. In this case the Stokes shift is much higher with 4622 cm^{-1} and the fluorescence quantum yield is decreased to only 9%. The change of the emission properties can be attributed to the formation of an excimer state in the aggregate, which is characteristic for π-stacking PBI chromophores.[40-41] Additionally, below 600 nm a small shoulder corresponding to remaining monomer fluorescence can be recognized. Moreover, the excitation spectra (Figure 23, green dashed lines) are in good agreement with the corresponding absorption spectra revealing single

state fluorescence for **Bis-PBI 1** dimers giving rise to a selective emission from only one species, the PBI quadruple π-stacks.

Further information were gained by fluorescence lifetime measurements (Table 2), where **Ref-PBI 1** exhibits a lifetime of ≈ 4 ns in chloroform at low concentrations ($c_0 = 10^{-7}$ M) and ≈ 5 ns in toluene at high concentrations ($c_0 = 10^{-3}$ M). These values are in good agreement with the ones of previously reported monomeric PBI chromophores.[109-111] For **Bis-PBI 1** similar values (≈ 5 ns) could be obtained in chloroform ($c_0 = 10^{-7}$ M) corresponding to **Bis-PBI 1** monomers, whereas in toluene ($c_0 = 10^{-3}$ M) two fluorescence lifetimes (Table 2) could be found, where the shorter lifetime (≈6 ns) with significantly lower amplitude is highly comparable to the values of **Ref-PBI 1**. Thus, the shorter lifetime can be attributed to the emission from the monomeric, more emissive species, whereas the second lifetime ≈ 25 ns can be attributed to **Bis-PBI 1** quadruple π-stacks. Corresponding emission data are summarized in Table 2.

Table 2. Fluorescence spectroscopic data of **Bis-PBI 1** and **Ref-PBI 1** measured in chloroform at low concentrations ($c_0 = 10^{-7}$ M) and in toluene at high concentrations ($c_0 = 10^{-3}$ M) at room temperature.

	Ref-PBI 1		**Bis-PBI 1**	
	chloroform ($c_0 = 10^{-7}$ M)	toluene ($c_0 = 10^{-3}$ M)	chloroform ($c_0 = 10^{-7}$ M)	toluene ($c_0 = 10^{-3}$ M)
λ_{Em} / nm	561	561	560	667
$\Delta\tilde{\nu}_{Stokes}$ / cm^{-1}	490	520	525	4622
Φ_{Fl} / %	85	81	76	9
τ_{Fl}[a] / ns	4.4	5.6	4.6	6.2, 25.3
(amplitude)	(100%)	(100%)	(100%)	(27%, 73%)

[a] τ_{Fl} were determined by tail fit analysis of data obtained from time-correlated single photon counting measurements with ps laser diode at 505 nm using the magic angle setup.

In order to get deeper insights into the initial Frenkel exciton state and concomitant excimer formation dynamics in H-type PBI quadruple stacks, transient fluorescence spectra were measured in cooperation with the Dongho Kim group (Figure 24) using femtosecond broadband fluorescence upconversion spectroscopy (FLUPS).[112] THF was chosen as a solvent for the time-resolved fluorescence measurements, because it allows already at quite low concentrations ($c_0 \approx 1 \times 10^{-3}$ M) and at room temperature the almost exclusive presence of quadruple PBI

stacks owing to a larger dimerization constant. As shown in Figure 24a, the early-time transient fluorescence spectra of **Bis-PBI 1** not only deviate from the steady-state fluorescence spectrum but also show drastic spectral changes within 1 ps. At initial time delay, emission from the excimer state is negligible but that from the antisymmetric lower Frenkel state is rather prominent. The ultrafast (< 50 fs) population of the latter is evident from the apparent vibronic features of the fluorescence spectra,[112] especially the vibronic peak ratio between 0−0 electronic and 0−1 vibronic side bands. However, within less than 1 ps these spectral signatures disappear with the appearance of broad excimer bands at longer wavelength region. These spectral changes revealed in PBI quadruple stacks are totally in line with the previous observation of the Kim group done for Frenkel exciton and excimer formation dynamics in PBI dimeric and oligomeric H-aggregates.[106]

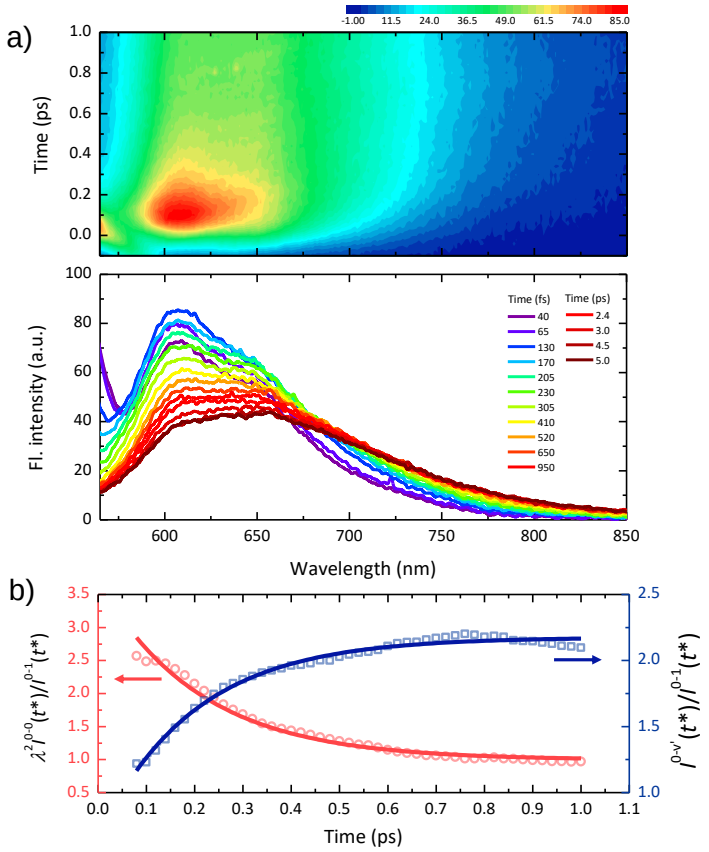

Figure 24. a) Two-dimensional transient fluorescence contour map (top) and transient fluorescence spectra (bottom) of **Bis-PBI 1** ($c_0 \approx 1$ x 10^{-3} M) in THF. The excitation wavelength was tuned to be resonant with the electronic transition of the symmetric upper Frenkel excitonic state (λ_{pump} = 510 nm). The pump power at the sample was approximately 300 μW (~ 0.25 W/cm^2). b) Kinetic traces of $\lambda^2 I^{0-0}(t^*)/I^{0-1}(t^*)$ (red circle) and $I^{0-v'}(t^*)/I^{0-1}(t^*)$ (blue square). Adapted with permissions from ref.[113] Copyright 2018 American Chemical Society.

Meanwhile, **Ref-PBI 1** monomer merely shows a dynamic red-shift occurring on a few picosecond time scale (Figure 25) which can be assigned to a minor structural relaxation, *i.e.* flattening process, of the slightly distorted aromatic core induced by the bay-substituent.[114-115] The ultrafast time resolution and broadband spectral detection of the FLUPS method[112] enables a quantification of the extent of exciton delocalization, the so-called coherence length (N_{coh}), after photoexcitation and its time-dependent behavior along the quadruple stacks. Kim and co-workers scrutinized the transient fluorescence spectra on the basis of a theoretical model proposed by Jansen, Spano and co-workers.[116]

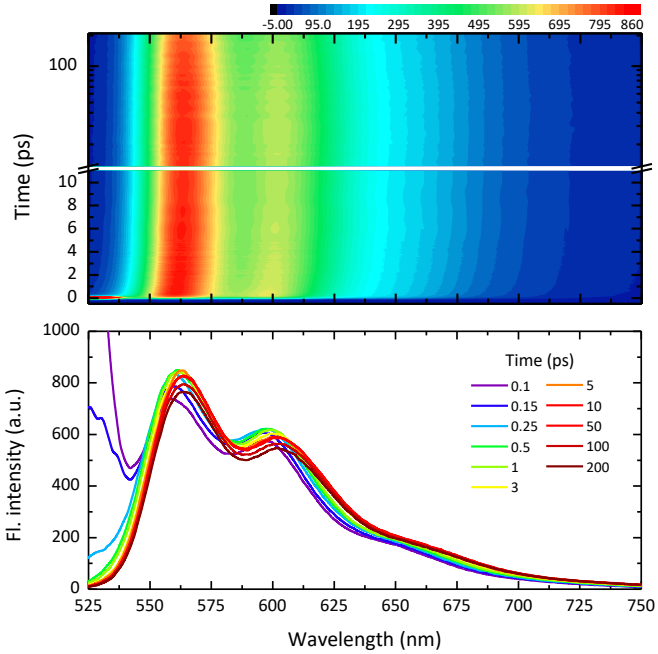

Figure 25. Two-dimensional transient fluorescence contour map (top) and transient fluorescence spectra (bottom) of **Ref-PBI 1** ($c_0 \approx 1 \times 10^{-3}$ M) in THF after photoexcitation at 510 nm. The pump power at the sample was approximately 300 μW (~ 0.25 W/cm^2, 30 nJ/pulse). Adapted with permissions from ref.[113] Copyright 2018 American Chemical Society.

It was suggested that the range of spatial coherence both in H- and J- aggregates consecutively alters the vibronic peak ratio between 0−0 and 0−1 peaks in the transient fluorescence spectra. Given that the intensity of 0−0 peak is sensitive to the exciton coherence but that 0–1 peak is not, N_{coh} can be reproduced by the 0−0 to 0−1 vibronic peak ratio scaled by the Huang-Rhys factor (λ^2), which is,[116-117]

$$N_{\mathrm{coh}}(t^*) \approx \lambda^2 \frac{I^{0-0}(t^*)}{I^{0-1}(t^*)}.$$

Here, the Huang-Rhys factor (λ^2 = 0.714, **Ref-PBI 1** in THF) can be simply estimated from the linear absorption spectrum of the monomeric units.[117] In the case of J-aggregates, N_{coh} accords with the vibronic peak ratio throughout the entire time window. In contrast, the vibronic peak ratio traces in H-aggregates do not totally follow the evolution of coherence length over time due to gradual population from the symmetric upper to the antisymmetric lower Frenkel excitonic states, giving rise to an additional fluorescence quenching from the 0−0 electronic transition.[8, 116] Therefore, especially for H-aggregates, $\lambda^2 I^{0-0}(t^*)/I^{0-1}(t^*)$ values at later time delays should underestimate the size of excitation. As shown in Figure 24, the experimental $\lambda^2 I^{0-0}(t^*)/I^{0-1}(t^*)$ kinetic traces indicate that the initial N_{coh} value of PBI quadruple stacks is approximately 3. Nevertheless, considering the limitations for the time-resolution of the FLUPS setup, this result reflects that the nascent Frenkel exciton within a highly defined H-aggregate is almost fully delocalized over the whole quadruple stack. This value rapidly decays to 1 with a time constant of ~ 200 fs, which can be attributed to decoherence of the delocalized Frenkel exciton, *i.e*. exciton localization process. With the same time constant, the accompanying rise dynamics of the $I^{0-v'}(t^*)/I^{0-1}(t^*)$ peak ratio (v' > 1, the assumption is that the excimer emission rather than the higher vibronic progression from the Frenkel state mainly contributes to the $I^{0-v'}(t^*)$ band) could be observed which previously[106] was suggested as an indicator of excimer formation (Figure 24b). These results emphasize two important aspects of Frenkel exciton relaxation and excimer formation dynamics in PBI H-aggregates: (i) the excimer formation processes suppresses the coherence of the delocalized Frenkel exciton,[105] (ii) the mixing between Frenkel exciton and charge-transfer states and/or the existence of conical intersection can trigger the ultrafast (< 1 ps) excimer formation processes. [66, 118-119]

Combining the time-resolved fluorescence results of the PBI quadruple stacks with the previous work of the Kim group on PBI dimeric and oligomeric aggregates[106] it can be recapitulated that the Frenkel exciton relaxation and excimer formation dynamics strongly depends on the size of PBI aggregates. This comparative analysis should be valid because these systems have nearly the same intermolecular packing geometry with similar exciton coupling strengths appertaining to the intermediate coupling regime.[56, 106] According to the previous observation,[106] extended PBI oligomeric H-aggregates showed the initial value of about 3 and double exponential decay with the time constants of < 80 and 250 fs in kinetic profiles of N_{coh} ($\lambda^2 I^{0-0}(t^*)/I^{0-1}(t^*)$). The former decay component was assigned to the exciton localization process caused by coherent exciton propagation along the long one-dimensional aggregate, which was also evident from the nearly constant $I^{0-v'}(t^*)/I^{0-1}(t^*)$ peak ratio within the first 110 fs. This is due to the result that the energy fluctuation during exciton propagation in a coherent

fashion leads to a reduction in the size of excited-state wave function along the molecular aggregate[106, 120] giving rise to an ultrafast decay of N_{coh} to the value of about 2. Actually, this process and its time scale are quite similar to coherent excitation energy transfer (EET) observed in conjugated polymers in the intermediate coupling regime where the delocalization is perturbed by nuclear vibrational modes.[121-123] In this case, a partially delocalized exciton undergoes quantum-assisted transport within long polymer chains on the ~100 fs time scale, thereby the exciton is finally relaxed to a more localized site. On the other hand this kind of coherent transport process was not revealed in PBI quadruple stacks, despite of the similar initial N_{coh} value of about 3. Likewise, PBI dimeric aggregates did not show any fast decay component before relaxing to the excimer state with the initial N_{coh} value of about 2. The instantaneous rise dynamics in kinetic profiles of excimer formation processes ($I^{0-v'}(t^*)/I^{0-1}(t^*)$) without a plateau also substantiates that the excimer state of PBI dimer and quadruple stacks is directly formed alongside the localization of the initial fully-delocalized Frenkel exciton. The disparity of the initial Frenkel exciton relaxation and excimer formation dynamics between highly defined dimer/tetramer stacks and extended oligomeric aggregates can be attributed to the size-limit of molecular aggregates. Since the PBI quadruple stacks are composed of only 'four' monomeric units, the initially fully-delocalized exciton is immobile within a highly defined aggregate and thereby it only has a relaxation pathway to the excimer state with ultrafast exciton localization. This situation can be applied in the case of PBI dimer aggregates in the same manner.

Interestingly, another size-effect on exciton dynamics in the aggregates was revealed by femtosecond transient absorption spectroscopy (see the Appendix, Figure 28). Contrary to the oligomeric aggregates,[124] there are no excitation power dependent behaviors in the quadruple stacks, like in the case of dimeric aggregates,[125] implying that multiple excitons cannot be generated. Namely, only 'one' delocalized exciton, which is also immobile, can be formed in a stack of four PBIs, further supporting the time-resolved fluorescence results. With this all time-resolved fluorescence data additionally support the fact that **Bis-PBI 1** can solely form dimerized quadruple stacks, not larger aggregates.

4.3 Conclusion

In this chapter, a PBI quadruple dye stack formed by the self-assembly of two bay-tethered Bis-PBI dyes provided for the first time insights into the exciton dynamics within a highly defined synthetic dye aggregate beyond dimers. The unambiguous detection of the initial fully-delocalized Frenkel exciton state and its localization, *i.e.* exciton decoherence, occurring within 1 ps are important outcomes of this study. With the now available spectroscopic insights for the series of structurally defined dimer[106], tetramer[113] and extended π-stacks[106] a sound understanding of exciton migration versus exciton relaxation in H-aggregates has been achieved. Unraveling such processes in artificial dye aggregates is of relevance for their comparison to natural dye arrays as given in the light-harvesting systems of photosynthesis[103-104] as well as for the design of materials for organic electronics[20, 126] and photonics.[127-129]

4.4 Appendix

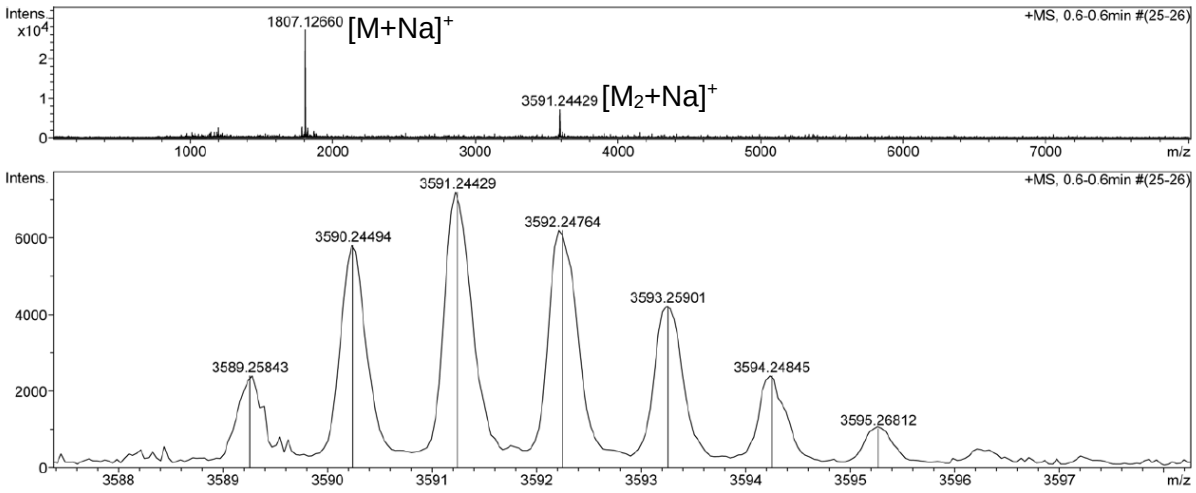

Figure 26. ESI mass spectrum of **Bis-PBI 1** in positive-ion mode. Sample preparation was done out of a chloroform/methanol 3:1 solvent mixture. $[M+Na]^+$ and $[M_2+Na]^+$ are corresponding to the singly charged monomer (calcd. for $C_{118}H_{151}NaN_4O_{10}$, 1806.12442; found, 1806.12553) and dimer cation (calcd. for $C_{236}H_{300}N_8NaO_{20}$, 3589.25962; found, 3589.25843), respectively.

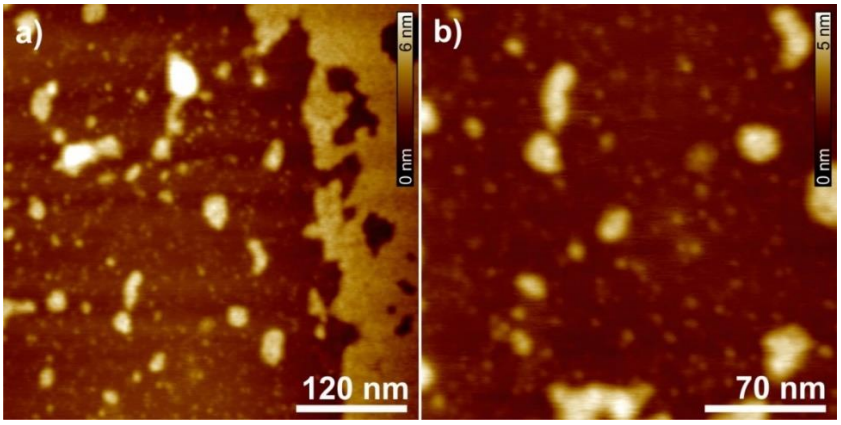

Figure 27. AFM images were prepared by spin-coating a solution of **Bis-PBI 1** in methylcyclohexane on HOPG to create a thin-film (c_0 = 2 x 10^{-5} M^{-1}, 4000 rpm) showing small spherical nanoparticles with an average diameter of 4.4 ± 0.2 nm and height of 0.7 – 0.9 nm. Particles of a second layer appear brighter.

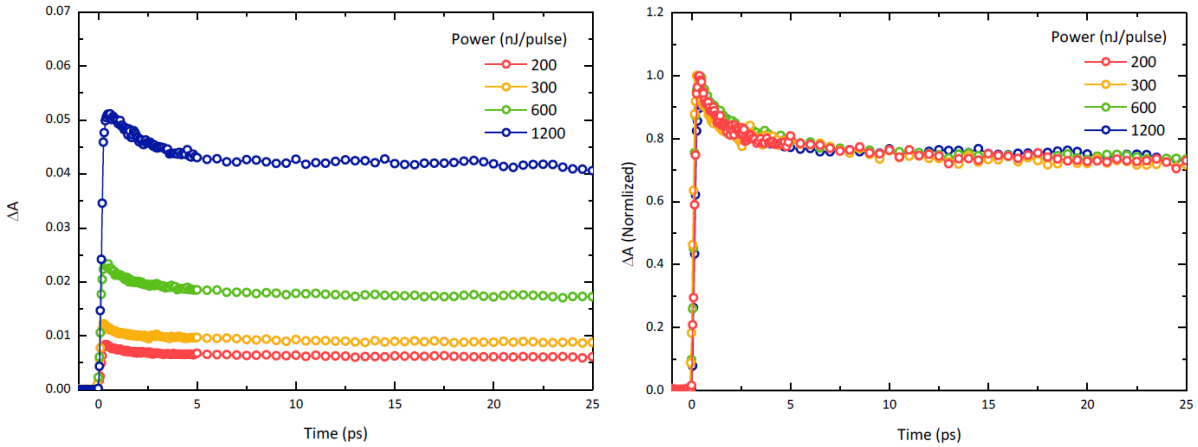

Figure 28. Pump-power dependent transient absorption decay profiles (left: raw data, right: normalized data, λ_{probe} = 910 nm) of **Bis-PBI 1** in THF ($c_0 \approx 1 \times 10^{-3}$ M). Adapted with permissions from ref.[113] Copyright 2018 American Chemical Society.

Chapter 5

–

Discrete π-Stacks of Perylene Bisimide Dyes within Folda-Dimers: Insight into Long- and Short-range Exciton Coupling[2]

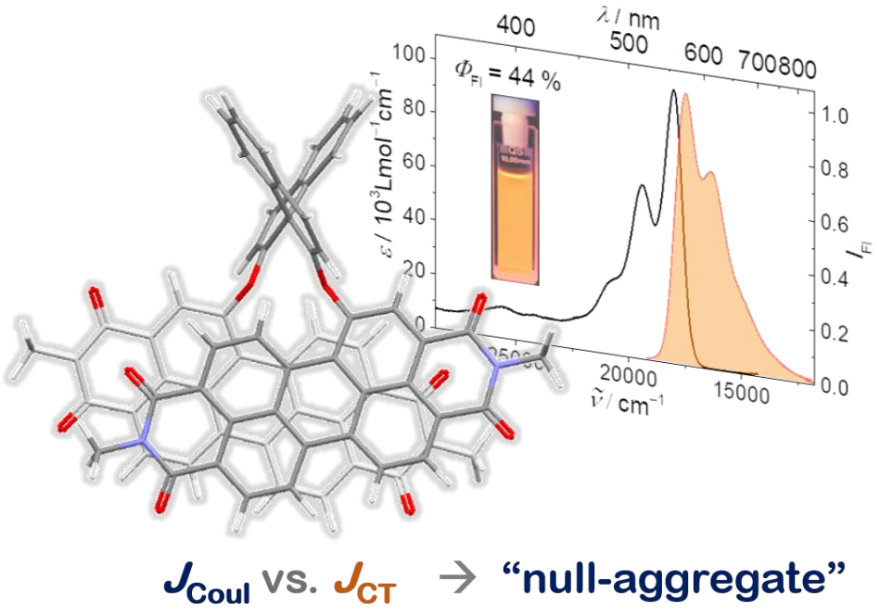

ABSTRACT: Four well-defined π-stacks of perylene bisimide (PBI) dyes were obtained in solution by covalent linkage of two chromophores with spacer units of different length and sterically demand. Structural elucidation of the folda-dimers by in-depth NMR studies and DFT calculations suggest different, but highly defined molecular arrangements of the two chromophores in the folded state. Remarkably, the dye stacks exhibit distinct absorption properties that can be rationalized by an interplay of long- and short-range exciton coupling resulting in optical signatures ranging from conventional H-type to monomer-like absorption features, which presents the first experimental proof of a PBI-based "null-aggregate", in which long- and short-range exciton coupling fully compensate each other.

[2] This chapter was published in: Kaufmann C., Bialas D., Stolte M., Würthner F., *J. Am. Chem. Soc*, **2018**, *140*, 9986-9995. Reproduced and adopted with permissions. Copyright 2018 American Chemical Society.
DFT calculations and theoretical investigations were performed by Dr. David Bialas. AFM measurements were performed by Dr. Vladimir Stepanenko.

5.1 Introduction

Due to their outstanding properties, the class of perylene bisimide (PBI) dyes has attracted lots of interest during the past decade. Easily tuneable absorption and fluorescence properties[28, 130] excellent photostability,[26, 131-132] and unique self-assembly features[25] make them highly attractive for application in the field of organic electronics,[29-30, 133] photovoltaics[31-32, 134-135] and photonics.[136-139] In general, the performances of these devices strongly depend on the optical properties of the active material, which are significantly influenced by inter-chromophoric interactions in the (poly-)crystalline phase.[140-141] Therefore, it is of prime importance to understand the interaction between the dyes that affect the optical properties of the assemblies. Based on Kasha's exciton theory, the exciton coupling is described in terms of a long-range Coulomb interaction between the transition dipole moments (μ_{eg}) of the chromophores (point-dipole-approximation). Albeit the optical properties of many PBI dye aggregates can be rationalized by assuming conventional long-range coupling between the chromophores along with vibrational coupling,[40, 58-60] several examples are known where this picture fails.[10-12] In a recent work, Spano *et al.* could demonstrate that charge-transfer mediated exciton coupling leads to enhanced Davydov splitting in PBI crystals.[142] This short-range coupling arises from orbital overlap of adjacent chromophores and can be significant for closely π-stacked chromophores[13-16] as it is also the case for most PBI aggregates in solution.[25] Also the large colour range observed for PBI crystals, known as crystallochromy, can be attributed to an interplay of short- and long-range exciton coupling at the different chromophore arrangements.[65, 143-144] Notably, the interference between both couplings may lead to unexpected optical properties that can be beneficial for applications, which motivates for further investigation.[54, 61] However, in-depth studies require well-defined orientations of the chromophores as given in the crystalline state.[145-146] Unfortunately, dye aggregates in crystals are usually not of limited size, which complicates theoretical studies, and investigation of the optical properties in the solid state can be quite challenging, *e.g.* due to reabsorption.[147-148] Alternatively, well-defined dye assemblies can be realized in solution by covalent linkage of chromophores with appropriate spacer moieties leading to foldamers,[86, 149-151] cyclophanes[152-154] or macrocycles,[155-156] which enable the investigation of interchromophoric interactions in prearranged geometries of a finite number of dyes.[157]

Thus, **Bis-PBIs 2-4** (Figure 29a) were synthesized, but different from the *inter*molecular self-assembly presented in *Chapter 4*, now, the concept of *intra*molecular folding should be used to study the optical properties of PBI π-stacks comprising two chromophores in dependence of

their arrangements enforced by linker units of different length and sterical demand (for synthetic details see *Chapter 3*).

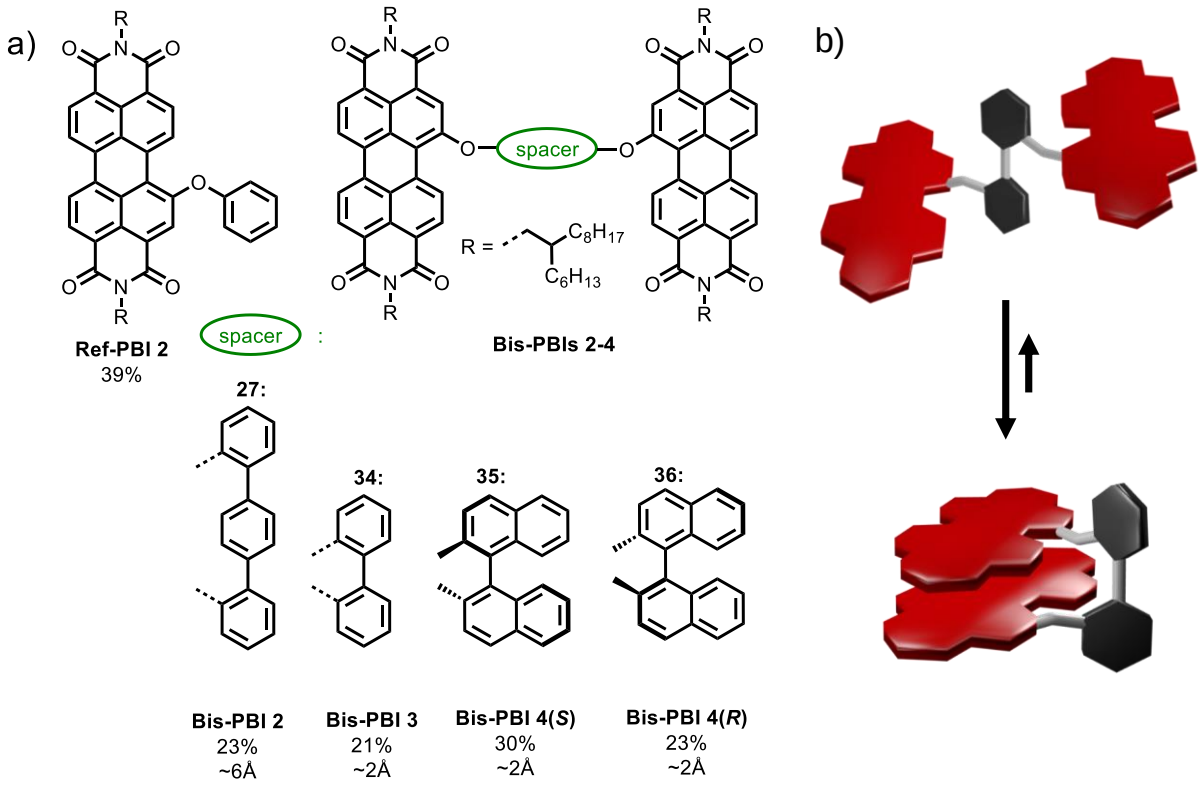

Figure 29. a) Covalently linked **Bis-PBIs 2-4** and chemical structure of reference compound **Ref-PBI 2**. b) Schematic representation of the folding process into a discrete π-stack of two chromophores with defined molecular arrangement exemplified for **Bis-PBI 3**.

5.2 Results and Discussion

5.2.1 UV/Vis Spectroscopy

First, UV/Vis absorption studies were performed for **Ref-PBI 2** and **Bis-PBIs 2-4** in 1,1,2,2-tetrachloroethane (TCE) at room temperature (Figure 30). No spectral changes can be observed at different concentrations (c_0 = 10^{-3}–10^{-6} M), thus, *inter*molecular aggregation of the investigated dyes under the applied experimental conditions can be excluded.

Ref-PBI 2 shows an absorption spectrum characteristic for monomeric PBI dyes, with a main absorption band at 537 nm corresponding to the S_0–S_1 transition and a molar extinction coefficient (ε_{max}) of 50100 M^{-1} cm^{-1} (Figure 31a and Table 3).[132, 158]

Furthermore, additional absorption bands at 503 nm and 463 nm can be observed, which represent vibronic progressions of the main absorption band resulting from a coupling of the electronic transition to C–C-stretching modes of the perylene core with an average frequency of ~ 1400 cm^{-1}.[52-53]

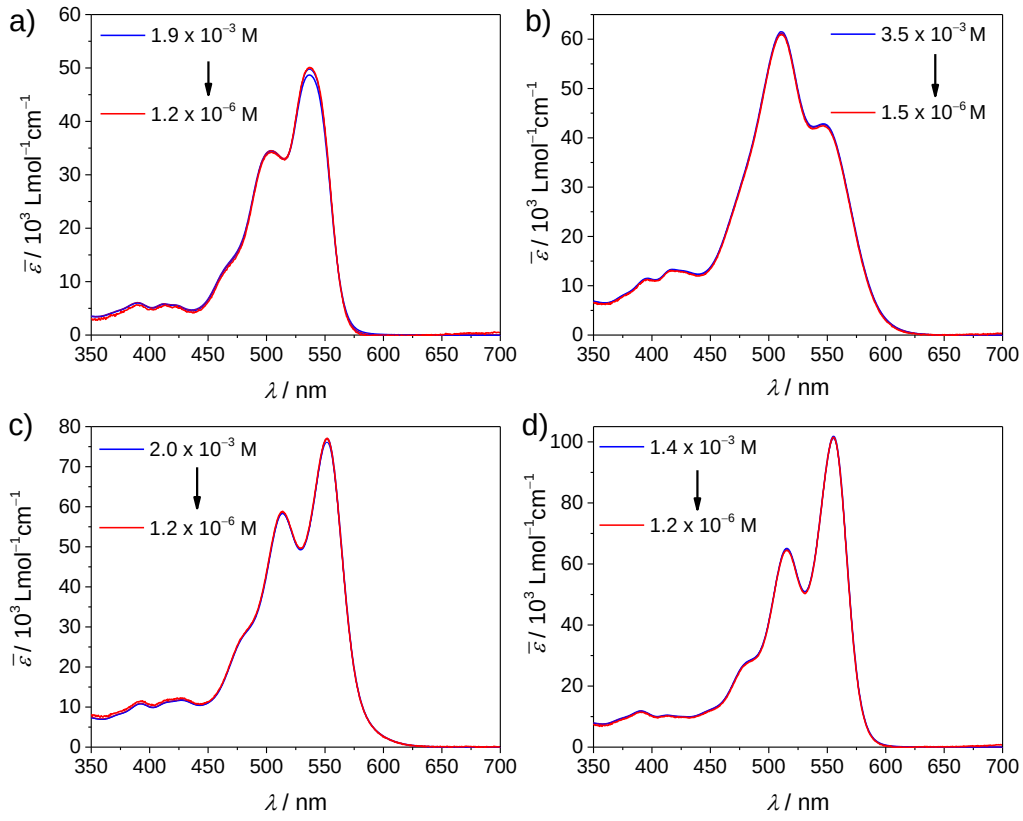

Figure 30. Concentration-dependent UV/Vis absorption spectra (c_0 = 10^{-6} – 10^{-3} M) of a) **Ref-PBI 2**, b) **Bis-PBI 2**, c) **Bis-PBI 3** and d) **Bis-PBI 4(*S*)** in TCE at 298 K.

The ratio of the intensities of the 0–0 and the 0–1 absorption bands (A_{0-0}/A_{0-1}) amounts to 1.45 (Table 3). Changes of this ratio are commonly used to monitor the aggregation process of PBI dyes[37, 159] and enable to determine the exciton coupling energy.[56] The weak absorption in the range of 350 - 450 nm can be assigned to the S_0–S_2 transition of the PBI chromophore.[158]

In comparison to **Ref-PBI 2**, the spectrum of **Bis-PBI 2** shows a blue-shifted absorption maximum at 511 nm with an extinction coefficient of 61000 M^{-1} cm^{-1} and a reversal of the intensities of the 0–0 and 0–1 absorption bands, with a drastically decreased ratio of A_{0-0}/A_{0-1} = 0.69 (Figure 31b and Table 3). This indicates the presence of co-facially π-stacked PBI chromophores[41, 52, 56, 75] with pronounced H-type coupling. The reversal of the band intensities arises from an interplay of exciton and vibrational coupling in the so-called intermediate coupling regime.[52-53, 56] Thus, a folding of **Bis-PBI 2** into a stack of two PBI

chromophores seems reasonable (Figure 29b), as no concentration-dependent changes could be observed.

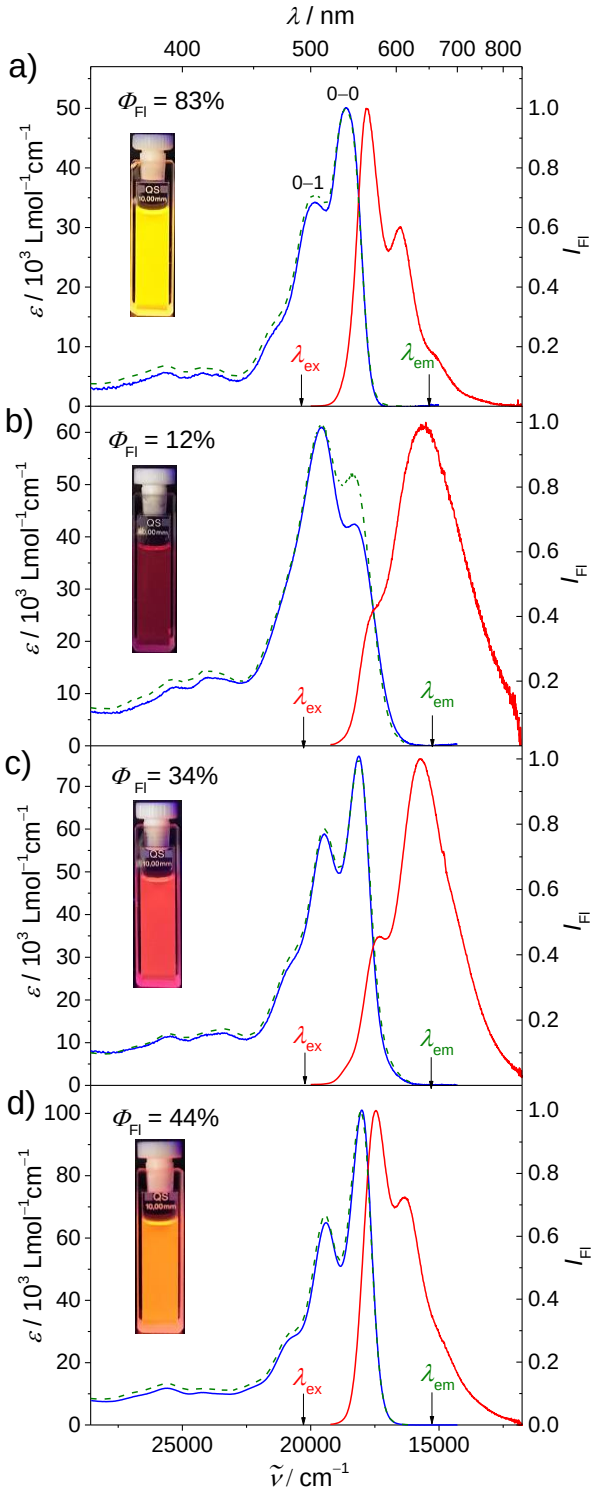

Figure 31. Absorption (blue solid lines, $c_0 = 10^{-5}$ M), normalized fluorescence (red solid lines, $c_0 = 10^{-7}$ M) and excitation spectra (green dashed lines, $c_0 = 10^{-7}$ M) of a) **Ref-PBI 2**, b) **Bis-PBI 2**, c) **Bis-PBI 3** and d) **Bis-PBI 4(*S*)** in TCE at room temperature. The wavelengths for excitation (λ_{ex}) and detection (λ_{Em}) to obtain the fluorescence and excitation spectra, respectively, are highlighted by arrows in the graphs. Insets: Samples of **Ref-PBI 2** and **Bis-PBIs 2-4(*S*)** under UV light (λ = 365 nm) and fluorescence quantum yields (Φ_{Fl}).

Quite differently, for **Bis-PBI 3** a bathochromic shift of the absorption maximum to 551 nm with ε_{max} = 76700 M^{-1} cm^{-1} and only a minor decrease of the ratio A_{0-0}/A_{0-1} = 1.30 can be observed (Figure 31c and Table 3). The minor decrease of the intensity ratio indicates only weak H-type coupling between the PBI chromophores.[56] Thus, on first glance the absorption properties of **Bis-PBI 3** do not suggest a π-stacking of the PBI chromophores, which should result in a prominent decrease of the ratio of the intensities of the 0–0 and 0–1 bands.

Table 3. UV/Vis and fluorescence spectroscopic data of **Bis-PBIs 2-4** and **Ref-PBI 2** measured in TCE at rt.

	Ref-PBI 2	**Bis-PBI 2**	**Bis-PBI 3**	**Bis-PBI 4(S)**
$\lambda_{abs}(A_{0-0})$ [a] / nm	537	549	551	555
$\lambda_{abs}(A_{0-1})$ [a] / nm	503	511	513	515
$\varepsilon_{max}(A_{0-0})$ [a] / $M^{-1}cm^{-1}$	50100	42300	76700	101500
$\varepsilon_{max}(A_{0-1})$ [a] / $M^{-1}cm^{-1}$	34500	61000	59200	65500
$\tilde{\nu}_{1/2}$ [a] / cm^{-1}	1260	–	930	840
$[A_{0-0} / A_{0-1}]$ [a] / 1	1.45	0.69	1.30	1.55
λ_{em} [b] / nm	561	641	635	573
$\Delta\tilde{\nu}_{Stokes}$ [b] / cm^{-1}	800	3970	2400	570
Φ_{Fl} [b] / %	83	12	34	44
$\tau_{Fl,1}$ [b,c] / ns (amplitude)	4.4 (100%)	3.9 (10%)	4.1 (1%)	3.9 (11%)
$\tau_{Fl,2}$ [b,c] / ns (amplitude)	-	16.7 (90%)	10.9 (99%)	8.4 (89%)

[a] $c_0 = 10^{-5}$ M.

[b] $c_0 = 10^{-7}$ M, OD < 0.05.

[c] τ_{Fl} were determined by tail fit analysis of data obtained from time-correlated single photon counting measurements with ps laser diode at 505 nm using the magic angle setup.

This also holds true for **Bis-PBI 4(*S*)**, for which a slightly larger bathochromic shift (555 nm) of the absorption bands with a small increase of the ratio of the band intensities to A_{0-0}/A_{0-1} = 1.55 can be observed indicating very weak J-type coupling (Figure 31d and Table 3).[56] In addition, a narrowing of the absorption bands is present ($\tilde{\nu}_{1/2}$ = 840 cm^{-1}) along with an increase of ε_{max} to 101200 M^{-1} cm^{-1}, that is characteristic for J-type aggregates.[9, 160-161] As expected for a pair of two enantiomers, **Bis-PBIs 4(*R*)** and **4(*S*)** exhibit the same

absorption properties (Figure 32) and thus, the main focus lies on the optical features of **Bis-PBI 4(*S*)** in the following parts.

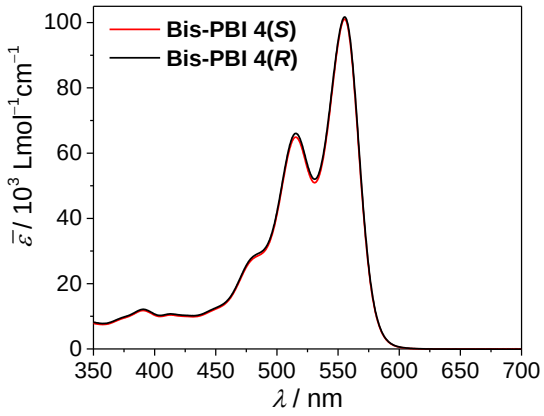

Figure 32. UV/Vis absorption spectra of **Bis-PBI 4(*S*)** (red) and **Bis-PBI 4(*R*)** (black) in TCE at 298 K (c_0 = 1 x 10^{-5} M).

Hence, while the absorption properties of **Bis-PBI 2** indicate a π-stacked arrangement of the PBI chromophores with pronounced H-type coupling, the absorption spectra of **Bis-PBI 3** and **Bis-PBI 4(*S*)** reveal weak H- or J-type coupling, respectively. Therefore, one might expect clearly different orientations of the chromophores for all Bis-PBI folda-dimers, leading to the distinct absorption features.

Furthermore, temperature-dependent UV/Vis studies were performed, where **Ref-PBI 2** reveals a hypochromic effect and a concomitant blue-shift of the absorption upon heating (see the Appendix, Figure 39a). This phenomenon can be attributed to the flipping of the naphthalene moieties of the perylene core, which is more pronounced at higher temperatures. The temperature-dependent spectra of **Bis-PBIs 2-4(*S*)** show a similar behaviour suggesting no significant changes of the chromophore arrangement upon heating (see the Appendix, Figure 39b-d). However, for **Bis-PBI 2** the 0–0 absorption band gains slightly intensity upon heating, that can be attributed to an increase of the amount of unfolded species.

Also the decrease of solvent polarity has no considerable effect on the folding process as evident from the UV/Vis absorption spectra in solvents of different polarity (see the Appendix, Figure 40). Only the for PBI dyes typical positive solvatochromism can be observed,[162] whereas the intensities of the 0–0 and 0–1 absorption bands are almost the same.

5.2.2 CD Spectroscopy

As expected, circular dichroism (CD) spectroscopy reveals no CD signal for **Ref-PBI 2** (Figure 33a), since the atropo-enantiomers arising from the slight twist of the naphthalene units of the PBI core can easily convert into each other at room temperature.[163] This also holds true for **Bis-PBIs 2-3** where no CD signal can be observed.

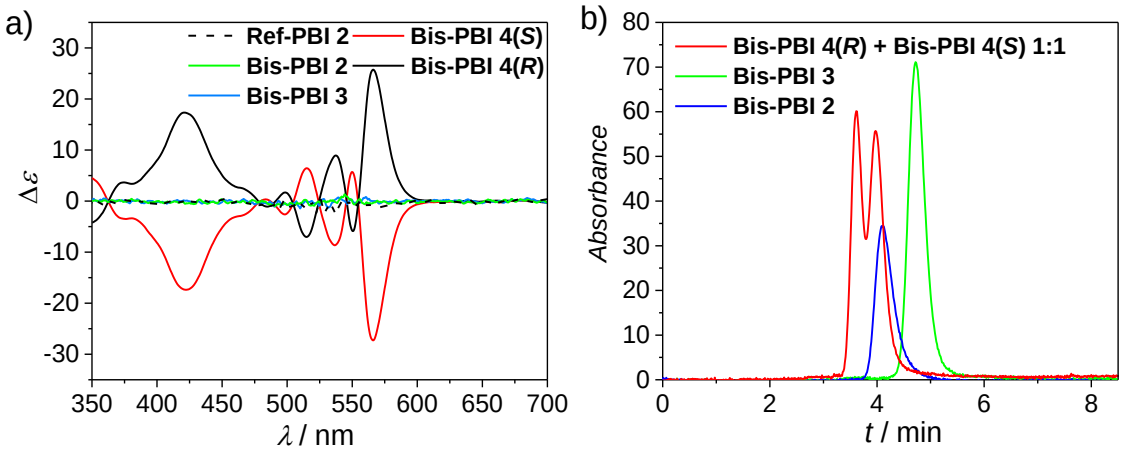

Figure 33. a) CD spectra of **Ref-PBI 2** and **Bis-PBIs 2-4** at ($c_0 = 2 \times 10^{-5}$ M) in TCE at room temperature. b) Chiral semi-analytical HPLC separation of **Bis-PBI 2**, **Bis-PBI 3** and **Bis-PBIs 4(*S*)** and **4(*R*)** (*v*:*v* = 1:1) from a methylcyclohexane solution.

In contrast, the CD spectra of **Bis-PBI 4(*R*)** and **Bis-PBI 4(*S*)** each show pronounced (bisignated) Cotton effects with mirror image behaviour as expected for two enantiomers arising from the hindered rotation around the 1,1'-binaphthyl axis. Notably, Cotton effects are not only present in the UV region where the spacer moiety absorbs, but also in the visible absorption range of the PBI´s S_0–S_1 (450 - 650 nm) and S_0–S_2 (350 - 450 nm) transitions. The corresponding zero-crossings are located at the absorption maxima of the respective Bis-PBIs revealing chiral exciton coupling between the two chromophores, which indicates close proximity of the PBI moieties in a fixed chiral arrangement[59] with locked twist of the naphthalene units of the two PBI cores.[164]

This could be further proven by performing chiral semi-analytical HPLC (Figure 33b) for a 1:1 mixture of **Bis-PBIs 4(*R*)** and **4(*S*)** in methylcyclohexane, where it was possible to separate the two enantiomers due to the locked twist of the naphthalene units as it is depicted in Figure 33b. In contrast, for **Bis-PBIs 2** and **3** no separation of the respective enantiomers could be achieved by performing chiral semi-analytical HPLC in methylcyclohexane, which is in good agreement with their absent CD signals.

5.2.3 Fluorescence Spectroscopy

To gain further insight into the electronic coupling of the herein investigated Bis-PBI dyes, steady state fluorescence spectroscopy was performed under high diluted conditions in TCE ($c_0 = 10^{-7}$ M, Figure 31) to avoid reabsorption effects.[147] **Ref-PBI 2** shows a fluorescence spectrum characteristic for PBI monomers with an emission maximum (λ_{Em}) at 561 nm and well-resolved vibronic fine structure with mirror-image relationship to the absorption band (Figure 31a and Table 3). Furthermore, a small Stokes shift of 800 cm^{-1} and a high fluorescence quantum yield of 83% was determined, which is typical for monomeric PBI chromophores.[25, 28, 165]

In contrast, the well-resolved fine structure is lost in the fluorescence spectrum of **Bis-PBI 2** and a broad, unstructured emission band at 641 nm with a considerably large Stokes shift of 3970 cm^{-1} is present (Figure 31b and Table 3). Further, the fluorescence quantum yield is drastically decreased to 12%, which is indicative for the formation of an excimer.[106, 125] The excimer state is commonly observed for π-stacked PBI dyes and arises from structural rearrangement of the chromophores in the excited state.[125] Additionally, the emission spectrum of **Bis-PBI 2** exhibits a small shoulder at ~570 nm, probably due to traces of remaining monomer fluorescence from a small amount of unfolded species, which can be observed for the other Bis-PBIs as well (*vide infra*).[36]

Surprisingly, despite of its monomer-like absorption features **Bis-PBI 3** likewise shows a typical excimer emission band at 635 nm, however with a reduced Stokes shift of 2400 cm^{-1} and a significantly higher fluorescence quantum yield of 34% (Figure 31c, Table 3). Thus, also the fluorescence spectrum of **Bis-PBI 3** suggests a π-stacking of the chromophores, which is surprising due to the weak H-type coupling observed in the corresponding absorption spectrum. In contrast, monomer-like signatures can be observed in the emission spectrum of **Bis-PBI 4(*S*)** (λ_{Em} = 573 nm) with a well-resolved vibronic fine structure and a small Stokes shift of 570 cm^{-1} (Figure 31d, Table 3). This is in accordance with the UV/Vis absorption spectrum indicating very weak J-type exciton coupling between the two PBI chromophores. However, the fluorescence spectrum of **Bis-PBI 4(*S*)** is slightly broadened compared to **Ref-PBI 2** and a decreased fluorescence quantum yield of 44% was determined, which is rather unusual for conventional J-type PBI aggregates with a large longitudinal displacement of the chromophores.[48] The measured excitation spectra for all Bis-PBI dyes are in accordance with the corresponding absorption profiles revealing species selective emission from the corresponding folded state (Figure 31, green dotted lines).

Further information on the excited state properties of the PBI dyes was gained by fluorescence lifetime measurements (Figure 34).

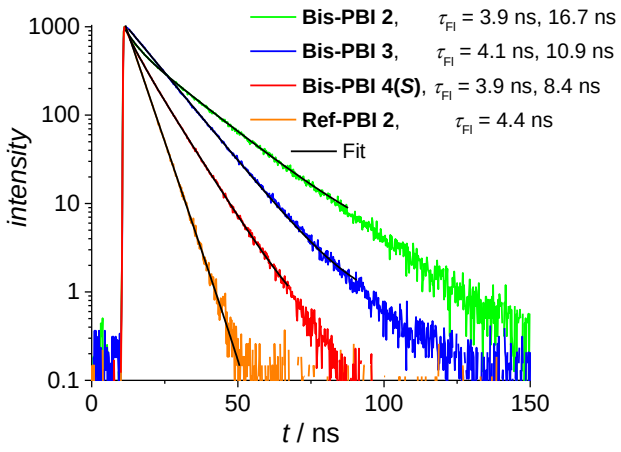

Figure 34. Lifetime measurements of **Bis-PBI 2**-**4(*S*)** and **Ref-PBI 2** in TCE at 298 K ($c_0 = 10^{-7}$ M).

Ref-PBI 2 exhibits a fluorescence lifetime of 4.4 ns in the TCE at room temperature (Table 3), which is in agreement with previously reported values for monomeric PBI chromophores.[109-111] On the contrary, for **Bis-PBIs 2**-**4(*S*)** two fluorescence lifetimes were determined (Table 3). The shorter lifetime of ~ 4 ns (Table 3) with significantly lower amplitude is comparable to the value of **Ref-PBI 2** and thus, can be attributed to emission from unfolded and presumably more emissive species. In the case of **Bis-PBIs 2** and **3**, the second lifetime is distinctly longer as expected for PBI excimers (16.7 and 10.9 ns, respectively) due to the more forbidden radiative transition to the ground state potential surface.[25] The second fluorescence lifetime of 8.4 ns determined for **Bis-PBI 4(*S*)** is also increased, despite the monomer-like emission spectrum, indicating considerable interaction between the chromophores.

Hence, the spectroscopic investigations by UV/Vis, CD and fluorescence spectroscopy reveal distinct variations of the optical properties of the presumably folded Bis-PBI dyes, which can only be rationalized by different structural arrangements of the two chromophores.

5.2.4 NMR Spectroscopy

One of the striking outcomes of the herein performed spectroscopic studies is that **Bis-PBI 3** shows almost negligible electronic coupling in the absorption data, whereas the excimer emission properties indicate strong π-π-interaction between the chromophores. Structural information on supramolecular aggregates can be gleaned by NMR spectroscopy. Therefore,

NMR studies have been performed for **Ref-PBI 2** and **Bis-PBIs 2-4(*S*)** in 1,1,2,2-tetrachloroethane-d_2 (TCE-d_2) to investigate the structural arrangement of the dyes. First, diffusion-ordered spectroscopy (DOSY) was applied to all target compounds (Figure 35) and comparable hydrodynamic radii of 11.0–11.3 Å were determined that are reasonably larger than the one determined for **Ref-PBI 2** (8.4 Å, see the Appendix Figure 41).

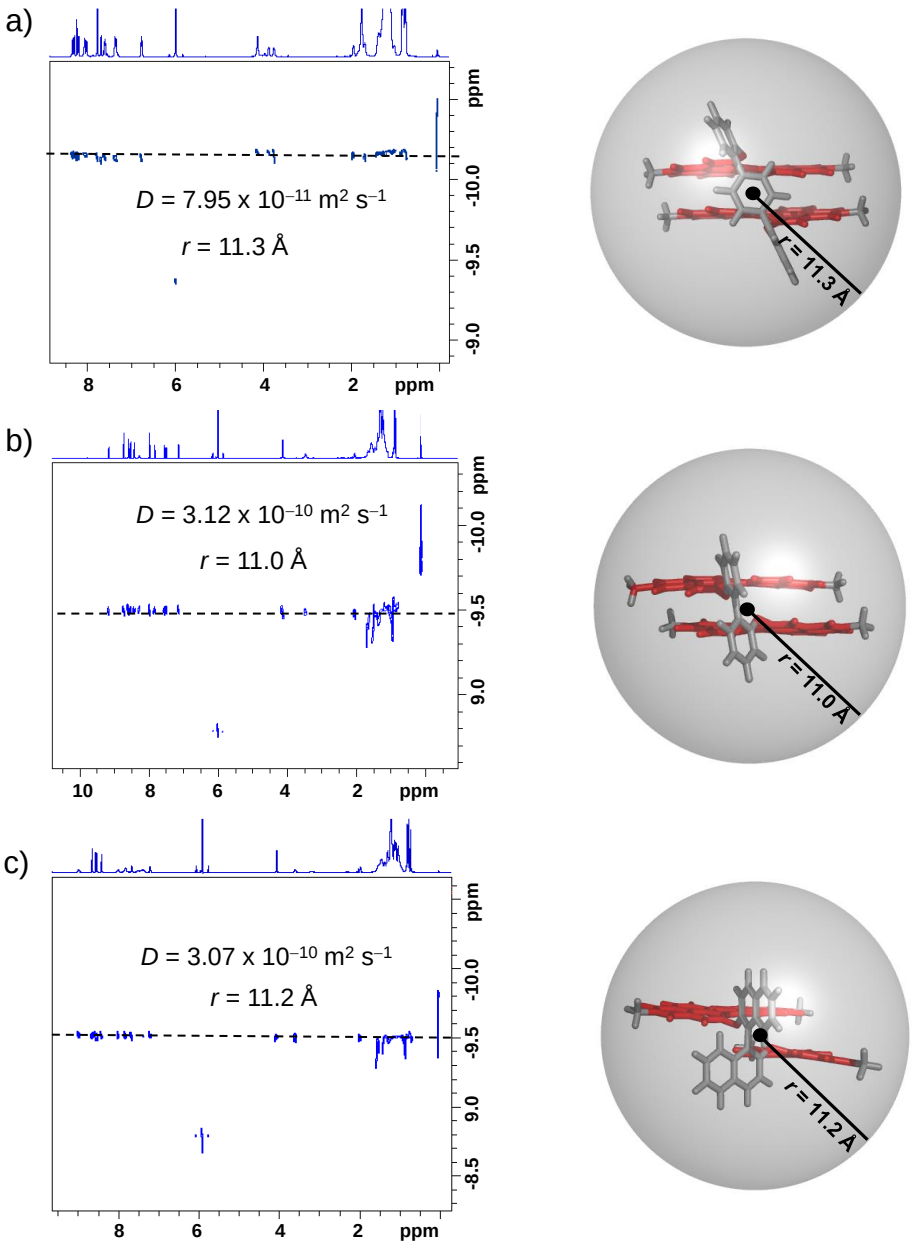

Figure 35. Left: 2D plot of DOSY NMR (600 MHz, TCE-d_2) spectra of a) **Bis-PBI 2** (c_0 = 3.5 x 10^{-3} M, 273 K), b) **Bis-PBI 3** (c_0 = 2.0 x 10^{-3} M, 348 K) and c) **Bis-PBI 4(*S*)** (c_0 = 1.4 x 10^{-3} M, 348 K). Right: Illustration of the energy-minimized structures of **Bis-PBIs 2-4(*S*)** obtained from DFT calculations (B97D3/def2-SVP) with the hydrodynamic radius as received from the Stokes-Einstein equation.

According to the previously discussed UV/Vis studies, temperature has no significant influence on the folding process of the Bis-PBI dyes (see the Appendix, Figure 39). Thus, the ^{1}H NMR spectra shown in Figure 36 were recorded at 370 K as all three folda-dimers show remarkably sharp and well resolved proton signals under these conditions.

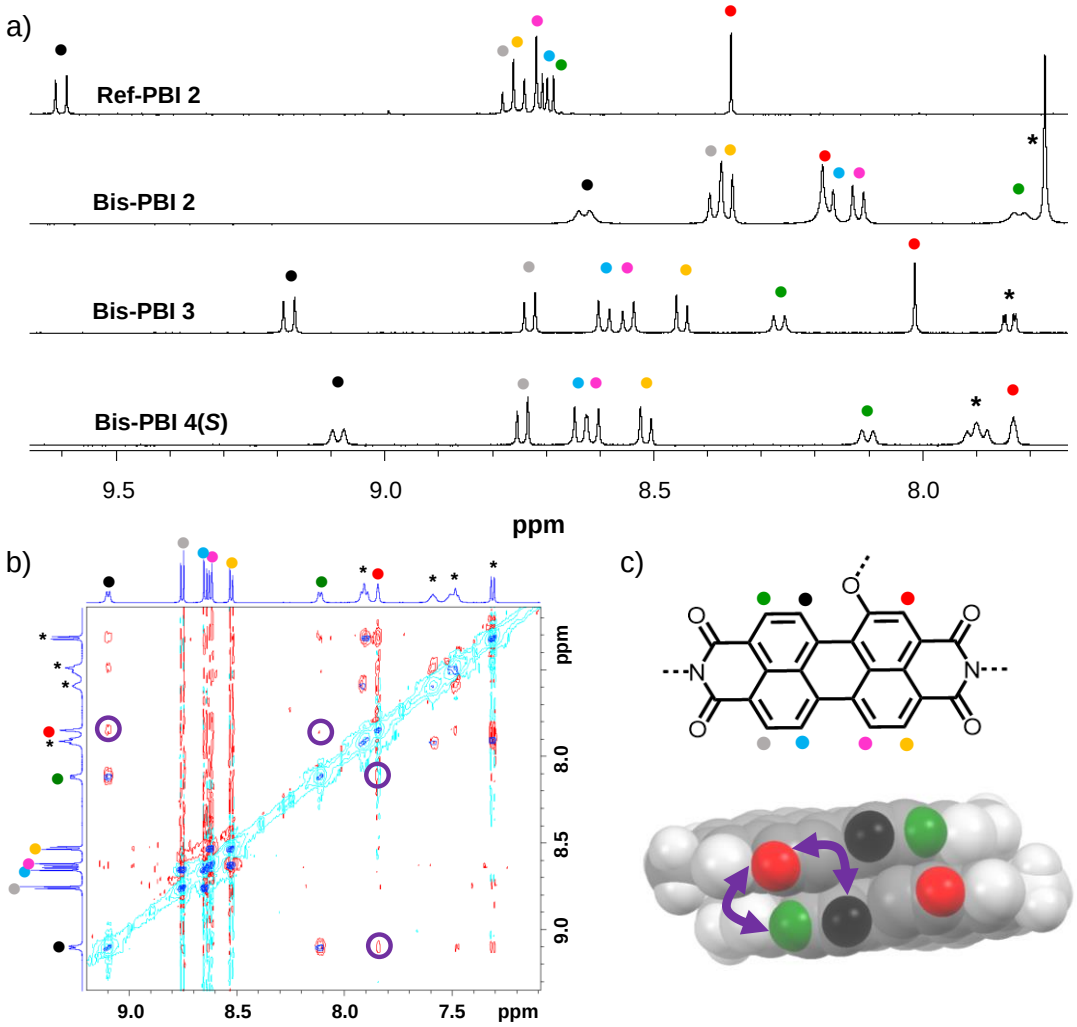

Figure 36. a) Selected area of the ^{1}H NMR (400 MHz) spectra of **Ref-PBI 2** and **Bis-PBIs 2-4(*S*)** in TCE-d_2 at 370 K (c_0 = 2 x 10^{-3} M) with PBI protons marked as indicated in the molecular structure displayed in panel c). The protons marked with an asterisk represent protons of the spacer moieties. b) Superposition of COSY (blue) and ROESY (red: positive signal/cyan: negative signal) spectra of **Bis-PBI 4(*S*)** at 373 K in TCE-d_2 (c_0 = 1.4 x 10^{-3} M, 600 MHz). c) Molecular structure of the PBI chromophore with marked protons and space-filling model of a PBI π-stack comprising two chromophores. The purple double-headed arrows indicate close spatial proximity between the protons according to the cross-peaks observed in the ROESY spectrum of **Bis-PBI 4(*S*)**. Only the interaction for one side of the π-stack is shown and the spacer moiety is omitted for clarity.

This is rather unusual for π-stacked PBI chromophores, for which broad and undefined proton signals are usually observed.[40, 72]

Ref-PBI 2 exhibits a typical monomer spectrum of a phenoxy bay-substituted PBI chromophore (Figure 36a).[158] The signals were assigned to the individual protons based on 2D homonuclear correlation spectroscopy (COSY), rotating frame nuclear Overhauser effect spectroscopy (ROESY) and in addition with heteronuclear single quantum correlation (HSQC) and heteronuclear multiple-bond correlation (HMBC) NMR measurements. Remarkably, the proton marked in black (9.60 ppm, Table 4) shows a significant downfield shift in comparison to the other protons of the PBI chromophore. This downfield shift can be explained as a C–H···O hydrogen bonding interaction of the aromatic bay proton to the oxygen atom of the phenoxy-substituent, which is in close proximity.[158] Hence, the chemical shift of this proton can give insight into the conformation of the oxygen-substituent and its electron lone pairs. In contrast, the proton marked in red (8.35 ppm, Table 4) exhibits an upfield shift due to the ring current of the phenoxy substituent leading to a magnetic shielding.[158]

Table 4. Summary of ^{1}H NMR proton shifts from Figure 36 (600 MHz, TCE-d_2, 370K): chemical shifts δ (ppm) and assignment of significant PBI protons of **Bis-PBI 2-4(*S*)** and **Ref-PBI 2**.

	●	●	●	●	●	●	●
Ref-PBI 2	9.60	8.77	8.70	8.72	8.75	8.69	8.35
Bis-PBI 2	8.63	8.38	8.17	8.12	8.36	7.82	8.19
Bis-PBI 3	9.17	8.73	8.59	8.55	8.45	8.27	8.01
Bis-PBI 4(*S*)	9.08	8.74	8.63	8.61	8.51	8.10	7.83

The NMR spectra of **Bis-PBIs 2-4(*S*)** also show only one set of sharp signals revealing a well-defined arrangement of the chromophores with high symmetry (Figure 36a). The pronounced upfield shift of the PBI protons in comparison with **Ref-PBI 2** indicate a stacking of the chromophores, which results in a shielding of the protons by the adjacent π-surface.[166-167] Whereas the ^{1}H NMR spectra of **Bis-PBI 3** and **Bis-PBI 4(*S*)** look rather similar, larger deviations can be observed for **Bis-PBI 2**. Especially the protons highlighted in black (8.63 ppm, Table 4) and green (7.82 ppm, Table 4) show a drastic upfield shift, which is less pronounced for **Bis-PBIs 3** and **4(*S*)**. Hence, a similar conformation of the oxygen-substituent

for **Bis-PBIs 3** and **4(*S*)** seems reasonable, while a distinctly different arrangement of the bay-substituent can be assumed for **Bis-PBI 2**. To unambiguously confirm the π-stacking of the PBI chromophores, 2D ROESY measurements were performed, that allow to determine protons in close spatial proximity. Hereby, for all Bis-PBI dyes a cross-peak between the protons marked in red (so-called headland position) and black (bay position, Figure 36b and see the Appendix Figure 43 - 44) could be observed. This cross-peak is not present in the ROESY spectrum of **Ref-PBI 2** (see the Appendix Figure 42), so that it can be ruled out that the signal arises from spatial proximity of these protons within one chromophore. Since the cross-peak is furthermore not observed in the COSY spectrum of the Bis-PBI dyes (Figure 36b and see the Appendix Figure 43 - 44), it does not represent a COSY artefact. For **Bis-PBIs 2** and **4(*S*)** additionally a cross-peak between the headland protons marked in green and red (Figure 36b and see the Appendix Figure 43) can be observed, which is also not the case for **Ref-PBI 2** (see the Appendix Figure 42). All these findings support a tight π-stacked arrangement of the PBI chromophores in which the protons are in close proximity (Figure 36c).

5.2.5 Geometry Optimizations

The results obtained by NMR spectroscopy reveal for all Bis-PBI dyes a π-stacked geometry of the chromophores, which is not at all obvious from the UV/Vis data. To gain deeper insight into the structural arrangement of the chromophores, geometry optimizations at the density functional theory (DFT) level were performed. Hereby, the def2-SVP basis set[168] and the B97D3 functional including Grimme's dispersion correction[169] was employed, which is necessary to adequately describe the structures of PBI aggregates[60, 118] The geometry-optimized structures are depicted in Figure 37 (for each Bis-PBI the structure of the *S*-enantiomer was calculated regarding the axial chirality of the spacer moiety).

Accordingly, all three Bis-PBI dyes exhibit a π-stacked arrangement of the chromophores with an interchromophoric distance of 3.3 - 3.5 Å and C_2 symmetry. **Bis-PBI 2** shows the largest distance (3.5 Å) due to the *p*-terphenyl-spacer moiety, which does not enable a closer contact between the two PBI chromophores. The chromophores in **Bis-PBIs 3** and **4(*S*)** both have a distance of about 3.3 Å because of the same length of the biphenyl and 1,1'-binaphthyl spacer units. For all Bis-PBI dyes a torsional displacement between the chromophores can be observed with increasing angle from **Bis-PBI 2** (14°), **Bis-PBI 3** (22°) to **Bis-PBI 4(*S*)** (25°) accompanied by a displacement of the dyes' centers by 1.0 Å (**Bis-PBI 2**), 1.9 Å (**Bis-PBI 3**) and 2.1 Å (**Bis-PBI 4(*S*)**). According to Fink *et al.*, the optimal ground state geometry of a π-

stack comprising two non-substituted PBI chromophores exhibits a π-distance of 3.4 Å and a rotational angle of 29° without transversal and longitudinal shift of the chromophores.[118]

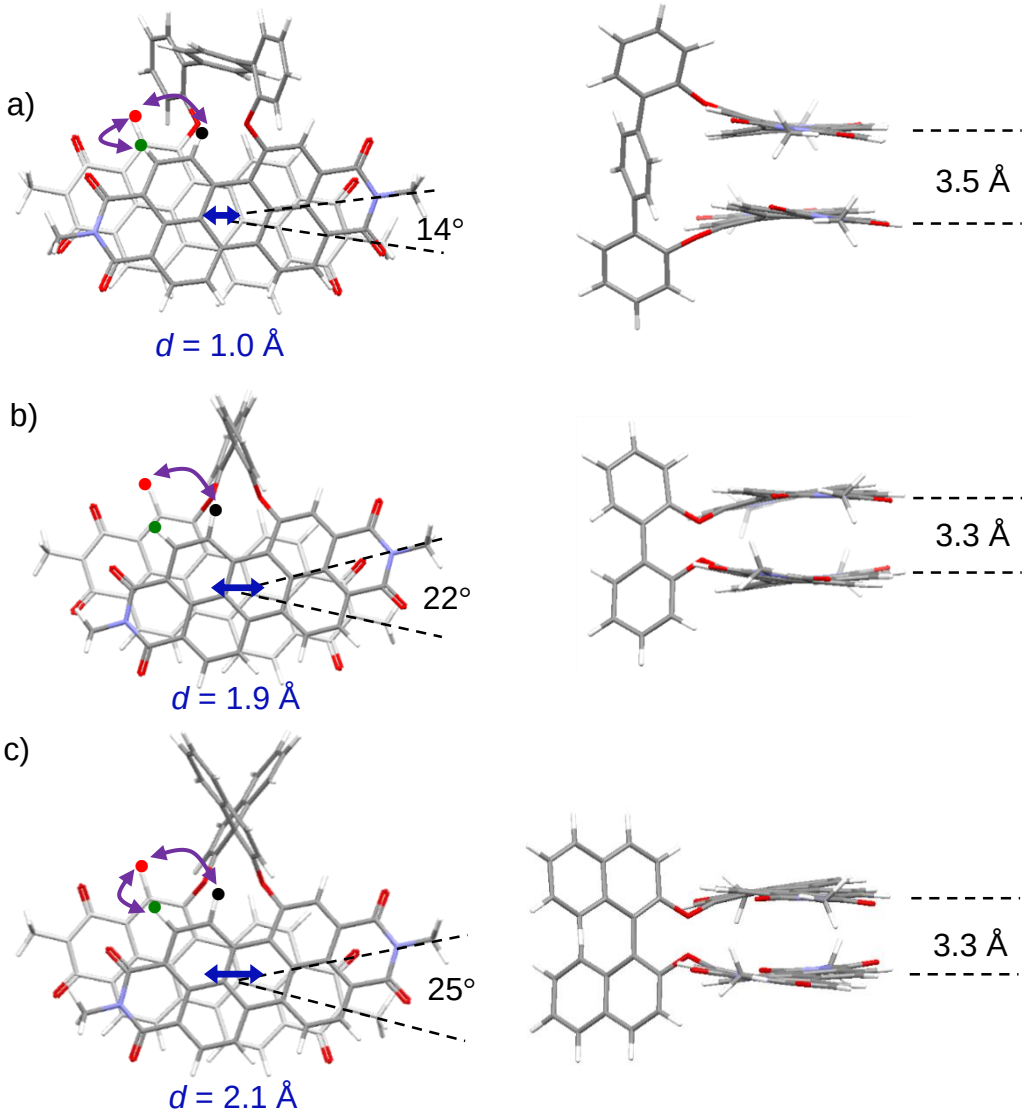

Figure 37. Top view (left) and side view (right) onto the geometry-optimized structures of a) **Bis-PBI 2**, b) **Bis-PBI 3** and c) **Bis-PBI 4(*S*)** obtained by DFT (B97D3/def2-SVP) calculations. For all Bis-PBI dyes the structure of the *S*-enantiomer regarding the axial chirality of the spacer moiety was calculated. Purple double arrows indicate close spatial proximity between the protons depicted in red, black and green according to the cross peaks observed in the ROESY NMR spectra. For clarification only the coupling on one side of the chromophore is displayed.

Hence, the employed spacer moieties force the two PBI chromophores to stack in an unusual manner. The two naphthalene moieties of the PBI chromophores exhibit a twist of 12° (*p*-terphenyl), 11° (biphenyl) and 10° (1,1'-binaphthyl) arising from the sterical hindrance of the bay-substituents. The twist can be also observed for the geometry-optimized structure of **Ref-**

PBI 2, however less pronounced (5°) due to the lower steric hindrance of the phenoxy group in the bay position. The geometry-optimized structures are in agreement with our results obtained by NMR studies. The C_2 symmetry leads to only one set of signals for the chromophores since the respective protons are chemically equivalent. In addition, whereas for **Bis-PBIs 3** and **4(*S*)** the oxygen of the bay substituents of the PBI chromophores have similar conformation (Figure 37b, c right), the arrangement is distinctly different in the case of **Bis-PBI 2** (Figure 37a, right). Therefore, the hydrogen bonding of the proton marked in black is less pronounced for **Bis-PBI 2** resulting in an increased upfield shift of the signal in the ^{1}H NMR spectrum (Figure 36a). The cross-peaks observed in the ROESY NMR spectra between the red and black marked protons as well as between the red and green marked protons (for **Bis-PBIs 2** and **4(*S*)**) can be rationalized by the close proximity of the protons within the π-stacks (Figure 37). Further, the likeness of the ^{1}H NMR spectrum of **Bis-PBIs 3** and **4(*S*)** suggests a very similar arrangement of the chromophores as evident from the geometry-optimized structures. The excimer emission observed for **Bis-PBIs 2-3** is also in accordance with a π-stacked arrangement of the chromophores. It is well known that the excimer state of PBI aggregates is reached by structural reorganization leading to a geometry with a torsion angle between the chromophores of almost zero.[66, 106] However, this arrangement is not possible for the more rigid **Bis-PBI 4(*S*)** with a large rotational barrier around the 1,1'-binaphthyl axis.[170] Therefore, the typical excimer emission band is not observed for **Bis-PBI 4(*S*)** but a rather sharp and well-resolved emission spectrum with a small Stokes shift being quite unusual for π-stacked PBI dyes.[25]

5.2.6 Theoretical Investigation

Whereas the herein obtained results from fluorescence and NMR studies provide strong evidence for a stacking of the PBI chromophores in the folded state, UV/Vis spectra apparently do not support the presence of a folded π-stacked arrangement. As shown for a large number of self-assembled and folded PBI aggregates,[25, 50-51, 149] close co-facial $\pi-\pi$-stacking should lead to a drastic decrease of the ratio A_{0-0}/A_{0-1} in the UV/Vis spectra, which is not observed for **Bis-PBIs 3** and **4(*S*)** (Figure 31).

The spectral changes upon aggregation of PBI dyes are commonly described in terms of exciton-vibrational coupling, where the electronic transition couples to the vibrational modes of the chromophores.[52, 56] The exciton coupling is mainly assigned to long-range Coulomb coupling between the transition dipole moments of the chromophores leading to H- or J-type

coupling with positive or negative exciton coupling energy, respectively. To determine the Coulomb coupling for **Bis-PBIs 2-4(*S*)** the transition charge method[171] was used. Hereby, the transition dipole moments of the chromophores are replaced by point atomic charges and the exciton coupling energy equals the Coulomb interaction between the transition charges of the different chromophores:[171]

$$J = \frac{1}{4\pi\varepsilon_0} \sum_i \sum_j \frac{q_i^{(1)} \cdot q_j^{(2)}}{|\mathbf{r}_i^{(1)} - \mathbf{r}_j^{(2)}|} \,. \tag{3}$$

Here, $q_i^{(a)}$ represents the transition charge on atom *i* of chromophore *a*, $\mathbf{r}_i^{(a)}$ corresponds to the position vector of the respective transition charge and ε_0 is the vacuum permittivity. This method gives reliable results for interchromophoric distances shorter than the size of the chromophores,[172] whereas the dipole-dipole approximation usually dramatically overestimates the exciton coupling energy.[173] Further, time-dependent DFT (TDDFT) calculations were used with the long-range corrected functional ωB97[174] and def2-SVP[168] as basis set to calculate the transition density for **Ref-PBI 2** (for further information see the Appendix).

The density was fitted to atomic partial charges and the exciton coupling energies were then calculated by equation 3 using the structures obtained from geometry optimizations (Figure 37). The results are shown in Table 5. Accordingly, all Bis-PBI dyes studied in this chapter exhibit pronounced H-type coupling ($J_{Coul} > 0$) in the range of 545 - 678 cm^{-1}. Such coupling should lead to the reversal of the intensities of the 0–0 and 0–1 absorption bands as observed for **Bis-PBI 2** with respect to **Ref-PBI 2** (Figure 31), which arises from the interplay of exciton and vibrational coupling.[52, 56] However, for **Bis-PBIs 3** and **4(*S*)** no significant decrease of the ratio A_{0-0}/A_{0-1} could be observed contradicting the presence of pronounced H-type coupling according to the calculated exciton coupling energies.

Spano *et al.* have developed a method to determine the exciton coupling energy based on the intensities of the 0–0 and 0–1 absorption bands of aggregates that show exciton-vibrational coupling.[56, 59] This model was then applied for **Bis-PBIs 2-4(*S*)**. The resulting values were then compared with the ones obtained by the transition charge method (Table 5, for details concerning the theoretical investigation see the Appendix).

Whereas the exciton coupling energy for **Bis-PBI 2** obtained by the method of Spano *et al.* is in very good agreement with the one obtained by the transition charge method, large deviations are observed in the case of **Bis-PBIs 3** and **4(*S*)**. For **Bis-PBI 3**, an exciton coupling energy of $J_{Coul} = 554$ cm^{-1} was estimated based on the transition charge method, while our analysis based

on the absorption spectrum reveals significantly weaker coupling (J = 77 cm^{-1}). The same is true for **Bis-PBI 4(*S*)**, for which the transition charge method gives an exciton coupling energy of J_{Coul} = 545 cm^{-1} and thus, pronounced H-type coupling should be observed. However, the results according to Spano's method predict negligible J-type coupling (J = –7 cm^{-1}).

Table 5. Calculated exciton coupling energies and hole/electron transfer integrals for **Bis-PBIs 2-4(*S*)**.

	Bis-PBI 2	**Bis-PBI 3**	**Bis-PBI 4(*S*)**
J^a / cm^{-1}	713	152	–7
J^b / cm^{-1}	643	77	–10
$J_{Coul}{}^c$ / cm^{-1}	678	554	545
t_e / cm^{-1}	66	697	658
t_h / cm^{-1}	428	547	675
$J_{CT}{}^d$ / cm^{-1}	–35	–477	–555

[a] Estimated from the intensity ratio of the A_{0-0} and A_{0-1}absorption bands in the UV/Vis spectra.
[b] Determined based on equation 5.
[c] Calculated by the transition charge method.
[d] Determined based on equation 4.

Thus, whereas the absorption spectrum of **Bis-PBI 2** can be rationalized by exciton-vibrational coupling between the PBI chromophores, assuming that the exciton coupling can be mainly described by (long-range) Coulomb interaction between the transition charges, this description fails for **Bis-PBIs 3** and **4(*S*)**. Therefore, additional contributions have to be taken into account to understand the absorption spectra of these PBI dye stacks. For short interchromophoric distances as present in π-stacks, charge-mediated short-range coupling can be significant and thus, influence the absorption properties of aggregates.[14, 16, 54, 61] This short-range coupling arises from HOMO–HOMO and LUMO–LUMO overlap enabling charge-transfer between the molecules.[14, 62] Under the assumption that the charge-transfer state and the local Frenkel exciton state are well separated (perturbative limit), the exciton coupling energy for the short-range coupling can be calculated by:[14, 54]

$$J_{CT} = -2\frac{t_e t_h}{E_{CT} - E_{S_1}}. \quad (4)$$

where t_e and t_h represent the electron and hole transfer integrals, respectively, and $E_{CT} - E_{S_1}$is the energy difference between the charge transfer and the local Frenkel exciton state. The

overall coupling can be then described as the sum of the (long-range) Coulomb coupling and the charge-transfer mediated short-range coupling: [14, 54]

$$J = J_{Coul} + J_{CT}. \quad (5)$$

The interference effect between long- and short-range coupling can be constructive or destructive depending on the sign of the coupling energies.

The transfer integrals for **Bis-PBIs 2-4(*S*)** were calculated employing the unique fragment approach[175] as implemented in the Amsterdam Density Functional program package.[176-178] The TZP basis set[179] and the PW91 functional[180] was used, which gives reliable results for PBI dyes.[181] Accordingly, all three Bis-PBI dyes exhibit J-type short-range coupling according to equation 4, since the electron and transfer integrals are both positive (Table 5) and $E_{CT} - E_{S_1} > 0$. Hence, the overall coupling should be weakened due to the charge-transfer mediated coupling. **Bis-PBIs 3** and **4(*S*)** show a significant HOMO–HOMO and LUMO–LUMO overlap as evident from the large values of the hole and electron transfer integrals. In contrast, while also **Bis-PBI 2** exhibits a considerable HOMO–HOMO overlap (t_h = 428 cm^{-1}), the LUMO–LUMO overlap is remarkably small (t_e = 66 cm^{-1}). This is reflected in the different energy splitting of the frontier molecular orbitals of the Bis-PBI dyes (Figure 38). Therefore, a significantly weaker J-type short-range coupling for **Bis-PBI 2** might be assumed.

To determine the short-range coupling energy (J_{CT}) for the PBI stacks, the energy difference $E_{CT} - E_{S_1}$ between the charge transfer state and the local Frenkel exciton state is required (equation 4). Unfortunately, it is difficult to calculate reliable values for this energy difference.[182] Assuming that the charge transfer state is 1600 cm^{-1} above the local Frenkel state, which is in good agreement with the results obtained for PBI crystals,[142] respective short-range coupling energies were obtained which are shown in Table 5.

Accordingly, **Bis-PBI 2** shows weak J-type short-range coupling (J_{CT} = −35 cm^{-1}) so that the overall coupling is mainly due to long-range Coulomb coupling, which is of H-type nature. In contrast, **Bis-PBIs 3** and **4(*S*)** show strong J-type short-range coupling, being of similar magnitude as the H-type long-range coupling. This leads to a negligible overall coupling according to equation 5. Therefore, only small changes of the intensity ratio of the 0–0 and 0–1 absorption bands are observed in the UV/Vis spectra of **Bis-PBIs 3** and **4(*S*)**, whereas **Bis-PBI 2** shows the typical signature of an H-type aggregate with significantly reduced A_{0-0}/A_{0-1} ratio (Figure 31, Table 3). For **Bis-PBI 4(*S*)** the short-range coupling even slightly exceeds the

long-range coupling resulting in a small increase of A_{0-0}/A_{0-1}. It has to be noted that the perturbative approach represents an approximation since the requirement of pronounced energetic separation between the local Frenkel exciton state and charge transfer state is not fully given.[11, 182] However, the herein performed analysis reveals strong competition between short- and long-range coupling explaining the distinct spectral signatures of the PBI π-stacks.

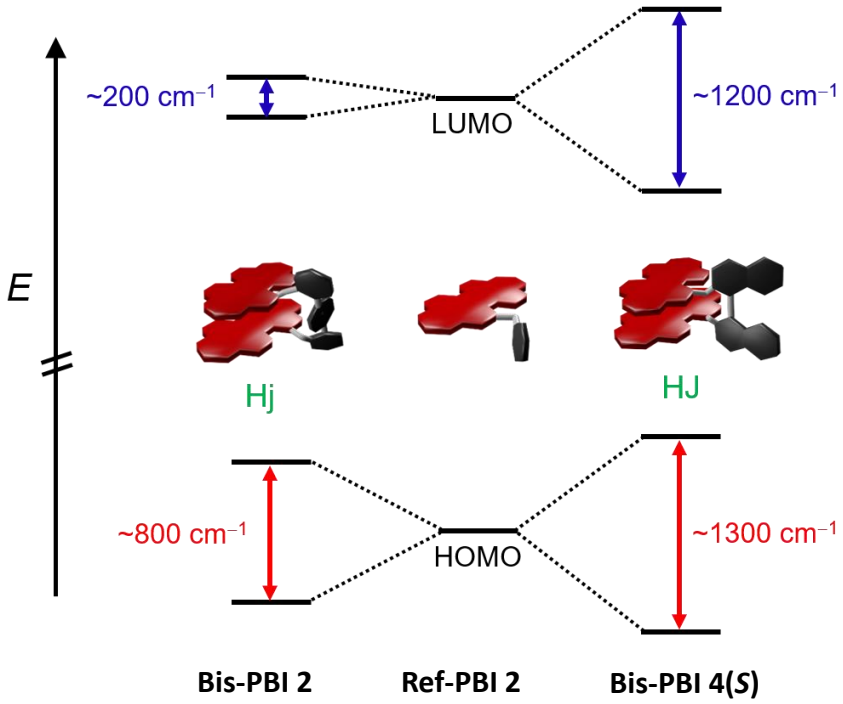

Figure 38. Schematic energy diagram of the relative positions of the frontier molecular orbitals of **Bis-PBI 2**, **Ref-PBI 2** and **Bis-PBI 4(*S*)** along with a schematic representation of their folded structure in solution. The orbital energies were obtained from single point calculations (PW91/TZP) on the geometry-optimized structures.

As evident from the calculated exciton coupling energies (Table 5), the long-range Coulomb coupling shows only minor changes within the series of **Bis-PBIs 2-4(*S*)**. The interaction of the transition charges is less sensitive towards structural rearrangements than the charge-transfer mediated short-range coupling, which depends on the HOMO–HOMO and LUMO–LUMO overlap of the chromophores.[54] Since the HOMO and LUMO distribution of **Ref-PBI 2** exhibits a significant number of nodal planes (Figure 47) the orbital overlap of the chromophores is hypersensitive to the geometry of the π-stack.[65, 183] Therefore, subtle changes of the chromophores' arrangements may lead to unexpected optical properties of dye stacks as demonstrated for **Bis-PBIs 2-4(*S*)**. In addition, the orbital overlap decreases exponentially with increasing distance, whereas the Coulomb coupling between the transition charges only shows

a reciprocal dependence (equation 3). Hence, the smaller π–π-distance in **Bis-PBIs 3** and **4(*S*)** leads to a further increase of the charger-transfer mediated short-range coupling. Moreover, the lack of observable splitting in the absorption spectra which could be expected for rotational displacement of the two chromophores, can be attributed to the much weaker oscillator strength for the lower Davydov component.[59]

According to the nomenclature proposed by Spano *et al.*,[54] the π-stack of **Bis-PBI 2** can be classified as an Hj aggregate, while **Bis-PBIs 3** and **4(*S*)** represent HJ aggregates. Here, the first letter stands for the long-range Coulomb coupling and the second letter for the short-range coupling, respectively, and a small/capital letter describes weak/strong coupling. Remarkably, theoretical investigations performed by the same group predicted the existence of so-called "null-aggregates", in which the interference between short- and long-range coupling leads to a complete vanishing of the overall coupling.[11] These types of aggregates are supposed to show a vibronic signature similar to the one observed for the monomer species but with a small bathochromic shift. As this is indeed the case for **Bis-PBI 4(*S*)** (Figure 31d), this hypothesis for PBI dyes could be proven and the first experimental proof for the existence of PBI-based "null-aggregates" could be provided within this work. Interestingly, the exciton mobility within "null-aggregates" is expected to be supressed as theoretically investigated for 7,8,15,16-tetraaza-terrylene crystals.[184] Hence, the interplay of long- and short-range coupling can have significant influence on the (photo-)physical properties of dye aggregates being of high importance for applications. Further, the fact that monomer-like UV/Vis absorption spectra can be observed also for closely stacked dyes with large transition dipole moments, as given for PBIs, should raise our awareness that there are cases in which UV/Vis spectroscopy does not allow to distinguish between stacked (folded) and non-stacked structures.

5.3 Conclusion

In conclusion, four new well-defined Bis-PBI folda-dimers were synthesized, in which two chromophores are covalently linked in the bay position by different spacer moieties. All of these molecules undergo folding in solution resulting in discrete π-stacks of two PBI chromophores as elucidated by in-depth UV/Vis, CD, fluorescence and NMR spectroscopic studies. The geometry-optimized structures obtained from DFT calculations reveal slightly different chromophore arrangements in the folded state. However, the dye stacks exhibit distinctly different absorption properties that can be rationalized by an interplay of long- and short-range exciton coupling resulting in optical signatures ranging from conventional H-type to monomer like absorption features, which presents the first experimental proof of a PBI-based "null-aggregate", in which long- and short-range exciton coupling fully compensate each other. Theoretical investigation reveal that the charge-transfer mediated coupling arises from HOMO–HOMO and LUMO–LUMO overlap of the chromophores, which is very sensitive to the structural arrangement of the dyes. Hence, small changes of the geometry can have considerable influence on the optical properties of the π-stack as demonstrated in this work. These insights are of significant importance for the fundamental understanding of dye aggregates, the application of UV/Vis spectroscopy for the assignment of folded or self-assembled π-stacked species, as well as for the design of organic materials for applications in *e.g.* photovoltaics and photonics.

5.4 Appendix

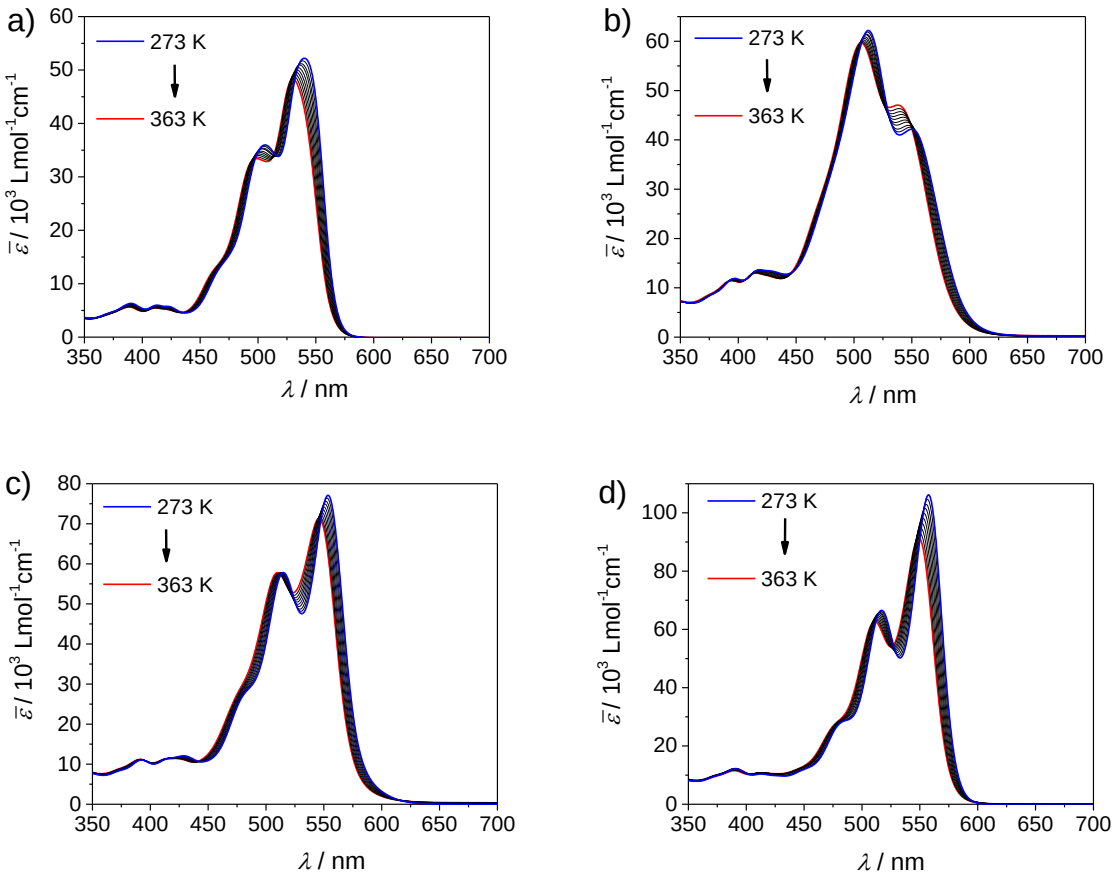

Figure 39. Temperature-dependent UV/Vis absorption spectra of a) **Ref-PBI 2**, b) **Bis-PBI 2**, c) **Bis-PBI 3** and d) **Bis-PBI 4(*S*)** (c_0 = 1 x 10^{-5} M) in TCE in steps of 10 K between 273 K (blue) and 363 K (red).

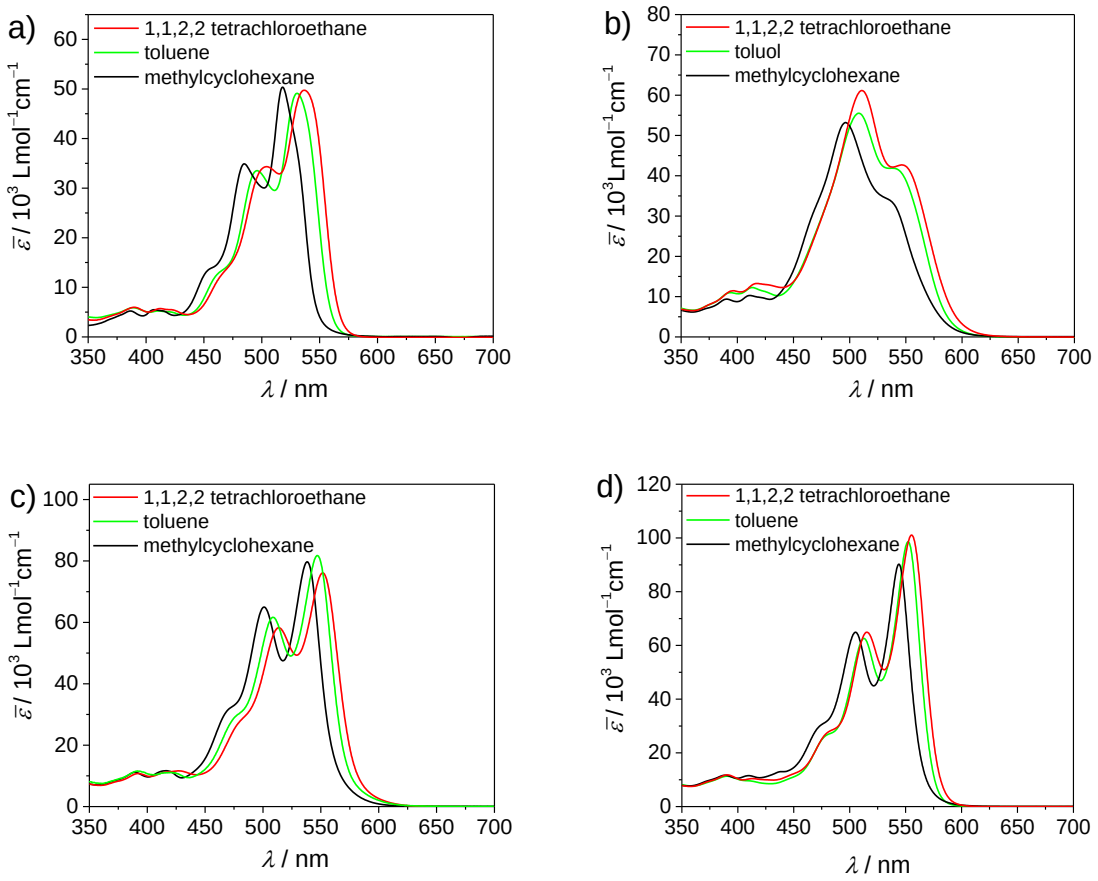

Figure 40. UV/Vis absorption spectra of a) **Ref-PBI 2**, b) **Bis-PBI 2**, c) **Bis-PBI 3** and d) **Bis-PBI 4(*S*)** (c_0 = 2 x 10^{-5} M) in TCE (red), toluene (green) and methylcyclohexane (black) at 298 K.

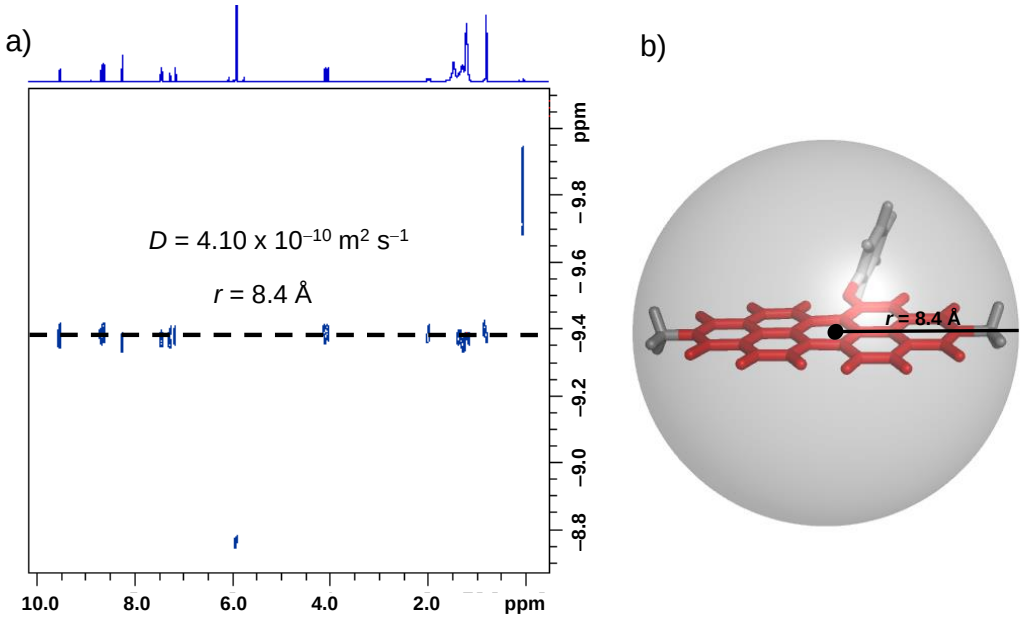

Figure 41. Left: 2D plot of DOSY NMR (600 MHz, TCE-d_2) spectra of **Ref-PBI 2** (c_0 = 2.0 x 10^{-3} M, 348 K) Right: Illustration of the energy-minimized structure of **Ref-PBI 2** obtained from DFT calculations (B97D3/def2-SVP) with the hydrodynamic radius as received from the Stokes-Einstein equation.

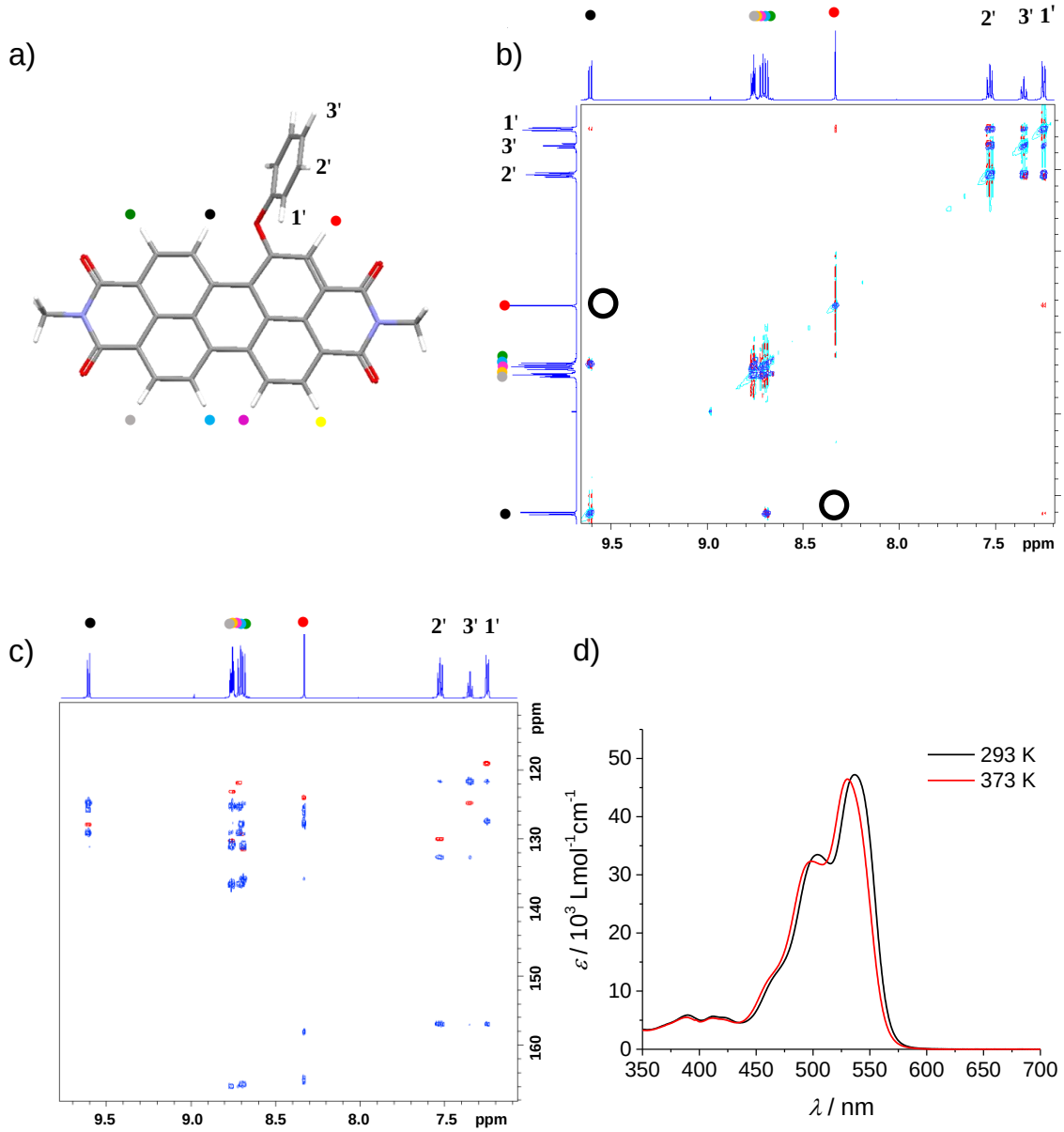

Figure 42. a) Top view on geometry-optimized structure of **Ref-PBI 2** obtained by DFT (B97D3/def2-SVP) calculations. b) Superposition of COSY (blue) and ROESY (red: positive signal/cyan: negative signal) spectra and c) HSQC (red) and HMBC (blue) spectra of **Ref-PBI 2** at 348 K in TCE-d_2 (c_0 = 2 x 10^{-3} M, 600 MHz). d) UV/Vis spectra of respective NMR sample of **Ref-PBI 2** at 293 K (black) and 373 K (red) (c_0 = 2 x 10^{-3} M).

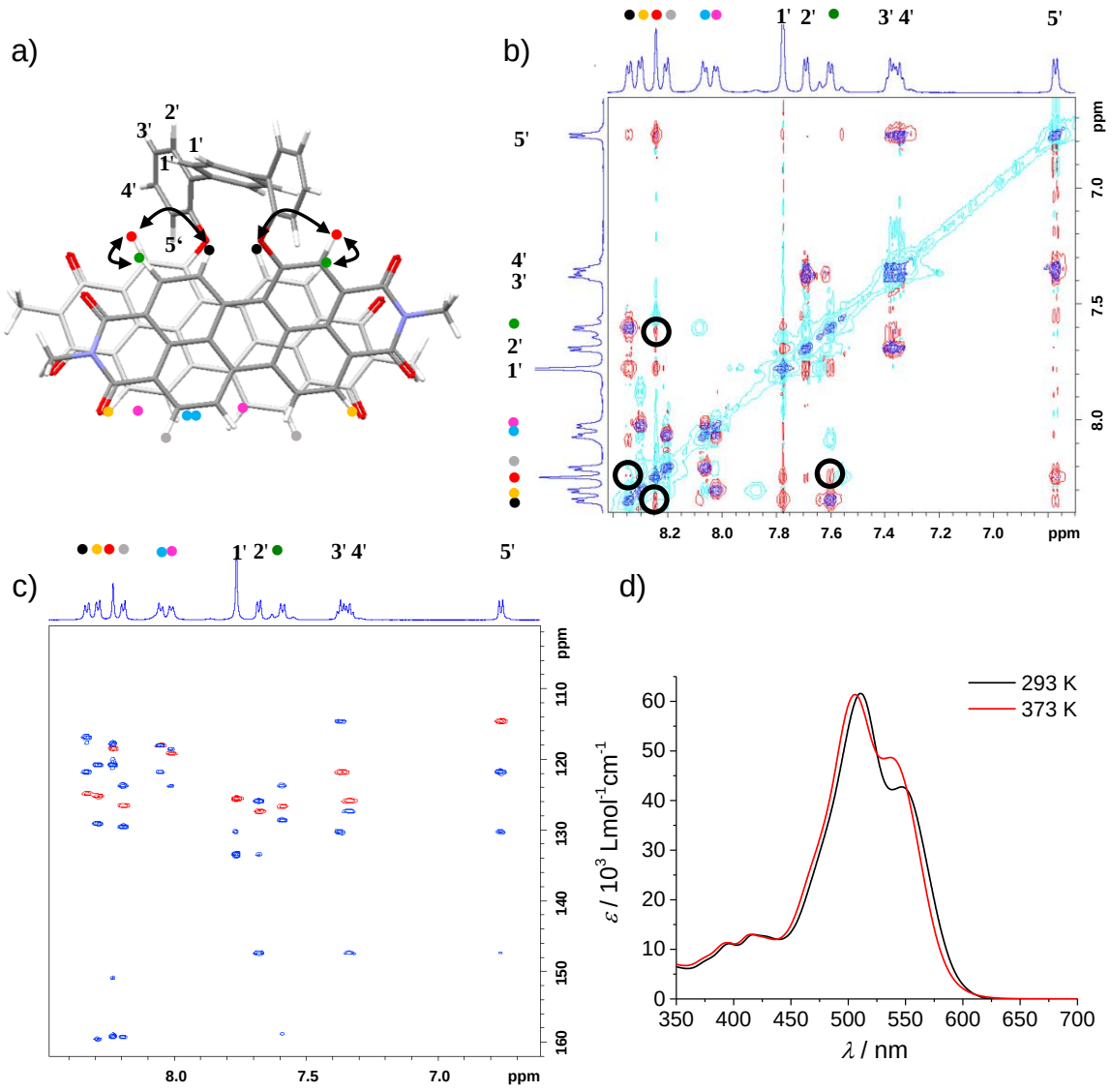

Figure 43. a) Top view on geometry-optimized structure of **Bis-PBI 2** obtained by DFT (B97D3/def2-SVP) calculations. b) Superposition of COSY (blue) and ROESY (red: positive signal/cyan: negative signal) spectra and c) HSQC (red) and HMBC (blue) spectra of **Bis-PBI 2** at 273 K in TCE-d_2 (c_0 = 3.5 x 10^{-3} M, 600 MHz). d) UV/Vis spectra of respective NMR sample of **Bis-PBI 2** at 293 K (black) and 373 K (red) (c_0 = 3.5 x 10^{-3} M).

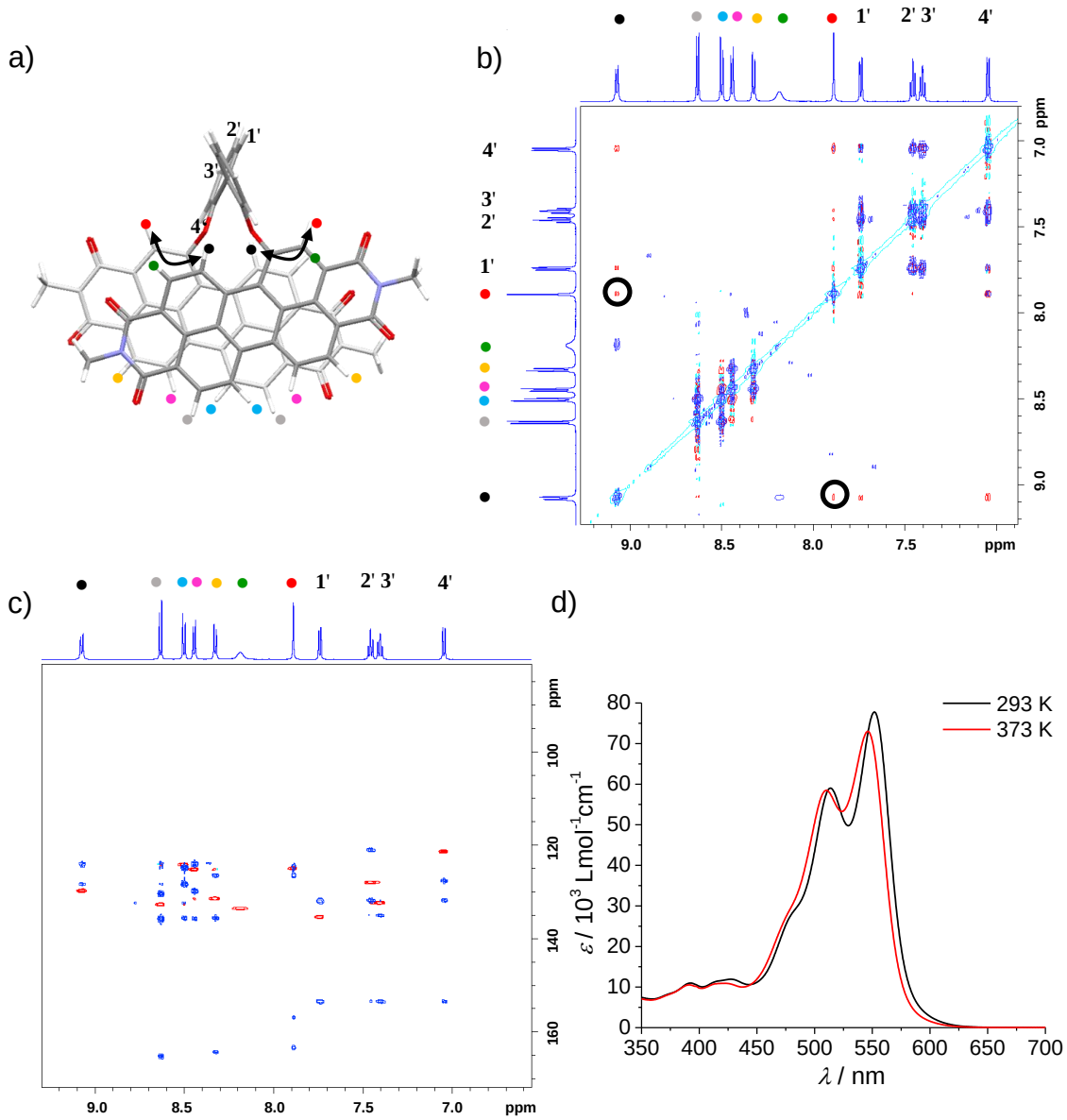

Figure 44. a) Top view on geometry-optimized structure of **Bis-PBI 3** obtained by DFT (B97D3/def2-SVP) calculations. b) Superposition of COSY (blue) and ROESY (red: positive signal/cyan: negative signal) spectra and c) HSQC (red) and HMBC (blue) spectra of **Bis-PBI 3** at 348 K in TCE-d_2 (c_0 = 2 x 10^{-3} M, 600 MHz). d) UV/Vis spectra of respective NMR sample of **Bis-PBI 3** at 293 K (black) and 373 K (red) (c_0 = 2 x 10^{-3} M).

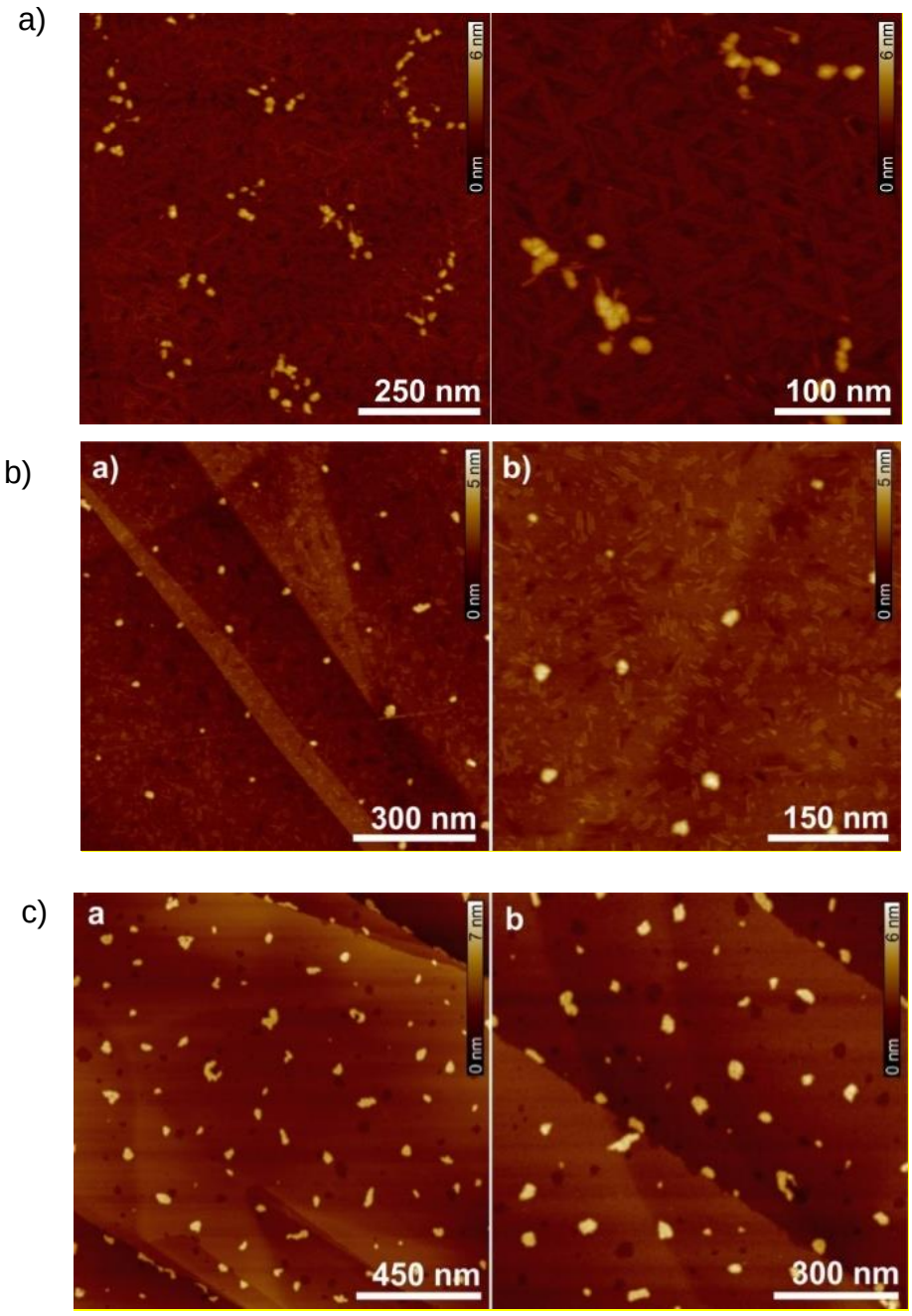

Figure 45. AFM images of thin-films prepared by spin-coating from a solution in MCH on HOPG (c = 2 x 10^{-5} M^{-1}, 4000 rpm) of the dyes a) **Bis-PBI 2**, b) **Bis-PBI 3** and c) **Bis-PBI 4(*S*)**.

Determination of the Transition Dipole Moment of Ref-PBI 2.

The transition dipole moment of **Ref-PBI 2** was determined from the UV/Vis absorption spectrum measured in TCE at 298 K. It was calculated from the integral of the reduced absorption band as[185]

$$\left|\mu_{eg}\right|^2 = \frac{3hc\varepsilon_0 \ln 10}{2\pi^2 N_A} \cdot \int_{\tilde{\nu}_1}^{\tilde{\nu}_2} \frac{\varepsilon(\tilde{\nu})}{\tilde{\nu}}\, d\tilde{\nu}\,. \qquad (6)$$

Here, $\varepsilon(\tilde{\nu})$ is the molar extinction coefficient, c the speed of light, h the Planck constant, ε_0 the vacuum permittivity and N_A represents the Avogadro constant. In this way, a value of μ_{eg} = 7.73 D was obtained.

Calculation of the Exciton Coupling Energies from UV/Vis Absorption Spectra

Neglecting rotational displacement of the transition dipole moments of two chromophores, the ratio of the intensities of the 0–0 and 0–1 absorption band of a dimer aggregate exhibiting exciton-vibrational coupling in the perturbative limit can be calculated by[11, 59]

$$\frac{I_A^{(0-0)}}{I_A^{(0-1)}} = \frac{1}{\lambda^2}\left[\frac{1 - G(0,\lambda^2)\, e^{-\lambda^2} J/\omega_0}{1 - G(1,\lambda^2)\, e^{-\lambda^2} J/\omega_0}\right]^2, \quad \omega_0,\, J \ll \left|E_{CT} - E_{S_1}\right| \qquad (7)$$

where λ^2 is the Huang-Rhys factor, J represents the exciton coupling energy and ω_0 stands for the vibrational frequency. Equation 7 is a good approximation for small rotational displacements (< 45°), since mainly one Davydov component is optically allowed for small rotations,[59] as it is the case for **Bis-PBIs 2–4(*S*)**. The vibrational function $G(v_t; \lambda^2)$ is defined as

$$G(v_t; \lambda^2) = \sum_{\substack{u=0,\,1,\ldots \\ (u \neq v_t)}} \frac{\lambda^{2u}}{u!\,(u - v_t)}\,. \quad v_t = 0,\, 1,\, 2,\, \ldots \qquad (8)$$

The Huang-Rhys factor can be determined from the UV/Vis absorption spectrum of the monomeric dye, *i.e.* **Ref-PBI 2**. For this, the absorption spectrum was fitted by Gaussian functions assuming a one effective mode model (Figure 46). For this, the absorption spectrum in the range of 16900–22600 cm^{-1} was taken into account, since the absorption at higher frequencies arises from transition to higher excited states.[186] The best fit was obtained for a full width at half maximum of the Gaussian functions of 1296 cm^{-1}. The Huang-Rhys factor was then calculated from the height of the 0–1 and 0–0 Gaussian peaks:[59]

$$\lambda^2 = \frac{I^{0-1}_{\text{Gaussian}}}{I^{0-0}_{\text{Gaussian}}}. \qquad (9)$$

With this, $\lambda^2 = 0.65$ was obtained, which is in good agreement with previously reported values for PBI dyes.[59] The frequency ω_0 was set to 1446 cm^{-1} and equals the energy difference between the maxima of the Gaussian functions of the 0–0 and 0–1 absorption bands used for the fitting of the absorption spectrum. This value fits well the C–C stretching mode of the perylene core of ~1400 cm^{-1}.[59] Finally, the exciton coupling energies were determined based on equation 7 giving the results shown in Table 5 in the main text.

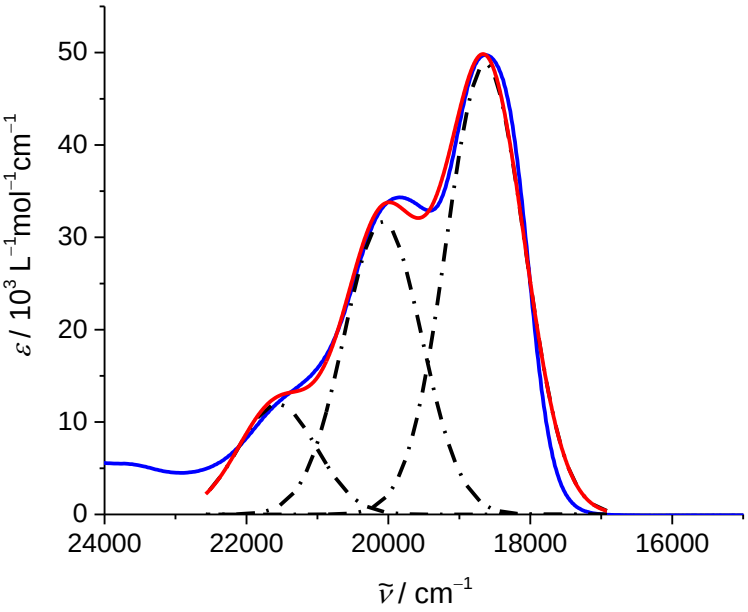

Figure 46. UV/Vis absorption spectrum of **Ref-PBI 2** (blue line) in TCE at 298 K (c_0 = 2 x 10^{-5} M). Also shown is the fit of the absorption spectrum (red line) as the sum of the three Gaussian functions (black dash-dotted lines).

Quantum Chemical Calculations

Geometry optimizations were performed for **Ref-PBI 2** and **Bis-PBIs 2-4(*S*)** at the density functional theory (DFT) level using the Gaussian 09 program package[187] with the def2-SVP basis set[168] and B97D3[169] as functional. For the Bis-PBI dyes only the *S*–enantiomer regarding the axial chirality of the spacer moieties was calculated. The structures were geometry-optimized followed by frequency calculations to prove the existence of true minima. Small imaginary frequencies (< 21i cm^{-1}) were obtained, which can be regarded as artefacts of the calculations.[188]

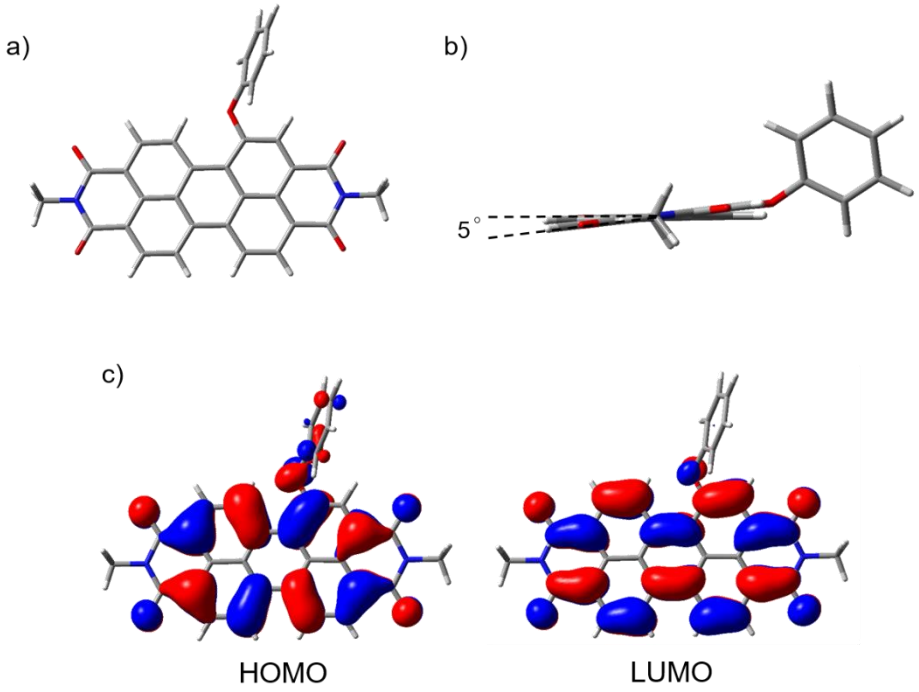

Figure 47. a) Top and b) side view on the geometry-optimized structure of **Ref-PBI 2** (B97D3/def2-SVP). c) HOMO and LUMO distribution (isovalue = 0.02 a.u.) of **Ref-PBI 2** at the same level of theory.

In order to determine the Coulomb exciton coupling energy, time-dependent DFT (TDDFT) calculations were performed for **Ref-PBI 2** on the geometry-optimized structure obtained from DFT calculations. For this, the def2-SVP basis set[168] was employed in combination with the long-range corrected ωB97 functional.[174] The transition density was then fitted to atomic partial charges by Mulliken population analysis using the Multiwfn software package.[189] The TDDFT calculations overestimate the transition dipole moment for **Ref-PBI 2** by a factor of 1.16 in comparison to the experimental value obtained from the integral of the reduced absorption band. Therefore, the transition charges were scaled by a factor of 0.86.[190]

The exciton coupling energy was then calculated as[171]

$$J = \frac{1}{4\pi\varepsilon_0} \sum_i \sum_j \frac{q_i^{(1)} \cdot q_j^{(2)}}{|\mathbf{r}_i^{(1)} - \mathbf{r}_j^{(2)}|} \,. \tag{10}$$

Here, $q_i^{(a)}$ represents the transition charge on atom *i* of chromophore *a*, $\mathbf{r}_i^{(a)}$ corresponds to the position vector of the respective transition charge and ε_0 is the vacuum permittivity. For this, the geometry-optimized structures of **Bis-PBIs 2-4(*S*)** obtained from DFT calculations were used.

The transfer integrals were calculated within the unique fragment approach[175] as implemented in the Amsterdam Density Functional package[176-178] employing the TZP basis set[179] and the PW91 functional.[180] The structures of **Bis-PBIs 2-4(*S*)** obtained from geometry optimizations were used. In doing so, the spacer moieties were removed and the oxygen bay substituents were replaced by methoxy groups.

The output of the calculations provided the overlap integrals S_e (S_h) of the LUMO (HOMO) as well as the electron (hole) site energies $E_{e,1}$ ($E_{h,1}$) and $E_{e,2}$ ($E_{h,2}$) of the corresponding fragment 1 and 2. With this, the effective electron and hole transfer integral t_e and t_h can be calculated by[191]

$$t_e = \frac{t_e' - \frac{1}{2}(E_{e,1} + E_{e,2})S_e}{1 - S_e^2} \,, \tag{11}$$

$$t_h = \frac{t_h' - \frac{1}{2}(E_{h,1} + E_{h,2})S_h}{1 - S_h^2} \,. \tag{12}$$

Here, t_e' and t_h' represent the electron and hole transfer integrals in the nonorthogonal basis as directly provided from the calculations, respectively.

The eigenvalues of the orbitals displayed in Figure 38 in the main text were obtained from the calculations of the transfer integrals.

Chapter 6

–

Spacer-Controlled Self-Assembly of Bay-linked Bis-PBI Dyes[3]

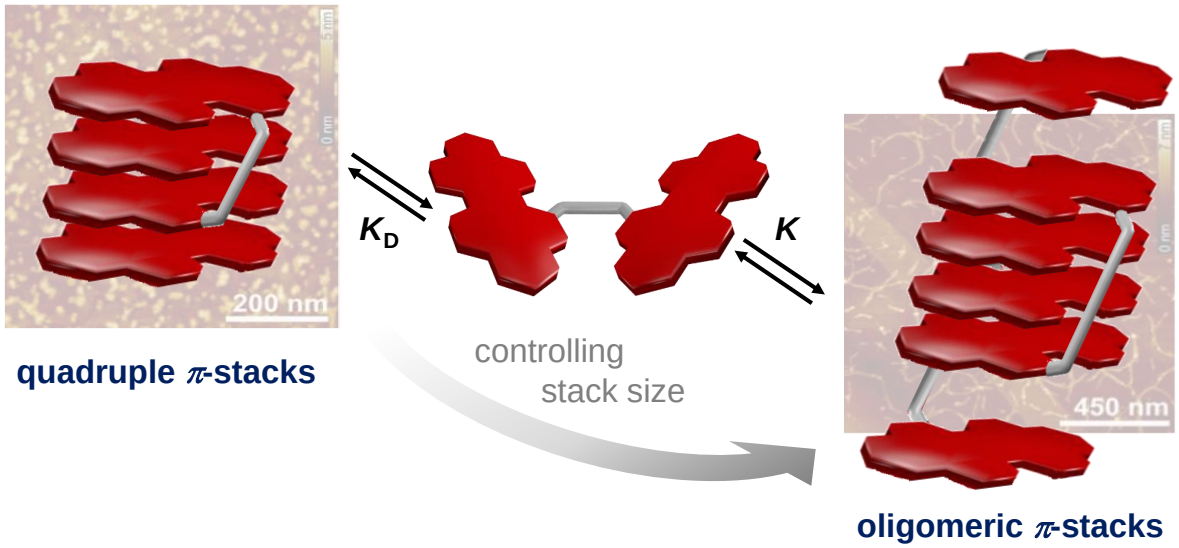

ABSTRACT: By tethering two PBI dyes in the bay-position with spacer units of various length and steric demand different architectures from highly defined quadruple PBI π-stacks to larger oligomers could be obtained upon self-assembly in toluene and methylcyclohexane. The self-assembly process could be analyzed by UV/Vis spectroscopy and the supramolecular structures were deduced by DOSY NMR and AFM measurements as well as DFT calculations.

[3] DFT calculations were performed by Dr. David Bialas. AFM measurements were performed by Dr. Vladimir Stepanenko.

6.1 Introduction

Extended dye stacks with an undefined number of interacting chromophores are not suitable for analysing structure-property relationships. Towards this goal well defined model systems need to be created where the exact size and structure of the dye assemblies are known. Using such systems fundamental insights can be gained concerning dye-dye interactions in the ground and exited states which are needed for the development of functional materials. Accordingly, changes of the optical properties upon aggregation can be correlated to the structural arrangements of the respective dyes giving insights into exciton and charge carrier properties, which are relevant for organic electronic[17] or photovoltaics.[18-20] Both, exciton and charge carrier mobility drastically decrease by an increasing structural and energetic disorder as present in undefined dye assemblies. Therefore, the investigation of exciton coupling has become a central point of current research in order to gain insights into functional properties and structural information of dye aggregates consisting of a discrete number of chromophores ($n < 10$).[21-24]
As PBI dyes evolved as one of the most utilized chromophores for such studies due to their outstanding photophysical properties and their high aggregation tendency, the great challenge of the present work was to limit their usual growth into long fibres to finite-sized PBI π-stacks. In *Chapter 5* it could be demonstrated, that defined π-stacks of only two PBI chromophores are accessible by intramolecular folding of several Bis-PBI dyes (**Bis-PBI 2-4**) using *ortho*-phenylene linker moieties that differ in both their length (3 - 6 Å) and their steric demand. The question that arises from this previous work is, whether it is possible to generate larger but still well-defined PBI π-stacks by further extending the respective backbone length. For this, *ortho*-phenylene and *meta*-phenylene linker units with a length ranging between 8 - 15 Å (Figure 48) were used as well as an alkoxyphenylene spacer (7 Å, Figure 48) which exhibits slightly higher flexibility due to the additional CH_2-group between the oxygen atom and the phenyl group as it is the case for **Bis-PBI 1**, which was already proven to form highly defined PBI quadruple π-stacks upon self-assembly (*Chapter 4*).[113]
Thus, in this Chapter, four covalently linked Bis-PBI dyes **Bis-PBIs 5-8** (Figure 48) will be introduced and analysed concerning their aggregation behaviour dependent on the geometry and size of the respective spacer units. For this, **Ref-PBI 1** (*Chapter 4*) and **Ref-PBI 2** (*Chapter 5*) are used to compare the optical properties of **Bis-PBIs 5-8** in solution both, in the monomeric and aggregated state. Hereby, **Ref-PBI 1** refers to the alkoxy-substituted **Bis-PBI 5**, whereas **Ref-PBI 2** refers to the oligo-phenylene substituted **Bis-PBIs 6-8** as different substitution motives, consequently, enforce different optical features for **Bis-PBIs 5-8** upon aggregation.

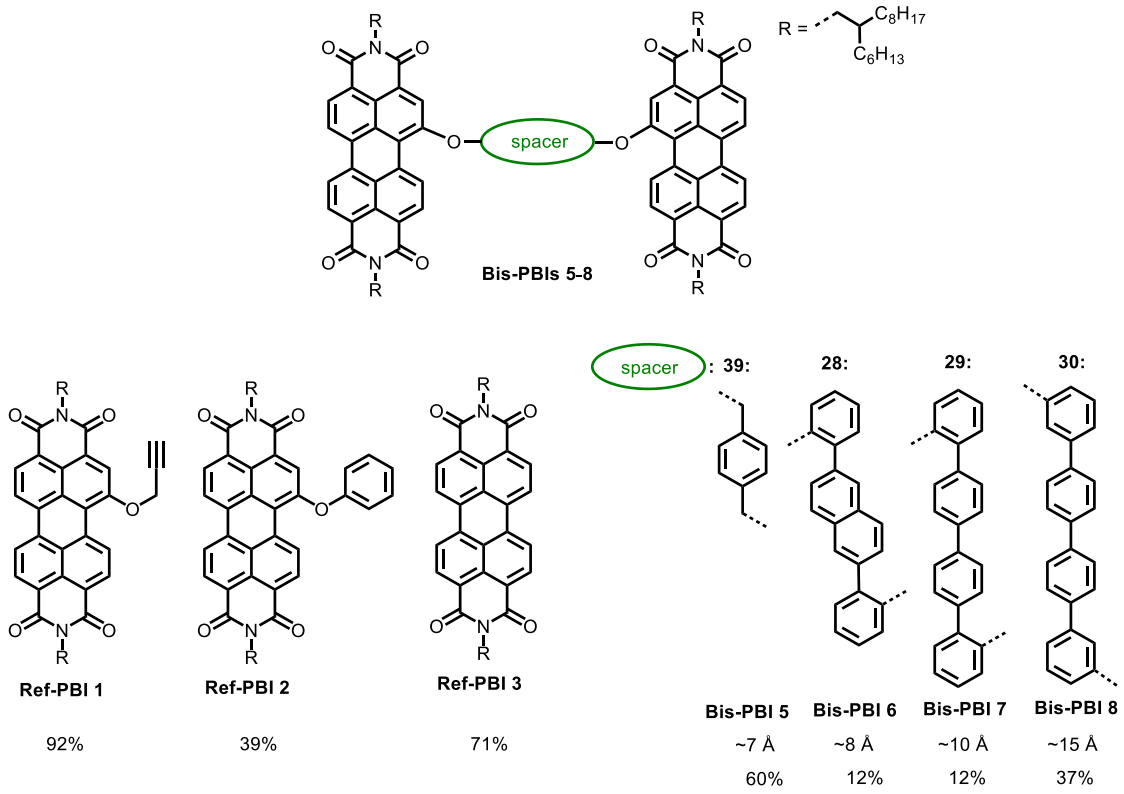

Figure 48. Chemical structures of **Bis-PBIs 5-8** and corresponding reference compounds **Ref-PBIs 1-3**.

6.2 Results and Discussion

6.2.1 UV/Vis Spectroscopy

First insights into the self-assembly behaviour of **Bis-PBIs 5-8** (for synthetic details see *Chapter 3*) were obtained from concentration-dependent UV/Vis studies. To find suitable conditions for these studies, first, absorption spectra of **Bis-PBIs 5-8** and **Ref-PBIs 1-2** were recorded in solvents of different polarity ($c_0 = 10^{-5}$ M) at room temperature (see the Appendix, Figure 59), ranging from nonpolar methylcyclohexane to more polar solvents like chloroform. Subsequently, concentration-dependent UV/Vis studies were performed in pure methylcyclohexane, where the aggregation tendency of all target compounds is most pronounced. Unfortunately, under these conditions the systems suffered from low solubility, especially at high concentrations ($c_0 > 10^{-4}$ M). In contrast, using pure toluene, the whole transition from monomeric to almost fully aggregated species could be analysed in the accessible concentration range of UV/Vis experiments ($c_0 = 10^{-4}$ - 10^{-7} M) at room temperature. The corresponding concentration-dependent spectra of **PBIs 5-8** in toluene are shown in Figure 49 where significant spectral changes are induced by continuous concentration variations.

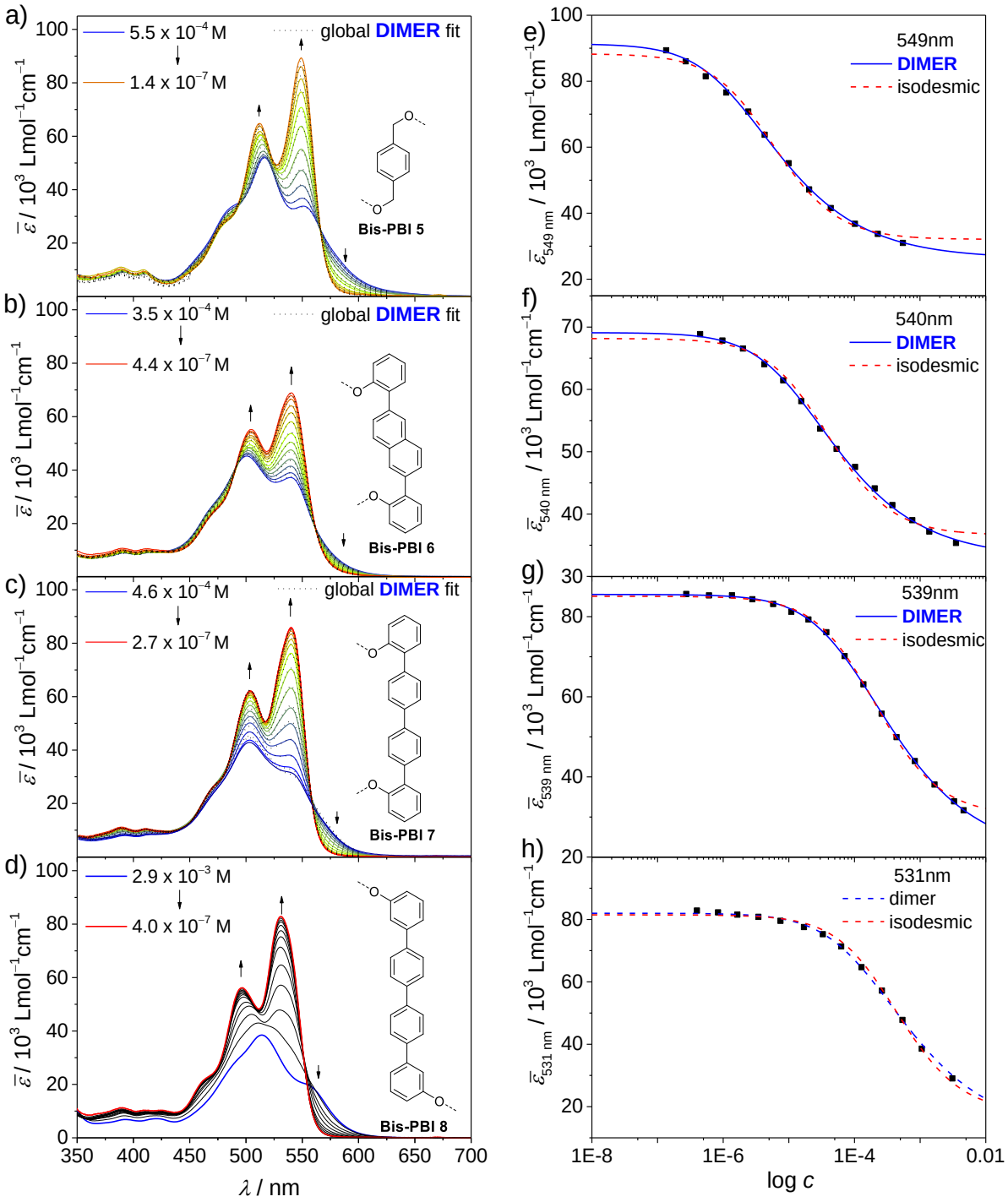

Figure 49. Left: Concentration-dependent absorption spectra of a) **Bis-PBI 5**, b) **Bis-PBI 6**, c) **Bis-PBI 7** and d) **Bis-PBI 8** in toluene at room temperature (c_0 = 10^{-4} - 10^{-7} M^{-1}). Calculated spectra for **Bis-PBIs 5-7** obtained by applying the global fit analysis for the dimer model (black dashed lines) are shown as well. Arrows indicate the changes in intensity of the monomer band (red line) and the aggregate band (blue line) with decreasing concentration. Right: Plot of the extinction coefficient (ε) at $\lambda_{max,M}$ against the total concentration of e) **Bis-PBI 5**, f) **Bis-PBI 6**, g) **Bis-PBI 7** and h) **Bis-PBI 8**. For all Bis-PBI dyes the corresponding data were fitted with the dimer (blue) and isodesmic (red) model at $\lambda_{max,M}$.

At low concentrations (c_0 = 10^{-7} M), **Bis-PBIs 5-8** display monomer-like signatures with two absorption bands with λ_{max} ranging between 531 - 549 nm along with a small shoulder around 470 nm and extinction coefficients ε_{max} up to 89400 L mol^{-1} cm^{-1} (Figure 49). The second main band of the absorption spectra at roughly 400 nm can be assigned to the S_0–S_2 transition.[186] These observations are highly comparable to the optical signatures that can be observed for the respective reference dyes **Ref-PBIs 1** and **2** (Figure 50) which also reveal a similar vibronic pattern with an absorption maximum at λ_{max} = 545 and 530 nm and with extinction coefficients ε_{max} = 56400 and 51900 L mol^{-1} cm^{-1}, respectively.

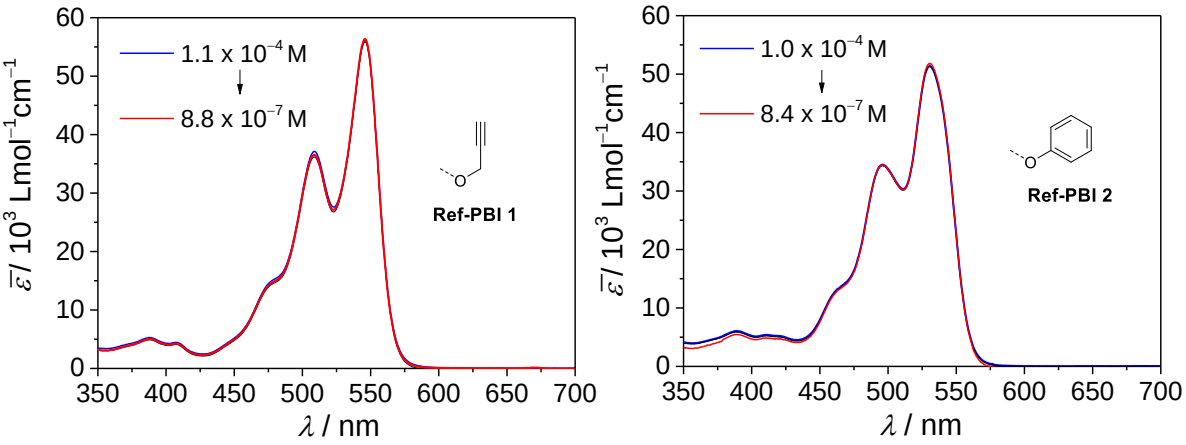

Figure 50. Concentration-dependent UV/Vis absorption spectra of **Ref-PBIs 1** and **2** in toluene at room temperature (c_0 = 1 x 10^{-4} M^{-1} - 8 x 10^{-7} M^{-1}).

This clearly indicates, that at very low concentrations ($c_0 \approx 10^{-7}$ M) **Bis-PBIs 5-8** are present in a non-aggregated state in toluene at room temperature.

By increasing concentration ($c_0 > 10^{-4}$ M) all target compounds show a blue-shifted λ_{max} ranging between 501 - 517 nm with decreased ε_{max} below 52000 L mol^{-1} cm^{-1} and a reversal of the intensities of the 0–0 and 0–1 absorption bands with drastically decreased A_{0-0}/A_{0-1} ratios between 0.50 - 0.82. This is characteristic for a co-facial π-stacking of PBI dyes[40-41] and arises from the interplay of exciton and vibrational couplings[52, 54] clearly indicating the formation of H-type aggregates. For monomeric reference dyes **Ref-PBIs 1** and **2** (Figure 50), no prominent changes could be observed upon dilution. Moreover, the A_{0-0}/A_{0-1} ratios remain close to 1.54 (**Ref-PBI 1**) and 1.49 (**Ref-PBI 2**) during the whole concentration-dependent measurements (c_0 = 1 x 10^{-4} M^{-1} - 8 x 10^{-7} M^{-1}). All corresponding spectroscopic data are summarized in Table 6.

Table 6. UV/Vis spectroscopic data of **Ref-PBI 1**, **Bis-PBI 5**, **Ref-PBI 2**, **Bis-PBI 6**, **Bis-PBI 7** and **Bis-PBI 8**, measured in toluene at room temperature after global fit analysis of the concentration-dependent data to yield the monomeric (M) and dimeric (D) or aggregated (A) state.

	state	ε_{max}/Lmol^{-1}cm^{-1}(λ_{max}/nm)	(λ_{iso}/nm)	d/Å	A_{0-0}/A_{0-1}	K / M^{-1}
Ref-PBI 1		56.400 (545), 36.700 (508)			1.54	
Bis-PBI 5	M	89.400 (549), 64.800 (512)	566	7	1.38	1.4 x 10^5
	D	34.000 (552), 51.900 (517)			0.66	
Ref-PBI 2		51.900 (530), 34.700 (495)			1.49	
Bis-PBI 6	M	69.300 (540), 55.600 (504)	562	8	1.25	2.0 x 10^4
	D	37.200 (541), 45.500 (501)			0.82	
Bis-PBI 7	M	86.300 (539), 62.500 (503)	559	10	1.38	2.9 x 10^3
	D	31.200 (542), 42.800 (502)			0.73	
Bis-PBI 8	M	83.200 (531), 56.300 (496)	-	15	1.48	(1.3 x 10^3)[a]
	A	19.500 (558), 38.700 (514)			0.50	

[a] obtained from isodesmic fit at 531 nm.

The spectral changes of **Bis-PBIs 5-8** upon aggregation can be explained by the long-range Coulomb coupling J_{Coul} between closely π-stacked PBI chromophores, if the strong vibronic coupling given for the transitions from the electronic ground state (S_0) to the first excited state (S_1) is taken into account.[40, 192] In *Chapter 5*, it could be demonstrated that additionally to this long-range coupling J_{Coul} also the charge-transfer mediated coupling J_{CT} has to be taken into account to understand the absorption spectra of **Bis-PBIs 3** and **4(*S*)** folda-dimers. In contrast, the absorption spectrum of folda-dimer **Bis-PBI 2** displaying similar spectral features as the herein investigated aggregates of **Bis-PBIs 5-8**, can be rationalized by exciton-vibrational coupling between the interacting PBI chromophores, assuming that the exciton coupling can be mainly described by Coulomb interactions J_{Coul} between the transition charges. Thus, according to the nomenclature introduced by Spano *et al.* (*vide supra*) the dye assemblies of **Bis-PBIs 5-8** can be classified as common Hj-aggregates, as it was the case for **Bis-PBI 2**, without displaying significant contributions of the so-called short-range exciton coupling J_{CT}.

Well-defined isosbestic points (Table 6) observed during the concentration-dependent UV/Vis studies for **Bis-PBIs 5-7** in toluene indicate the presence of a thermodynamic equilibrium between only two discrete species that can be clearly attributed to the respective monomers and aggregates. This allows a thermodynamic analysis[33, 74] of the respective self-assembly processes. For **Bis-PBIs 5-7** the concentration-dependent UV data could be properly fitted by using the monomer-dimer model, also in a global fit approach providing dimerization constants K_D in the range of 10^3 - 10^5 M^{-1} (Figure 49). Hereby, a clear relationship between the binding strength and the length of the corresponding linker units could be established, which will be explained later in more detail (*vide infra*). In the case of **Bis-PBI 8** bearing the longest (15 Å) and most flexible linker unit of all target compounds, no clear isosbestic points could be observed during the concentration-dependent measurements in toluene. Moreover, under the applied conditions it was not possible to reach the fully aggregated state of **Bis-PBI 8** within the accessible concentration range of UV experiments (Figure 49d and h) due to an obviously less favourable geometry for the formation of a PBI π-stack.

Therefore, a methylcyclohexane / toluene mixture (1:1) was used to analyse the aggregation behaviour of **Bis-PBI 8** at 313 K (Figure 51a). Indeed, under these conditions the data could be properly fitted with the isodesmic model at 526 nm (Figure 51b) providing an aggregation constant of K_{313K} = 1.2 x 10^4 M^{-1}, whereas the monomer-dimer fit failed especially at high concentrations.

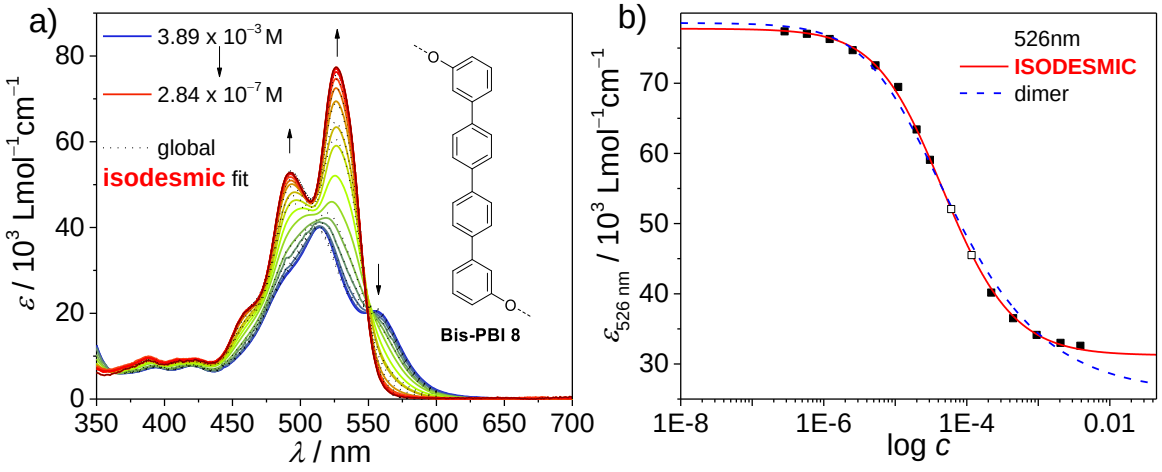

Figure 51. a) Concentration-dependent UV/Vis absorption spectra (colored lines) of **Bis-PBI 8** in methylcyclohexane/toluene 1:1 at 313 K. Also shown are the calculated spectra obtained by applying the global fit analysis of the isodesmic model (black dashed lines). Arrows indicate the transition from the aggregate (blue line) to the monomer (red line) with decreasing concentration. b) Plot of the extinction coefficient (ε) at 526 nm against the concentration *c*. Fitting of the data with the isodesmic model (red solid line) was satisfactory, whereas the dimer model (blue dashed line) fails.

This strongly indicates a self-assembly process of **Bis-PBI 8** into larger oligomeric π-stacks, which could be further substantiated by atomic force microscopy (AFM) measurements (Figure 52) where large, fibre-like structures could be observed with a length up to 500 nm by spin coating a solution of **Bis-PBI 8** in methylcyclohexane (c = 2 x 10^{-5} M) on HOPG (highly-ordered pyrolytic graphite, Figure 52a) or silicon wafers (SiO_x, Figure 52b). For the latter, a network-like film consisting of thin aggregates with a diameter of 2.2±0.1 nm could be observed on the hydrophobic silicon wafer surface. The aggregates exhibit a helical structure with a helical pitch between 5.5-6.0 nm (Figure 52b). Therefore, assuming the distance between two aggregated PBI chromophores to be approximately 0.35 nm (π-π distance), seven to eight **Bis-PBI 8** molecules are involved in one aggregate rotation. Based on these aggregate dimensions obtained from AFM experiments an "arm-in-arm" aggregation of **Bis-PBI 8** into oligomeric PBI π-stacks appears to be most reasonable (Figure 52c) as it was already considered for imide-linked PBI **14**[35] (*Chapter 2.3.1*, Figure 14), bearing a diacetylene-phenylene linker unit with a length of 10.9 Å. In contrast, for **Bis-PBIs 5-7** only small spherical nanoparticles with a diameter ~ 5 nm could be obtained by performing AFM studies (see the Appendix, Figure 60)

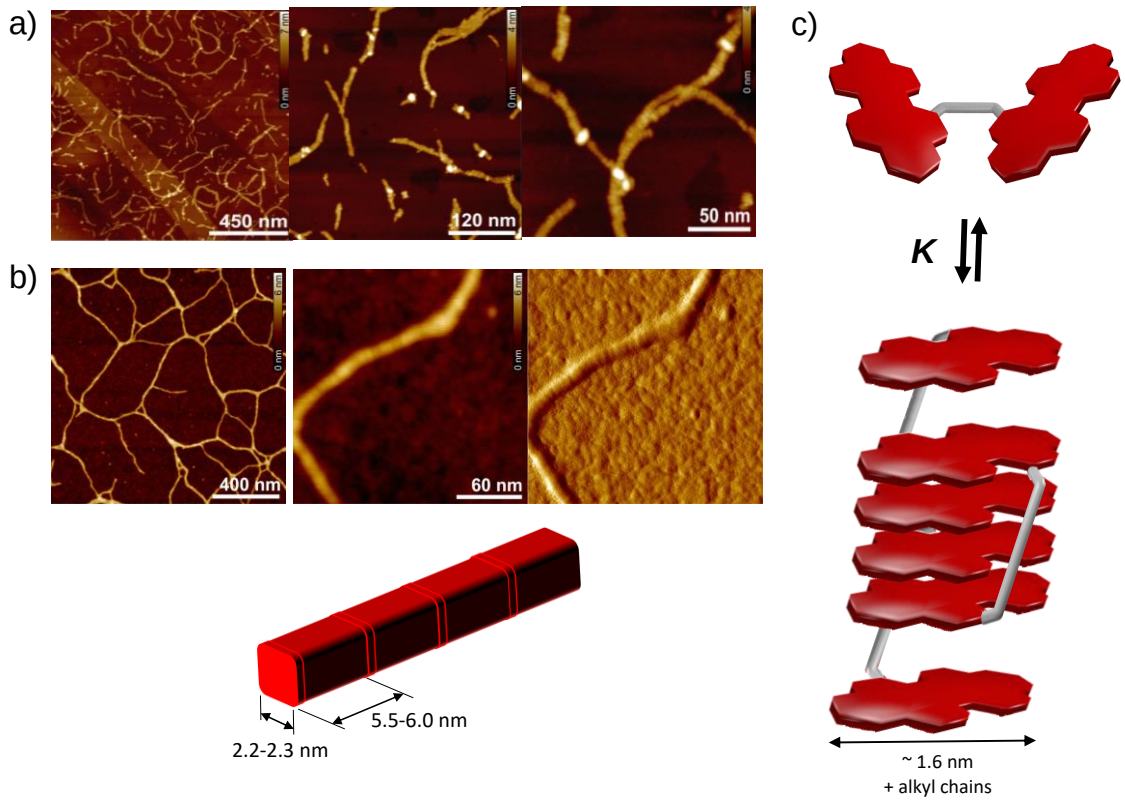

Figure 52. AFM images of **Bis-PBI 8** prepared by spin-coating a solution of **Bis-PBI 8** in methylcyclohexane (c = 2 x 10^{-5} M^{-1}, 2000 rpm) on a) HOPG and b) silicon wafer (SiO_x). Also shown is a schematic representation of the aggregate dimensions of **Bis-PBI 8** on the silicon wafer surface. c) Schematic illustration of the estimated self-assembly of **Bis-PBI 8** into extended oligomers.

For a better comparison of the binding strengths of **Bis-PBIs 5-8**, the degree of aggregation α_{agg} in toluene at room temperature was plotted against the total concentration c_0 (Figure 53) in comparison to **Bis-PBI 1** (*Chapter 4*), folda-dimer **Bis-PBI-2** (*Chapter 5*), **Ref-PBI 2** and unsubstituted **Ref-PBI 3** (Figure 48). Here one can nicely see, that the highest dimerization constant (K_D = 1.4 x 10^5 M^{-1}) in pure toluene at room temperature is provided by **Bis-PBI 5** which bears the shortest linker unit (7 Å) of all target compounds and which is structurally highly comparable to **Bis-PBI 1** (*Chapter 4*) displaying a likewise high dimerization constant (K_D = 1.5 x 10^5 M^{-1}) under the same conditions. In contrast, all *ortho*- and *meta*-phenylene substituted Bis-PBI dyes provide smaller binding constants in a range of 10^3 - 10^4 M^{-1}. Hereby, a clear relationship between the binding strength and the length of the corresponding linker unit could be established, as the smallest binding constant K = 1.3 x 10^3 M^{-1} (Figure 53) of all target compounds could be determined for **Bis-PBI 8** (15 Å), whereas the highest dimerization constant (K = 2.0 x 10^4 M^{-1}) of all oligo-phenyl-bridged Bis-PBI dyes was deduced for **Bis-PBI 6** (8 Å). In addition, **Bis-PBI 8** self-assembly does not stop at the dimer state, *i.e.* quadruple PBI π-stacks, but further grows into oligomeric π-stacks. Here the comparison with **Ref-PBI 2** and unsubstituted **Ref-PBI 3**, which also form larger oligomers *via* isodesmic self-assembly (Figure 53), reveals a significant increase in the thermodynamic driving force. Thus, the covalent linkage of the respective PBI units in **Bis-PBI 8** lead to increased binding constants for the isodesmic self-assembly compared to monochromophoric **Ref-PBIs 2** and **3**. Consequently, at a concentration of ~ 10^{-2} M **Bis-PBI 8** already forms extended aggregates whereas **Ref-PBIs 2** and **3** still mostly prevail as monomeric or dimeric species (Figure 53).

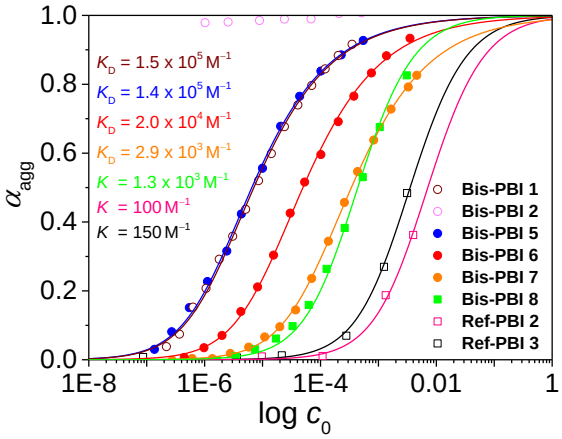

Figure 53. a) Plot of the degree of aggregation (α_{agg}) of **Bis-PBIs 5-8** at $\lambda_{max,M}$ against the concentration c_0 in toluene by fitting the data with the dimer (circles) or isodesmic (squares) model compared to **Bis-PBIs 1 - 2** and **Ref-PBIs 2 - 3**.

Respective ΔG^{o}_{298K} values for a thermodynamic analysis of the binding strengths of **Bis-PBIs 5-8** compared to **Bis-PBI 1** and reference compounds **Ref-PBIs 2** and **3** obtained from the Gibbs free energy isotherm equation ($\Delta G^{o} = -RT\ln K$) are shown in Figure 54 using the dimerization and aggregation constants K_D and K (Figure 53) of the herein investigated target compounds. This further demonstrates the relationship between the binding strength and the length of the corresponding linker units that were used to covalently link the PBI chromophores in the bay-position, respectively.

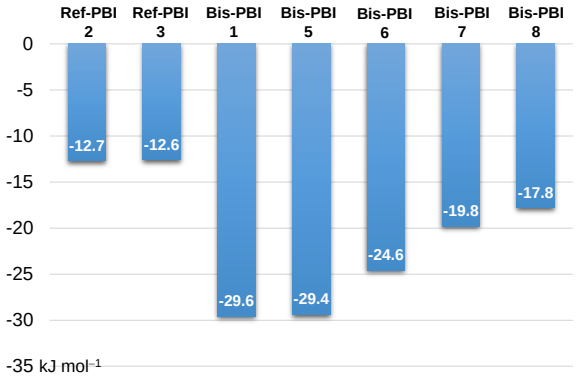

Figure 54. Comparison of the respective ΔG^{o}_{298K} values of **Ref-PBIs 2** and **3**, **Bis-PBI 1** and **Bis-PBIs 5-8** obtained from the Gibbs free energy isotherm equation in toluene.

Thus, spacer units that pre-organize two PBI chromophores with an inter-planar distance of $r < 7$ Å lead to an *intra*molecular folding of the respective Bis-PBIs dyes (**Bis-PBIs 2-4**, *Chapter 5*), whereas spacer units with a length between 7 to 11 Å result in an *inter*molecular self-assembly of the respective dyes into well-defined quadruple PBI π-stacks (**Bis-PBI 1**, *Chapter 4* and **Bis-PBIs 5-7**, *Chapter 6*). Finally, by using linker units with an inter-planar distance $r > 14$ Å larger oligomeric PBI π-stacks are formed (**Bis-PBI 8**, *Chapter 6*). These observations are in good agreement with the previously reported zipper-type aggregation of the imide-linked Bis-PBI dyes **13** and **14** (*Chapter 2.3.1*, Figure 13-14), where well-defined quadruple PBI π-stacks as well as larger PBI oligomers were formed by using different linker units with a length of 6.9 Å and 10.9 Å, respectively.[34-35]

For a better comparison of the distinct spectral features of **Bis-PBIs 5-8** all calculated monomer and aggregate absorption spectra obtained from global fit analysis are shown in Figure 55 together with **Bis-PBI 1** (*Chapter 4*) and the reference compounds **Ref-PBIs 1** and **2**.

Hereby, one can see that in their non-aggregated, monomeric state all target compounds display significantly lower A_{0-0}/A_{0-1} ratios compared to the corresponding reference compounds. This

points to an electronic interaction and thus to a pre-organisation of the two PBI chromophores of **Bis-PBIs 5-8** already in their non-aggregated state. Furthermore, it is noticeable that in the series of oligo-phenylene-substituted **Bis-PBIs 6-8**, the A_{0-0}/A_{0-1} ratio increases from 1.25 to 1.48 with increasing length of the respective spacer units (from 8 to 15 Å). Consequently, the electronic interaction between the two PBI chromophores decreases with increasing inter-planar distances. This result is not surprising as we may expect for the shorter spacers some interaction between the two chromophores, similar as observed for the folda-dimers in *Chapter 5*. The difference to the observations made for the folda-dimers **Bis-PBIs 2-4** (*Chapter 5*), is the preferential self-assembly of **Bis-PBIs 5-8** at higher concentration. Thus, for **Bis-PBIs 5-8** *inter*molecular interactions prevail whereas for **Bis-PBIs 2-4** strong *intra*-molecular interactions lock the dyes in a conformation where further self-assembly is disfavoured. For this reason, no spectral changes could be observed in concentration-dependent UV/Vis studies for **Bis-PBIs 2-4**. Thus, the utilization of linker moieties that pre-organize the chromophores at an inter-planar distance of at least 7 Å prevents an *intra*molecular folding of the respective Bis-PBI dyes (*vide supra*) and favours the *inter*molecular aggregation of **Bis-PBIs 5-8** into larger PBI architectures.

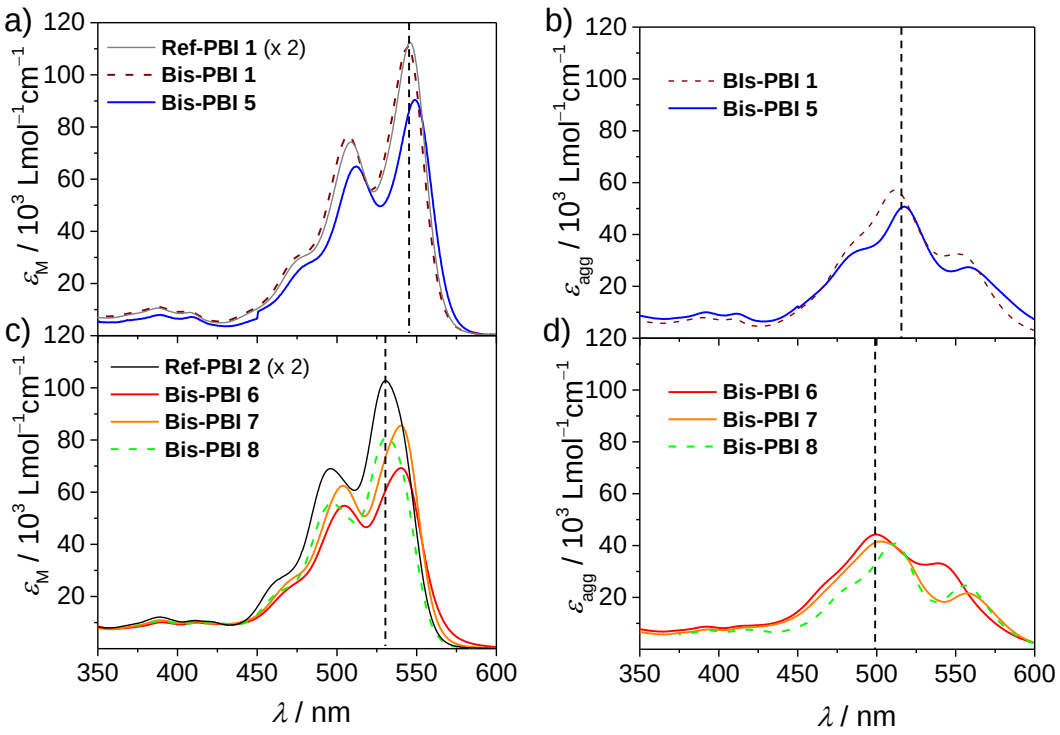

Figure 55. Overview of the calculated spectra and relative positions of calculated absorption maxima determined by global fit analysis for the monomer-dimer (**Bis-PBIs 5-7**) and isodesmic (**Bis-PBI 8**) model for a) **Bis-PBI 5** monomers, b) **Bis-PBI 5** aggregates, c) **Bis-PBIs 6-8** monomers and d) **Bis-PBIs 6-8** aggregates in toluene at room temperature. Also shown are the spectra of **Ref-PBIs 1-2** and **Bis-PBI 1**.

By having a closer look, one can see from Figure 55a that **Bis-PBI 5** exhibits a slightly bathochromically shifted absorption maximum in its non-aggregated state compared to **Bis-PBI 1** and **Ref-PBI 1** (Table 6). Upon aggregation **Bis-PBI 5** still reveals well-resolved but slightly bathochromically shifted absorption bands (Figure 55b, Table 6), as it was the case for structure-related **Bis-PBI 1**, strongly indicating similar defined orientations of all four PBI units in **Bis-PBI 5** dimers as it was already proven for **Bis-PBI 1** upon aggregation.[113] This further explains why the highest binding constant of all target compounds could be determined for **Bis-PBI 5**.

Furthermore, *ortho*-phenylene substituted **Bis-PBIs 6** and **7** show a slightly bathochromically shifted absorption maximum in the monomeric state compared to **Ref-PBI 2**, whereas in the case of *meta*-substituted **Bis-PBI 8** monomers, no bathochromic shift of the absorption maximum can be observed (Figure 55c, Table 6). Moreover, different as for **Bis-PBI 6** (1.25) and **Bis-PBI 7** (1.38), the A_{0-0}/A_{0-1} ratio of **Bis-PBI 8** (1.48) is highly comparable to the one of **Ref-PBI 2** (1.49). Consequently, no electronic interaction between the two PBI units of **Bis-PBI 8** is present in its non-aggregated state. This can be assigned to the length (15 Å) and *meta*-substitution of **Bis-PBI 8** which results in a higher flexibility of the PBI dye, where the chromophores can freely rotate around the linker axis. For **Bis-PBIs 6** and **7** this flexibility is hindered due to the *ortho*-substitution of the linker units.

In contrast to **Bis-PBI 5**, all oligo-phenylene substituted **Bis-PBIs 6-8** reveal very broad and structureless absorption bands upon aggregation (Figure 55d), where **Bis-PBI 7** shows a more bathochromically shifted 0–0 absorption band in contrast to **Bis-PBI 6**. This indicates a slightly longitudinal slipped arrangement of the respective PBI units in **Bis-PBI 7** quadruple π-stacks, in order to gain sufficient π-π-contact between the interacting PBI chromophores resulting in a bathochromically shifted absorption band due to an increased J-type character. This further explains why **Bis-PBI 7** displays a smaller dimerization constant compared to **Bis-PBI 6**, as less π-π-interaction between interacting chromophores results in smaller binding constants.

6.2.2 Further Structural Investigations

To support the spectroscopic observations and to gain deeper insight into the structural arrangement of the chromophores, DFT calculations (B97D3/def2-SVP) were performed for **Bis-PBIs 5-7** dimers where close π–π–stacking (3.3 - 3.4 Å) could be observed between the respective PBI chromophores (Figure 56). Here, **Bis-PBI 7** shows the largest distance (3.4 Å) due to the *p*-tetraphenyl-spacer moiety, which does not enable a closer contact between the two

PBI chromophores. This further explains why the lowest dimerization constant of all Bis-PBI dimers could be found for **Bis-PBI 7** compared to **Bis-PBIs 5** and **6**.

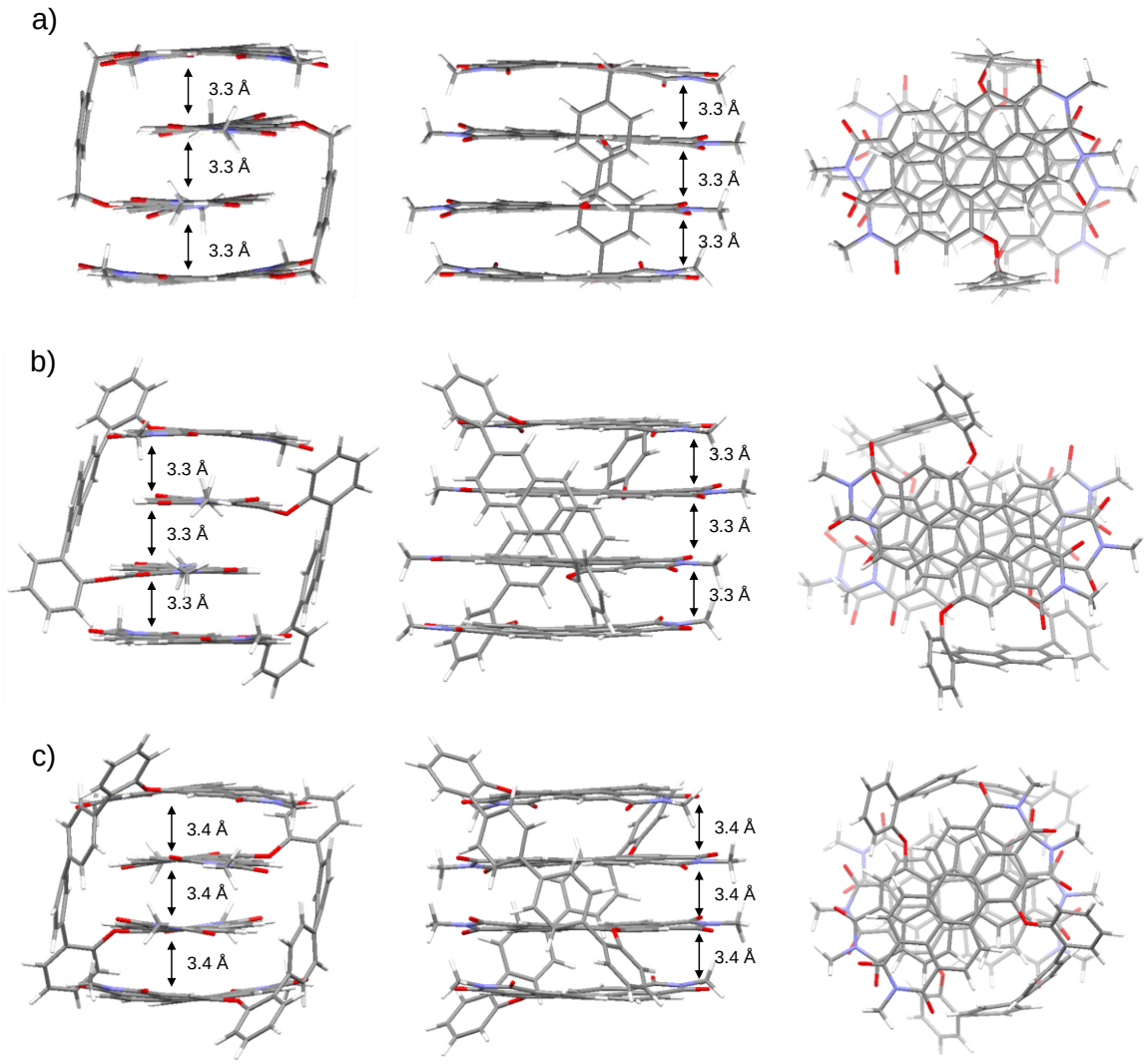

Figure 56. Side views and top view of one possible geometry optimized structure of a) **Bis-PBI 5** b) **Bis-PBI 6** and c) **Bis-PBI 7** by DFT (B97D3/def2-SVP) calculations.

Further indication for the exclusive presence of discrete **Bis-PBIs 5-7** dimers even at higher concentrations was obtained by ESI mass spectrometry (see the Appendix, Figure 61 - 63), where not only the singly charged monomer cations but also the singly charged dimer cations could be observed. In contrast, for **Bis-PBI 8** just the singly charged monomer cation could be detected (see the Appendix, Figure 64), suggesting a disassembly of **Bis-PBI 8** aggregates. This might originate from the lower thermodynamic stability and dispersity of the formed oligomers due to the long inter-planar distance between the two PBI chromophores enforced by the length of the *meta*-phenylene linker unit.

To further confirm the DFT-calculated structures for **Bis-PBIs 5-8** under the applied conditions, two-dimensional diffusion ordered spectroscopy (DOSY) NMR studies (Figure 57a and see the Appendix Figure 65) were performed in toluene at room temperature (c_0 = 2 x 10^{-3} M).

Thus, diffusion coefficients in the range of D = 3 x 10^{-10} m^2 s^{-1} could be measured for **Bis-PBI 6** (Figure 57a) and **Bis-PBI 7** (see the Appendix, Figure 65a). By applying the Stokes-Einstein equation the hydrodynamic radii *r* (Figure 57b) of the respective quadruple π-stacks could be calculated to be 11.0 Å (**Bis-PBI 6**) and 13.5 Å (**Bis-PBI 7**), that are reasonably larger than the one obtained for **Ref-PBI 2** (8.4 Å, *Chapter 5*). These results are in good agreement with the dimensions of the structures which could be obtained from DFT calculations, taking into account that the long alkyl chains were not included in the calculations, but were replaced by small methyl groups. For **Bis-PBI 5**, no hydrodynamic radius could be calculated because of solubility issues during the experiment.

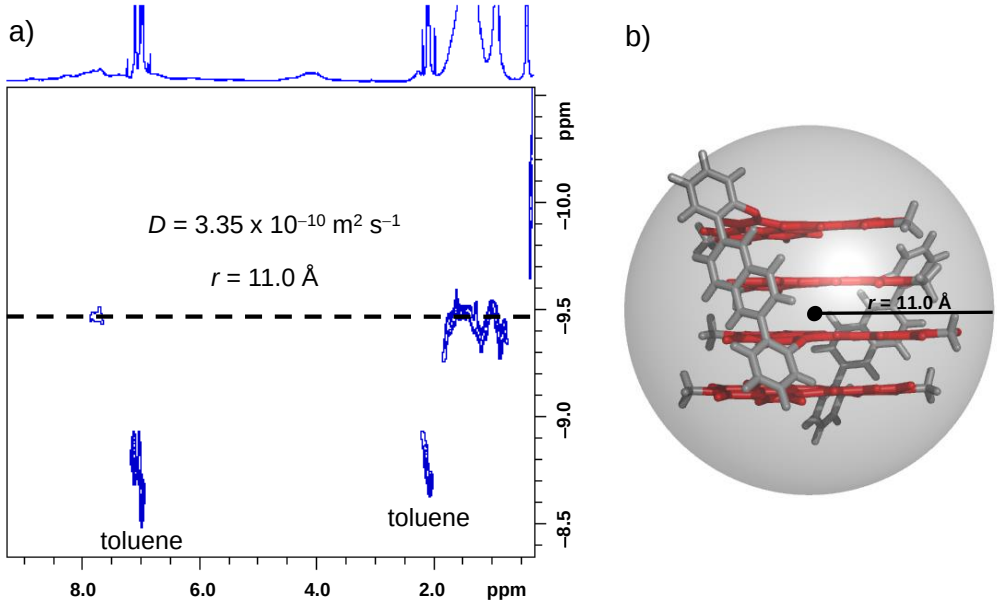

Figure 57. a) 2D plot of DOSY NMR (600 MHz, 293 K) spectrum of **Bis-PBI 6** in toluene-d_8 (c_0 = 2 x 10^{-3} M). b) Illustration of the energy minimized dimer structure of **Bis-PBI 6** from DFT calculations (B97D3/def2-SVP) with hydrodynamic radius *r* as obtained from the Stokes-Einstein equation.

Also for **Bis-PBI 8** the presence of larger aggregates could be further substantiated by 2D-DOSY NMR studies, where the respective hydrodynamic radius of the aggregated species ranges between 10 – 26 Å (see the Appendix Figure 65b) indicating a larger distribution of different aggregate species.

Furthermore, temperature-dependent ^{1}H NMR studies of **Bis-PBIs 5-8** were performed in toluene-d_8 to gain deeper insight into the exact structure of the respective aggregates. For **Ref-PBI 2** the ^{1}H NMR spectrum in toluene-d_8 (c_0 = 2 x 10^{-3} M, 295 K) shows sharp and well resolved proton signals over the whole temperature range from 100 °C to 20 °C, as expected for non-interacting monomeric PBI-chromophores (see the Appendix, Figure 66). By cooling down to –40 °C the signals become slightly broader and a small up-field shift can be observed indicating intermolecular interactions between the PBI chromophores at very low temperatures. This observation complies with the aggregation process observed by UV/Vis experiments for **Ref-PBI 2** at lower temperature and higher concentrations (Figure 53).

Also **Bis-PBIs 5-8** show sharp and well-resolved ^{1}H proton signals at high temperatures (~ 100 °C) where mainly the respective monomers are present in solution as detected by UV/Vis spectroscopy (see the Appendix, Figure 67 - 70). In contrast to **Ref-PBI 2**, the proton signals of **Bis-PBIs 5-8** become much broader with decreasing temperature. Already at room temperature the corresponding signals can no longer be clearly assigned to the respective PBI protons, until the coalescence temperature was reached around 0 °C, where the fully aggregated species could be detected by UV/Vis spectroscopy (see the Appendix, Figure 67 - 70). For a dimer structure with a zipper-type stacking of the PBI chromophores the two halves of each monomer are no more chemically equivalent. Thus, a splitting of the monomer proton signals should be observed at low temperatures if the exchange between monomer and dimer species is slow enough on the NMR time scale. For **Bis-PBIs 5-8** no splitting of the monomer proton signals could be observed under the applied conditions in the accessible temperature range of the NMR experiment, even by further decreasing the temperature to –40 °C. Thus, the exchange between monomer and dimer species of the herein investigated target compounds is too fast for detecting the respective defined aggregated species within the NMR time scale.

6.2.3 Fluorescence Spectroscopy

To get insight into the electronic interaction between the PBI chromophores of **Bis-PBIs 5-8** in the excited state fluorescence spectroscopy (Figure 58) was applied. The measurements were performed in chloroform under highly diluted conditions (OD > 0.05) and in toluene at a higher concentration ($c_0 = 10^{-3}$ M) using a front-face-setup to avoid reabsorption effects.[147] Corresponding data are summarized in Table 7. In chloroform at low concentrations ($c_0 = 10^{-7}$ M) as well as in toluene at high concentrations ($c_0 = 10^{-3}$), **Ref-PBI 1** (Figure 23a, *Chapter 4*) and **Ref-PBI 2** (Figure 58a) display typical monomer-like emission with characteristic, well-resolved vibronic structures, mirror-image relationship and a small Stokes

shift of 490 and 850 cm^{-1} in chloroform and 520 and 850 cm^{-1} in toluene, respectively, as well as high fluorescence quantum yields up to 89% (Table 7).

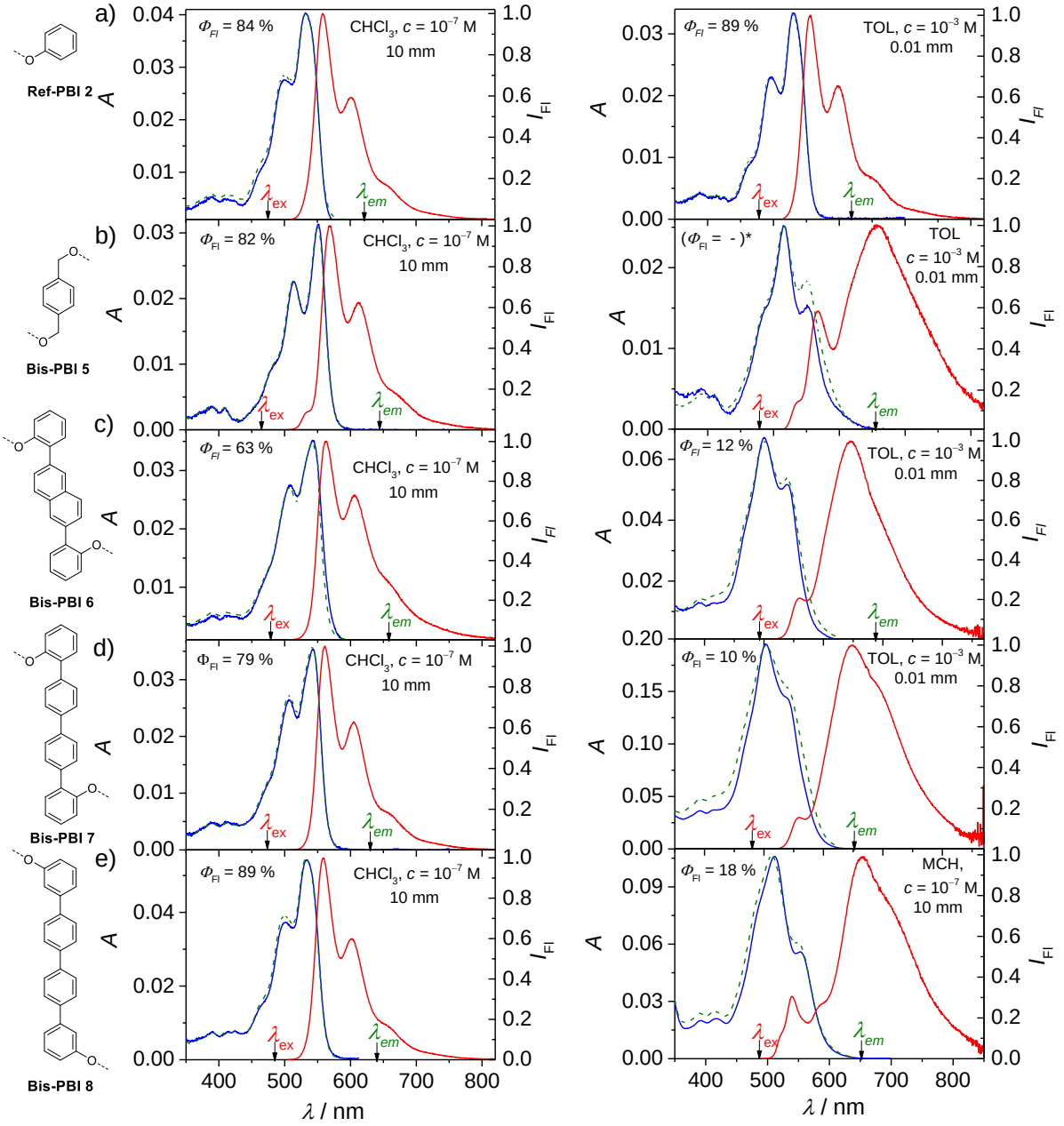

Figure 58. Steady state absorption (blue solid lines), fluorescence (red solid lines) and excitation spectra (green dashed lines) of the dyes a) **Ref-PBI 2**, b) **Bis-PBI 5***, c) **Bis-PBI 6**, d) **Bis-PBI 7**, and e) **Bis-PBI 8** in chloroform (left, $c = 10^{-7}$ M) and dimers/oligomers in toluene or methylcyclohexane (right, $c = 10^{-3}$ M) at 298 K. (*) For **Bis-PBI 5** no reliable fluorescence quantum yields could be obtained in toluene because of solubility issues during the experiment.

For **Bis-PBIs 5-8** similar monomer-like emission signatures could be observed in chloroform at low concentrations ($c_0 = 10^{-7}$ M) with well-resolved vibronic structures, mirror-image relationship and small Stokes shifts below 840 cm^{-1} (Table 7). Moreover, all Bis-PBI dyes show high fluorescence quantum yields, which is very characteristic for monomer-like PBI dyes, increasing from 63% (**Bis-PBI 6**) to 79% (**Bis-PBI 7**) and 89% (**Bis-PBI 8**) with increasing inter-planar distances and therefore decreasing electronic interactions between the respective PBI chromophores (Table 7).

Table 7. Fluorescence spectroscopic data of **Ref-PBI 2**, **Bis-PBI 5**, **Ref-PBI 1**, **Bis-PBI 6**, **Bis-PBI 7** and **Bis-PBI 8** in chloroform at low concentrations ($c_0 = 10^{-7}$ M) and in toluene at high concentrations ($c_0 = 10^{-3}$ M) at room temperature.

		Ref-PBI 1	**Bis-PBI 5**	**Ref-PBI 2**	**Bis-PBI 6**	**Bis-PBI 7**	**Bis-PBI 8**
$\lambda_{max,\,Fl}$ / nm	$CHCl_3$	561	569	558	562	562	558
	toluene	561	658 (567)	556	647 (557)	649 (557)	653[b](540)[b]
$\Delta\bar{\upsilon}_{stokes}/cm^{-1}$	$CHCl_3$	490	590	850	690	590	840
	toluene	520	4200	850	4550	4540	(4200)[b]
Φ_{Fl} / %	$CHCl_3$	85	82	84	63	79	89
	toluene	81	(-)[a]	89	12	10	(18)[b]
τ_{Fl} / ns amplitude	$CHCl_3$	4.4	5.0	4.4	5.0	5.0	4.5
	toluene	5.6	(-)[a]	5.2	7.9, 23.2 11%, 98%	7.8, 32.0 13%, 87%	7.7, 28.8 [b] 6%, 94%

[a] solubility issues during fluorescence measurements

[b] measurement in methylcyclohexane at 298 K because of low aggregation tendency in toluene

On the contrary, the well-resolved fine structure for **Bis-PBIs 5-7** is totally lost in toluene at high concentrations ($c_0 = 10^{-3}$ M), where prominent hypsochromic shifts of the absorption maxima can be observed, with broad, structureless emission bands and pronounced Stokes shifts > 4200 cm^{-1}. In the case of **Bis-PBI 8**, the amount of remaining monomeric und with this more emissive species was too high under the applied conditions in toluene. Thus, fluorescence studies of **Bis-PBI 8** were performed in pure methylcyclohexane at low concentrations ($c_0 = 10^{-7}$ M, Figure 58e), where the aggregation tendency was much higher. Under these

conditions, **Bis-PBI 8** also exhibits a broad emission band with a large Stokes shift of 4200 cm^{-1}. The changed emission properties of **Bis-PBIs 5-8** can be attributed to the formation of an excimer[106, 125] state in the excited aggregate, which is characteristic for π-stacked PBI H-aggregates.[40-41] The excimer state usually arises from structural rearrangement of the chromophores in the excited state. Additionally, the emission spectra of all Bis-PBI dyes **Bis-PBIs 5-8** exhibit a small shoulder at ~560 nm (**Bis-PBIs 5-7**, Table 7) and 540 nm (**Bis-PBI 8**, Table 7), probably due to traces of remaining monomer fluorescence from a small amount of monomeric, not aggregated species.

Moreover, measured excitation spectra (Figure 58, green dashed lines) are in good agreement with the corresponding absorption spectra, revealing single state fluorescence giving rise to an emission from only one species, the aggregated PBI π-stacks. Furthermore, fluorescence quantum yields of **Bis-PBIs 5-8** were drastically decreased below 13%, which can be again attributed to the formation of excimers in the aggregated states. Unfortunately, for **Bis-PBI 5** the fluorescence quantum yield could not be determined because of precipitation during the measurements in toluene at high concentrations ($c_0 = 10^{-3}$ M) as well as in methylcyclohexane at lower concentrations ($c_0 = 10^{-7}$ M).

Further information on the excited state properties of the herein investigated Bis-PBI dyes was gained by fluorescence lifetime measurements (Table 7), where **Ref-PBIs 1-2** exhibit lifetimes of ~ 4 ns in chloroform at low concentrations ($c_0 = 10^{-7}$ M) and ~ 5 ns in toluene at high concentrations ($c_0 = 10^{-3}$ M), which is in good agreement with previously reported values for monomeric PBI chromophores.[109-111] Similar values between 4.5 and 5 ns could be obtained for **Bis-PBIs 5-8** monomers in chloroform ($c_0 = 10^{-7}$ M). In contrast, **Bis-PBIs 6-8** exhibit two fluorescence lifetimes (Table 7) in toluene at higher concentrations ($c_0 = 10^{-3}$ M), where the shorter lifetime (~5 ns) with significantly lower amplitude is highly comparable to the values of **Ref-PBIs 1-2**. Thus, the shorter lifetime can be attributed to the emission from the monomer-like, more emissive species. The second lifetime ranging between 23 and 32 ns is much longer and among the highest reported values for PBI excimers,[193] which might be explained by the more forbidden radiative transition to the ground state.[25] For **Bis-PBI 5** no fluorescence lifetime could be determined because of precipitation during the measurements.

6.3 Conclusion

In this chapter, *inter*molecular self-assembly of four new Bis-PBI dyes into well-defined supramolecular architectures was investigated. By systematically extending the backbone length from 7Å to 15Å it was possible to generate discrete quadruple π-stacks (**Bis-PBIs 5-7**) as well as larger oligomeric π-stacks (**Bis-PBI 8**) upon self-assembly. The herein performed investigations reveal that the aggregation process and the aggregate structures are defined by the nature of the spacer unit that is used to connect the two PBI chromophores in the bay-position. A more rigid spacer unit (*ortho*-substitution) that pre-organizes the chromophores with an inter-planar distance of roughly 8 Å results in the formation of well-defined quadruple PBI π-stacks with high binding constants up to $K_D \approx 10^5$ M^{-1} in toluene. In contrast, the utilization of a more flexible linker unit (*meta* substitution) with an inter-planar distance around 15 Å leads to the formation of larger oligomeric π-stacks revealing a drastically decreased binding strength two magnitudes lower in intensity with $K \approx 10^3$ M^{-1} in toluene. Moreover, it could be demonstrated that common analytical methods, like UV/Vis and fluorescence spectroscopy are suitable techniques to adequately elucidate the structure of the herein introduced supramolecular architectures. Finally, the spectroscopic observations could be further proven by DOSY-NMR spectroscopy, ESI mass spectrometry, AFM measurements and DFT calculations.

6.4 Appendix

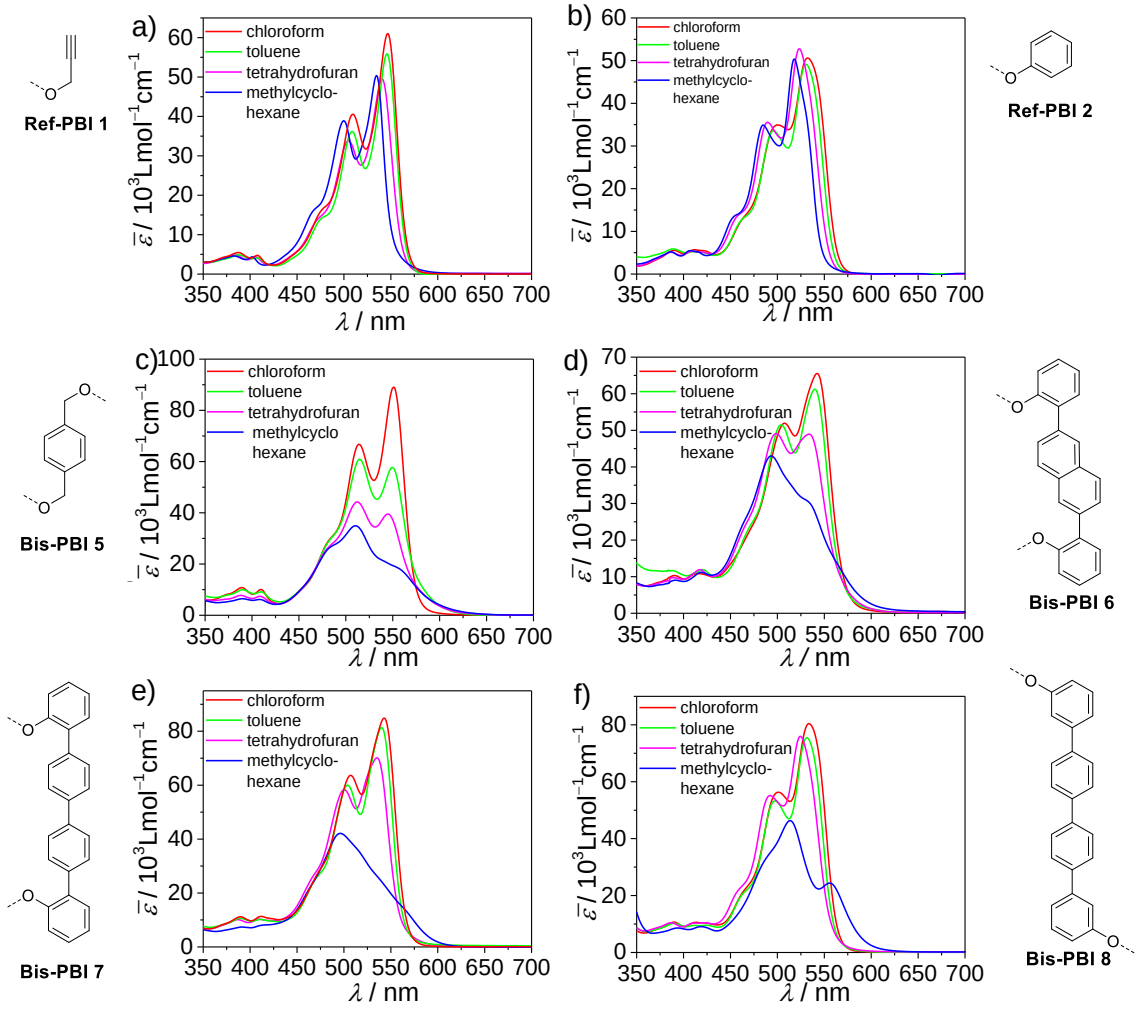

Figure 59. UV/Vis absorption spectra of a) **Ref-PBI 1**, b) **Ref-PBI 2**, c) **Bis-PBI 5**, d) **Bis-PBI 6**, e) **Bis-PBI 7**, and f) **Bis-PBI 8** with $c_0 = 2 \times 10^{-5}$ M in chloroform (red), toluene (green), tetrahydrofuran (magenta) and methylcyclohexane (blue) at room temperature.

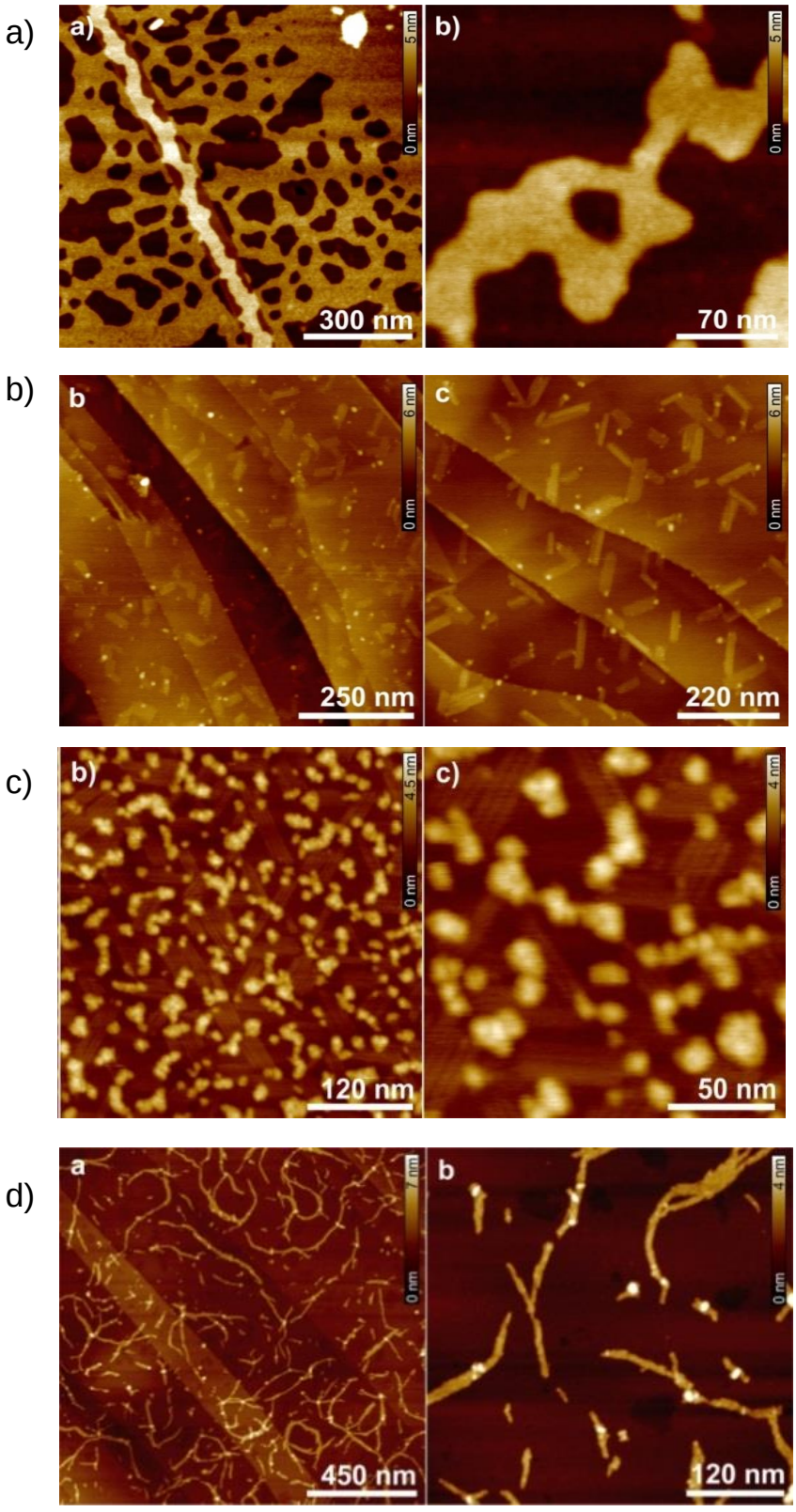

Figure 60. AFM images of thin-films prepared by spin-coating from a solution (c = 2 x 10^{-5} M^{-1}, 2000 rpm) of a) **Bis-PBI 5** in toluene and b) **Bis-PBI 6**, c) **Bis-PBI 7** and d) **Bis-PBI 8** in methylcyclohexane on HOPG.

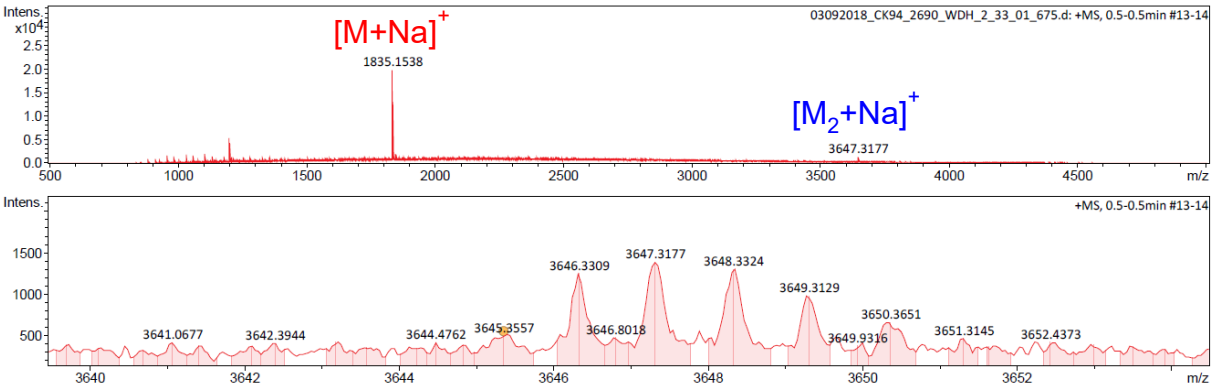

Figure 61. ESI mass spectrum of **Bis-PBI 5** in positive-ion mode. The sample was prepared out of a toluene solution. $[M+Na]^+$ and $[M_2+Na]^+$ denote the mass peaks corresponding to the singly charged monomer and dimer cation of **Bis-PBI 5**.

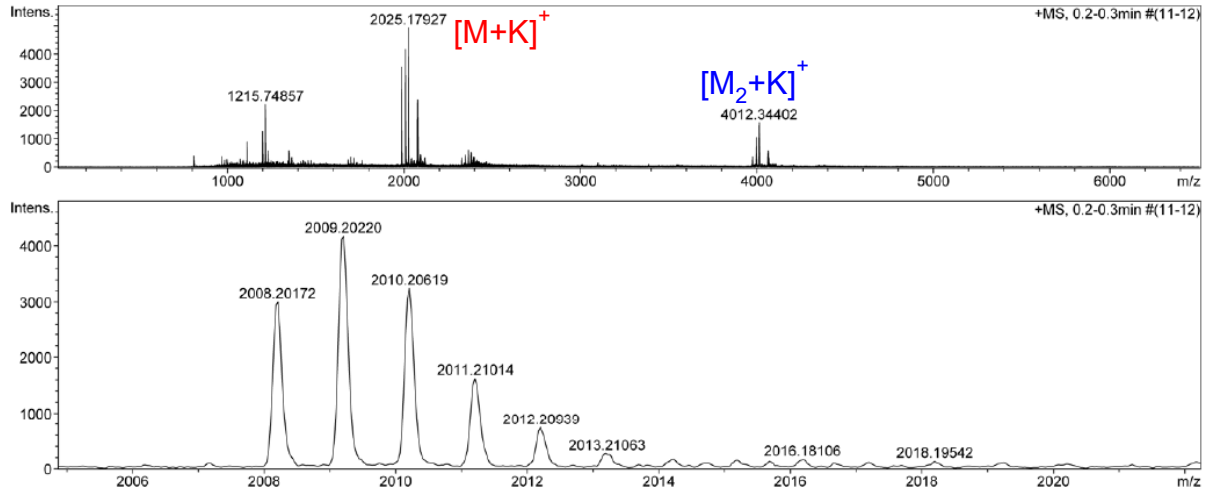

Figure 62. ESI mass spectrum of **Bis-PBI 6** in positive-ion mode. The sample was prepared out of a toluene solution. $[M+K]^+$ and $[M_2+K]^+$ denote the mass peaks corresponding to the singly charged monomer and dimer cation of **Bis-PBI 6**.

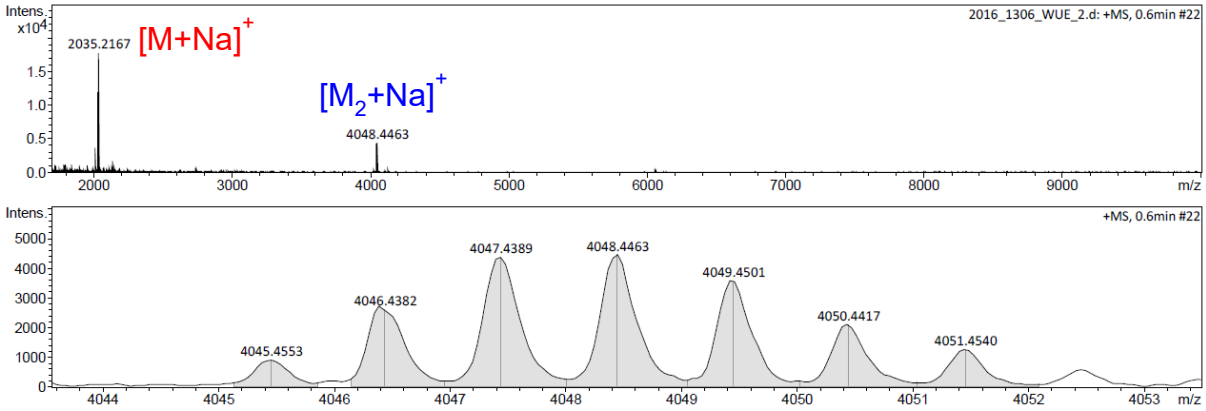

Figure 63. ESI mass spectrum of **Bis-PBI 7** in positive-ion mode. The sample was prepared out of a toluene solution. $[M+Na]^+$ and $[M_2+Na]^+$ denote the mass peaks corresponding to the singly charged monomer and dimer cation of **Bis-PBI 7**.

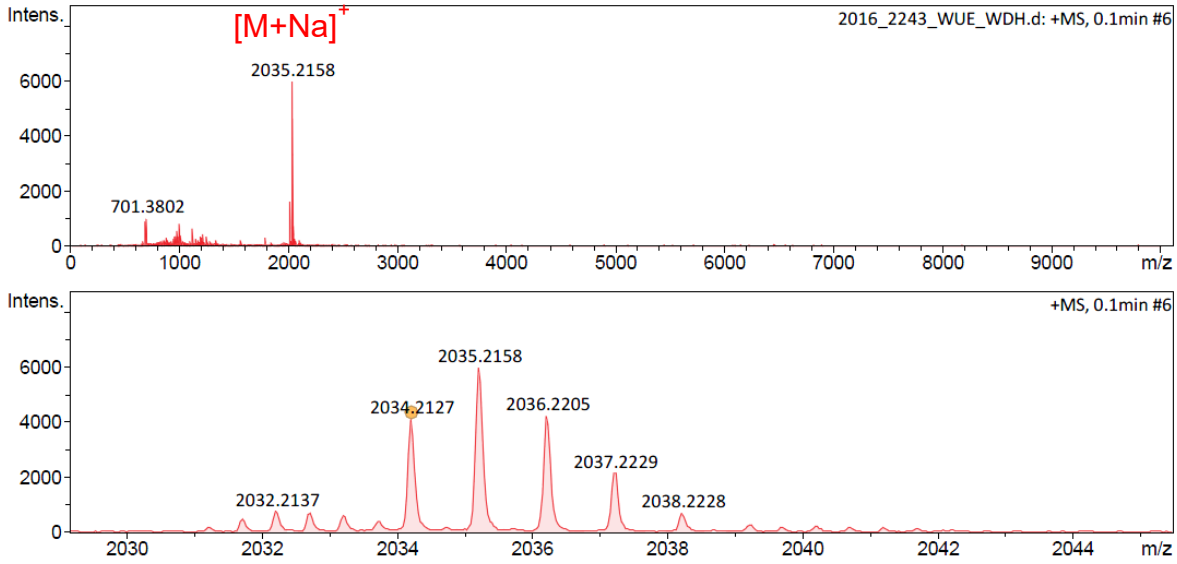

Figure 64. ESI mass spectrum of **Bis-PBI 8** in positive-ion mode. The sample was prepared out of a toluene solution. $[M+Na]^+$ denote the mass peaks corresponding to the singly charged monomer cation of **Bis-PBI 8.**

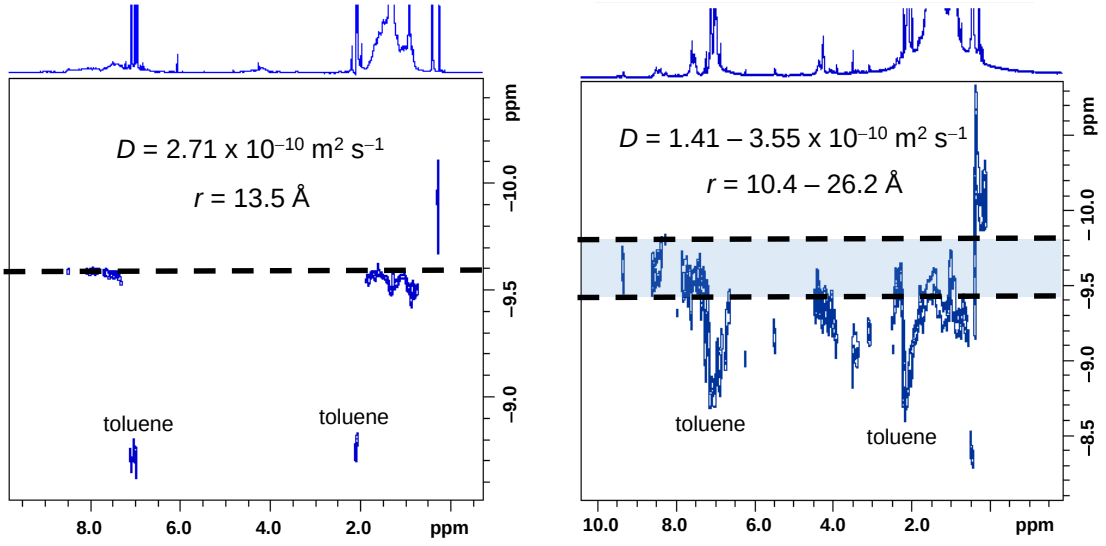

Figure 65. 2D plot of DOSY NMR (600 MHz, 293 K) spectrum of a) **Bis-PBI 7** and b) **Bis-PBI 8** in toluene-d_8 (c_0 = 2 x 10^{-3} M) and hydrodynamic radius as received from the Stokes-Einstein equation.

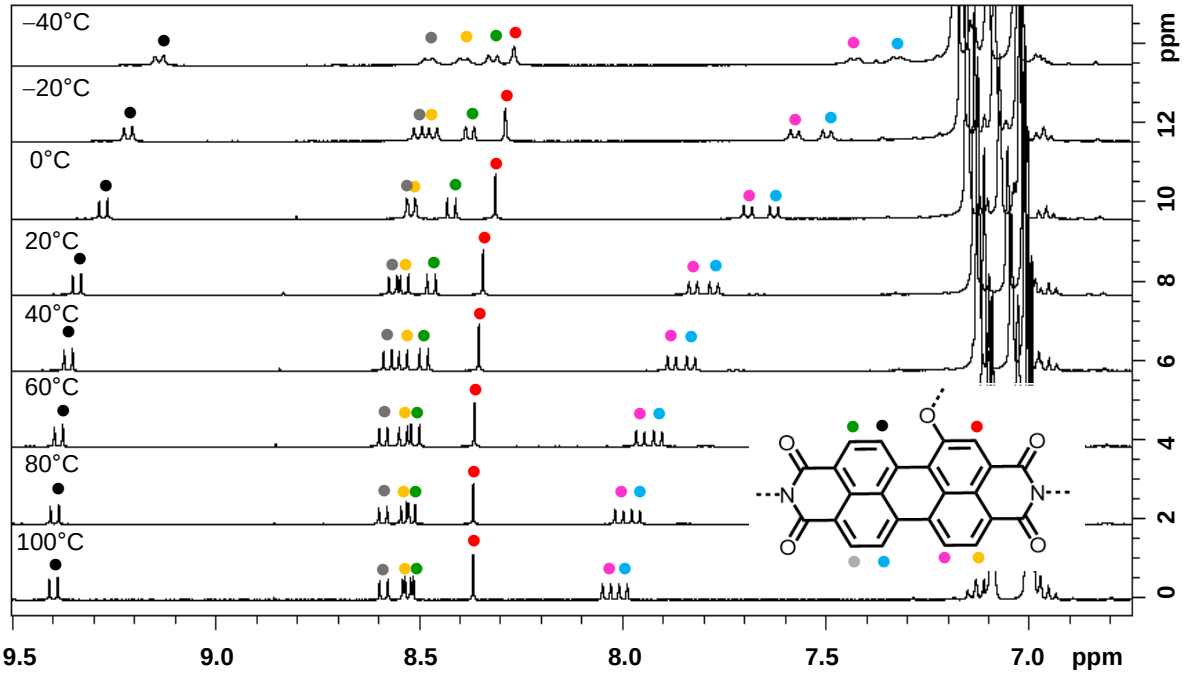

Figure 66. Temperature-dependent ^{1}H NMR-spectra of the aromatic protons of **Ref-PBI 2** in toluene-d_8, from 100 °C to –40 °C (c_0 = 3 mM).

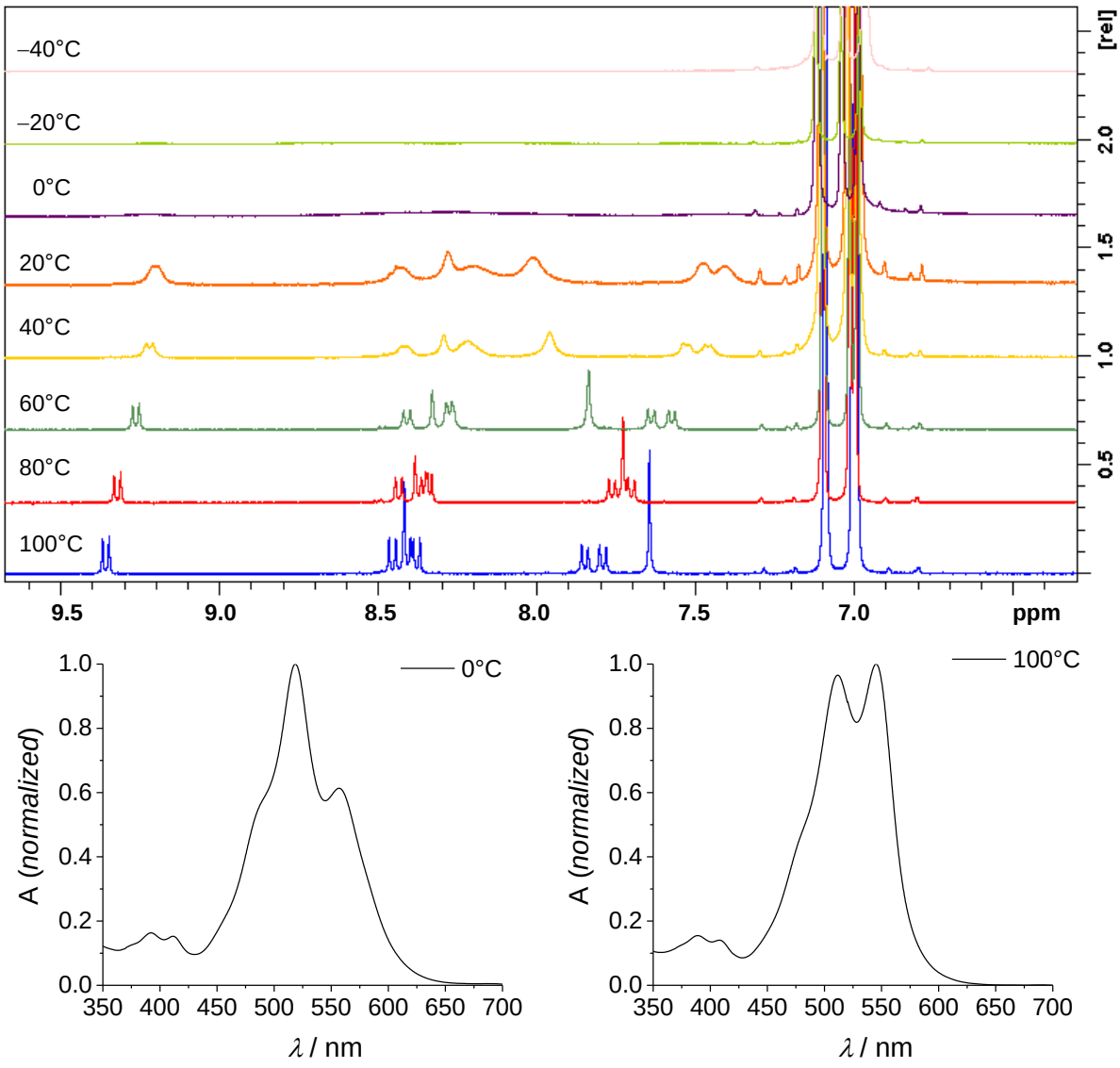

Figure 67. Temperature-dependent ^{1}H NMR-spectra of the aromatic protons of **Bis-PBI 5** in toluene-d_8, from 100 °C to –40 °C (c_0 = 0.5 mM) and UV/Vis spectra of **Bis-PBI 5** in toluene-d_8 (c_0 = 0.5 mM) at 0°C and 100°C.

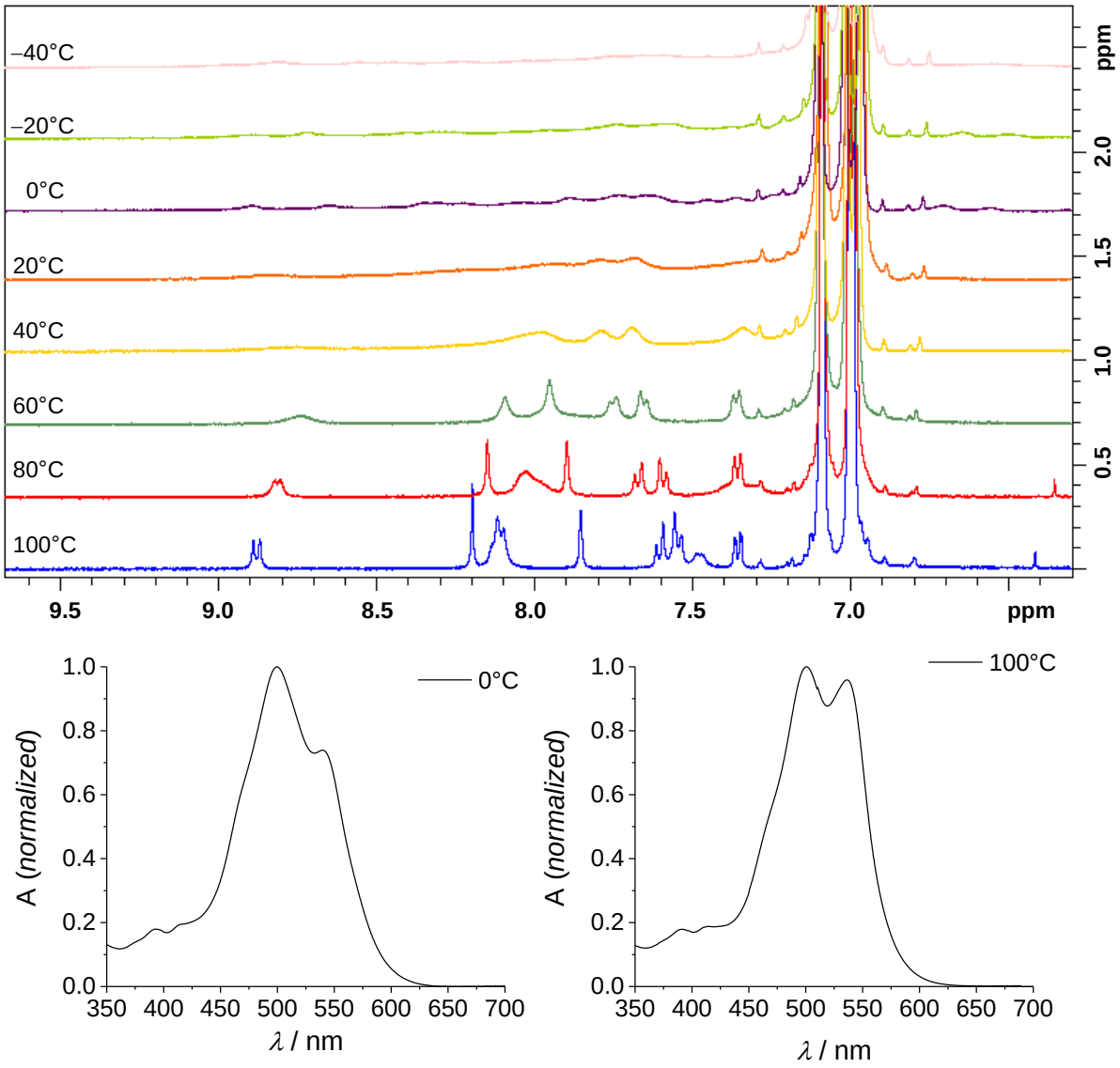

Figure 68. Temperature-dependent ^{1}H NMR-spectra of the aromatic protons of **Bis-PBI 6** in toluene-d_8, from 100 °C to –40 °C (c_0 = 2 mM) and UV/Vis spectra of **Bis-PBI 6** in toluene-d_8 (c_0 = 2 mM) at 0°C and 100°C.

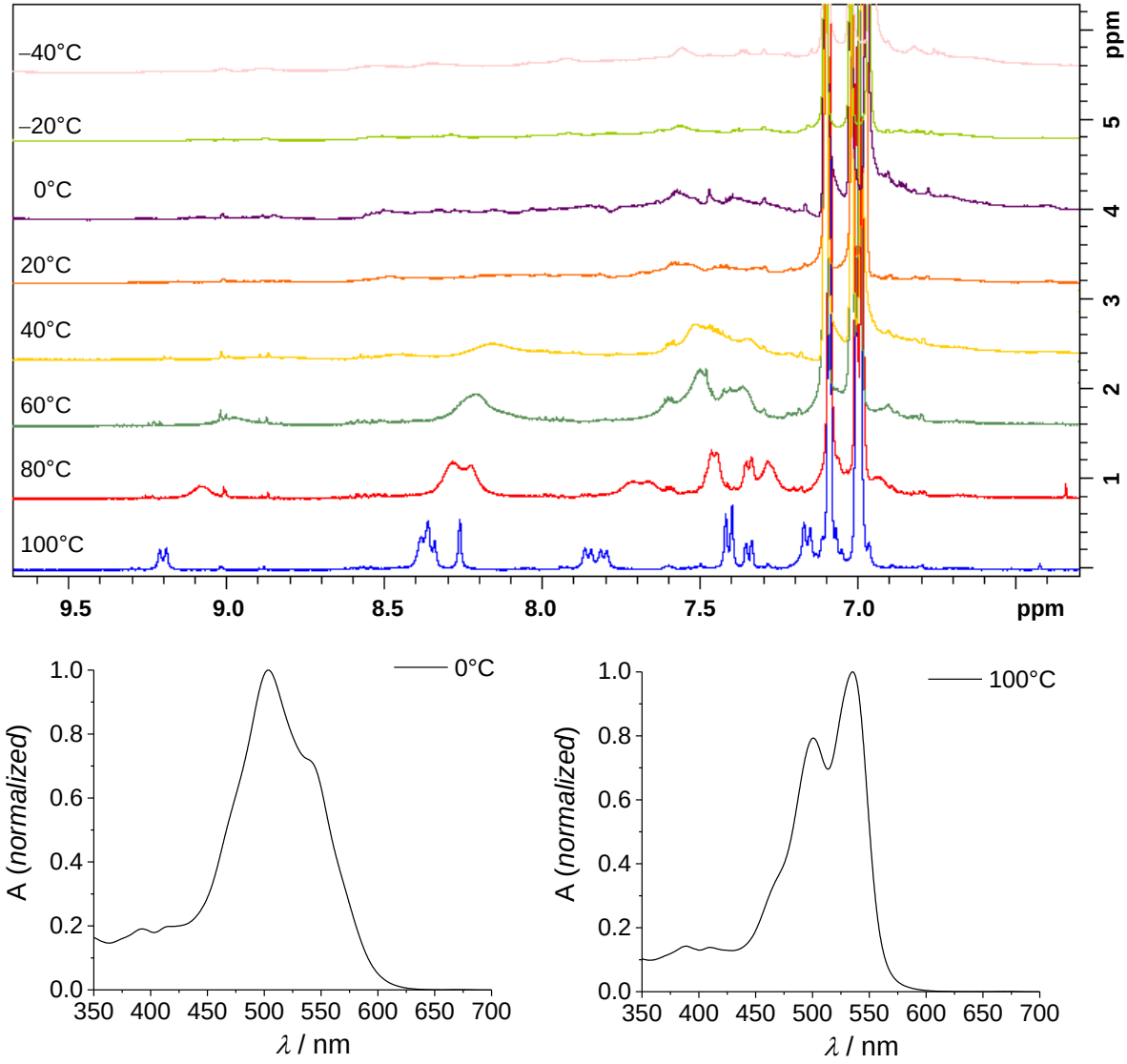

Figure 69. Temperature-dependent ^{1}H NMR-spectra of the aromatic protons of **Bis-PBI 7** in toluene-d_8, from 100 °C to –40 °C (c_0 = 2 mM) and UV/Vis spectra of **Bis-PBI 7** in toluene-d_8 (c_0 = 2 mM) at 0°C and 100°C.

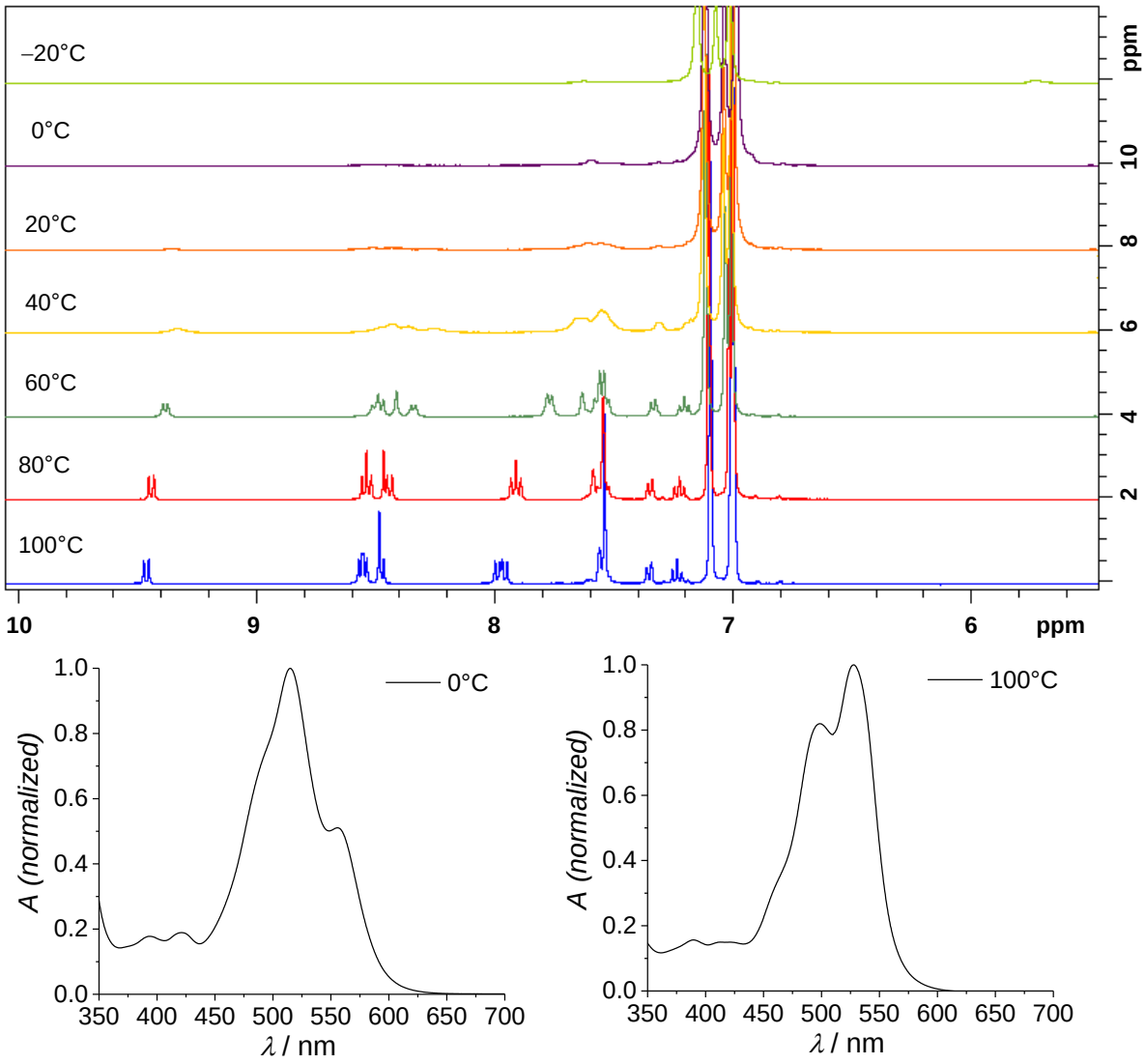

Figure 70. Temperature-dependent ^{1}H NMR-spectra of the aromatic protons of **Bis-PBI 8** in toluene-d_8, from 100 °C to –40 °C (c_0 = 5 mM) and UV/Vis spectra of **Bis-PBI 8** in toluene-d_8 (c_0 = 5 mM) at 0°C and 100°C.

Chapter 7

–

Summary

Supramolecular self-assembly of perylene bisimide (PBI) dyes *via* non-covalent forces gives rise to a high number of different PBI architectures with unique optical and functional properties. As these properties can be drastically influenced by only slightly structural changes of the formed supramolecular ensembles (*Chapter 2.1*) the controlled self-assembly of PBI dyes became a central point of current research to design innovative materials with a high potential for different applications as for example in the fields of organic electronics or photovoltaics.

As PBI dyes show a strong tendency to form infinite π-aggregated structures (*Chapter 2.2*) the aim of this thesis was to precisely control their self-assembly to create small, structurally well-defined PBI assemblies in solution. *Chapter 2.3* provides an overview on literature known strategies that were established to realize this aim. It could be demonstrated that especially backbone-directed *intra*- and *inter*molecular self-assembly of covalently linked Bis-PBI dyes evolved as one of the most used strategies to define the number of stacked PBI chromophores by using careful designed spacer units with regard to their length and flexibility.

Based on this literature survey, covalently linked PBI dyes were synthesized and analysed within this thesis bearing acetylene and polyphenyl spacer units with a length ranging between 3 - 15 Å. Different from previous examples of tethered Bis-PBI dyes, the imide positions of the herein investigated target compounds **Bis-PBIs 1-8** should be available for solubilizing side chains ensuring adequate solubility in different organic solvents and accordingly, for the first time an ether functionality in bay area was used to anchor the tether.

Hence, **Bis-PBIs 1-8** were successfully obtained based on well-known metal-mediated cross-coupling reactions by either copper- and palladium-catalysed Glaser coupling reaction (**Bis-PBI 1)** or Suzuki coupling reaction followed by a nucleophilic aromatic substitution reaction (**Bis-PBIs 2-8**) which was described in *Chapter 3*. Subsequently, all Bis-PBI dyes were fully

characterized by ^{1}H and ^{13}C NMR spectroscopy as well as high resolution ESI mass spectrometry. The corresponding synthetic route for **Bis-PBIs 1-8** is summarized in Scheme 8.

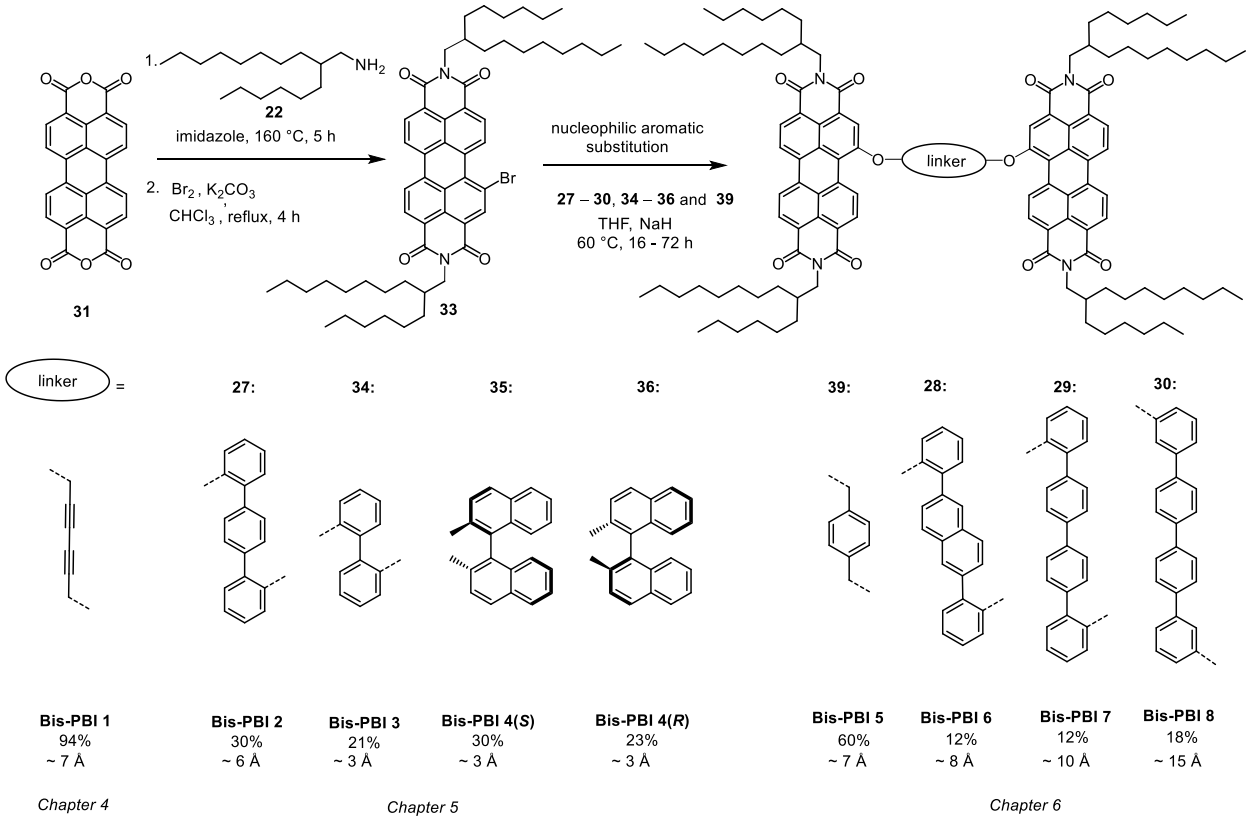

Scheme 8. Synthesis of covalently linked **Bis-PBIs 1-8**.

By using conventional spectroscopic methods like UV/Vis and fluorescence experiments in combination with NMR measurements an in-depth comparison of the molecular and optical properties in solution both in the non-stacked and aggregated state of **Bis-PBIs 1-8** could be elucidated to reveal structure-property relationships of different PBI architectures. Thus, it could be demonstrated, that spacer units that pre-organize two PBI chromophores with an inter-planar distance of $r < 7$ Å lead to an *intra*molecular folding (**Bis-PBIs 2-4**), whereas linker moieties with a length between 7 to 11 Å result in an *inter*molecular self-assembly (**Bis-PBIs 1** and **5-7**) of the respective Bis-PBIs dyes *via* dimerization to form well-defined quadruple PBI π-stacks. Hence, if the used spacer units ensure an inter-planar distance $r > 14$ Å larger oligomeric PBI π-stacks are generated (**Bis-PBI 8**).

In *Chapter 4* a detailed analysis of the exciton coupling in a highly defined H-aggregate quadruple PBI-π stack is presented. Therefore, bay-tethered PBI dye **Bis-PBI 1** was

investigated, in which two PBI chromophores are covalently linked by a diacetylene linker that ensures a distance of approximately 7 Å between the π-surfaces. This is exactly twice the π–π-distance which is known to enable the intercalation of an additional chromophore. The aggregation behaviour of **Bis-PBI 1** was then investigated by concentration-dependent UV/Vis spectroscopy in THF and toluene (Figure 71a), where pronounced spectral changes could be observed upon increasing concentration. The absorption data in toluene could be properly fitted with the monomer-dimer model also in a global fit approach providing a dimerization constant of $K_D = 10^5$ M^{-1}. Further confirmation for the exclusive existenz of PBI quadruple π-stacks was gained by 2D-DOSY-NMR spectroscopy, ESI mass spectrometry and AFM measurements. The spectroscopic observations were finally rationalized by DFT calculations (Figure 71b). These studies clearly confirm that **Bis-PBI 1** self-assembles exclusively into dimers with four closely π-stacked PBI chromophores.

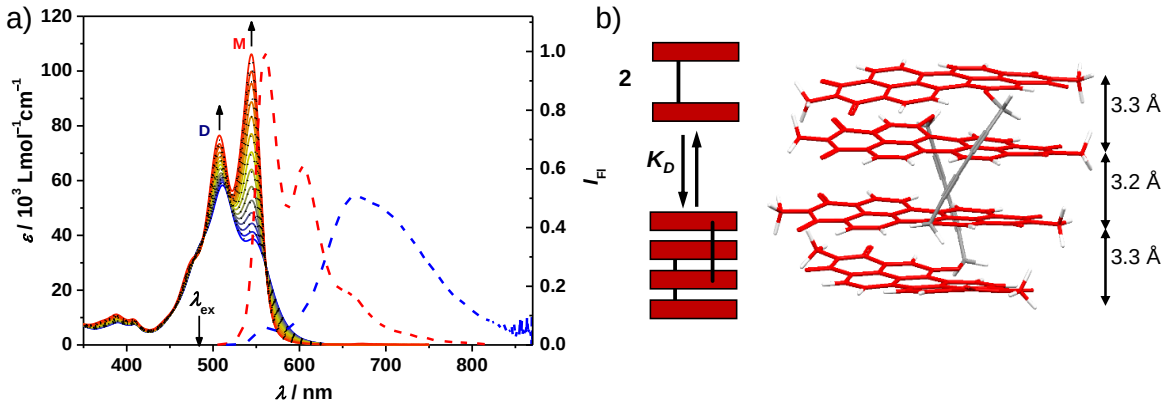

Figure 71. a) Concentration-dependent UV/Vis absorption spectra (coloured lines) of **Bis-PBI 1** (c_0 = 3.51 x 10^{-4} M – 3.75 x 10^{-7} M) in toluene at 298 K. Also shown are the calculated spectra obtained by a global fit analysis for supramolecular dimerization (black dashed lines). Arrows indicate the changes in intensity of the 0–0 and the 0–1 band with decreasing concentration. Furthermore, depicted are steady state fluorescence spectra of **Bis-PBI 1** monomers in $CHCl_3$ (red dashed line, $c_0 = 10^{-7}$ M) and dimers in toluene (blue dashed line, $c_0 = 10^{-3}$ M) at 298 K. b) Schematic representation of the self-assembly of **Bis-PBI 1** into a quadruple dye stack and geometry optimized structure (B97D3/def2-SVP) of the dimer aggregate of **Bis-PBI 1**.

Furthermore, with the aid of broadband fluorescence upconversion spectroscopy (FLUPS) ensuring broadband detection range and ultrafast time resolution at once, ultrafast Frenkel exciton relaxation and excimer formation dynamics in the PBI quadruple π-stack within 1 ps was successfully investigated in cooperation with the group of Dongho Kim (Figure 71c). Thus, it was possible to gain for the first time insights into the exciton dynamics within a highly

defined synthetic dye aggregate beyond dimers. By analysing the vibronic line shape in the early-time transient fluorescence spectra in detail, it could be demonstrated that the Frenkel exciton is entirely delocalized along the quadruple stack after photoexcitation and immediately loses its coherence followed by the formation of the excimer state.

In *Chapter 5* four well-defined Bis-PBI folda-dimers **Bis-PBIs 2-4** were introduced, where linker units of different length (r < 7 Å) and steric demand were used to gain distinct PBI dye assemblies in the folded state. Structural elucidation based on in-depth UV/Vis, CD and fluorescence experiments in combination with 1D and 2D NMR studies reveals a stacking of the two PBI chromophores upon folding for all Bis-PBI dyes **Bis-PBIs 2-4** in 1,1,2,2-tetrachloroethane, where geometry-optimized structures obtained from DFT calculations suggest only slightly different arrangements of the PBI units enforced by the distinct spacer moieties (Figure 72).

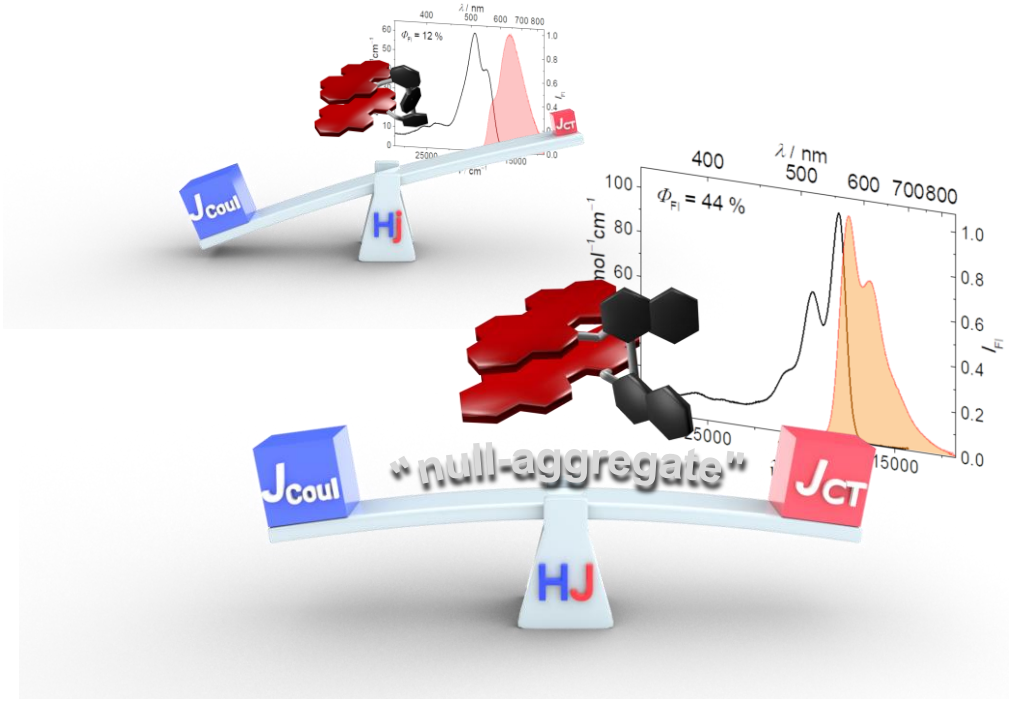

Figure 72. Graphical illustration of the competition between short-range (J_{CT}) and long-range (J_{Coul}) exciton coupling for π-stacked **Bis-PBI 2** and **4** with optical signatures ranging from conventional H-type (Hj) aggregates (**Bis-PBI 2**, back) to monomer-like absorption features, which presents the first experimental proof of a PBI-based "null-aggregate", in which long- and short-range exciton coupling fully compensate each other. Also shown are the corresponding absorption and fluorescence spectra of **Bis-PBI 2** and **4**, respectively.

Remarkably, the chromophore stacks exhibit very distinct optical properties as explored by UV/Vis absorption and fluorescence spectroscopy (Figure 72). This can be rationalized by the interplay of long- (J_{Coul}) and short-range (J_{CT}) coupling, which leads to completely unexpected

optical signatures underlying the importance of charge-transfer mediated exciton coupling for π-stacked PBI chromophores Theoretical investigation reveal that the latter arises from HOMO–HOMO and LUMO–LUMO overlap of the chromophores, which is very sensitive to the structural arrangement of the dyes. Hence, small changes of the geometry have considerable influence on the optical properties of the π-stacks. With the resulting optical signatures of **Bis-PBIs 2-4** ranging from conventional Hj-type to monomer like absorption features, the first experimental proof of a PBI-based "null-aggregate" could be presented, in which long- and short-range exciton coupling fully compensate each other (Figure 72). Hence, the insights of this chapter pinpoint the importance of charge-transfer mediated short-range exciton coupling that can significantly influence the properties of π-stacked PBI chromophores.

In the last part of this thesis (*Chapter 6*), spacer-controlled self-assembly of four bay-linked Bis-PBI dyes **Bis-PBIs 5-8** into well-defined supramolecular architectures was investigated, where the final aggregate structures are substantially defined by the nature of the used spacer units. By systematically extending the backbone length from 7 to 15 Å defining the inter-planar distance between the tethered chromophores, different assemblies from defined quadruple PBI π-stacks to larger oligomeric π-stacks could be gained upon aggregation.

By using conventional spectroscopic methods like UV/Vis spectroscopy pronounced spectral changes could be observed for **Bis-PBIs 5-8** in toluene upon increasing concentration, revealing H-type aggregation for all target compounds. Corresponding absorption data of **Bis-PBIs 5-7** could be properly fitted with the monomer-dimer model also in a global fit approach confirming the exclusively existenz of PBI quadruple π-stacks in solution, which could be further substantiated by 2D-DOSY-NMR spectroscopy, ESI mass spectrometry, AFM measurements and DFT calculations. These studies clearly confirm that **Bis-PBIs 5-7** self-assemble exclusively into dimers with dimerization constants ranging between $K_D = 10^3$ - 10^5 M^{-1}. In striking contrast, for **Bis-PBI 8** the concentration-dependent absorption data could be fitted with the isodesmic model, indicating the formation of larger oligomeric π-stacks, which could be further proven by 2D-DOSY-NMR spectroscopy and AFM measurement, where long fibres could be observed up to 500 nm in length. Hereby, the absorption spectra of **Bis-PBIs 5-8** monomers and aggregates (Figure 73a) could be rationalized and a relationship between the optical properties and the nature of the respective linker moieties could be revealed. Thus, a more rigid spacer unit (*ortho*-substitution) that pre-organizes the chromophores with an inter-planar distance of roughly 8 Å results in the formation of well-defined quadruple π-stacks,

whereas the utilization of a more flexible linker unit (*meta*-substitution) with an inter-planar distance around 15 Å leads to the formation of larger oligomeric π-stacks (Figure 73b).

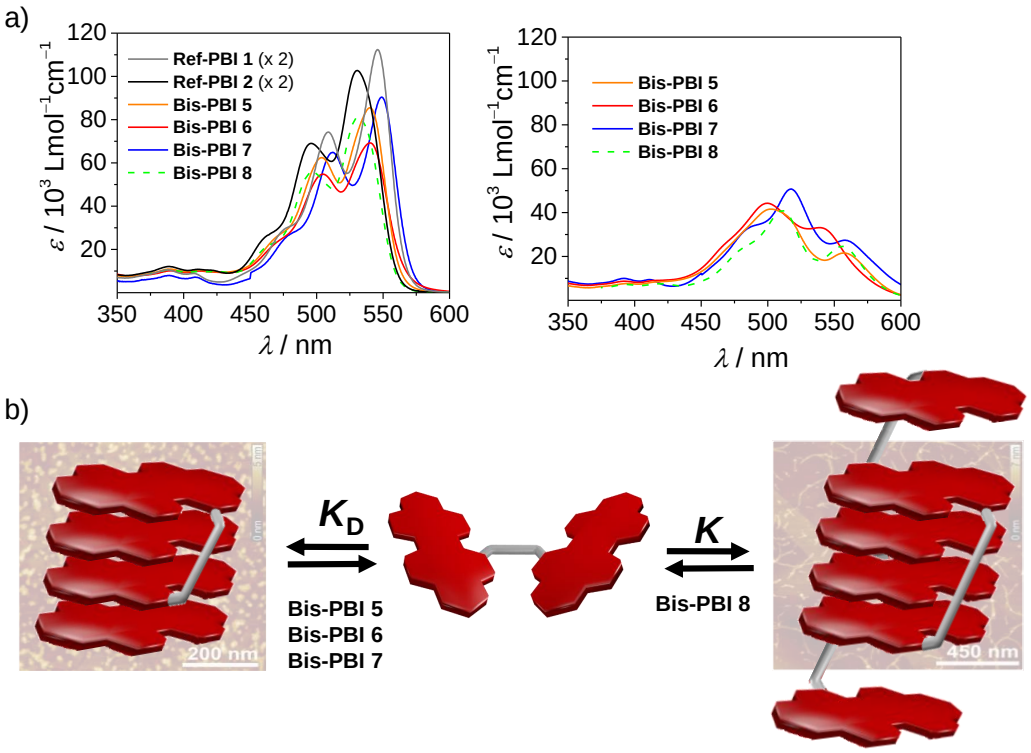

Figure 73. a) Comparison of the spectral shapes and relative position of calculated absorption spectra of **Bis-PBIs 5-8** monomer and aggregated species in toluene at room temperature determined by global fit analysis for the monomer-dimer resp. isodesmic model b) Schematic illustration of the self-assembly pathways of bay tethered perylene bisimide dyes **Bis-PBIs 5-8** into bimolecular stacks of four PBI units and supramolecular polymers, respectively.

In conclusion, the synthesis of nine covalently linked PBI dyes in combination with a detailed investigation of their spacer-mediated self-assembly behaviour in solution concerning structure-properties-relationships was presented within this thesis. The results confirm a strong exciton coupling in different types of Bis-PBI architectures *e.g.* folda-dimers or highly defined quadruple π-stacks, which significantly influences their optical properties upon self-assembly. The structural elucidation of artificial dye aggregates facilitates the design of new organic materials with particular optical and electronic properties. This further provides important information for developing suitable functional materials for applications *e.g.* in the fields of organic electronics or photovoltaics by mimicking the sophisticated properties shown by natural light-harvesting systems.

Chapter 8

–

Zusammenfassung

Supramolekulare Selbstorganisationsprozesse von Perylenbisimid-(PBI)-Farbstoffen über nichtkovalente Kräfte führen zu einer Vielzahl unterschiedlicher PBI-Aggregatstrukturen welche sich in ihren einzigartigen optischen und funktionellen Eigenschaften unterscheiden. Diese Eigenschaften können bereits durch leichte strukturelle Veränderungen der gebildeten supramolekularen Strukturen drastisch beeinflusst werden (*Kapitel 2.1*), was die kontrollierte Selbstassemblierung von PBI-Farbstoffen zu einem zentralen Punkt aktueller Forschungsarbeiten macht. Dadurch soll es ermöglicht werden, innovative Materialien zu generieren, welche ein hohes Potenzial für unterschiedlichste Anwendungen aufzeigen, wie z.B. im Bereich der organischen Elektronik oder Photovoltaik.

Da PBI-Farbstoffe eine starke Tendenz zur Bildung ausgedehnter Aggregatstrukturen aufweisen (*Kapitel 2.2*), war das Ziel dieser Arbeit, kleine, hoch-definierte PBI-Stapel zu generieren, was über die kontrollierte Steuerung ihres Aggregationsverhaltens ermöglicht werden sollte. *Kapitel 2.3* gibt dabei einen Überblick über die hierfür in der Literatur verwendeten Strategien. Dabei konnte gezeigt werden, dass vor allem eine *intra*- bzw. *inter*molekulare Organisation von kovalent-verknüpften Bis-PBI-Farbstoffen herangezogen wird, um die Anzahl der PBI-Chromophore innerhalb des Aggregates zu limitieren. Dies konnte unter anderem durch eine sorgfältige Auswahl der verwendeten Linker-Einheiten realisiert werden, vor allem hinsichtlich ihrer Länge und Flexibilität.

In Anlehnung an jene Strategien wurden auch in dieser Arbeit zwei kovalent-verknüpfte Perylenfarbstoffe analysiert, wobei die Länge der jeweiligen Acetylen- und Polyphenyl-Linker-Einheiten zwischen 3 Å - 15 Å variierte. Anders als bei früheren Beispielen von kovalent-verknüpften Bis-PBI-Farbstoffen wurde in dieser Arbeit erstmals eine Etherfunktionalität in Bucht-Position der PBI-Farbstoffe zur Verknüpfung der Chromophore verwendet. Dies

ermöglicht das Einführen von bis zu vier löslichkeitsvermittelnden Alkylketten in den Imidpositionen der PBI-Farbstoffe, um eine ausreichende Löslichkeit dieser in verschiedenen organischen Lösungsmitteln auch bei hohen Konzentrationen sicher zu stellen.

Basierend auf bekannten metallvermittelten Kreuzkupplungsreaktionen wurden die Zielverbindungen **Bis-PBI 1-8** schließlich durch eine kupfer- und palladiumkatalysierte Glaser-Kupplungsreaktion (**Bis-PBI 1**) bzw. durch eine Suzuki-Kupplung mit anschließender nukleophiler aromatischer Substitution erhalten (**Bis-PBIs 2-8**). Dies wurde ausführlich in *Kapitel 3* erläutert. Anschließend konnten alle Farbstoffe vollständig mittels ^{1}H- und ^{13}C-NMR Spektroskopie, sowie mittels hochauflösender ESI Massenspektrometrie charakterisiert werden. Der synthetische Weg zur Darstellung von **Bis-PBI 1-8** ist in Schema 9 nochmals zusammenfassend dargestellt.

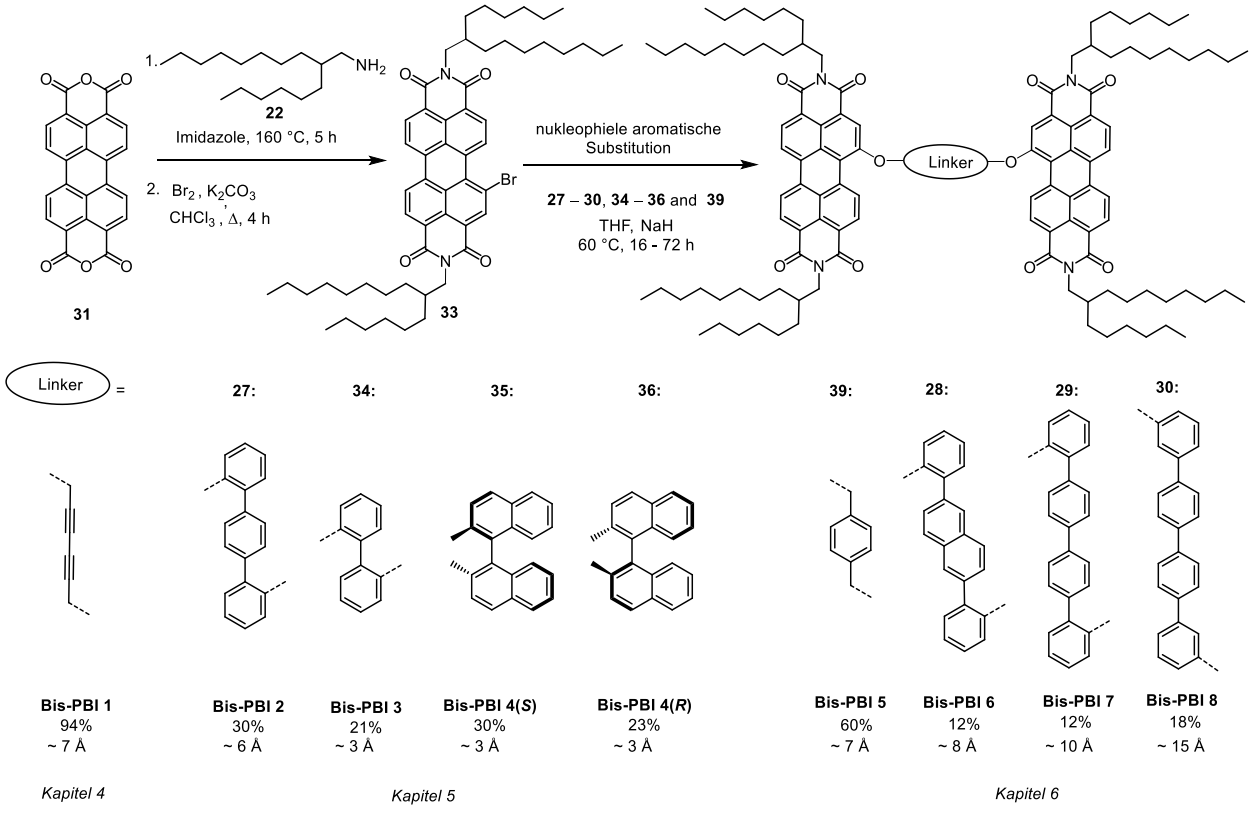

Schema 9. Synthese der kovalent verknüpften Farbstoffe **Bis-PBI 1-8**.

Durch den Einsatz von UV/Vis-, Fluoreszenz- und NMR-Spektroskopie kann ein eingehender Vergleich der molekularen und optischen Eigenschaften der Farbstoffe **Bis-PBI 1-8** in Lösung sowohl im monomeren als auch im aggregierten Zustand durchgeführt werden. So konnte gezeigt werden, dass Linker-Einheiten, welche zwei PBI-Chromophore mit einem interplanaren

Abstand von r < 7 Å vororganisieren, zu einer *intra*molekularen Faltung der Bis-PBI-Farbstoffe führen (**Bis-PBIs 2-4**), wohingegen Linker-Einheiten mit einer Länge zwischen 7 - 11 Å eine *inter*molekulare Selbstorganisation (**Bis-PBIs 1** und **5-7**) der jeweiligen Bis-PBI-Farbstoffe begünstigen. Gewährleistet die verwendete Linker-Einheit einen interplanaren Abstand r > 14 Å zwischen den beiden PBI-Einheiten, so kommt es zur Erzeugung größerer, oligomerer PBI-Farbstoff-Stapel (**Bis-PBI 8**).

Im ersten Teil dieser Arbeit (*Kapitel 4*) wurde die Exzitonen-Kopplung in einem hochdefinierten PBI-Viererstapel untersucht. Zu diesem Zweck wurde **Bis-PBI 1** synthetisiert, dessen PBI-Chromophore kovalent durch einen Diacetylen-Linker in der Bucht-Position verknüpft wurden. Dieser stellt einen Abstand von ca. 7 Å zwischen den π-Flächen der Farbstoffe sicher, von dem bekannt ist, dass er die Interkalation eines zusätzlichen Chromophores ermöglicht. Das Aggregationsverhalten von **Bis-PBI 1** wurde anschließend mittels konzentrationsabhängiger UV/Vis-Spektroskopie in THF und Toluol (Abb. 74a) ermittelt.

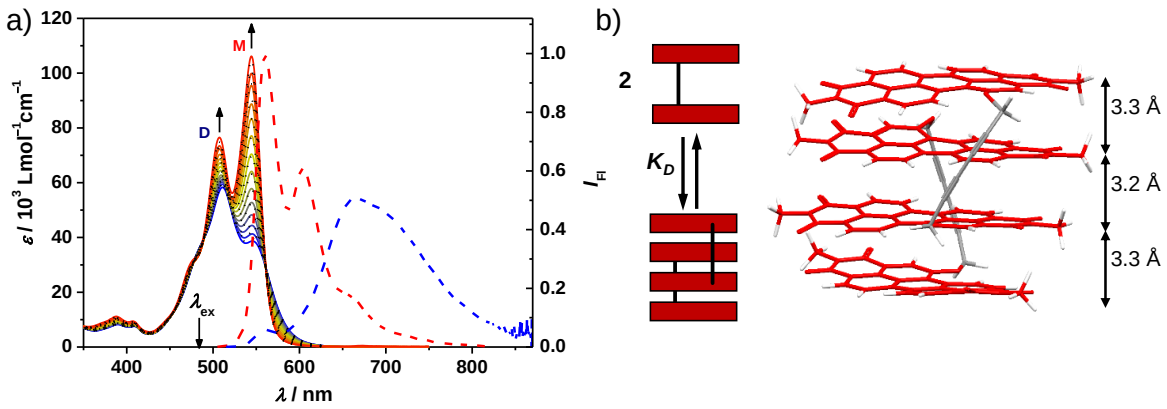

Abbildung 74. a) Konzentrationsabhängige UV/Vis-Absorptionsspektren (farbige Linien) von **Bis-PBI 1** (c_0 = 3.51 x 10^{-4} M – 3.75 x 10^{-7} M) in Toluol bei 298 K. Dargestellt sind auch die berechneten Spektren, die durch eine globale Anpassung der Daten an das Monomer-Dimer-Model (schwarze gestrichelte Linien) erhalten wurden. Pfeile zeigen die Intensitätsveränderungen der 0–0 und 0–1 Banden mit abnehmender Konzentration an. Des Weiteren sind die Fluoreszenzspektren der **Bis-PBI 1** Monomere in $CHCl_3$ (rote gestrichelte Linie, c_0 = 10^{-7} M) und Dimere in Toluol (blaue gestrichelte Linie, c_0 = 10^{-3} M) bei 298 K dargestellt. b) Schematische Darstellung der Selbstorganisation von **Bis-PBI 1** zu hoch-definierten PBI-Viererstapeln mittels Dimerisierung. Außerdem dargestellt ist die geometrieoptimierte Struktur (B97D3/def2-SVP) eines **Bis-PBI 1** Viererstapels.

Hierbei konnte durch Erhöhung der Konzentration eine signifikante spektrale Veränderung der Absorptionsbanden von **Bis-PBI 1** beobachtet werden. Die so erhaltenen Daten konnten

erfolgreich an das Monomer-Dimer-Modell angepasst werden, was auch bei einer globalen Datenanalyse über den gesamten spektralen Bereich gelang. Dies lieferte den ersten Beweis für die intermolekulare Dimerisierung von **Bis-PBI 1** und damit zur Ausbildung hoch-definierter PBI-Viererstapel nach erfolgter Aggregation, was mittels 2D-DOSY-NMR-Spektroskopie, ESI-Massenspektrometrie und AFM-Messungen weiter bestätigt werden konnte. Die experimentellen Beobachtungen wurden anschließend auch durch DFT-Rechnungen (Abb. 74b) weiter untermauert. In Zusammenarbeit mit der Gruppe von Dongho Kim konnten weiterhin mittels Femtosekunden-Breitband-Fluoreszenz-Aufkonversions-Spek-troskopie (FLUPS) erstmals Einblicke in die Exzitonendynamik innerhalb eines hoch definierten synthetischen Farbstoffaggregats jenseits von Dimeren gewonnen werden (Abb. 74c). Durch die detaillierte Analyse der vibronischen Linienform der frühen transienten Fluoreszenz-spektren konnte gezeigt werden, dass das anfänglich gebildete Frenkel-Exciton nach erfolgter Anregung vollständig entlang des gesamten Viererstaples delokalisiert ist. Der eindeutige Nachweis des initialen, vollständig delokalisierten Frenkel-Exziton-Zustandes und seiner Lokalisation, stellen wichtige Ergebnisse dieser Studie dar.

Der zweite Teil dieser Arbeit (*Kapitel 5)* befasste sich mit der Einführung von vier hoch-definierten Bis-PBI-Folda-Dimeren **Bis-PBI 2-4**, für deren Synthese Linker-Einheiten unterschiedlicher Länge (r < 7 Å) und Flexibilität verwendet wurden. So konnte jeweils eine leicht variierende Anordnung der PBI-Chromophore im gefalteten Zustand generiert werden. Durch die Strukturaufklärung auf Basis von eingehenden UV/Vis-, CD-, Fluoreszenz- und 1D- und 2D-NMR-Studien konnte für alle Farbstoffe **Bis-PBIs 2-4** die Faltung zu diskreten π-Stapeln in 1,1,2,2-Tetrachlorethan gezeigt werden (Abb. 75). Die aus DFT-Berechnungen gewonnenen geometrieoptimierten Strukturen lassen nur geringfügig unterschiedliche Anordnungen der PBI-Farnstoffe erkennen, welche durch die verschiedenen Linker-Einheiten verursacht werden. Dabei war es sehr bemerkenswert, dass die jeweiligen Chromophorstapel dennoch sehr unterschiedliche optische Eigenschaften aufweisen, was durch UV/Vis-Absorptions- und Fluoreszenzspektroskopie gezeigt werden konnte. Die unterschiedlichen Absorptionseigenschaften können auf das Zusammenspiel zwischen lang- (J_{Coul}) und kurzreichweitiger (J_{CT}) Exzitonen-Kopplung zurückgeführt werden, was zu völlig unerwarteten optischen Signaturen führt. Theoretische Untersuchungen zeigen, dass letztere aus dem HOMO-HOMO- und LUMO-LUMO-Überlapp der Chromophore resultiert, welche sehr empfindlich auf strukturelle Veränderungen der Farbstoffaggregate reagieren. Kleine Änderungen der Geometrie haben daher erheblichen Einfluss auf die optischen Eigenschaften der π-Stapel. Durch die resultierenden optischen Signaturen der Folda-Dimere **Bis-PBIs 2-4**,

welche vom konventionellen Hj-Aggregat bis hin zu monomerenähnlichen Absorptionsmerkmalen reichen, konnte erstmals der experimentelle Nachweis eines PBI-basierten "Null-Aggregats" erbracht werden, bei dem sich J_{Coul} und J_{CT} vollständig gegenseitig kompensieren (Abb. 75). Die Erkenntnisse dieses Kapitels verdeutlichen daher den erheblichen Einfluss der sogenannte kurzreichweitigen Exzitonen-Kopplung J_{CT} auf die optischen Eigenschaften von PBI-Aggregaten.

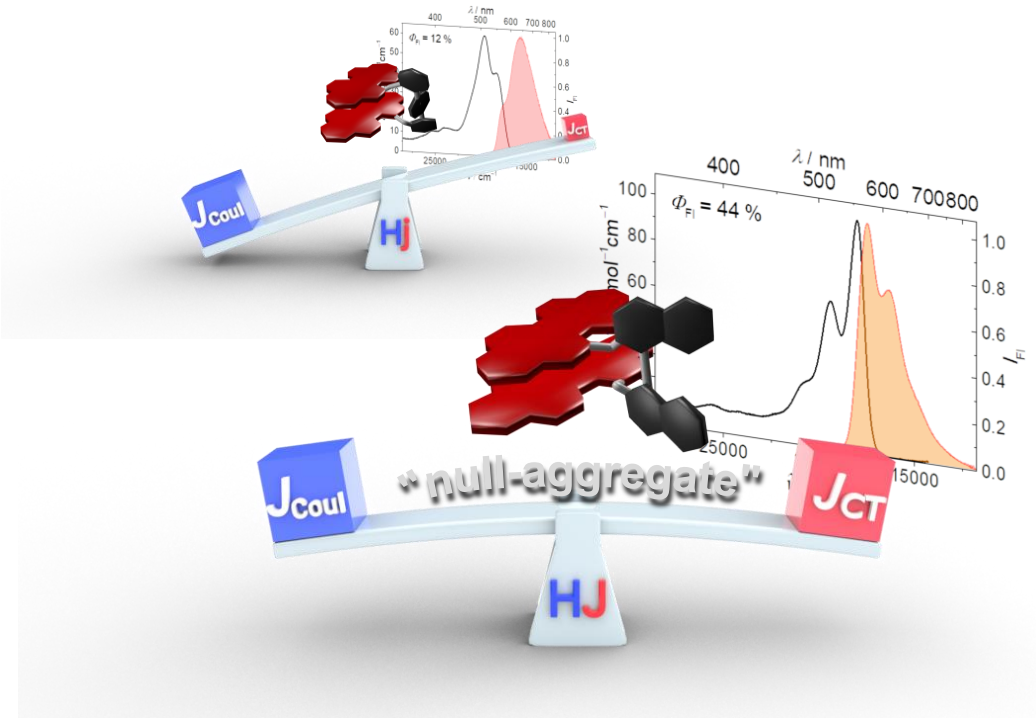

Abbildung 75. Grafische Darstellung des Zusammenspiels von lang- (J_{Coul}) und kurzreichweitigen (J_{CT}) Exzitonen-Kopplung, welches je nach Stärke zur Ausbildung konventioneller H-Aggregatee (Hj, hinten, **Bis-PBI 2**) oder sogenannter „Null-Aggregate“ (HJ, vorne, **Bis-PBI 4**) führt. Außerdem gezeigt sind die Absorptions- und Fluoreszenzspektren von **Bis-PBI 2** und **4**.

Im letzten Teil dieser Arbeit (*Kapitel 6*) wurden die Selbstorganisationsprozesse in klar definierten supramolekularen Aggregatstrukturen untersucht. Durch die systematische Verlängerung der Linker-Einheiten von 7 auf 15 Å, konnten durch Selbstorganisation unterschiedliche Aggregatstrukturen von hochdefinierten PBI-Viererstapeln bis hin zu längeren PBI-Oligomeren generiert werden. Dabei ist die endgültige Aggregatstruktur im Wesentlichen von der Art der eingesetzten Linker-Einheit abhängig, welche zur Verknüpfung der beiden PBI-Chromophore in der Bucht-Position verwendet wird. Durch den Einsatz UV/Vis-spektroskopischer Methoden konnten für die Farbstoffe **Bis-PBI 5-8** ausgeprägte spektrale Veränderungen in Toluol bei steigender Konzentration beobachtet werden. Dabei konnten die konzentrationsabhängigen Absorptionsdaten von **Bis-PBI 5-7** erfolgreich an das Monomer-

Dimer-Model angepasst werden, was auf die ausschließliche Ausbildung hochdefinierter PBI Vierer-Stapel in Lösung hinweist. Dies konnte durch 2D-DOSY-NMR-Spektroskopie, ESI-Massenspektrometrie, AFM-Messungen sowie durch DFT-Rechnungen weiter bestätigt werden.

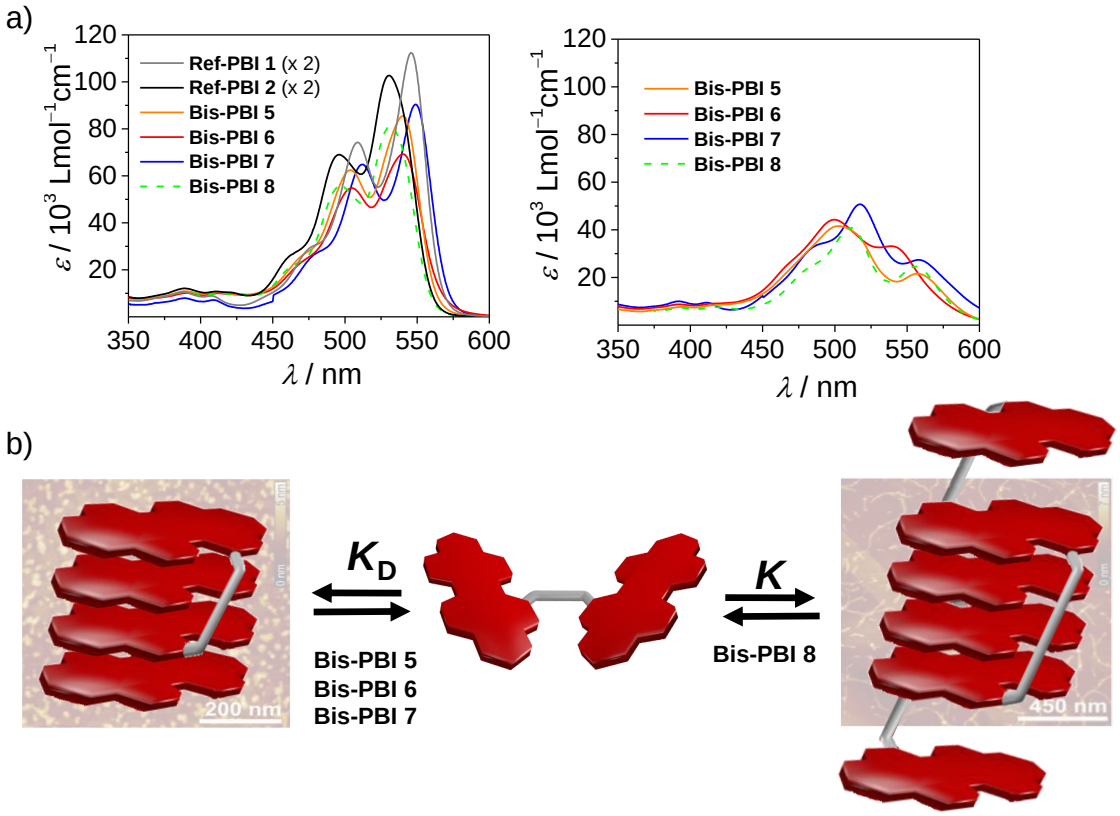

Abbildung 76. a) Vergleich der spektralen Formen und relativen Position der Absorptionsspektren von **Bis-PBIs 5-8** im monomeren und aggregierten Zustand in Toluol bei Raumtemperatur. Die Spektren wurden dabei durch jeweilige globale Fit-Analyse des Monomer-Dimer- bzw. isodesmischen Modells bestimmt. b) Schematische Abbildung der möglichen Selbstassemblierungsprozesse der Bucht-verknüpften Perylenebisimid-Farbstoffe **Bis-PBI 5-8** zu bimolekularen Stapeln aus vier PBI Einheiten oder supramolekularen Polymeren.

Im Gegensatz dazu konnten die konzentrationsabhängigen Absorptionsdaten für **Bis-PBI 8** erfolgreich an das isodesmische Modell angepasst werden, was auf die Bildung größerer, oligomerer π-Stapel hinweist. Diese Beobachtungen konnten durch 2D-DOSY-NMR-Spektroskopie, ESI-Massenspektrometrie und AFM-Messungen weiter untermauert werden, bei denen lange, faserartige Aggregate mit einer Länge von bis zu 500 nm beobachtet werden konnten. Hierdurch konnten die Absorptionsspektren von **Bis-PBIs 5-8** sowohl im monomeren als auch im aggregierten Zustand (Abb. 76a) gedeutet und ein Zusammenhang zwischen den optischen Eigenschaften und den jeweiligen Verbindungseinheiten aufgezeigt werden. So führt

der Einsatz einer rigideren Linker-Einheit (*ortho*-Substitution), welche die Chromophore mit einem Abstand von etwa 8 Å vororganisiert, zur Bildung klar definierter PBI-Viererstapel, wohingegen eine flexiblerere Linker-Einheit (*meta*-Substitution) mit einem interplanaren Abstand von ca. 15 Å zur Bildung größerer, oligomerer π-Stapel führt (Abb. 76b).

Zusammenfassend wurde in dieser Arbeit eine detaillierte Übersicht des Selbstorganisationsverhaltens von neun kovalent verknüpften Bis-PBI-Farbstoffen vorgestellt, welche anschließend hinsichtlich ihrer Struktur-Eigenschafts-Beziehung untersucht wurden. Die Ergebnisse bestätigen eine starke Excitonen-Kopplung in verschiedenen Bis-PBI-Aggregaten wie z.B. PBI-Folda-Dimeren oder hochdefinierten PBI-Viererstapeln, welche die optischen Eigenschaften der Farbstoffsysteme im aggregierten Zustand signifikant beeinflusst. Die aus den Untersuchungen der synthetisch hergestellten Farbstoffaggregate gewonnen Erkenntnisse sind von hoher Relevanz für den Vergleich mit natürlichen Lichtsammelsystemen der Photosynthese sowie für die Gestaltung photonischer Materialien. Dabei dienen die einzigartigen Eigenschaften der in der Natur vorkommenden Systeme als Vorbild, um synthetische Materialien herzustellen, welche ähnlich effektiv für die Gewinnung von Energie durch Sonnenlicht genutzt werden sollen.

Chapter 9

–

Experimental Section

9.1 Materials and Methods

General: All reagents and solvents were used without further purification after recievement from commercial sources. If needed they were dried *via* literature known procedures.[194] Column chromatography was performed using Silica 60M with a particle size of 0.04–0.063 mm. ^{1}H and ^{13}C NMR spectra were recorded on Avance DMX 600 and 400 spectrometers. Chemical shifts δ are given in ppm and *J* values in Hz. For all multiplicities the following abbreviations were used: s = singlet, d = doublet, t = triplet, sept = septet, m = multiplet.

Gel Permeation Chromatography: Final purification of the target compounds was achieved by recycling gel permeation chromatography (Shimadzu, LC-20AD pump, SPD-MA20A detector) using ethanol stabilized chloroform as solvents and three columns with a flow rate of 3.5 mL /min.

Mass Spectrometry: High-resolution ESI-TOF mass spectrometry was performed with a micrOTOF Focus spectrometer (Bruker Daltronics). MALDI-TOF-experiments were performed with a autoflex II (Bruker Daltonik GmbH) with *trans*-2-[3-(*tert*-Butylphenyl)-2-methyl-2-propenyliden]malono-nitril (DCTB) as matrix.

Melting Points: Melting points were detected on an optical microscope (Olympus BX41) and are uncorrected.

Optical UV/Vis Absorption: All spectroscopic measurements were performed on a JASCO 770V spectrometer with a spectral bandwith of 1 nm and a scan rate of 400 nm min^{-1} using conventional quartz cell cuvettes (from 0.01 cm to 10 cm) and spectroscopic grade solvents (Uvasol). Temperature-dependent UV/Vis absorption spectra are density-corrected.

Steady-State Fluorescence Spectroscopy: For emission measurements an Edinburgh Instruments FLS980 spectrometer was used, equipped with a double monochromator for emission and excitation. A right-angle geometry mode or a front face setup was used depending on the concentration and optical density of the samples while applying a magic angle setup. The fluorescence quantum yields were calculated by the optical dilute method (A < 0.05) using *N*,*N*-Bis(2,6-diisopropylphenyl)-1,6,7,12-tetraphenoxyperylene-3,4:9,10-tetracarboxylicacid-bisimide (Φ_{fl} = 96% in chloroform)[195] or *N*,*N*-Bis(2,6-diisopropylphenyl)-3,4:9,10-tetracarboxylicacidbisimide (Φ_{fl} = 100% in chloroform)[196] as standards. Time-resolved measurements were performed with a ps laser diode at 505 nm and a TCSPC detection unit.

Femtosecond Broadband Fluorescence Upconversion Spectroscopy (FLUPS): A Femtosecond broadband fluorescence up-conversion apparatus[112, 197-200] was used for obtaining the transient fluorescence spectra at Yonsei University in Seoul. For details see ref.[113]

Femtosecond Transient Absorption Spectroscopy: The femtosecond time-resolved transient absorption (fs-TA) spectrometer utilized at Yonsei University in Seoul consists of an optical parametric amplifier (OPA; Palitra, Quantronix) pumped by a Ti:sapphire regenerative amplifier system (Integra-C, Quantronix) operating at 1 kHz repetition rate and an optical detection system. For details see ref.[113]

DFT Calculations: DFT calculations were obtained by using the Gaussian09 program[187] with the def2-SVP basis set[168] and B97D3[169] as functional.

Atomic Force Microscopy (AFM): AFM experiments were performed on a Bruker AXS MultiMode 8 instrument using Silicon cantilevers (Olympus) with a spring constant of 40 N m^{-1} and a resonance frequency of ~300 kHz.

9.2 Synthesis

9.2.1 Synthesis of Intermediates

General procedure for the synthesis of the methoxy-protected linker units 23- 26[97]

A degassed aqueous sodium carbonate solution was added to a degassed solution of the respective commercial available boronic acid (2.1 eq.), the respective dihalogen compound (1 eq.) and Pd-catalysator $Pd(PPh_3)_4$ (0.2 eq.) in DMF under nitrogen atmosphere. The reaction mixture was refluxed for 16 h at 95 °C. After cooling to room temperature the reaction mixture was extracted with DCM (5 x 10 mL). The combined organic phases were washed with water (3 x 30 mL) and dried over $MgSO_4$. The crude product was dried under vacuum overnight and purified by column chromatography on silica gel (DCM/pentane 1:2).

2,2´-Dimethoxyterphenyl (23)[97]

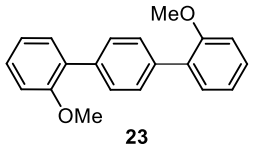

23

Compound **23** was synthesized according to the above general procedure using 200 mg (132 μmol) 2-methoxyphenylboronacid, 204 mg (620 μmol) diiodobenzol, 14.0 mg (120 μmol) $Pd(PPh_3)_4$ and 3.10 mL (660 mg, 6.10 mmol) aqueous sodium carbonate solution to give compound **23** (155 mg, 530 μmol, 86%) as a white solid. Mp.: 97 – 99 °C. ^{1}H NMR (400 MHz, $CDCl_3$): δ = 7.58 (s, 4 H, *ph-H*), 7.40–7.37 (m, 2 H, *ph-H*), 7.35–7.31 (m, 2 H, *ph-H*), 7.06–6.99 (m, 4 H, *ph-H*), 3.84 (s, 6 H, C*H*$_3$) ppm.

2,2´-Dimethoxynaphthyldiphenyl (24)

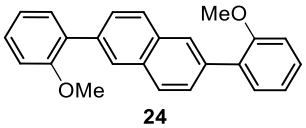

24

Compound **24** was synthesized according to the above general procedure using 200 mg (1.32 mmol) 2-methoxyphenylboronacid, 177 mg (620 μmol) 2,6-dibromonaphthaline, 14.0 mg (120 μmol) $Pd(PPh_3)_4$ and 3.10 mL (660 mg, 6.10 mmol) aqueous sodium carbonate solution to give compound **24** (95 mg, 260 μmol, 84%) as a white solid. Mp.: 193 – 195 °C. ^{1}H NMR (400 MHz, $CDCl_3$): δ = 7.97–7.96 (m, 2 H, *ph-H*), 7.88 (d, *J* = 8.4 Hz, 2 H, *ph-H*),

7.70–7.67 (m, 2 H, *ph-H*), 7.45–7.43 (m, 2 H, *ph-H*), 7.38–7.34 (m, 2 H, *ph-H*), 7.10–7.02 (m, 4 H, *ph-H*), 3.83 (s, 6 H, C*H*$_3$) ppm. ^{13}C NMR (101 MHz, $CDCl_3$): δ = 156.7, 136.1, 132.4, 131.0, 130.8, 128.7, 128.1, 127.8, 127.4, 120.9, 111.4, 55.6 ppm. HRMS (ESI, pos. Mode, acetonitrile/chloroform): *m/*z 358.1802 $[M+NH_4]^+$, calcd. for $C_{24}H_{24}NO_2$: 358.18016.

2,2´-Dimethoxytetraphenyl (25)[201]

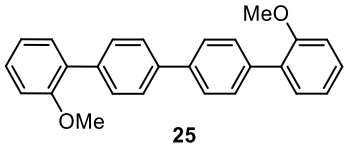

25

Compound **25** was synthesized according to the above general procedure using 100 mg (66.0 μmol) 2-methoxyphenylboronacid, 120 mg (310 μmol) 4,4´-diiodobiphenyl, 7.20 mg (60 μmol) $Pd(PPh_3)_4$ and 1.55 mL (330 mg, 3.10 mmol) aqueous sodium carbonate solution to give compound **25** (95 mg, 260 μmol, 84%) as a white solid. Mp.: 127 – 129 °C. ^{1}H NMR (400 MHz, $CDCl_3$): δ = 7.68–7.62 (m, 8 H, *ph-H*), 7.40-7.32 (m, 4 H, *ph-H*), 7.08–7.00 (m, 4 H, *ph-H*), 3.86 (s, 6 H, C*H*$_3$) ppm.

3,3´-Dimethoxytetraphenyl (26)[202]

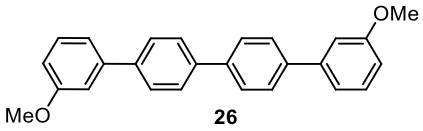

26

Compound **26** was synthesized according to the above general procedure using 500 mg (3.30 mmol) 3-methoxyphenylboronacid, 600 mg (1.55 mmol) 4,4´-diiodobiphenyl, 36.0 mg (300 μmol) $Pd(PPh_3)_4$ and 7.75 ml (1.65 g, 15.5 mmol) aqueous sodium carbonate solution to give compound **26** (424 mg, 1.16 mmol, 75%) as a white solid. Mp.: 133 – 135 °C. ^{1}H NMR (400 MHz, $CDCl_3$): δ = 7.74–7.68 (m, 8 H, *ph-H*), 7.39 (t, *J* = 7.9 Hz, 2 H), 7.26–7.23 (m, 2 H, *ph-H*), 7.19–7.18 (m, 2 H, *ph-H*), 6.94–6.91 (m, 2 H, *ph-H*), 3.89 (s, 6 H, C*H*$_3$) ppm.

General procedure for the synthesis of the linker units 27 - 30[97]

Borontribromid in dry DCM was added slowly to a solution of the respective methoxy-protected compounds **23** – **26** in dry DCM (10 mL) at 0 °C. The reaction mixture was stirred for 1 h at 0 °C and for additional 6 h at rt. After the reaction was quenched with 200 mL water the reaction mixture was extracted with DCM (5 x 10 mL). The combined organic phases were washed with water (3 x 30 mL) and brine (3 x 30 mL) and dried over $MgSO_4$. The crude product was used without further purification.

2,2´-Dihydroxyterphenyl (27)[97]

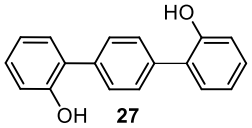

27

Linker unit **27** was synthesized according to the above general procedure using 100 mg (350 μmol) of compound **23** and 80.0 μL (220 mg, 860 μmol) borontribromid to give linker unit **27** (90.8 mg, 350 μmol, 99%) as a white solid. Mp.: 149 – 151 °C. ^{1}H NMR (400 MHz, $CDCl_3$): δ = 7.62 (s, 4 H, *ph-H*) 7.32–7.27 (m, 4 H, *ph-H*), 7.05–6.99 (m, 4 H, *ph-H*), 5.18 (s, 2 H, O*H*) ppm.

2,2´-Dihydroxynaphthyldiphenyl (28)

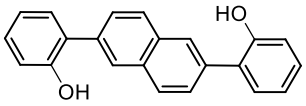

28

Linker unit **28** was synthesized according to the above general procedure using 100 mg (300 μmol) of compound **24** and 140 μL (370 mg, 1.46 mmol) borontribromid to give linker unit **28** (97.0 mg, 310 μmol, 97%) as a white solid. Mp.: 173 – 174 °C. ^{1}H NMR (400 MHz, $CDCl_3$): δ = 8.02-8.00 (m, 4 H, *ph-H*), 7.68–7.65 (m, 2 H, *ph-H*), 7.39–7.30 (m, 4 H, *ph-H*), 7.09–7.04 (m, 4 H, *ph-H*), 5.31 (s, 2 H, O*H*) ppm. ^{13}C NMR (101 MHz, $CDCl_3$): 152.5, 135.1, 132.8, 130.4, 129.3, 129.1, 127.9, 127.8, 127.7, 121.0, 115.9 ppm. HRMS (ESI, neg. Mode, acetonitrile/chloroform): *m/*z 311.1078 $[M-H]^-$, calcd. for $C_{22}H_{15}O_2$: 311.10775.

2,2´-Dihydroxytetraphenyl (29)[203]

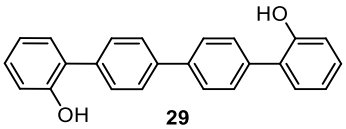

29

Linker unit **29** was synthesized according to the above general procedure using 180 mg (490 μmol) of compound **25** and 230 μL (620 mg, 2.46 mmol) borontribromid to give linker unit **29** (173 mg, 510 μmol, 99%) as a white solid. Mp.: 152 – 155 °C. ^{1}H NMR (400 MHz, $CDCl_3$): δ = 7.78–7.76 (m, 4 H, *ph-H*), 7.61–7.59 (m, 4 H, *ph-H*), 7.33–7.27 (m, 4 H, *ph-H*), 7.05–7.00 (m, 4 H, *ph-H*), 5.21 (s, 2 H, O*H*) ppm.

3,3´-Dihydroxytetraphenyl (30)

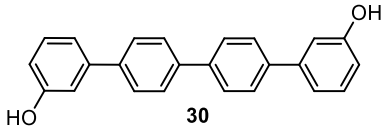

30

Linker unit **30** was synthesized according to the above general procedure using 400 mg (1.09 mmol) of compound **26** and 1.03 mL (2.74 g, 10.9 mmol) borontribromid to give linker unit **30** (365 mg, 1.08 mmol, 99%) as a white solid. Mp.: 112 – 114 °C. ^{1}H NMR (400 MHz, THF-d_8): δ = 8.33 (s, 2 H, O*H*), 7.75–7.67 (m, 8 H, *ph-H*), 7.22 (t, *J* = 7.8 Hz, 2 H, *ph-H*), 7.12–7.06 (m, 4 H, *ph-H*), 6.74–6.72 (m, 2 H, *ph*-H) ppm. ^{13}C-NMR (101 MHz, $CDCl_3$): 159.0, 142.7, 141.0, 140.1, 130.2, 127.9, 127.6, 118.4, 114.9, 114.3 ppm. HRMS (ESI, neg. Mode, acetonitrile/chloroform): *m/*z 337.1231 $[M-H]^-$, calcd. for $C_{24}H_{17}O_2$: 337.1234.

9.2.2 Synthesis of Perylene Bisimide Dyes

***N,N´*-Bis(hexyldecyl)-1-bromperylen-3,4:9,10-tetracarbonsäurebisimid (33)**[99]

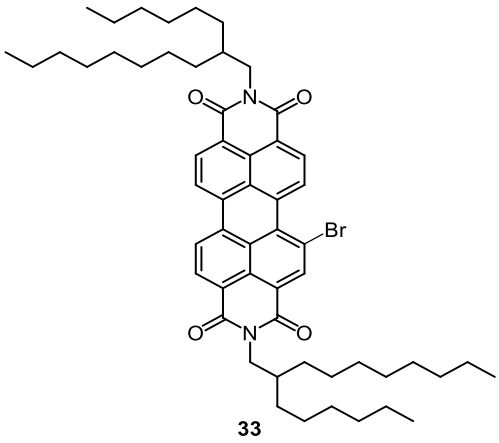

33

PBI dye **32** (1.00 g, 1.46 mmol) was dissolved in chloroform (20 mL) followed by the addition of potassium carbonate (570 mg, 4.55 mmol). The suspension was heated to 60 °C and 3.00 mL (9.63, 60.3 mmol) bromine were added quickly under stirring. The reaction mixture was refluxed for 4 h. After cooling down to room temperature, an aqueous solution of sodium sulfite (300 mL) was added and the mixture was extracted with DCM (5 x 10 mL). The combined organic phases were washed with water (3 x 30 mL) and dried over $MgSO_4$. The crude product was dried under vacuum overnight and purified by column chromatography on silica gel (DCM/hexane 5:1) to give the desired product **33** (704 mg, 770 µmol, 65%) as a red solid. Mp. 173 – 175 °C. ^{1}H NMR (400 MHz, $CDCl_3$): δ = 9.79 (d, *J* = 8.3 Hz, 1 H, perylene-*H*), 8.93 (s,

1 H, perylene-*H*), 8.72–8.69 (m, 3 H, perylene-*H*), 8.62–8.59 (m, 2 H, perylene-*H*), 4.16–4.12 (m, 4 H, CH_2), 2.00–2.01 (m, 2 H, C*H*), 1.33–1.25 (m, 48 H, CH_2), 0.86–0.82 (m, 12 H, CH_3) ppm. ^{13}C NMR (101 MHz, $CDCl_3$): 163.7, 163.4, 163.3, 162.5, 139.1, 133.8, 133.44, 133.42, 133.40, 131.0, 130.9, 130.5, 128.7, 128.6, 128.0, 127.8, 126.9, 123.7, 123.5, 123.3, 123.0, 122.9, 122.6, 120.9, 44.8, 44.7, 36.65, 36.61, 31.88, 31.85, 31.70, 31.67, 30.05, 30.03, 29.75, 29.72, 29.6, 29.3, 26.5, 22.7, 14.11, 14.10 ppm. HRMS (ESI, pos. mode, acetonitrile/chloroform): *m/*z 917.4780 $[M+H]^+$, calcd. for $C_{56}H_{74}BrN_2O_4^+$: 917.4826.

Ref-PBI 1

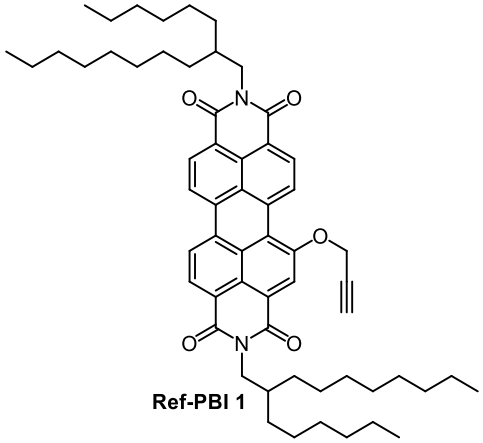

Propargylic alcohol (94.0 μL, 1.64 mmol, 91.5 mg) was added to a suspension of *N*,*N*´-bis(2-*n*-hexyldecyl)-1-bromoperylene-3,4:9,10-tetraccarboxylicacidbisimide **33** (50.0 mg, 54.0 μmol) and sodium hydride (7.00 mg, 1.44 mmol) in dry THF (5 mL) under stirring. The reaction mixture was stirred for one hour at 60 °C. After cooling down to room temperature, the reaction was quenched by the addition of water (10 mL) and the mixture was extracted with DCM (5 x 10 mL). The combined organic phases were washed with water (3 x 30 mL) and dried over Na_2SO_4. The crude product was dried under vacuum overnight and purified by column chromatography on silica gel (DCM/hexane 2:1) to give **Ref-PBI 1** (45.0 mg, 50.4 μmol, 92%) as a purple solid. Mp. 168 – 170 °C. ^{1}H NMR (400 MHz, $CDCl_3$, 295K): δ = 9.57 (d, *J* = 8.4 Hz, 1 H, perylene-*H*), 8.69–8.57 (m, 6 H, perylene-*H*), 5.23 (d, *J* = 2.4 Hz, 2 H, CH_2), 4.15 (d, *J* = 7.4 Hz, 4 H, CH_2), 2.05–1.98 (m, 2 H, C*H*), 1.40–1.22 (m, 48 H, CH_2), 0.85–0.82 (m, 12 H, CH_3) ppm. ^{13}C NMR (101 MHz, $CDCl_3$, 295K): 163.7, 163.51, 163.50, 163.1, 155.9, 133.9, 133.62, 133.60, 133.3, 131.6, 130.2, 129.0, 128.8, 128.6, 128.5, 128.0, 126.4, 124.3, 123.7, 123.2, 122.7, 121.8, 121.7, 121.1, 118.3, 57.4, 56.1, 44.8, 44.6, 36.7, 36.6, 31.9, 31.8, 31.72, 31.69, 30.1, 29.8, 29.6, 29.3, 26.49, 26.46, 22.6, 14.1 ppm. HRMS (ESI, pos. Mode, acetonitrile/chloroform): *m/*z 893.58195 $[M+H]^+$, calcd. for $C_{59}H_{77}N_2O_5^+$: 893.58270.

Bis-PBI 1

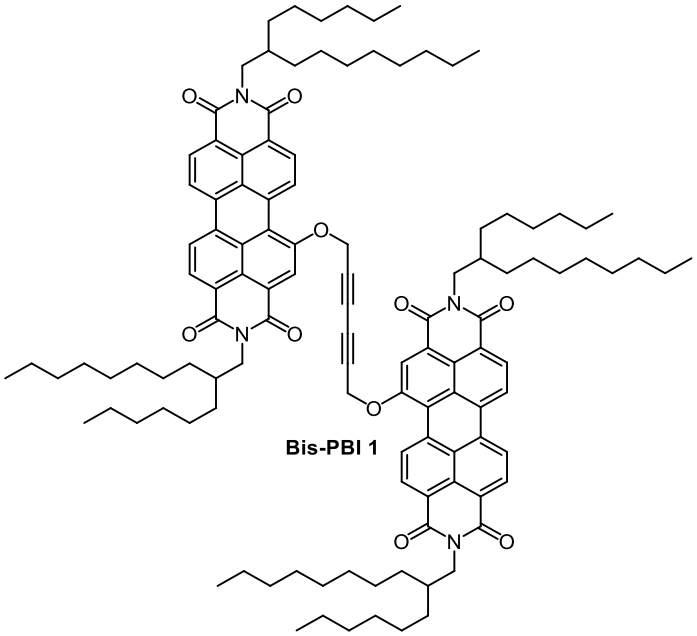

A degassed solvent mixture of THF/NEt_3 (*v*:*v* = 1:1, 12 mL) was added under argon atmosphere to a Schlenk flask containing **Ref-PBI 1** (130 mg, 143 μmol), 1,4 benzoquinone (13.0 mg, 14.0 μmol), $PdCl_2(PPh_3)_2$ (8.00 mg, 6.00 μmol) and copper(I) iodide (1.20 mg, 6.00 μmol). After stirring the reaction mixture for 60 min at 30 °C, it was extracted with DCM (5 x 10 mL). The combined organic phases were washed with 6 N hydrochloride acid (1 x 20 mL) and an aqueous solution of sodium hydrogen carbonate (2 x 30 mL) and dried over Na_2SO_4. The crude product was dried under vacuum overnight and purified by column chromatography on silica gel (DCM) to give **Bis-PBI 1** (120 mg, 67.3 μmol, 94%) as a purple solid. Mp: 220 – 222 °C. ^{1}H NMR (600 MHz, $C_2D_2Cl_4$, 340 K): δ = 9.12 (d, *J* = 8.2 Hz, 2 H, perylene-*H*), 8.30 (s, 2 H, perylene-*H*), 8.29–8.26 (m, 4 H, perylene-*H*), 8.16 (d, *J* = 7.7 Hz, 2 H, perylene-*H*), 8.06 (d, *J* = 7.5 Hz, 2 H, perylene-*H*), 8.02 (d, *J* = 7.4 Hz, 2 H, perylene-*H*), 5.33 (s, 4 H, CH_2), 4.02 (d, *J* = 6.5 Hz, 8 H, CH_2), 1.99 (sept, *J* = 6.5 Hz, 4 H, C*H*), 1.36–1.26 (m, 96 H, CH_2), 0.89–0.87 (m, 24 H, CH_3) ppm. ^{13}C NMR (151 MHz, $C_2D_2Cl_4$, 340 K): 163.2, 162.9, 162.8, 162.7, 155.1, 133.3, 133.1, 132.9, 131.1, 129.9, 128.6, 128.5, 128.2, 127.7, 125.9, 124.2, 123.7, 122.8, 122.44, 122.41, 121.6, 121.4, 121.2, 120.2, 118.0, 99.5, 57.4, 44.8, 44.6, 36.6, 31.7, 31.65, 31.63, 29.95, 29.93, 29.59, 29.57, 29.4, 29.1, 26.33, 26.31, 26.30, 22.4, 13.9 ppm. UV/Vis ($CHCl_3$, nm): λ_{max} (ε_{max} M^{-1} cm^{-1}) = 545 (93200), 509 (73300). HRMS (ESI, pos. mode, acetonitrile/chloroform) *m/z*: 1806.12354 [*M*+H]$^+$, calcd. for $C_{118}H_{150}N_4NaO_{10}^+$, 1806.12442.

General procedure for the synthesis of target compounds Ref-PBI 2 and Bis-PBIs 2-8

To a suspension of 2.1 equivalents of *N*,*N*´-Bis(hexyldecyl)-1-bromperylene-3,4:9,10-tetraccarboxylicbisimid **33** and 3.0 equivalents of sodium hydride in dry THF, 1.0 equivalent of the corresponding spacer unit **27 - 30** and **34 - 39** was added under stirring. The reaction mixture was stirred at 60 °C for 16 – 72 h. After cooling to room temperature the reaction mixture was quenched with 50 mL of water. The resulting solution was extracted with DCM (5 x 10 ml). The combined organic phases were washed with water (3 x 30 mL) and dried over $MgSO_4$. The crude product was dried under vacuum overnight and purified by column chromatography on silica gel (DCM/pentane 2:1). The final purification was achieved *via* GPC (chloroform) to give the desired products.

Ref-PBI 2

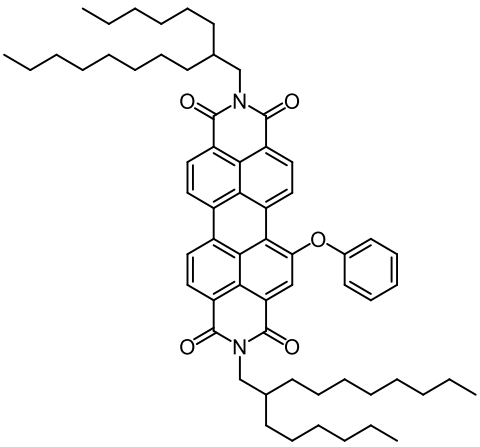

Ref-PBI 2

Ref-PBI 2 was synthesized according to the general procedure described above stirring *N*,*N*´-bis(2-*n*-hexyldecyl)-1-bromoperylene-3,4:9,10-tetraccarboxylicacidbisimide **33** (100 mg, 108 μmol), phenol **38** (102 mg, 1.08 mmol) and sodium hydride (9.0 mg, 378 μmol) at 40 °C for 18 h to give desired **Ref-PBI 2** (98 mg, 105 μmol, 97%) as a red solid. Mp. 170 – 172 °C. ^{1}H NMR (600 MHz, d_2-TCE, 390 K): δ = 9.61 (d, *J* = 8.4 Hz, 1 H, perylene-*H*), 8.77–8.68 (m, 5 H, perylene-*H*), 8.33 (s, 1 H, perylene-*H*), 7.54–7.51 (m, 2 H, *ph*-*H*), 7.36–7.34 (m, 1 H, *ph*-*H*), 7.26–7.24 (m, 2 H, *ph*-*H*), 4.18 (d, *J* = 7.3 Hz, 2 H, CH_2), 4.13 (d, *J* = 7.3 Hz, 2 H, CH_2), 2.10–1.93 (m, 2 H, C*H*), 1.40–1.27 (m, 48 H, CH_2), 0.90-0.87 (m, 12 H, CH_3) ppm. ^{13}C NMR (151 MHz, d_2-TCE, 390 K): 163.7, 163.49, 163.48, 162.9, 155.9, 154.7, 134.44, 134.40, 133.6, 131.9, 130.8, 130.5, 129.7, 129.0, 128.6, 128.4, 127.0, 125.6, 125.2, 124.5, 124.2, 123.58, 123.55, 123.11, 123.06, 122.6, 122.3, 120.2, 119.5, 44.8, 44.7, 36.5, 31.81, 31.76, 31.74, 31.65,

31.64, 31.59, 31.56, 29.84, 29.83, 29.51, 29.48, 29.31, 29.29, 29.03, 29.02, 26.39, 26.36, 26.31, 22.41, 22.39, 13.83, 13.81 ppm. UV/Vis ($CHCl_3$, nm): λ_{max} (ε_{max} M^{-1} cm^{-1}) = 532 (50700), 500 (35000). HRMS (ESI, pos. mode, acetonitrile/chloroform) *m/*z: 931.5969 [*M*+H]$^+$, calcd. for $C_{62}H_{79}N_2O_5^+$, 931.5984.

Bis-PBI 2

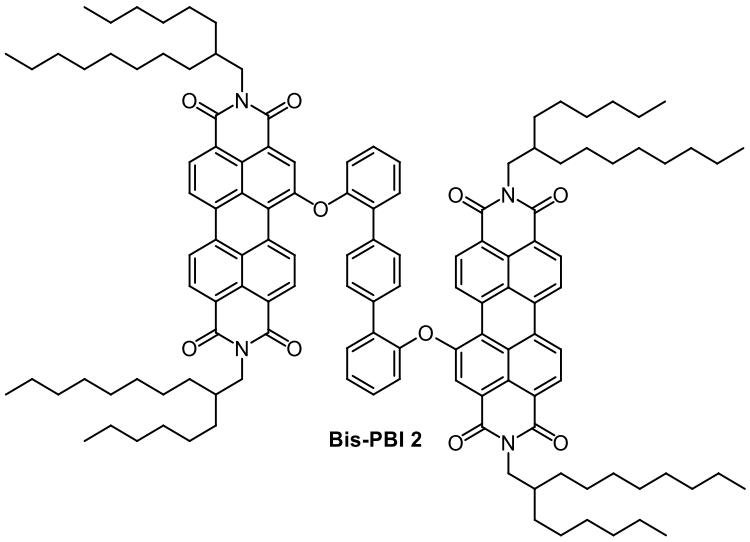

Bis-PBI 2 was synthesized according to the general procedure described above stirring *N, N´*-bis(2-*n*-hexyldecyl)-1-bromoperylene-3,4:9,10-tetraccarboxylicacidbisimide **33**, (100 mg, 108 μmol), 2,2‘-dihydroxyterphenyl **27** (13.6 mg, 51.8 μmol) and sodium hydride (3.70 mg, 155 μmol) at 60 °C for 16 h to give desired **Bis-PBI 2** (23.0 mg ,11.9 μmol, 23%) as a red solid. Mp.: > 300 °C. ^{1}H NMR (600 MHz, d_2-TCE, 390 K): δ = 8.67 (d, *J* = 7.8 Hz, 2 H, perylene-*H*), 8.40–8.37 (m, 4 H, perylene-*H*), 8.20–8.13 (m, 6 H, perylene-*H*), 7.86 (d, *J* = 8.1 Hz, 2 H, perylene-*H*), 7.76 (s, 4 H, *ph*-*H*), 7.69–7.68 (m, 2 H, *ph*-*H*), 7.41–7.37 (m, 4 H, *ph*-*H*), 6.84 (d, *J* = 7.8 Hz, 2 H, *ph*-*H*), 4.18 (d, *J* = 7.3 Hz, 4 H, CH_2), 3.97 (d, *J* = 6.9 Hz, 4 H, CH_2), 2.13–2.11 (m, 2 H, C*H*), 1.91–1.90 (m, 2 H, C*H*), 1.46–1.28 (m, 96 H, CH_2), 0.93–0.88 (m, 24 H, CH_3) ppm. ^{13}C NMR (151 MHz, d_2-TCE, 390 K): 163.0, 162.9, 162.6, 162.4, 154.8, 151.4, 137.0, 134.3, 133.4, 133.1, 132.4, 130.9, 130.4, 129.9, 129.3, 129.0, 128.8, 128.0, 127.9, 126.0, 125.2, 125.0, 124.2, 123.1, 122.7, 122.6, 122.0, 121.6, 121.3, 118.4, 45.0, 44.5, 36.7, 36.5, 32.0, 31.99, 31.9, 31.54, 31.50, 31.47, 31.44, 29.8, 29.7, 29.41, 29.35, 29.2, 29.1, 28.91, 28.87, 26.39, 26.36, 26.32, 22.22, 22.19, 13.54, 13.53, 13.50, 13.49 ppm. UV/Vis ($CHCl_3$, nm): λ_{max} (ε_{max} M^{-1} cm^{-1}) = 545 (42700), 511 (55500). HRMS (ESI, pos. mode, acetonitrile/chloroform): *m/*z 1936.20123 [*M*+H]$^+$, calcd. for $C_{130}H_{159}N_4O_{10}^+$: 1936.20507.

Bis-PBI 3

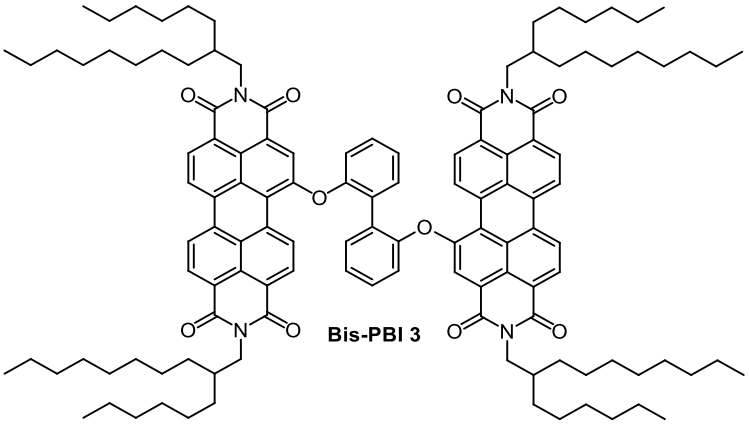

Bis-PBI 3 was synthesized according to the general procedure described above stirring *N, N´*-bis(2-*n*-hexyldecyl)-1-bromoperylene-3,4:9,10-tetraccarboxylicacidbis-imide **33**, (200 mg, 216 μmol), 2,2´-dihydroxybiphenyl **34** (19.0 mg, 103 μmol) and sodium hydride (7.00 mg, 310 μmol) at 60 °C for 16 h to give desired **Bis-PBI 3** (42.0 mg, 22.6 μmol, 21%) as a red solid. Mp.: 201 – 203 °C. ^{1}H NMR (600 MHz, d_2-TCE, 390 K): δ = 9.19 (d, *J* = 8.3 Hz, 2 H, perylene-*H*), 8.74 (d, *J* = 8.0 Hz, 2 H, perylene-*H*), 8.60 (d, *J* = 8.2 Hz, 2 H, perylene-*H*), 8.56 (d, *J* = 8.2 Hz, 2 H, perylene-*H*), 8.47 (d, *J* = 8.0 Hz, 2 H, perylene-*H*), 8.27 (d, *J* = 8.3 Hz, 2 H, perylene-*H*), 8.04 (s, 2 H, perylene-*H*), 7.85–7.83 (m, 2 H, *ph-H*), 7.55–7.48 (m, 4 H, *ph-H*), 7.15–7.14 (m, 2 H, *ph-H*), 4.16 (d, *J* = 7.2 Hz, 4 H, CH_2), 3.59 (d, *J* = 7.2 Hz, 4 H, CH_2), 2.10 (m, 2 H, C*H*), 1.76 (m, 2 H, C*H*), 1.46–1.22 (m, 96 H, CH_2), 0.94–0.89 (m, 24 H, CH_3) ppm. ^{13}C NMR (151 MHz, d_2-TCE, 390 K): 163.4, 163.1, 162.7, 161.7, 155.1, 152.0, 134.1, 134.0, 133.2, 133.1, 131.3, 130.5, 130.2, 130.1, 129.3, 128.8, 128.3, 127.7, 126.8, 125.6, 124.9, 123.4, 123.3, 123.0, 122.90, 122.88, 122.6, 122.4, 121.9, 119.2, 44.7, 44.5, 36.7, 36.4, 31.99, 31.98, 31.8, 31.53, 31.49, 31.48, 31.37, 29.8, 29.6, 29.4, 29.3, 29.2, 29.1, 28.9, 28.8, 26.39, 26.36, 26.23, 26.17, 22.20, 22.16, 13.52, 13.49 ppm. UV/Vis ($CHCl_3$, nm): λ_{max} (ε_{max} M^{-1} cm^{-1}) = 549 (85700), 512 (65700). HRMS (ESI, pos. mode, acetonitrile/chloroform): *m/*z 1882.1476 [*M*+Na]$^+$, calcd. for $C_{124}H_{154}N_4NaO_{10}^+$: 1882.1557.

Bis-PBI 4(*S*)

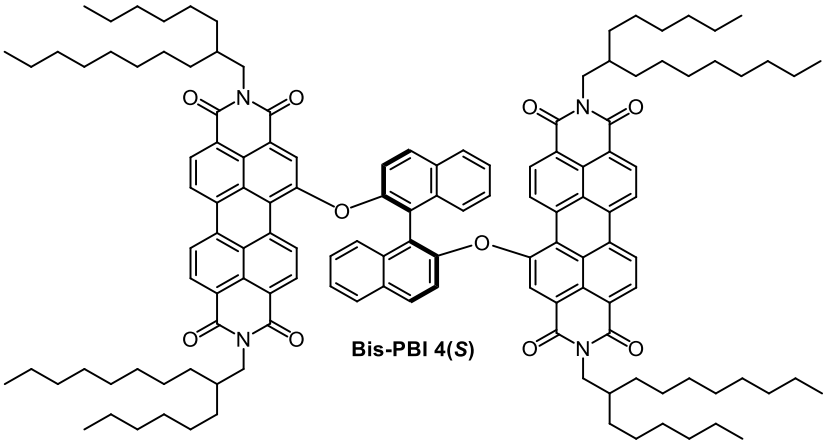

Bis-PBI 4(*S*) was synthesized according to the general procedure described above stirring *N*,*N*´-bis(2-*n*-hexyldecyl)-1-bromoperylene-3,4:9,10-tetraccarboxylicacid-bisimide **33** (200 mg, 216 μmol), (*S*)-binaphthol **35** (103 mg, 103 μmol) and sodium hydride (7.00 mg, 310 μmol) at 60 °C for 72 h to give desired **Bis-PBI 4(*S*)** (61.0 mg, 31.1 μmol, 30%) as a red solid. Mp. 233 – 235 °C. ^{1}H NMR (600 MHz, d_2-TCE, 390K): δ = 9.10 (d, *J* = 8.1 Hz, 2 H, perylene-*H*), 8.75 (d, *J* = 8.1 Hz, 2 H, perylene-*H*), 8.62–8.64 (m, 4 H, perylene-*H*) 8.53 (d, *J* = 8.1 Hz, 2 H, perylene-*H*), 8.11 (d, *J* = 8.1 Hz, 2 H, perylene-*H*), 7.92–7.89 (m, 4 H, binaphthol-*H*), 7.86 (s, 2 H, binaphthol-*H*), 7.60–7.57 (m, 2 H, binaphthol-*H*), 7.51–7.47 (m, 4 H, binaphthol-*H*), 7.31 (d, *J* = 8.1 Hz, 2 H, perylene-*H*), 4.18 (m, 4 H, CH_2), 3.78–3.74 (m, 2 H, CH_2), 3.42–3.37 (m, 2 H, CH_2), 2.13–2.10 (m, 2 H, C*H*), 1.72–1.71 (m, 2 H, C*H*), 1.49–1.14 (m, 96 H, CH_2), 0.93–0.84 (m, 24 H, CH_3) ppm. ^{13}C NMR (151 MHz, d_2-TCE, 390 K): 163.6, 163.3, 162.7, 161.6, 155.6, 134.3, 134.24, 134.17, 133.2, 131.3, 131.1, 130.9, 130.4, 129.2, 128.8, 128.3, 128.27, 128.26, 127.4, 126.9, 126.0, 125.4, 124.7, 123.4, 123.2, 123.1, 123.0, 122.5, 122.4, 121.8, 120.2, 119.4, 99.5, 44.7, 44.4, 36.6, 36.31, 36.27 ,31.94, 31.93, 31.7, 31.6, 31.51, 31.49, 31.45, 31.41, 31.3, 29.8, 29.7, 29.6, 29.4, 29.3, 29.2, 29.13, 29.07, 28.91, 28.90, 28.85, 28.83, 26.41, 26.37, 26.33, 26.20, 26.17, 26.1, 22.24, 22.22, 22.21, 22.18, 22.1, 13.59, 13.57, 13.56, 13.55, 13.50 ppm. UV/Vis ($CHCl_3$, nm): λ_{max} (ε_{max} M^{-1} cm^{-1}) = 555 (101600), 515 (67200). HRMS (ESI, pos. mode, acetonitrile/chloroform) *m/z*: 1982.18292 [*M*+Na]$^+$, calcd. for $C_{132}H_{158}N_4NaO_{10}^+$, 1982.18702.

Bis-PBI 4(*R*)

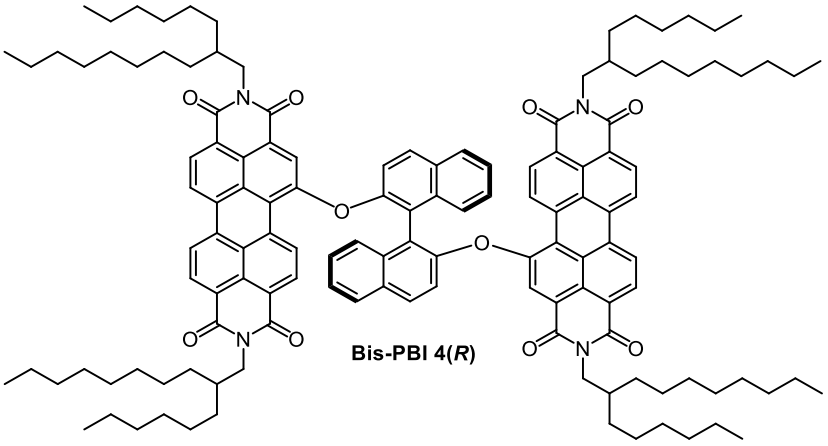

Bis-PBI 4(*R*) was synthesized according to the general procedure described above stirring *N,N´*-bis(2-*n*-hexyldecyl)-1-bromoperylene-3,4:9,10-tetraccarboxylicacidbisimide **33**(200 mg, 216 μmol), (*R*)-binaphthol **36** (103 mg, 103 μmol) and sodium hydride (7.00 mg, 310 μmol) at 50 °C for 76 h to give desired **Bis-PBI 4(*R*)** (46.7 mg, 23.8 μmol, 23%) as a red solid. Mp. 235 – 237 °C. ^{1}H NMR (600 MHz, d$_2$-TCE, 390K): δ = 9.10 (d, *J* = 8.1 Hz, 2 H, perylene-*H*), 8.75 (d, *J* = 8.1 Hz, 2 H, perylene-*H*), 8.65–8.61 (m, 4 H, perylene-*H*), 8.54 (d, *J* = 8.1 Hz, 2 H, perylene-*H*), 8.12 (d, *J* = 8.1 Hz, 2 H, perylene-*H*), 7.92–7.90 (m, 4 H, binaphthol-*H*), 7.90–7.88 (m, 2 H, binaphthol-*H*), 7.60–7.57 (m, 2 H, binaphthol-*H*), 7.51–7.48 (m, 4 H, binaphthol-*H*), 7.32 (d, *J* = 8.1 Hz, 2 H, perylene-*H*), 4.19 (m, 4 H, C*H*$_2$), 3.79–3.76 (m, 2 H, C*H*$_2$), 3.45–3.39 (m, 2 H, C*H*$_2$), 2.12 (m, 2 H, C*H*), 1.75–1.69 (m, 2 H, C*H*), 1.46–1.18 (m, 96 H, C*H*$_2$), 0.93–0.84 (m, 24 H, C*H*$_3$) ppm. ^{13}C NMR (151 MHz, d$_2$-TCE, 390 K): 163.6, 163.3, 162.7, 161.7, 155.6, 149.9, 134.3, 134.24, 134.16 133.2, 131.3. 131.1, 130.9, 130.4, 129.2, 128.8, 128.3, 128.2, 127.4, 126.9, 125.9, 125.4, 124.7, 123.4, 123.2, 123.1, 123.0, 122.5, 122.4, 121.84, 121.78, 120.2, 119.4, 99.5, 44.7, 44.4, 36.7, 36.34, 36.31, 31.98, 31.96, 31.7, 31.52, 31.48, 31.46, 31.42, 31.38, 31.32, 29.7, 29.63, 29.58, 29.4, 29.33, 29.31, 29.2, 29.1, 29.0, 28.88, 28.87, 28.82, 28.80, 26.41, 26.37, 26.33, 26.19, 26.18, 26.12, 26.09, 22.21, 22.17, 22.15, 22.11, 13.53, 13.50, 13.48, 13.4 ppm. UV/Vis ($CHCl_3$, nm): λ_{max} (ε_{max} M^{-1} cm^{-1}) = 555 (101600), 515 (67200). HRMS (ESI, pos. mode, acetonitrile/chloroform) *m/z*: 1982.1813 [*M*+Na]$^+$, calcd. for $C_{132}H_{158}N_4NaO_{10}^+$, 1982.1870.

Bis-PBI 4(*rac.*)

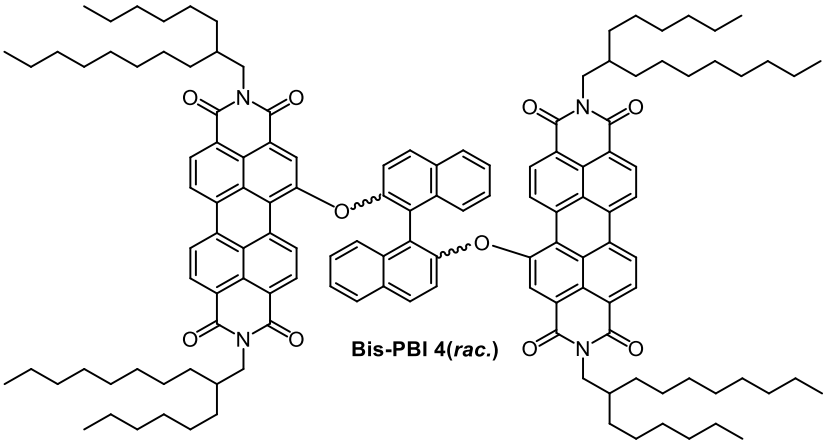

Bis-PBI 4(*rac.*) was synthesized according to the general procedure described above stirring *N*,*N´*-bis(2-*n*-hexyldecyl)-1-bromoperylene-3,4:9,10-tetraccarboxylicacidbisimide **33**(300 mg, 327 μmol), (±)-binaphthol **37** (137 mg, 137 μmol) and sodium hydride (11.0 mg, 410 μmol) at 60 °C for 72 h to give desired **Bis-PBI 4(*rac.*)** (62.5 mg, 31.9 μmol, 20%) as a red solid. Mp. 232 – 234 °C. ^{1}H NMR (600 MHz, d_2-TCE, 390K): δ = 9.09 (d, *J* = 8.2 Hz, 2 H, perylene-*H*), 8.74 (d, *J* = 8.2 Hz, 2 H, perylene-*H*), 8.63–8.60 (m, 4 H, perylene-*H*), 8.52 (d, *J* = 8.2 Hz, 2 H, perylene-*H*), 8.10 (d, *J* = 8.2 Hz, 2 H, perylene-*H*), 7.91–7.87 (m, 6 H, binaphthol-*H*), 7.57–7.56 (m, 2 H, binaphthol-*H*), 7.49–7.46 (m, 4 H, binaphthol-*H*), 7.30 (d, *J* = 8.2 Hz, 2 H, perylene-*H*), 4.18 (m, 4 H, CH_2), 3.78–3.74 (m, 2 H, CH_2), 3.43–3.39 (m, 2 H, CH_2), 2.12–2.08 (m, 2 H, C*H*), 1.73–1.69 (m, 2 H, C*H*), 1.50–1.14 (m, 96 H, CH_2), 0.93–0.83 (m, 24 H, CH_3) ppm^{13}C NMR (151 MHz, d_2-TCE, 390 K): 163.6, 163.3, 162.8, 161.7, 155.6, 149.9, 134.4, 134.3, 134.2, 133.2, 131.3, 131.1, 130.9, 130.4, 129.3, 128.9, 128.30, 128.27, 127.4, 127.0, 126.0, 125.4, 124.8, 123.5, 123.2, 123.2, 123.0, 122.6, 122.4, 121.9, 121.8, 119.4, 44.8, 44.5, 36.7, 36.39, 36.36, 32.03, 32.02, 31.8, 31.6, 31.52, 31.50, 31.47, 31.42, 31.36, 29.8, 29.7, 29.6, 29.40, 29.36, 29.29, 29.23, 29.22, 29.14, 29.09, 28.92, 28.91, 28.86, 28.8, 26.45, 26.42, 26.41, 26.38, 26.24, 26.22, 26.16, 26.14, 22.24, 22.22, 22.21, 22.18, 22.14, 13.56, 13.54, 13.52, 13.48 ppm. HRMS (ESI, pos. mode, acetonitrile/chloroform) *m/*z: 1982.18421 [*M*+Na]$^{+}$, calcd. for $C_{132}H_{158}N_4NaO_{10}^{+}$, 1982.18702.

Bis-PBI 5

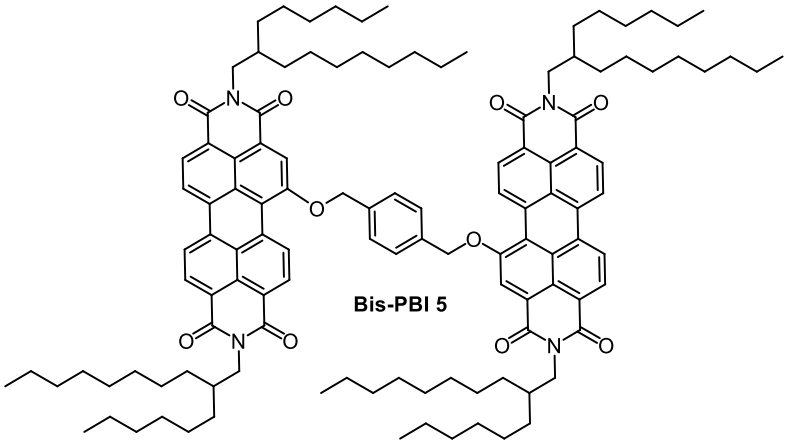

Bis-PBI 5 was synthesized according to the general procedure described above stirring *N*,*N*´-bis-2-*n*-(hexyldecyl)-1-bromperylene-3,4:9,10-tetraccarboxylicbisimid **33** (50 mg, 54.4 μmol), 1,4-benzenemethanole **39** (37.0 mg, 27.2 μmol) and sodium hydride (2.00 mg, 81.6 μmol) at 60 °C for 16 h to give **Bis-PBI 5** (29.8 mg, 16.4 μmol, 60%) as a violet solid. Mp.: 280 – 283 °C. ^{1}H NMR (600 MHz, $C_2D_2Cl_4$, 390 K): δ = 9.65 (d, J = 8.3 Hz, 2 H, perylene-*H*), 8.37–8.63 (m, 10 H, perylene-*H*), 8.59 (d, J = 8.3 Hz, 2 H, perylene-*H*), 7.82 (s, 4 H, *ph*-*H*), 5.73 (s, 4 H, CH_2), 4.23 (d, J = 7.3 Hz, 4 H, CH_2), 4.18 (d, J = 7.2 Hz, 4 H, CH_2), 2.16–2.10 (m, 4 H, C*H*), 1.37–1.30 (m, 96 H, CH_2), 0.93–0.91 (m, 24 H, CH_3) ppm. ^{13}C NMR (151 MHz, $C_2D_2Cl_4$, 390 K): 163.6, 163.5, 163.4, 163.1, 157.3, 136.1, 134.5, 134.1, 134.0, 131.4, 130.4, 129.0, 128.97, 128.6, 128.5, 127.1, 124.6, 124.4, 123.3, 123.2, 123.1, 122.2, 121.8, 121.6, 119.4, 99.6, 45.0, 44.8, 36.72, 36.67, 32.1, 32.04, 32.02, 31.55, 31.52, 31.48, 31.46, 29.75, 29.73, 29.37, 29.36, 29.19, 29.16, 28.89, 28.86, 26.45, 26.43, 26.41, 26.39, 22.22, 22.21, 22.20, 22.19, 13.53, 13.52, 13.51 ppm. UV/Vis ($CHCl_3$, nm): λ_{max} (ε_{max} M^{-1} cm^{-1}) = 551 (89700), 514 (67100). HRMS (ESI, pos. Mode, acetonitrile/ chloroform): *m/*z 1834.15572 $[M+Na]^+$, calcd. for $C_{120}H_{154}N_4NaO_{10}$: 1834.15572.

Bis-PBI 6

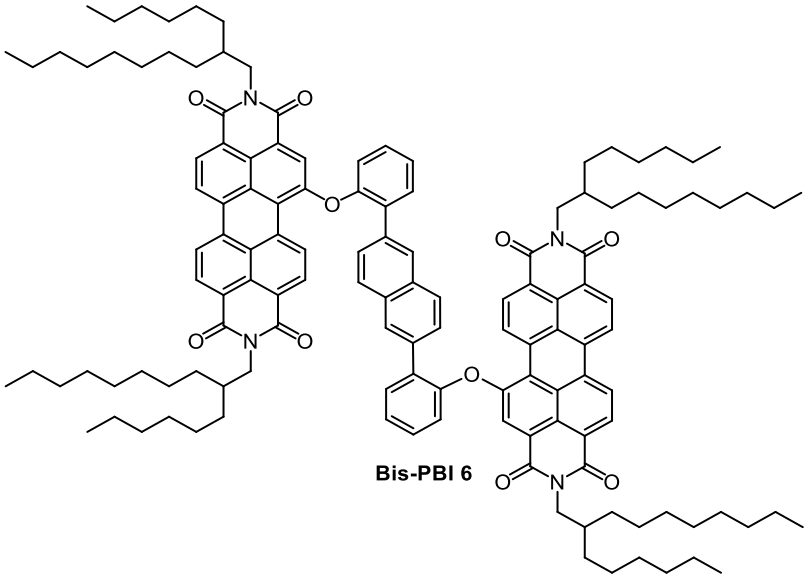

Bis-PBI 6 was synthesized according to the general procedure described above stirring *N*,*N´*-bis(2-*n*-hexyldecyl)-1-bromoperylene-3,4:9,10-tetraccarboxylicacidbisimide **33**, (200 mg, 216 μmol), 2,2´-dihydroxynaphthyldiphenyl **28** (32.0 mg, 104 μmol) and sodium hydride (7.00 mg, 310 μmol) at 45 °C for 42 h to give **Bis-PBI 6** (24.8 mg, 12.5 μmol, 12%) as a violet solid. Mp.: >300 °C. ^{1}H NMR (600 MHz, $C_2D_2Cl_4$, 390 K): δ = 9.21 (d, *J* = 8.3 Hz, 2 H, perylene-*H*), 8.58–8.50 (m, 6 H, perylene-*H*), 8.46 (d, *J* = 8.1 Hz, 2 H, perylene-*H*), 8.40 (d, *J* = 8.3 Hz, 2 H, perylene-*H*), 8.28 (s, 2 H, perylene-*H*), 7.86 (s, 2 H, *ph*-*H*), 7.62–7.60 (m, 2 H, *ph*-*H*), 7.53 (s, 4 H, *ph*-*H*), 7.47–7.44 (m, 4 H, *ph*-*H*), 7.18–7.16 (m, 2 H, *ph*-*H*), 4.13 (d, *J* = 7.3 Hz, 4 H, CH_2), 4.06 (d, *J* = 7.3 Hz, 4 H, CH_2), 2.08–2.04 (m, 4 H, C*H*), 1.41–1.32 (m, 96 H, CH_2), 0.91–0.89 (m, 24 H, CH_3) ppm. ^{13}C NMR (151 MHz, $C_2D_2Cl_4$, 390 K): 163.3, 163.2, 163.1, 162.7, 155.5, 152.0, 135.0, 134.08, 134.04, 134.00, 133.2, 132.1, 131.7, 131.3, 130.3, 129.4, 129.3, 128.7, 128.3, 128.1, 127.7, 127.5, 127.3, 126.7, 125.5, 125.3, 124.1, 123.7, 123.1, 123.0, 122.4, 121.8, 120.2, 119.6, 44.9, 44.6, 36.7, 36.6, 31.99, 31.97, 31.52, 31.51, 31.45, 31.43, 29.7, 29.3, 29.2, 28.9, 26.39, 26.36, 26.34, 26.31, 22.20, 22.19, 22.18, 13.5 ppm. UV/Vis ($CHCl_3$, nm): λ_{max} (ε_{max} M^{-1} cm^{-1}) = 542 (85800), 507 (52000). HRMS (ESI, pos. Mode, acetonitrile/chloroform): *m/*z 2008.20267 $[M+Na]^+$, calcd. for $C_{134}H_{160}N_4NaO_{10}$: 2008.20267.

Bis-PBI 7

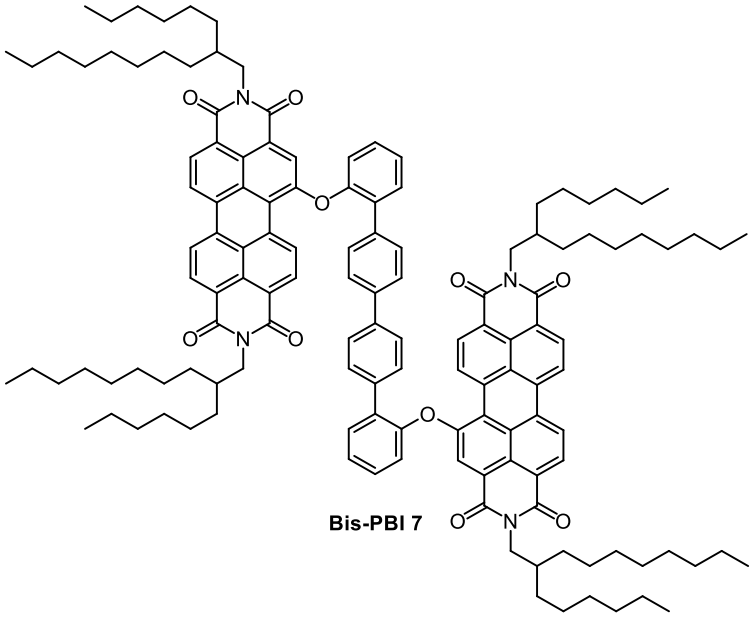

Bis-PBI 7 was synthesized according to the general procedure described above stirring *N,N´*-bis(2-*n*-hexyldecyl)-1-bromoperylene-3,4:9,10-tetraccarboxylicacidbisimide **33**, (100 mg, 108 μmol), 2,2'-dihydroxytetraphenyl **29** (17.5 mg, 51.8 μmol) and sodium hydride (3.70 mg, 155 μmol) at 60 °C for 16 h to give **Bis-PBI 7** (12.4 mg, 6.16 μmol, 12%) as a violet solid. Mp.: > 300 °C. ^{1}H NMR (600 MHz, $C_2D_2Cl_4$, 390 K): δ = 9.46 (d, *J* = 8.4 Hz, 2 H, perylene-*H*), 8.67–8.60 (m, 8 H, perylene-*H*), 8.56 (d, *J* = 8.3 Hz, 2 H, perylene-*H*), 8.26 (s, 2 H, perylene-*H*), 7.63–7.61 (m, 2 H, *ph*-*H*), 7.52–7.51 (m, 4 H, *ph*-*H*), 7.49–7.43 (m, 4 H, *ph*-*H*), 7.26–7.25 (m, 4 H, *ph*-*H*), 7.22–7.20 (m, 2 H, *ph*-*H*), 4.16 (d, *J* = 7.3 Hz, 4 H, CH_2), 4.13 (d, *J* = 7.2 Hz, 4 H, CH_2), 2.10–2.05 (m, 4 H, C*H*), 1.41–1.30 (m, 96 H, CH_2), 0.97–0.88 (m, 24 H, CH_3) ppm. ^{13}C NMR (151 MHz, $C_2D_2Cl_4$, 390 K): 163.5, 163.38, 163.31, 162.8, 155.9, 151.7, 139.11, 136.17, 134.3, 134.2, 134.0, 133.5, 131.7, 131.5, 130.4, 130.3, 129.33, 129.31, 129.2, 128.9, 128.5, 128.2, 126.9, 126.1, 125.7, 125.3, 124.2, 123.5, 123.2, 123.1, 123.0, 122.6, 122.0, 120.2, 120.1, 44.9, 44.7, 36.6, 32.0, 31.9, 31.52, 31.50, 31.45, 31.41, 29.7, 29.35, 29.33, 29.16, 29.13, 28.9, 26.40, 26.36, 26.32, 22.2, 13.5 ppm. UV/Vis ($CHCl_3$, nm): λ_{max} (ε_{max} M^{-1} cm^{-1}) = 543 (85000), 508 (67000). HRMS (ESI, pos. Mode, acetonitrile/ chloroform): *m/*z 2012.23637 $[M+H]^+$, calcd. for $C_{136}H_{163}N_4O_{10:}$ 2012.23637.

Bis-PBI 8

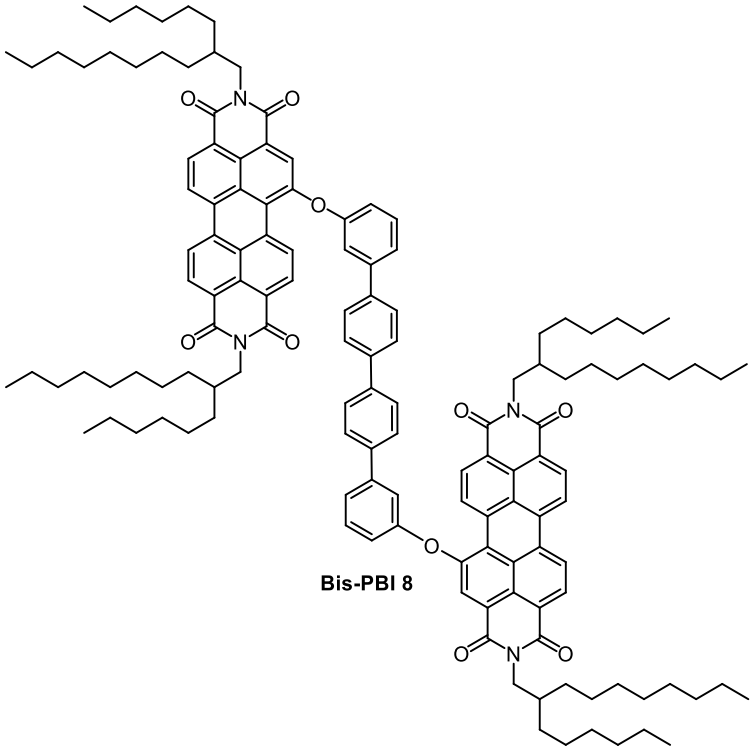

Bis-PBI 8 was synthesized according to the general procedure described above stirring *N*,*N´*-bis(2-*n*-hexyldecyl)-1-bromoperylene-3,4:9,10-tetraccarboxylicacidbisimide **33**, (300 mg, 327 μmol), 3,3´-dihydroxytetraphenyl **30** (52.5 mg, 155 μmol) and sodium hydride (11.0 mg, 465 μmol) at 60 °C for 16 h to give **Bis-PBI 8** (120 mg, 59.6 μmol, 37%) as a violet solid. Mp.: 289 – 293 °C. ^{1}H NMR (600 MHz, $C_2D_2Cl_4$, 390 K): δ = 9.66 (d, *J* = 8.3 Hz, 2 H, perylene-*H*), 8.79 (d, *J* = 8.0 Hz, 2 H, perylene-*H*), 8.77–8.71 (m, 8 H, perylene-*H*), 8.47 (s, 2 H, perylene-*H*), 7.74 (s, 8 H, *ph*-*H*), 7.65–7.59 (m, 4 H, *ph*-*H*), 7.56–7.55 (m, 2 H, *ph*-*H*), 7.24–7.22 (m, 2 H, *ph*-*H*), 4.22 (d, *J* = 7.2 Hz, 4 H, CH_2), 4.18 (d, *J* = 7.2 Hz, 4 H, CH_2), 2.16–2.08 (m, 4 H, C*H*), 1.46–1.30 (m, 96 H, CH_2), 0.93–0.89 (m, 24 H, CH_3) ppm. ^{13}C NMR (151 MHz, $C_2D_2Cl_4$, 390 K): 164.0, 163.8, 163.6, 163.0, 155.9, 155.6, 143.8, 140.2, 139.1, 134.69, 134.64, 133.7, 132.0, 130.87, 130.84, 129.9, 129.3, 128.9, 128.6, 127.6(2), 127.4(2), 127.3, 126.0, 124.8, 124.7, 124.0, 123.97, 123.65, 123.61, 123.56, 123.1, 122.4, 120.4, 118.1, 45.2, 45.0, 36.9, 32.2, 31.7 31.69, 31.66, 29.9, 29.59, 29.56, 29.40, 29.37, 29.1, 26.66, 26.62, 26.5, 22.4, 13.7 ppm. UV/Vis ($CHCl_3$, nm): λ_{max} (ε_{max} M^{-1} cm^{-1}) = 534 (80600), 501 (56400). HRMS (ESI, pos. Mode, methanol/chloroform): *m/*z 2034.2183 $[M+Na]^+$, calcd. for $C_{136}H_{162}N_4NaO_{10}$: 2034. 21832.

References

[1] T. Seki, X. Lin, S. Yagai, *Asian JOC* **2013**, *2*, 708-724.

[2] G. Scheibe, L. Kandler, H. Ecker, *Naturwissenschaften* **1937**, *25*, 75-75.

[3] G. Scheibe, *Angew. Chem.* **1937**, *50*, 212-219.

[4] E. E. Jelley, *Nature* **1937**, *139*, 631.

[5] A. S. Davydov, *Phys. Usp.* **1964**, *7*, 145-178.

[6] M. Kasha, *Radiat. Res.* **1963**, *20*, 55-70.

[7] E. G. McRae, M. Kasha, *Physical Processes in Radiation Biology*, Academic Press, N. Y., **1964**, 23 - 42.

[8] M. Kasha, H. R. Rawls, M. A. El-Bayoumi, *Pure Appl. Chem.* **1965**, *11*, 371-392.

[9] F. Würthner, T. E. Kaiser, C. R. Saha-Möller, *Angew. Chem., Int. Ed.* **2011**, *50*, 3376-3410.

[10] E. A. Margulies, L. E. Shoer, S. W. Eaton, M. R. Wasielewski, *Phys. Chem. Chem. Phys.* **2014**, *16*, 23735-23742.

[11] N. J. Hestand, F. C. Spano, *J. Chem. Phys.* **2015**, *143*, 244707.

[12] B. A. Gregg, M. E. Kose, *Chem. Mater.* **2008**, *20*, 5235-5239.

[13] R. D. Harcourt, K. P. Ghiggino, G. D. Scholes, S. Speiser, *J. Chem. Phys.* **1996**, *105*, 1897-1901.

[14] G. D. Scholes, K. P. Ghiggino, *J. Phys. Chem.* **1994**, *98*, 4580-4590.

[15] H. Yamagata, D. S. Maxwell, J. Fan, K. R. Kittilstved, A. L. Briseno, M. D. Barnes, F. C. Spano, *J. Phys. Chem. C* **2014**, *118*, 28842-28854.

[16] R. P. Fornari, P. Rowe, D. Padula, A. Troisi, *J. Chem. Theory Comput.* **2017**, *13*, 3754-3763.

[17] L.-L. Chua, J. Zaumseil, J.-F. Chang, E. C.-W. Ou, P. K.-H. Ho, H. Sirringhaus, R. H. Friend, *Nature* **2005**, *434*, 194.

[18] D. G. Lidzey, D. D. C. Bradley, M. S. Skolnick, S. Walker, *Synth. Met.* **2001**, *124*, 37-40.

[19] N. J. Hestand, R. V. Kazantsev, A. S. Weingarten, L. C. Palmer, S. I. Stupp, F. C. Spano, *J. Am. Chem. Soc.* **2016**, *138*, 11762-11774.

[20] A. C. Jakowetz, M. L. Böhm, A. Sadhanala, S. Huettner, A. Rao, R. H. Friend, *Nat. Mater.* **2017**, *16*, 551.

[21] S. Das, T. L. Thanulingam, K. G. Thomas, P. V. Kamat, M. V. George, *J. Phys. Chem.* **1993**, *97*, 13620-13624.

[22] Y. Kobuke, H. Miyaji, *J. Am. Chem. Soc.* **1994**, *116*, 4111-4112.

[23] D. M. Eisele, C. W. Cone, E. A. Bloemsma, S. M. Vlaming, C. G. F. van der Kwaak, R. J. Silbey, M. G. Bawendi, J. Knoester, J. P. Rabe, D. A. Vanden Bout, *Nat. Chem.* **2012**, *4*, 655.

[24] J. Megow, M. I. S. Rohr, M. Schmidt am Busch, T. Renger, R. Mitric, S. Kirstein, J. P. Rabe, V. May, *Phys. Chem. Chem. Phys.* **2015**, *17*, 6741-6747.

[25] F. Würthner, C. R. Saha-Möller, B. Fimmel, S. Ogi, P. Leowanawat, D. Schmidt, *Chem. Rev.* **2016**, *116*, 962-1052.

[26] W. Herbst, K. Hunger, *Industrial Organic Pigments: Production, Properties, Applications*, 2nd ed, WILEY-VCH Weinheim, **1997**.

[27] F. Würthner, *Chem. Comm.* **2004**, 1564-1579.

[28] C. Huang, S. Barlow, S. R. Marder, *J. Org. Chem.* **2011**, *76*, 2386-2407.

[29] X. Zhan, A. Facchetti, S. Barlow, T. J. Marks, M. A. Ratner, M. R. Wasielewski, S. R. Marder, *Adv. Mater.* **2011**, *23*, 268-284.

[30] Z. Liu, G. Zhang, Z. Cai, X. Chen, H. Luo, Y. Li, J. Wang, D. Zhang, *Adv. Mater.* **2014**, *26*, 6965-6977.

[31] Y. Zhong, M. T. Trinh, R. Chen, G. E. Purdum, P. P. Khlyabich, M. Sezen, S. Oh, H. Zhu, B. Fowler, B. Zhang, W. Wang, C.-Y. Nam, M. Y. Sfeir, C. T. Black, M. L. Steigerwald, Y.-L. Loo, F. Ng, X. Y. Zhu, C. Nuckolls, *Nat. Commun.* **2015**, *6*, 8242.

[32] D. Meng, D. Sun, C. Zhong, T. Liu, B. Fan, L. Huo, Y. Li, W. Jiang, H. Choi, T. Kim, J. Y. Kim, Y. Sun, Z. Wang, A. J. Heeger, *J. Am. Chem. Soc.* **2016**, *138*, 375-380.

[33] Z. Chen, A. Lohr, C. R. Saha-Moller, F. Würthner, *Chem. Soc. Rev.* **2009**, *38*, 564-584.

[34] C. Shao, M. Stolte, F. Würthner, *Angew. Chem., Int. Ed.* **2013**, *52*, 7482-7486.

[35] C. Shao, M. Stolte, F. Würthner, *Angew. Chem., Int. Ed.* **2013**, *52*, 10463-10467.

[36] B. Fimmel, M. Son, Y. M. Sung, M. Grüne, B. Engels, D. Kim, F. Würthner, *Chem. Eur. J.* **2015**, *21*, 615-630.

[37] J. M. Giaimo, J. V. Lockard, L. E. Sinks, A. M. Scott, T. M. Wilson, M. R. Wasielewski, *J. Phys. Chem. A* **2008**, *112*, 2322-2330.

[38] S. Samanta, D. Chaudhuri, *J. Phys. Chem. Lett.* **2017**, *8*, 3427-3432.

[39] H. Langhals, *Heterocycles* **1995**, 477-500.

[40] Z. Chen, V. Stepanenko, V. Dehm, P. Prins, L. D. A. Siebbeles, J. Seibt, P. Marquetand, V. Engel, F. Würthner, *Chem. Eur. J.* **2007**, *13*, 436-449.

[41] V. Dehm, Z. Chen, U. Baumeister, P. Prins, L. D. A. Siebbeles, F. Würthner, *Org. Lett.* **2007**, *9*, 1085-1088.

[42] T. E. Kaiser, H. Wang, V. Stepanenko, F. Würthner, *Angew. Chem., Int. Ed.* **2007**, *46*, 5541-5544.

[43] J. Frenkel, *Phys. Rev.* **1931**, *37*, 17-44.

[44] J. Gierschner, M. Ehni, H.-J. Egelhaaf, B. Milián Medina, D. Beljonne, H. Benmansour, G. C. Bazan, *J. Chem. Phys.* **2005**, *123*, 144914.

[45] X.-F. Zhang, Q. Xi, J. Zhao, *J. Mater. Chem.* **2010**, *20*, 6726-6733.

[46] E. E. Jelley, *Nature (London)* **1936**, *138*, 1009-1010.

[47] S. Ghosh, X.-Q. Li, V. Stepanenko, F. Würthner, *Chem. Eur. J.* **2008**, *14*, 11343-11357.

[48] T. E. Kaiser, V. Stepanenko, F. Würthner, *J. Am. Chem. Soc.* **2009**, *131*, 6719-6732.

[49] F. Würthner, T. E. Kaiser, C. R. Saha-Möller, *Angew. Chem.* **2011**, *123*, 3436-3473.

[50] C. Pierre, Z. Yingjie, T. Raluca, L. Santiago, S. Naomi, M. Stefan, *Chem. Eur. J.* **2014**, *20*, 17143-17151.

[51] L. Xu, H. Misaki, K. Hiroki, S. Tomohiro, M. Yukihiro, N. Ken-ichi, Y. Shiki, *Asian JOC* **2014**, *3*, 128-132.

[52] J. Seibt, P. Marquetand, V. Engel, Z. Chen, V. Dehm, F. Würthner, *Chem. Phys.* **2006**, *328*, 354-362.

[53] J. Seibt, T. Winkler, K. Renziehausen, V. Dehm, F. Würthner, H. D. Meyer, V. Engel, *J. Phys. Chem. A* **2009**, *113*, 13475-13482.

[54] N. J. Hestand, F. C. Spano, *Acc. Chem. Res.* **2017**, *50*, 341-350.

[55] R. L. Fulton, M. Gouterman, *J. Chem. Phys.* **1964**, *41*, 2280-2286.

[56] F. C. Spano, *Acc. Chem. Res.* **2010**, *43*, 429-439.

[57] J. Seibt, V. Dehm, F. Würthner, V. Engel, *J. Chem. Phys.* **2007**, *126*, 164308.

[58] C. M. Pochas, K. A. Kistler, H. Yamagata, S. Matsika, F. C. Spano, *J. Am. Chem. Soc.* **2013**, *135*, 3056-3066.

[59] K. A. Kistler, C. M. Pochas, H. Yamagata, S. Matsika, F. C. Spano, *J. Phys. Chem. B* **2012**, *116*, 77-86.

[60] D. Bialas, C. Brüning, F. Schlosser, B. Fimmel, J. Thein, V. Engel, F. Würthner, *Chem. Eur. J.* **2016**, *22*, 15011-15018.

[61] N. J. Hestand, F. C. Spano, *Chem. Rev.* **2018**, DOI:10.1021/acs.chemrev.1027b00581.

[62] V. Settels, W. Liu, J. Pflaum, R. F. Fink, B. Engels, *J. Comput. Chem.* **2012**, *33*, 1544-1553.

[63] R. D. Harcourt, G. D. Scholes, K. P. Ghiggino, *J. Chem. Phys.* **1994**, *101*, 10521-10525.

[64] H. Yamagata, C. M. Pochas, F. C. Spano, *J. Phys. Chem. B* **2012**, *116*, 14494-14503.

[65] P. M. Kazmaier, R. Hoffmann, *J. Am. Chem. Soc.* **1994**, *116*, 9684-9691.

[66] A. Schubert, V. Settels, W. Liu, F. Würthner, C. Meier, R. F. Fink, S. Schindlbeck, S. Lochbrunner, B. Engels, V. Engel, *J. Phys. Chem. Lett.* **2013**, *4*, 792-796.

[67] J. van Herrikhuyzen, A. Syamakumari, A. P. H. J. Schenning, E. W. Meijer, *J. Am. Chem. Soc.* **2004**, *126*, 10021-10027.

[68] B. Jancy, S. K. Asha, *Chem. Mater.* **2008**, *20*, 169-181.

[69] K. Balakrishnan, A. Datar, R. Oitker, H. Chen, J. Zuo, L. Zang, *J. Am. Chem. Soc.* **2005**, *127*, 10496-10497.

[70] K. Balakrishnan, A. Datar, T. Naddo, J. Huang, R. Oitker, M. Yen, J. Zhao, L. Zang, *J. Am. Chem. Soc.* **2006**, *128*, 7390-7398.

[71] Z. Chen, B. Fimmel, F. Würthner, *Org. Biomo. Chem.* **2012**, *10*, 5845-5855.

[72] S. Changzhun, G. Matthias, S. Matthias, W. Frank, *Chem. Eur. J.* **2012**, *18*, 13665-13677.

[73] F. Würthner, C. Thalacker, S. Diele, C. Tschierske, *Chem. Eur. J.* **2001**, *7*, 2245-2253.

[74] T. F. A. De Greef, M. M. J. Smulders, M. Wolffs, A. P. H. J. Schenning, R. P. Sijbesma, E. W. Meijer, *Chem. Rev.* **2009**, *109*, 5687-5754.

[75] F. Würthner, Z. Chen, V. Dehm, V. Stepanenko, *Chem. Comm.* **2006**, 1188-1190.

[76] H. Langhals, W. Jona, *Angew. Chem., Int. Ed.* **1998**, *37*, 952-955.

[77] S. Demmig, H. Langhals, *Chem. Ber.* **1988**, *121*, 225-230.

[78] M. W. Holman, R. Liu, L. Zang, P. Yan, S. A. DiBenedetto, R. D. Bowers, D. M. Adams, *J. Am. Chem. Soc.* **2004**, *126*, 16126-16133.

[79] H. Langhals, J. Gold, *J. Prakt. Chem.* **1996**, *338*, 654-659.

[80] H. Langhals, A. Hofer, S. Bernhard, J. S. Siegel, P. Mayer, *J. Org. Chem.* **2011**, *76*, 990-992.

[81] H. Langhals, J. Gold, *Liebigs Ann.* **1997**, *1997*, 1151-1153.

[82] K. M. Lefler, K. E. Brown, W. A. Salamant, S. M. Dyar, K. E. Knowles, M. R. Wasielewski, *J. Phys. Chem. A* **2013**, *117*, 10333-10345.

[83] E. A. Margulies, J. L. Logsdon, C. E. Miller, L. Ma, E. Simonoff, R. M. Young, G. C. Schatz, M. R. Wasielewski, *J. Am. Chem. Soc.* **2017**, *139*, 663-671.

[84] C. Hippius, I. H. M. van Stokkum, E. Zangrando, R. M. Williams, M. Wykes, D. Beljonne, F. Würthner, *J. Phys. Chem. C* **2008**, *112*, 14626-14638.

[85] F. Würthner, *Acc. Chem. Res.* **2016**, *49*, 868-876.

[86] A.-B. Bornhof, A. Bauzá, A. Aster, M. Pupier, A. Frontera, E. Vauthey, N. Sakai, S. Matile, *J. Am. Chem. Soc.* **2018**, *140*, 4884-4892.

[87] C. C. Jumper, J. M. Anna, A. Stradomska, J. Schins, M. Myahkostupov, V. Prusakova, D. G. Oblinsky, F. N. Castellano, J. Knoester, G. D. Scholes, *Chem. Phys. Lett.* **2014**, *599*, 23-33.

[88] Z. Liu, Y. Wu, Q. Zhang, X. Gao, *J. Mater. Chem. A* **2016**, *4*, 17604-17622.

[89] W. Jiang, L. Ye, X. Li, C. Xiao, F. Tan, W. Zhao, J. Hou, Z. Wang, *Chem. Comm.* **2014**, *50*, 1024-1026.

[90] L. Ye, W. Jiang, W. Zhao, S. Zhang, Y. Cui, Z. Wang, J. Hou, *Org. Electron.* **2015**, *17*, 295-303.

[91] P. E. Hartnett, H. S. S. R. Matte, N. D. Eastham, N. E. Jackson, Y. Wu, L. X. Chen, M. A. Ratner, R. P. H. Chang, M. C. Hersam, M. R. Wasielewski, T. J. Marks, *Chem. Sci.* **2016**, *7*, 3543-3555.

[92] Q. Yan, Y. Zhou, Y.-Q. Zheng, J. Pei, D. Zhao, *Chem. Sci.* **2013**, *4*, 4389-4394.

[93] Y. Liu, C. Mu, K. Jiang, J. Zhao, Y. Li, L. Zhang, Z. Li, J. Y. L. Lai, H. Hu, T. Ma, R. Hu, D. Yu, X. Huang, B. Z. Tang, H. Yan, *Adv. Mater.* **2015**, *27*, 1015-1020.

[94] M. M. Safont-Sempere, P. Osswald, M. Stolte, M. Grüne, M. Renz, M. Kaupp, K. Radacki, H. Braunschweig, F. Würthner, *J. Am. Chem. Soc.* **2011**, *133*, 9580-9591.

[95] M. M. Safont-Sempere, P. Osswald, K. Radacki, F. Würthner, *Chem. Eur. J.* **2010**, *16*, 7380-7384.

[96] X. Guo, M. D. Watson, *Org. Lett.* **2008**, *10*, 5333-5336.

[97] R. Shukla, S. V. Lindeman, R. Rathore, *Chem. Comm.* **2009**, 5600-5602.

[98] Y. Yang, Y. Wang, Y. Xie, T. Xiong, Z. Yuan, Y. Zhang, S. Qian, Y. Xiao, *Chem. Comm.* **2011**, *47*, 10749-10751.

[99] X. A. Jeanbourquin, A. Rahmanudin, X. Yu, M. Johnson, N. Guijarro, L. Yao, K. Sivula, *ACS Appl. Mater. Interfaces* **2017**, *9*, 27825-27831.

[100] A. Fin, I. Petkova, D. A. Doval, N. Sakai, E. Vauthey, S. Matile, *Org. Biomo. Chem.* **2011**, *9*, 8246-8252.

[101] Q. Yan, D. Zhao, *Org. Lett.* **2009**, *11*, 3426-3429.

[102] V. E. Williams, T. M. Swager, *J. Polym. Sci. A Polym. Chem.* **2000**, *38*, 4669-4676.

[103] G. D. Scholes, G. R. Fleming, A. Olaya-Castro, R. van Grondelle, *Nat. Chem.* **2011**, *3*, 763.

[104] J. Dostál, J. Pšenčík, D. Zigmantas, *Nat. Chem.* **2016**, *8*, 705.

[105] A. Halpin, P. J. M. Johnson, R. Tempelaar, R. S. Murphy, J. Knoester, T. L. C. Jansen, R. J. D. Miller, *Nat. Chem.* **2014**, *6*, 196.

[106] J. Sung, P. Kim, B. Fimmel, F. Würthner, D. Kim, *Nat. Commun.* **2015**, *6*, 8646.

[107] J. Sung, A. Nowak-Król, F. Schlosser, B. Fimmel, W. Kim, D. Kim, F. Würthner, *J. Am. Chem. Soc.* **2016**, *138*, 9029-9032.

[108] A. L. Sisson, N. Sakai, N. Banerji, A. Fürstenberg, E. Vauthey, S. Matile, *Angew. Chem., Int. Ed.* **2008**, *47*, 3727-3729.

[109] W. E. Ford, P. V. Kamat, *J. Phys. Chem.* **1987**, *91*, 6373-6380.

[110] H. Langhals, J. Karolin, L. B-A. Johansson, *J. Chem. Soc. Faraday Trans.* **1998**, *94*, 2919-2922.

[111] Y. Wang, H. Chen, H. Wu, X. Li, Y. Weng, *J. Am. Chem. Soc.* **2009**, *131*, 30-31.

[112] M. Gerecke, G. Bierhance, M. Gutmann, N. P. Ernsting, A. Rosspeintner, *Rev. Sci. Instrum.* **2016**, *87*, 053115.

[113] C. Kaufmann, W. Kim, A. Nowak-Król, Y. Hong, D. Kim, F. Würthner, *J. Am. Chem. Soc.* **2018**, *140*, 4253-4258.

[114] E. Fron, G. Schweitzer, P. Osswald, F. Würthner, P. Marsal, D. Beljonne, K. Mullen, F. C. De Schryver, M. Van der Auweraer, *Photochem. Photobiol. Sci.* **2008**, *7*, 1509-1521.

[115] A. S. Lukas, Y. Zhao, S. E. Miller, M. R. Wasielewski, *J. Phys. Chem. B* **2002**, *106*, 1299-1306.

[116] R. Tempelaar, F. C. Spano, J. Knoester, T. L. C. Jansen, *J. Phys. Chem. Lett.* **2014**, *5*, 1505-1510.

[117] F. C. Spano, H. Yamagata, *J. Phys. Chem. B* **2011**, *115*, 5133-5143.

[118] R. F. Fink, J. Seibt, V. Engel, M. Renz, M. Kaupp, S. Lochbrunner, H.-M. Zhao, J. Pfister, F. Würthner, B. Engels, *J. Am. Chem. Soc.* **2008**, *130*, 12858-12859.

[119] J. Hoche, H.-C. Schmitt, A. Humeniuk, I. Fischer, R. Mitric, M. I. S. Rohr, *Phys. Chem. Chem. Phys.* **2017**, *19*, 25002-25015.

[120] E. G. McRae, M. Kasha, *J. Chem. Phys.* **1958**, *28*, 721-722.

[121] E. Collini, G. D. Scholes, *J. Phys. Chem. A* **2009**, *113*, 4223-4241.

[122] E. Collini, G. D. Scholes, *Science* **2009**, *323*, 369-373.

[123] N. Banerji, *J. Mater. Chem. C* **2013**, *1*, 3052-3066.

[124] J. M. Lim, P. Kim, M.-C. Yoon, J. Sung, V. Dehm, Z. Chen, F. Würthner, D. Kim, *Chem. Sci.* **2013**, *4*, 388-397.

[125] M. Son, K. H. Park, C. Shao, F. Würthner, D. Kim, *J. Phys. Chem. Lett.* **2014**, *5*, 3601-3607.

[126] S. T. Hoffmann, F. Jaiser, A. Hayer, H. Bässler, T. Unger, S. Athanasopoulos, D. Neher, A. Köhler, *J. Am. Chem. Soc.* **2013**, *135*, 1772-1782.

[127] D. M. Coles, N. Somaschi, P. Michetti, C. Clark, P. G. Lagoudakis, P. G. Savvidis, D. G. Lidzey, *Nat. Mater.* **2014**, *13*, 712.

[128] G. D. Scholes, G. Rumbles, *Nat. Mater.* **2006**, *5*, 683.

[129] T. Brixner, R. Hildner, J. Köhler, C. Lambert, F. Würthner, *Adv. Energy Mater.* **2017**, 1700236.

[130] A. C. Grimsdale, M. Klaus, *Angew. Chem., Int. Ed.* **2005**, *44*, 5592-5629.

[131] C. Flors, I. Oesterling, T. Schnitzler, E. Fron, G. Schweitzer, M. Sliwa, A. Herrmann, M. van der Auweraer, F. C. de Schryver, K. Müllen, J. Hofkens, *J. Phys. Chem. C* **2007**, *111*, 4861-4870.

[132] M. Haase, C. G. Hubner, F. Nolde, K. Mullen, T. Basche, *Phys. Chem. Chem. Phys.* **2011**, *13*, 1776-1785.

[133] G. Marcel, B. David, H. Lizhen, S. Matthias, W. Frank, *Adv. Mater.* **2016**, *28*, 3615-3645.

[134] F. Jiajing, J. Wei, W. Zhaohui, *Chem. Asian J.* **2018**, *13*, 20-30.

[135] C. Yan, S. Barlow, Z. Wang, H. Yan, A. K. Y. Jen, S. R. Marder, X. Zhan, *Nat. Rev. Mater.* **2018**, *3*, 18003.

[136] M. R. Wasielewski, *Acc. Chem. Res.* **2009**, *42*, 1910-1921.

[137] W. Tanja, V. Tom, H. Johan, P. Kalina, M. Klaus, *Angew. Chem., Int. Ed.* **2010**, *49*, 9068-9093.

[138] M. Signoretto, N. Zink-Lorre, I. Suárez, E. Font-Sanchis, Á. Sastre-Santos, V. S. Chirvony, F. Fernández-Lázaro, J. P. Martínez-Pastor, *ACS Photonics* **2017**, *4*, 114-120.

[139] S. Betzold, S. Herbst, A. A. P. Trichet, J. M. Smith, F. Würthner, S. Höfling, C. P. Dietrich, *ACS Photonics* **2018**, *5*, 90-94.

[140] C. Li, M. Liu, N. G. Pschirer, M. Baumgarten, K. Müllen, *Chem. Rev.* **2010**, *110*, 6817-6855.

[141] J. Gierschner, S. Y. Park, *J. Mater. Chem. C* **2013**, *1*, 5818-5832.

[142] A. Austin, N. J. Hestand, I. G. McKendry, C. Zhong, X. Zhu, M. J. Zdilla, F. C. Spano, J. M. Szarko, *J. Phys. Chem. Lett.* **2017**, *8*, 1118-1123.

[143] L. Gisslén, R. Scholz, *Phys. Rev. B* **2009**, *80*, 115309.

[144] G. Klebe, F. Graser, E. Hädicke, J. Berndt, *Acta. Cryst. B* **1989**, *45*, 69-77.

[145] H. Yamagata, J. Norton, E. Hontz, Y. Olivier, D. Beljonne, J. L. Brédas, R. J. Silbey, F. C. Spano, *J. Chem. Phys.* **2011**, *134*, 204703.

[146] J. Gierschner, L. Lüer, B. Milián-Medina, D. Oelkrug, H.-J. Egelhaaf, *J. Phys. Chem. Lett.* **2013**, *4*, 2686-2697.

[147] N. I. Krimer, D. Rodrigues, H. B. Rodríguez, M. Mirenda, *Analyt. Chem.* **2017**, *89*, 640-647.

[148] F. Fennel, J. Gershberg, M. Stolte, F. Würthner, *Phys. Chem. Chem. Phys.* **2018**, *20*, 7612-7620.

[149] V. Dehm, M. Buchner, J. Seibt, V. Engel, F. Würthner, *Chem. Sci.* **2011**, *2*, 2094-2100.

[150] Z. Yu, S. Hecht, *Chem. Comm.* **2016**, *52*, 6639-6653.

[151] X. Li, N. Markandeya, G. Jonusauskas, N. D. McClenaghan, V. Maurizot, S. A. Denisov, I. Huc, *J. Am. Chem. Soc.* **2016**, *138*, 13568-13578.

[152] M. Ball, B. Fowler, P. Li, L. A. Joyce, F. Li, T. Liu, D. Paley, Y. Zhong, H. Li, S. Xiao, F. Ng, M. L. Steigerwald, C. Nuckolls, *J. Am. Chem. Soc.* **2015**, *137*, 9982-9987.

[153] S. Peter, W. Frank, *Angew. Chem., Int. Ed.* **2015**, *54*, 10165-10168.

[154] X. Gong, R. M. Young, K. J. Hartlieb, C. Miller, Y. Wu, H. Xiao, P. Li, N. Hafezi, J. Zhou, L. Ma, T. Cheng, W. A. Goddard, O. K. Farha, J. T. Hupp, M. R. Wasielewski, J. F. Stoddart, *J. Am. Chem. Soc.* **2017**, *139*, 4107-4116.

[155] Z. Liu, S. K. M. Nalluri, J. F. Stoddart, *Chem. Soc. Rev.* **2017**, *46*, 2459-2478.

[156] P. Spenst, R. M. Young, B. T. Phelan, M. Keller, J. Dostál, T. Brixner, M. R. Wasielewski, F. Würthner, *J. Am. Chem. Soc.* **2017**, *139*, 2014-2021.

[157] P. Spenst, F. Würthner, *J. Photochem. Photobiol. C* **2017**, *31*, 114-138.

[158] A. J. Jimenez, M.-J. Lin, C. Burschka, J. Becker, V. Settels, B. Engels, F. Würthner, *Chem. Sci.* **2014**, *5*, 608-619.

[159] S. Yagai, M. Usui, T. Seki, H. Murayama, Y. Kikkawa, S. Uemura, T. Karatsu, A. Kitamura, A. Asano, S. Seki, *J. Am. Chem. Soc.* **2012**, *134*, 7983-7994.

[160] J. Knoester, *Proc. Int. Sch. Phys.* **2002**, *149*, 149-186.

[161] P. B. Walczak, A. Eisfeld, J. S. Briggs, *J. Chem. Phys.* **2008**, *128*, 044505.

[162] M. J. Ahrens, M. J. Tauber, M. R. Wasielewski, *J. Org. Chem.* **2006**, *71*, 2107-2114.

[163] P. Osswald, F. Würthner, *J. Am. Chem. Soc.* **2007**, *129*, 14319-14326.

[164] Z. Xie, V. Stepanenko, K. Radacki, F. Würthner, *Chem. Eur. J.* **2012**, *18*, 7060-7070.

[165] T. Vosch, E. Fron, J.-i. Hotta, A. Deres, H. Uji-i, A. Idrissi, J. Yang, D. Kim, L. Puhl, A. Haeuseler, K. Müllen, F. C. De Schryver, M. Sliwa, J. Hofkens, *J. Phys. Chem. C* **2009**, *113*, 11773-11782.

[166] J. Wu, A. Fechtenkötter, J. Gauss, M. D. Watson, M. Kastler, C. Fechtenkötter, M. Wagner, K. Müllen, *J. Am. Chem. Soc.* **2004**, *126*, 11311-11321.

[167] J. Gershberg, F. Fennel, T. H. Rehm, S. Lochbrunner, F. Würthner, *Chem. Sci.* **2016**, *7*, 1729-1737.

[168] F. Weigend, R. Ahlrichs, *Phys. Chem. Chem. Phys.* **2005**, *7*, 3297-3305.

[169] J. A. Stefan Grimme, Stephan Ehrlich, and Helge Krieg, *J. Chem. Phys.* **2010**, *132*, 154104.

[170] L. Meca, D. Řeha, Z. Havlas, *J. Org. Chem.* **2003**, *68*, 5677-5680.

[171] J. C. Chang, *J. Chem. Phys.* **1977**, *67*, 3901-3909.

[172] K. A. Kistler, F. C. Spano, S. Matsika, *J. Phys. Chem. B* **2013**, *117*, 2032-2044.

[173] D. Beljonne, J. Cornil, R. Silbey, P. Millié, J. L. Brédas, *J. Chem. Phys.* **2000**, *112*, 4749-4758.

[174] J.-D. Chai, M. Head-Gordon, *J. Chem. Phys.* **2008**, *128*, 084106.

[175] K. Senthilkumar, F. C. Grozema, F. M. Bickelhaupt, L. D. A. Siebbeles, *J. Chem. Phys.* **2003**, *119*, 9809-9817.

[176] G. te Velde, F. M. Bickelhaupt, E. J. Baerends, C. Fonseca Guerra, S. J. A. van Gisbergen, J. G. Snijders, T. Ziegler, *J. Comput. Chem.* **2001**, *22*, 931-967.

[177] C. Fonseca Guerra, J. G. Snijders, G. te Velde, E. J. Baerends, *Theor. Chem. Acc.* **1998**, *99*, 391-403.

[178] ADF2013, SCM, Theoretical Chemistry, Vrije Universiteit, Amsterdam, The Netherlands, http://www.scm.com.

[179] P. L. Barbieri, P. A. Fantin, F. E. Jorge, *Mol. Phys.* **2006**, *104*, 2945-2954.

[180] J. P. Perdew, K. Burke, Y. Wang, *Phys. Rev. B* **1996**, *54*, 16533-16539.

[181] M. C. Ruiz Delgado, E.-G. Kim, D. A. da Silva Filho, J.-L. Bredas, *J. Am. Chem. Soc.* **2010**, *132*, 3375-3387..

[182] W. Liu, V. Settels, P. H. P. Harbach, A. Dreuw, R. F. Fink, B. Engels, *J. Comput. Chem.* **2011**, *32*, 1971-1981.

[183] J. Vura-Weis, M. A. Ratner, M. R. Wasielewski, *J. Am. Chem. Soc.* **2010**, *132*, 1738-1739.

[184] N. J. Hestand, R. Tempelaar, J. Knoester, T. L. C. Jansen, F. C. Spano, *Phys. Rev. B* **2015**, *91*, 195315.

[185] N. Q. Chako, *J. Chem. Phys.* **1934**, *2*, 644-653.

[186] R. Gvishi, R. Reisfeld, Z. Burshtein, *Chem. Phys. Lett.* **1993**, *213*, 338-344.

[187] R. D. Gaussian 09, M. J. Frisch, G. W. Trucks, H. B. Schlegel, G. E. Scuseria,, J. R. C. M. A. Robb, G. Scalmani, V. Barone, B. Mennucci, G. A. Petersson,, M. C. H. Nakatsuji, X. Li, H. P. Hratchian, A. F. Izmaylov, J. Bloino,, J. L. S. G. Zheng, M. Hada, M. Ehara, K. Toyota, R. Fukuda, J. Hasegawa,, T. N. M. Ishida, Y. Honda, O. Kitao, H. Nakai, T. Vreven, J. A. Montgomery,, J. E. P. Jr., F. Ogliaro, M. Bearpark, J. J. Heyd, E. Brothers, K. N. Kudin, V. N., R. K. Staroverov, J. Normand, K. Raghavachari, A. Rendell, J. C. Burant, S., J. T. S. Iyengar, M. Cossi, N. Rega, J. M. Millam, M. Klene, J. E. Knox, J. B., V. B. Cross, C. Adamo, J. Jaramillo, R. Gomperts, R. E. Stratmann, O. Yazyev,, R. C. A. J. Austin, C. Pomelli, J. W. Ochterski, R. L. Martin, K. Morokuma, V., G. A. V. G. Zakrzewski, P. Salvador, J. J. Dannenberg, S. Dapprich, A. D. Daniels,, J. B. F. Ö. Farkas, J. V. Ortiz, J. Cioslowski, and D. J. Fox, Gaussian, Inc.,, Wallingford CT.

[188] E. A. Cobar, R. Z. Khaliullin, R. G. Bergman, M. Head-Gordon, *Proc. Natl. Acad. Sci. U.S.A.* **2007**, *104*, 6963-6968.

[189] L. Tian, C. Feiwu, *J. Comput. Chem.* **2012**, *33*, 580-592.

[190] E. P. Kenny, I. Kassal, *J. Phys. Chem. B* **2016**, *120*, 25-32.

[191] E. F. Valeev, V. Coropceanu, D. A. da Silva Filho, S. Salman, J.-L. Brédas, *J. Am. Chem. Soc.* **2006**, *128*, 9882-9886.

[192] R. van der Weegen, P. A. Korevaar, P. Voudouris, I. K. Voets, T. F. A. de Greef, J. A. J. M. Vekemans, E. W. Meijer, *Chem. Comm.* **2013**, *49*, 5532-5534.

[193] H. Yoo, J. Yang, A. Yousef, M. R. Wasielewski, D. Kim, *J. Am. Chem. Soc.* **2010**, *132*, 3939-3944.

[194] W. L. F. Armarego, C. Chai, *Purification of Laboratory Chemicals*, 7th ed., Elsevier, Amsterdam, **2013**.

[195] R. Gvishi, R. Reisfeld, Z. Burshtein, *Chem. Phys. Lett.* **1993**, *213*, 338−344.

[196] G. Seybold, G. Wagenblast, *Dyes Pigm.* **1989**, *11*, 303−317.

[197] R. Schanz, S. A. Kovalenko, V. Kharlanov, N. P. Ernsting, *Appl. Phys. Lett.* **2001**, *79*, 566-568.

[198] L. Zhao, J. Luis Perez Lustres, V. Farztdinov, N. P. Ernsting, *Phys. Chem. Chem. Phys.* **2005**, *7*, 1716-1725.

[199] X.-X. Zhang, C. Würth, L. Zhao, U. Resch-Genger, N. P. Ernsting, M. Sajadi, *Rev. Sci. Instrum.* **2011**, *82*, 063108.

[200] M. Sajadi, M. Quick, N. P. Ernsting, *Appl. Phys. Lett.* **2013**, *103*, 173514.

[201] E. Guillén, J. Hierrezuelo, R. Martínez-Mallorquín, J. M. López-Romero, R. Rico, *Tetrahedron* **2011**, *67*, 2555-2561.

[202] M. Rinke, H. Guesten, H. J. Ache, *J. Phys. Chem.* **1986**, *90*, 2661-2665.

[203] J. Harley-Mason, F. G. Mann, *J. Chem. Soc. (Resumed)* **1940**, 1379-1385.

Danksagung

Im Besonderen gilt mein Dank meinem Doktorvater Prof. Dr. Frank Würthner für die interessante Themenvergabe und seine Unterstützung während meiner gesamten Promotionszeit. Darüber hinaus danke ich für die Bereitstellung des hervorragenden Arbeitsumfeldes, die mir gewährten Freiheiten im Verfolgen eigener Ideen sowie die zahlreichen Diskussionen während der wissenschaftlichen Betreuung meiner Arbeit.

Mein weiterer Dank gilt Herrn. Prof. Dr. Dongho Kim für die reibungslose und vor allem schnelle Zusammenarbeit auf dem gemeinsamen Projekt bis hin zur erfolgreichen Publikation.

Herrn Dr. Matthias Stolte und Dr. David Bialas möchte ich ausdrücklich für die umfangreiche Betreuung meiner Arbeit und die damit verbundenen wertvollen wissenschaftlichen Diskussionen vor allem im Bezug auf spektroskopische sowie theoretische Belange während meiner Arbeit danken. Darüber hinaus bedanke ich mich für die sorgfältige und erstklassige Überarbeitung von Manuskripten sowie die ausgezeichnete Zusammenarbeit beim Publizieren.

Für das Korrekturlesen dieser Arbeit möchte ich mich herzlich bei Herrn Dr. Matthias Stolte, und Herrn Dr. David Bialas bedanken, sowie bei Frau Meike Sapotta und Frau Viktoria Leonhardt.

Mein weiterer Dank gilt Herrn Dr. Vladimir Stepanenko für die Durchführung sowie für die ausführlichen Diskussionen der AFM-Aufnahmen.

Herrn Dr. Matthias Grüne, Frau Patricia Altenberger, Frau Juliane Adelmann und Herrn Marvin Grüne möchte ich für die Durchführung der zahlreichen NMR-Experimente und die stete Hilfsbereitschaft bei auftauchenden Fragen herzlich danken.

Herrn Dr. Michael Büchner, Frau Antje Hautzinger und Frau Juliane Adelmann danke ich vielmals für die Aufnahme der Massenspektren.

Meinen Praktikantinnen Chantal Roger und Regina Drescher, sowie meiner Bachelorstudentin Lena Dietrich danke ich für ihr großes Interesse, Engagement sowie für die hervorragende Zusammenarbeit während ihrer Zeit an meiner Seite im Labor.

Frau Tamara Heinrich möchte ich für ihre talentierte und fleißige synthetische Unterstützung während ihrer Ausbildungszeit danken.

Herrn Joachim Bialas, Frau Jennifer Begall, Frau Anja Hofmann und Frau Petra Seufert-Baumbach danke ich vielmals für das tolle Arbeitsklima und die stete Hilfsbereitschaft im Laboralltag, die das tägliche Arbeiten um einiges erleichtert hat.

Frau Christiana Toussaint und Frau Eleonore Klaus möchte herzlich für die tolle Unterstützung bei allen bürokratischen Angelegenheiten danken.

Außerdem möchte ich mich bei Wolfgang und Marius für die unterhaltsame Atmosphäre im Labor bedanken. Unseren „Schlager-Freitag“ werde ich nicht so schnell vergessen.

Ein besonderer Dank gebührt dem gesamten AK Würthner für das freundschaftliche Arbeitsumfeld und das tolle Arbeitsklima, so dass mir meine Promotionszeit stets in guter Erinnerung bleiben wird.

Viki, Lysanne, Steffi, Andrea und Chantal danke ich für die vielen tollen Abende sowie Mittagspausen während meiner Promotionszeit. Mit Freude kann ich sagen, dass so aus Arbeitskollegen Freunde wurden.

Mein herzlichster Dank gilt meinen Eltern, die mich während des Studiums immer unterstützt und mir dieses erst ermöglicht haben. Außerdem gilt mein uneingeschränkter, ausdrücklicher Dank meinem Partner Jakobus, meinem Bruder Patrick, sowie meiner gesamten Familie und Freunden, die mich während meiner gesamten Studien- und Promotionszeit begleitet haben und mir stets motivierend zur Seite standen.

List of Publications

Discrete π-Stacks of Perylene Bisimide Dyes within Folda-Dimers: Insight into Long- and Short-range Exciton Coupling

C. Kaufmann, D. Bialas, M. Stolte, F. Würthner, *J. Am. Chem. Soc.* **2018**, *140*, 9986−9995.

Ultrafast Exciton Delocalization, Localization and Excimer Formation Dynamics in a Highly Defined Perylene Bisimide Quadruple π-Stack

C. Kaufmann, W. Kim, A. Nowak-Król, Y. Hong, D. Kim, F. Würthner, *J. Am. Chem. Soc.* **2018**, *140*, 4253−4258.

Gauging metal Lewis basicity of zerovalent iron complexes via metal-only Lewis pairs

H. Braunschweig, R. D. Dewhurst, F. Hupp, C. Kaufmann, A. K. Phukan, C. Schneider, Q. Yea, *Chem. Sci.* **2014**, *5*, 4099–4104.

Stepwise versus pseudo-concerted two-electron-transfer in a triarylamine–iridium dipyrrin–naphthalene diimide triad

J. H. Klein, T. L. Sunderland, C. Kaufmann, M. Holzapfel, A. Schmiedel, C. Lambert, *Phys. Chem. Chem. Phys.* **2013**, *15*, 16024-16030.